EXPERIMENTAL INVESTIGATIONS OF DIFFERENTIATION PROCESSES IN THE TERRESTRIAL PLANETS

by

GLENN ALLAN GAETANI

B.S. Geology
University of Massachusetts at Amherst, 1985

M.S. Geology
State University of New York at Albany, 1990

Submitted to the Department of
Earth, Atmospheric, and Planetary Sciences
in Partial Fulfillment of the Requirements for the Degree of

DOCTOR OF PHILOSOPHY

in

GEOLOGY

at the

MASSACHUSETTS INSTITUTE OF TECHNOLOGY

June 1996

Signature of Author _____
Department of Earth, Atmospheric, and Planetary Sciences
May 17, 1996

Certified by _____
Timothy L. Grove
Thesis Supervisor

Accepted by _____
Thomas H. Jordan
Department Head

EXPERIMENTAL INVESTIGATIONS OF DIFFERENTIATION PROCESSES IN THE TERRESTRIAL PLANETS

by

GLENN ALLAN GAETANI

Submitted to the Department of
Earth, Atmospheric, and Planetary Sciences
in Partial Fulfillment of the Requirements for the Degree
of Doctor of Philosophy in Geology

ABSTRACT

Experimental phase equilibria studies are used to place geochemical and petrologic constraints on the processes by which terrestrial planets differentiate into crust, mantle, and core. Chapter 1 presents melting experiments performed at 1.2 to 2.0 GPa to determine the influence of H_2O on partial melting of mantle peridotite. The experimental results indicate that the solidus-lowering effect of H_2O on peridotite has a strong influence on the phase equilibria of hydrous mantle melting. This study places experimental constraints on the conditions of melt generation in subduction zones, and the composition of material added to the crust by convergent margin magmatism. Chapter 2 presents experiments that determine the influence of f_{O_2}/f_{S_2} conditions on olivine/sulfide melt dihedral angles. The results demonstrate that increasing the concentration of oxygen dissolved in an FeS melt lowers the olivine/sulfide interfacial energy enough to produce dihedral angles less than 60° at upper mantle conditions. These experimental results indicate that during the later stages of accretion of the Earth, sulfide may have efficiently segregated from the upper mantle into the core via porous flow. Chapter 3 presents experiments performed over a range of f_{O_2}/f_{S_2} conditions, at constant pressure and temperature, that investigate the partitioning of first series transition metals and W among coexisting silicate melt, sulfide melt, and olivine. The experimental results quantify the effects of variable f_{O_2}/f_{S_2} ratio on partitioning. Trace element modeling performed using the experimentally-determined partition coefficients place constraints on the conditions at which core formation took place in the Earth and Mars. Chapter 4 presents experiments performed in the system CaO-MgO-Al_2O_3-SiO_2 at 1 atm pressure, over a small temperature range, that differentiate crystal-chemical controls on mineral/melt partitioning of rare earth elements from the effects of pressure and temperature. The experimental results demonstrate that the Ca-Tschermakite content of high-Ca clinopyroxene exercises an important control on rare earth element partitioning for pyroxene co-existing with basaltic melt. These results provide a clearer understanding of the geochemical behavior of the rare earth elements during mantle melting and crystallization differentiation of the basaltic magmas that form the oceanic crust.

Thesis Supervisor: Timothy L. Grove
Title: Professor of Geology

To Renée

I couldn't have done it without you.

ACKNOWLEDGMENTS

When I was young my grandmother liked to tell the story of my graduation from kindergarten. All of the graduates were standing in a church parking lot wearing our little red robes while the teacher went around and spoke with each of the families. When she came to us the teacher asked me what I wanted to be when I grew up, to which I replied without hesitation "A scientist". The teacher turned to my family and said "And he will be one too!" For better or worse, I guess that's what I am now. The six years that it took to earn my scientist's union card (also known as a Ph.D.) have enabled me to grow in ways that I never could have anticipated when I first came to MIT. During that time it has been my privilege to learn from an amazing group of people. Tim Grove has been both an advisor and a friend. The breadth of his knowledge and his scientific interests has provided me with the opportunity to work on a wider array of problems than I ever could have imagined 6 years ago. I will be forever grateful that he taught me the value of a good experiment. There is no way to properly acknowledge all of the hours that he spent helping me decide which experiment to do, listening to practice talks, bleeding red ink all over yet another version of some manuscript, looking at thin sections, or just drinking beer. Trekking across Oregon with the Grove family is an experience that I will never forget. Fred Frey's door was always open (well, it was actually slightly ajar), and he was never too busy to talk about some scientific problem, or the rigors of graduate school. His seminars taught me to think objectively and critically about science. Sam Bowring was always there to remind the lab rats about the geology. I also appreciated the fact that his office was messier than mine. Greg Hirth brought an unbridled enthusiasm to bear on every scientific problem and, perhaps more importantly, was always willing to talk baseball. I consider myself lucky to have him as a colleague and a friend. Paul Hess provided a refreshing point of view during my thesis defense. I am grateful to him for letting me know that it was supposed to be "a celebration, not a test". I was nervous anyway. I probably never would have done any of this if it were not for Tony Morse, who sparked my interest in experimental petrology more than 10 years ago.

I owe a debt of thanks to friends and fellow graduate students. Eiichi Takazawa, Huai-Jen Yang, and I arrived at MIT together and finished graduate school together. In the interim, I got to know them as dedicated scientists and great people. I had the unusual privilege of sharing an office with Tom Wagner for more than 5 years. I enjoyed the times we spent talking about science, smoking cigars at Fenway Park, or just being WG's. I don't know if I would have kept my sanity without the friendship of Alberto Saal (a.k.a. the Barbecue King). I will always carry a mental picture of him as a young boy (with a beard) wearing a Batman costume while jumping up and down on the furniture and yelling "It's okay". He is surely Argentina's most valuable export. Ro Kinzler has been a constant source of advice and support. I value her friendship more than she knows. Deb Hassler made every trip to WHOI fun (usually by getting me drunk). Ken Koga gave our office that special smell of stir-fried fish, even though he swore that he was having chicken for lunch. The friendship and support of Ben Hanson has been invaluable. I respect him as much as anyone I know (although I do question his sanity). I thoroughly enjoyed his late night, long distance telephone calls complaining about Mike Hargrove. Barry Croke provided a welcome relief from graduate school as a drinking buddy and fellow baseball

addict. The Friday night beer hours and trips to the Cambridge Brewery with Mike Jercinovic were great. Having Steve Parman and Jim Van Orman in the lab has made the past 2 years fun and interesting. Steve also provided me with a lifetime supply of bubble gum. Neel Chatterjee has been a wonderful addition to the microprobe lab. Living with all of the people in McCormick Hall has really made me feel like a part of MIT society. The friendship of Monica Gupta, Gargi Patel, and Umber Ahmad was especially important.

My family, both immediate and extended, contributed many things in many ways. The love and support of my parents, Nick and Joan Gaetani, through 6 more years of school has been greatly appreciated. I will always be indebted to my father for teaching me, through the way he lives his life, the value of hard work and family. I am also grateful to my in-laws, Bob and Carol Mandarano, for their support and for always being there with a rally when one was needed.

I did not earn this Ph.D. alone. My wife, Renée, made many sacrifices over the past 6 years. She worked at jobs she didn't like, lived in an apartment that was too small, and put up with having a husband who was never home. Her strength and courage during the most difficult times have served as an inspiration to others. This dissertation is dedicated to her. The arrival of Hope Claire has made the past year very special. I will always treasure the mornings I spent trying to feed her rice crispies while Sesame Street was so much more interesting than eating. May she always smile and enjoy life just the way that she does now. She sets an example for us all.

TABLE OF CONTENTS

INTRODUCTION

The terrestrial planets, of which the Earth is a prominent example, are differentiated bodies. Current theories for their origin invoke collisional accumulation of chondritic planetesimals to form a relatively homogeneous mass of silicates and metal (e.g, Safronov, 1969; Wetherill, 1986). Following accretion, processes driven by heat trapped within the juvenile planets produced spectacularly differentiated bodies consisting of a metallic core, a mantle composed dominantly of ferromagnesian silicates, and a crust enriched in silica, alumina, and incompatible elements (elements that partition strongly into silicate melts) (e.g., Ringwood, 1966). Evidence of early differentiation processes has been preserved on the Moon for 4 billion years by its geologic quiescence (e.g., Taylor, 1982). Conversely, clues to early differentiation processes on the Earth, as well as the other large terrestrial planets, have been obscured by subsequent geologic activity (e.g., Bowring and Housh, 1995). This dissertation is comprised of four chapters, each of which provides experimental phase equilibria constraints on the processes by which differentiation takes place in the terrestrial planets, and the conditions under which these processes operate.

The existence of a highly differentiated continental crust sets the Earth apart from all of the other terrestrial planets (Taylor, 1989). The generation of juvenile continental crust at convergent plate margins has been part of geologic dogma for the past 30 years. This hypothesis originally combined the notion that the bulk composition of the continental crust is andesitic with the observed predominance of andesitic lavas in island arc terranes (Taylor, 1967). Although accretion of arc terranes may represent a significant contribution to the growing continents, it is now recognized that arc magmatism contributes basaltic material to the crust (Grove and Kinzler, 1986). The andesites, dacites, and rhyolites associated with convergent margins are products of shallow-level processes, such as fractional crystallization and assimilation of felsic crust. Therefore, any

model for generation of juvenile continental crust at subduction zones requires a quantitative understanding of the compositions of partial melts generated by mantle wedge that has been fluxed by water-rich fluids from the subducted slab. Chapter 1 presents melting experiments performed at 1.2 to 2.0 GPa that place constraints on the nature of peridotite partial melts formed under hydrous conditions. The experimental results demonstrate that hydrous melts are compositionally distinct from anhydrous mantle melts. When compared on an anhydrous basis they are characterized by higher silica and alumina and lower iron and magnesium. The latter results from the strong temperature dependence of the partitioning of iron and magnesium between mantle minerals and basaltic melts and the dramatically lower solidus temperature of mantle peridotite under hydrous conditions. Isobaric batch melting calculations demonstrate that the mantle melting process is strongly dependent on the amount of water in the system. Although melting always starts at the water-saturated solidus (assuming that amphibole is not a stable phase), "wetter" mantles produce a higher percentage of melt at lower temperatures, and these melts are compositionally distinct.

Metallic cores are thought to exist in all of the terrestrial planets (e.g., Jacobs, 1987). Despite their common occurrence, and that they represent a significant mass fraction of each of the terrestrial planets, the origin of planetary cores remains enigmatic due to our limited understanding of the physical and chemical processes involved in segregation of material from mantle to core. Chapters 2 presents an experimental determination of the effect of variable oxygen and sulfur fugacity conditions on dihedral angles formed by sulfide melts in polycrystalline olivine aggregates. These experiments demonstrate that oxygen dissolved in the melt represents an important control on olivine/melt interfacial energy, and that at present-day upper mantle conditions sulfide melts can form an interconnected network at small melt fractions in olivine-rich rocks. Therefore, given the appropriate oxygen and sulfur fugacity conditions, porous flow could

have been an important mechanism for segregating material into the growing core during accretion of the Earth.

The absolute and relative abundances of siderophile elements (elements that partition strongly into metallic phases) in the silicate mantle of a terrestrial planet represent the only direct geochemical evidence relating to the core formation process. Despite its obvious importance, the siderophile element record preserved in the Earth's upper mantle has proved difficult to interpret. In the 30 years since Ringwood first noted their overabundance in mantle rocks (Ringwood, 1966), no consensus has emerged with respect to the origin of the mantle's siderophile element pattern. Chapter 3 presents experiments that determine the effect of variable oxygen and sulfur fugacity conditions on the partitioning of some of the first series transition metals (vanadium, chromium, manganese, cobalt, nickel, and copper) and tungsten among olivine, silicate melt, and sulfide melt. The experimental results demonstrate that the dependence of sulfide melt/silicate melt partition coefficients on oxygen and sulfur fugacity is proportional to the valence state of the element. Application of the experimentally-determined partition coefficients to modeling the segregation of sulfide and metal to form the Earth's core demonstrates that the presence of sulfur in the core does not explain the overabundance of siderophile elements in the Earth's mantle, as had been proposed by Brett (1984). Core formation in the parent body of the Shergottite meteorites (thought to be Mars) can be successfully modeled as segregation of metal and sulfide melt at low pressures, and this model provides an estimate for the size of the Martian core (~20 to 25 weight percent of the planet), and its sulfur content (~0.35 weight percent).

The rare earth elements represent a unique tool for understanding the magmatic processes involved in crust-mantle differentiation. Their utility stems from (1) the smooth, monotonic variation in their mineral/melt partition coefficients as a function of atomic number, (2) the strong affinity of certain rare earths for petrologically important minerals (i.e., divalent europium for plagioclase; heavy rare earths for garnet), (3) their chondritic

relative abundances in the Earth, and (4) their involvement in petrogenetically important isotopic system such as samarium-neodymium and lutetium-hafnium (e.g., McKay, 1989). Chapter 4 presents an experimental determination of the controls exerted by crystal chemistry on the partitioning of the trivalent rare earth elements between basaltic melts and high-calcium clinopyroxene. The experimental results demonstrate the importance of the calcium-Tschermakite component in clinopyroxene for controlling the partitioning behavior of the rare earth elements. The experiments also show that, for basaltic compositions, melt structure does not exert a strong influence on rare earth partitioning.

REFERENCES

Bowring S.A. and Housh T. (1995) The Earth's early evolution. *Science*, **269**, 1535-1540.

Brett R. (1984) Chemical equilibration of the Earth's core and upper mantle. *Geochim. Cosmochim. Acta*, **48**, 1183-1188.

Grove T.L. and Kinzler R.J. (1986) Petrogenesis of andesites. *Ann. Rev. Earth Planet. Sci.*, **14**, 417-454.

Jacobs J.A. (1987) *The Earth's Core.* Academic Press.

McKay G.A. (1989) Partitioning of rare earth elements between major silicate minerals and basaltic melts. In *Geochemistry and Mineralogy of the Rare Earth Elements, Reviews in Mineralogy*, **21** (ed. B.R. Lipin and G.A. McKay), 45-77.

Ringwood A.E. (1966) Chemical evolution of the terrestrial planets. *Geochim. Cosmochim. Acta.*, **30**, 41-104.

Safronov V.S. (1969) *Evolution of the Protoplanetary Cloud and Formation of the Earth and Planets.* Nauka, Moscow (Transl. 1972 NASA TT F-677).

Taylor S.R. (1967) The origin and growth of continents. *Tectonophysics*, **4**, 17-34.

Taylor S.R. (1982) *Planetary Science: A Lunar Perspective.* Lunar and Planetary Institute

Taylor S.R. (1989) Growth of planetary crusts. *Tectonophysics*, **161**, 147-156.

Wetherill G.W. Accumulation of the terrestrial planets and implications concerning lunar origin. In *Origin of the Moon* (ed. W.K. Hartmann, R.J. Phillips, and G.J. Taylor), pp. 519-550. Lunar and Planetary Institute.

CHAPTER 1.

THE INFLUENCE OF WATER ON MANTLE MELTING

ABSTRACT

This study uses melting experiments performed at upper mantle conditions to explore the effects of dissolved H_2O on the compositions of melts saturated with an upper mantle assemblage of olivine, orthopyroxene, clinopyroxene, and spinel or garnet. The compositional changes associated with increasing the concentration of H_2O dissolved in a mantle melt (increasing SiO_2; decreasing MgO and FeO) are opposite to those associated with increasing the pressure of melting. The lower FeO and MgO contents result from the relatively low temperatures at which these melts coexist with a mantle mineral assemblage. Peridotite melting reactions under hydrous conditions are also affected by the lowered mantle solidus. The compositions of orthopyroxene and high-Ca clinopyroxene that coexist at low temperatures are such that a smaller proportion of clinopyroxene is consumed by the spinel lherzolite melting reaction. Therefore, clinopyroxene remains in the mantle residue to a higher extent of partial melting under hydrous conditions (27% partial melting) than under anhydrous conditions (20.7% partial melting). Isobaric batch melting calculations performed for mantles containing varying amounts of H_2O vapor demonstrate that the melting process is a strong function of the bulk H_2O content of the mantle. A mantle containing 0.15 wt% H_2O at 1.5 GPa begins melting at the H_2O-saturated peridotite solidus. The vapor phase is exhausted at 1% partial melting, and a temperature increase of 237°C is required to increase the melt fraction to 5%. This results from the dilution of H_2O as the melt fraction increases. The composition of the partial melt changes significantly over the first few percent partial melting due to decreasing H_2O and increasing temperature. Mantles with higher H_2O contents remain vapor saturated to larger extents of melting, so that more melting occurs at low temperatures and melt compositions are less variable.

INTRODUCTION

Water plays a central role in melt production at subduction zones. Oceanic lithosphere is subducted at convergent plate margins, producing cool mantle downwelling. Flow induced in the mantle wedge by the subducted slab is manifested as high heat flow and active volcanism on the overriding plate (McKenzie, 1969). There are several lines of geological evidence to suggest infiltration of the mantle wedge by H_2O-rich fluids released during dehydration of the subducted oceanic lithosphere (Shcheka and Shcheka, 1973; Tanaka and Aoki, 1979; Vidal et al., 1989; Maury et al., 1992; Stolper and Newman, 1994; Schiano et al., 1995). These fluids have the potential to enrich mantle depleted by previous melting events, to significantly lower the mantle solidus, and to increase melt production rates. The process of melt generation in subduction zones is less well understood than at mid-ocean ridges, where it is thought to result from the decompression of adiabatically ascending mantle peridotite (Klein and Langmuir, 1987; McKenzie and Bickle, 1988; Kinzler and Grove, 1992a,b). To understand the processes involved in subduction zone melt generation, methods must be developed to allow forward modeling of various forms of melt generation under hydrous conditions. An experimental database pertaining to the compositions and liquidus temperatures of hydrous mantle melts is essential for calibrating these models.

This paper presents the results of melting experiments, performed at upper mantle conditions, designed to produce silicate melts in equilibrium with a mantle residual assemblage of olivine (Oliv) + orthopyroxene (Opx) ± clinopyroxene (Cpx) ± spinel (Sp) ± garnet (Gt) (hereafter referred to as multiply-saturated) at anhydrous and H_2O-undersaturated conditions. Comparisons of experiments in which the silicate melt contains varying amounts of dissolved H_2O provide insights into the effects of H_2O on the temperature of the peridotite solidus, the stoichiometry of mantle melting reactions, and the compositions of mantle melts. Isobaric batch melting calculations are used to

determine the effects of variable source regions H_2O content on the compositions and liquidus temperatures of mantle melts.

EXPERIMENTAL AND ANALYTICAL METHODS

Starting Materials

Starting materials consisted of natural rock powder, hydrous basaltic glass, and synthetic peridotite (Table 1). Three basalts from Medicine Lake volcano and Mount Shasta, in California, were chosen as starting materials. These basalts have molar Mg/(Mg + Fe) values (Mg#) of 0.65 to 0.71, and cover a range of alkali and incompatible element contents (Table 1). Hydrous glasses were prepared by melting natural rock powder at 200 MPa, H_2O-saturated, in a titanium-zirconium-molybdenum rapid quench cold-seal pressure vessel. Twenty-five μl of distilled H_2O were placed in a 32 mm long Au capsule that had been sealed on one end with an arc welder. The capsule was then packed with rock powder and welded shut. The sealed capsule was placed in the bottom of the pressure vessel and pressurized to 150 MPa at room temperature, using a 25:2000 mixture of CH_4 and Ar as a pressure medium. The vessel was placed into a Deltech furnace and the temperature was raised to 1050°C over ~1 hr. Pressure was allowed to increase with increasing temperature until it reached 200 MPa, and then was maintained by bleeding off small amounts of gas. The charge was held at 1050°C for 24 hrs; the experiment was terminated by removing the pressure vessel from the furnace and inverting it so that the capsule slid to the cold end and was rapidly quenched against the cooling head. If the capsule contained liquid H_2O, glass chips from the top and bottom of the charge were mounted in epoxy, polished, and analyzed by electron microprobe. The remaining material was ground under ethanol using an agate mortar and pestle for 1 hr and used as starting material for piston-cylinder experiments. The H_2O content of the glass was determined by summation deficit from electron microprobe analyses. This technique was shown by Sisson and Layne (1993) to be accurate to within ±0.2-0.3 wt%. The proportions of glass

and crystals were then determined by materials balance (Bryan et al., 1969), and the bulk H_2O content of the silicate portion of the charge was calculated.

Three synthetic peridotite compositions were used in this study. Peridotite FP1 was prepared from mantle minerals separated from a spinel lherzolite xenolith (KH-5-4) from Kilbourne Hole, New Mexico. The other two synthetic peridotites (PUM) correspond to the primitive upper mantle composition of Hart and Zindler (1986). One was synthesized from Johnson-Matthey high purity SiO_2, TiO_2, Al_2O_3, Cr_2O_3, Fe_2O_3, MnO, MgO, NiO, and prepared mixes of $CaSiO_3$, Na_2SiO_3, and $K_2Si_4O_9$. These components were weighed out and ground automatically for 5 hrs, under ethanol, using an agate mortar and pestle, after which Fe° sponge was added and the mix was ground for an additional hr (Lindsley et al., 1974). The resulting powder was pressed into 300 mg pellets, using elvanol as a binder, and conditioned by sintering in a gas-mixing furnace for 24 hrs at 1050°C, with the fugacity of oxygen (f_{O_2}) controlled at 1 log unit below the fayalite-magnetite-quartz (FMQ) oxygen buffer. The second peridotite was synthesized from Johnson-Matthey high purity SiO_2, TiO_2, Al_2O_3, Cr_2O_3, MnO, NiO, and prepared mixes of Fe_2SiO_4, $Mg(OH)_2$, $CaSiO_3$, Na_2SiO_3, and $K_2Si_4O_9$. These components were weighed out and ground for 6 hrs, under ethanol, using an automatic mortar and pestle. The $Mg(OH)_2$ was prepared following the methods described by Johnson and Walker (1993). The two PUM peridotites were used to control the H_2O content of the charges by varying the proportions of hydrous glass, hydrous peridotite, and anhydrous peridotite used in the starting mix.

Experimental Methods

Anhydrous and H_2O-undersaturated synthesis experiments were performed at upper mantle conditions (1.2-2.0 GPa; 1100-1370°C). The starting material for each experiment was prepared by weighing out the desired proportions of peridotite and basalt, then grinding them in an agate mortar and pestle under ethanol for 10 min. Experiments

were performed in a 0.5 inch solid-medium piston cylinder device (Boyd and England, 1960), using the piston-in technique (Johannes et al., 1971). The pressure medium consisted of sintered $BaCO_3$, which was found to have a friction correction of 300 MPa by calibrating against the pressure-dependent melting point of Au (Akella and Kennedy, 1971), and the Ca-Tschermakite breakdown reaction (Hays, 1966). This value is in good agreement with the friction correction determined for $BaCO_3$ by Fram and Longhi (1992). A 300 MPa correction has been applied to the pressures reported in Table 2. The temperature was monitored and controlled using $W_{97}Re_3$-$W_{75}Re_{25}$ thermocouples with no pressure correction for thermocouple EMF.

Hydrous melting experiments were performed by packing ~15 mg of starting material into a capsule made of Au (Experiments B310 and B326) or pre-conditioned $Au_{90}Pd_{10}$ or $Au_{80}Pd_{20}$ alloy, and welding it shut. The capsule was placed into a graphite sleeve, and then into an outer capsule made from either $Au_{80}Pt_{20}$ or Pt, depending on the temperature at which the experiment was to be performed. Graphite powder was packed into the outer capsule, and it was welded shut and placed into a high-density Al_2O_3 sleeve. This assembly was then centered in the hotspot of a graphite furnace using MgO spacers, and an MgO wafer was used to separate the thermocouple from the top of the capsule. The temperature difference between the position of the thermocouple and the hotspot was determined to be 20°C using offset thermocouples; the temperatures reported in Table 2 are corrected for this temperature difference.

Anhydrous experiments were performed by packing ~6 mg of starting material into a graphite capsule and placing a graphite lid on top. This assembly was placed into a Pt capsule that had been welded shut on the bottom, and then into a drying oven and held at 120°C for 14 to 65 hrs. The assembly was then removed from the oven, dried graphite powder was packed on top of the capsule, and the Pt capsule was welded shut. The capsule was then placed into an assembly identical to that used for the hydrous melting experiments.

Capsule Materials

Maintaining constant bulk composition is a prerequisite for producing an equilibrated experimental product. Capsules fabricated from Au are a good choice for hydrous melting experiments because they minimize loss of Fe from the charge to the capsule and they are less permeable to hydrogen than Pt, Ag, or AgPd alloys (Chou, 1985). Because the majority of our experiments were performed at temperatures in excess of the melting point of Au, AuPd alloys were used as capsule materials. The 0.1 MPa melting points for $Au_{90}Pd_{10}$ and $Au_{80}Pd_{20}$ alloys are 1220°C and 1350°C respectively, while Au melts at 1064°C (Hansen, 1958).

Iron loss from the silicate to unconditioned $Au_{90}Pd_{10}$ capsules was determined to be 30% relative after 24 hrs at 1.2 GPa, 1200°C, while in unconditioned $Au_{80}Pd_{20}$ capsules Fe loss from the silicate was 38% relative. Hirose and Kawamoto (1995) performed hydrous peridotite melting experiments in $Au_{75}Pd_{25}$ capsules and reported no loss of Fe from the silicate. This is attributable to the oxidizing conditions at which their experiments were performed (at or above the hematite-magnetite oxygen buffer; T. Kawamoto, pers. comm.). The solubility of Fe in AuPd alloys is a strong function of f_{O_2} (Kawamoto and Hirose, 1994), and unconditioned AuPd alloys do not behave as inert containers at the conditions of our experiments. The graphite in our assembly controls the f_{O_2} in the charge at conditions comparable to those in anhydrous experiments performed in graphite capsules through diffusion of O_2 along grain boundaries in the walls of the inner capsule.

Maintaining a constant bulk composition over the course of an experiment required that each inner capsule be pre-conditioned to minimize Fe exchange with the silicate. For experiments in which the $Au_{80}Pd_{20}$ alloy was used, this was accomplished by packing the capsule with 82-72f rock powder, placing it into an open MgO crucible, and hanging it in the hotspot of a vertical gas mixing furnace for 48 hrs. The temperature was held at 1250°C and the f_{O_2} was controlled at 1 log unit below the FMQ buffer. The

silicate melt had a strong tendency to climb out of the metal capsules, so that they had to be removed from the furnace and repacked with rock powder every 2-3 hrs until the melt remained in place. After completion of the conditioning run, the silicate glass was carefully chipped out of the capsule. The capsule was then placed into an ultrasonic cleaner for 2-3 hrs in a warm bath of HF and dilute HNO_3. The ternary alloy in the capsule from experiment B304, which experienced negligible Fe exchange with the silicate after 24 hrs at 1.2 GPa, 1215°C, consists of 78.2±0.6 wt% Au, 19.9±0.2 wt% Pd, and 1.35±0.05 wt% Fe.

The conditioning procedure was modified slightly for $Au_{90}Pd_{10}$ alloy due to its lower melting point (~1225°C versus ~1350°C for $Au_{80}Pd_{20}$ at 1 atm). For these capsules, a silicate melt with similar FeO content (7.23 wt% versus 7.82 wt%) but significantly lower MgO (4.45 wt% versus 10.49 wt%) was used to produce a large amount of melt at a lower temperature. These conditioning runs were performed for 72 hrs at 1155°C, with f_{O_2} controlled at 2 log units below FMQ. The ternary alloy in the capsule from experiment B359, which experienced negligible Fe exchange with the silicate after 20 hrs at 1.6 GPa, 1260°C, consists of 88.5±0.6 wt% Au, 10.0±0.1 wt% Pd, and 0.68±0.01 wt% Fe.

Analytical Methods

All experimental run products were analyzed using either a 4- or 5-spectrometer JEOL 733 Superprobe at the Massachusetts Institute of Technology. A 10 nA beam current and 15 kV accelerating voltage were used for all analyses. Beam widths were 20 μm for hydrous glasses, 10-20 μm for anhydrous glasses, and 1 μm for crystalline phases. On-line data reduction was accomplished using the phi-rho-z correction scheme. Migration of Na during the analysis of hydrous glasses was minimized through use of a defocused beam and by measuring Na for 5 s prior to measuring the other elements (Sisson and Grove, 1993a). Maximum counting times for the other elements was 40 s.

Replicate analyses of basaltic glass from an anhydrous, 1 atm melting experiment (Experiment 839b-23 of Gaetani et al., 1994) were used to estimate analytical precision. One standard deviation for 370 replicate analyses performed over 33 months expressed as percent relative are 0.53% for SiO_2, 0.92% for Al_2O_3, 0.97% for CaO, 1.3% for MgO, 2.1% for FeO, 4.6% for TiO_2, 6.2% for Na_2O, 7.7% for K_2O, 33% for MnO, 42% for Cr_2O_3, and 67% for P_2O_5. The mean sum for the 370 analyses is 100.06 wt% (Table 4). Replicate analyses of natural basalt glass 70-002 were used to determine whether use of updated standards and the phi-rho-z correction scheme results in systematic deviations from other analyses performed at MIT. A comparison of the mean of 30 replicate analyses with the analysis of the same glass reported by Kinzler and Grove (1992a) is given in Table 4.

EXPERIMENTAL RESULTS

Approach to Equilibrium

Several lines of evidence can be used to evaluate the approach to equilibrium represented by our experiments. First, a reversal of mineral compositions was performed. Experiment B359 was carried out at 1.6 GPa, 1260°C, using hydrous 82-72f glass and PUM peridotite, which was synthesized from oxides, while Experiment B277 was carried out at 1.6 GPa, 1255°C using hydrous 82-72f glass and FP1 peridotite, which was synthesized from mantle minerals. The use of different peridotites means that the minerals in Experiment B359 crystallized from the hydrous glass and synthetic oxide mix starting materials, while those in Experiment B277 (with the exception of Gt) reequilibrated through exchange among the melt and mantle minerals. There is good agreement between the compositions of the crystalline phases in the two experiments (Table 3), indicating that diffusion rates are fast enough under hydrous conditions to reequilibrate the rims of the mineral grains in 10 hrs. The cores of the larger pyroxene grains in Experiment B277 have compositions similar to the starting material, indicating that bulk equilibration of the

charge was not achieved. The agreement between the melt compositions suggests that experimental durations were sufficient to allow a close approach to equilibrium at hydrous conditions.

Several other criteria can be used to establish the approach to equilibrium in our experiments. Bulk composition was maintained, which is essential for equilibration. The average exchange $K_D^{Fe/Mg}$ values ($K_D^{Fe/Mg} = [FeO^{crystal} \times MgO^{melt}]/[FeO^{melt} \times MgO^{crystal}]$) for olivine (0.34±0.01), clinopyroxene (0.33±0.02), orthopyroxene (0.32±0.02), spinel (0.60±0.13), and garnet (0.61±0.03) are in agreement with those from the longer duration, anhydrous experiments of Kinzler (1996). This observation indicates that experimental durations were sufficient to achieve equilibrium with respect to mineral/melt exchange of Fe and Mg. Replicate analyses of the glass in the charges demonstrate that the majority of the experimentally-produced silicate melts are homogeneous within the analytical precision of the electron microprobe (±2σ), indicating a close approach to equilibrium.

Hydrous Melting Experiments

Seventeen hydrous melting experiments produced silicate melt saturated with a mantle residual assemblage of Oliv + Opx ± Cpx ± Sp ± Gt. Experiments performed using the 82-72f composition produced silicate melts saturated with a spinel or garnet lherzolite assemblage over a broad range of pressures (1.2 to 2.0 GPa), temperatures (1100°C to 1275°C), and dissolved H_2O contents (4.8 to ~12 wt%). Experiments performed using the 85-44 and 93-26 compositions produced hydrous melts saturated with Oliv + Opx ± Cpx.

Experimental charges contain large amounts of silicate melt (46.0 to 74.7 wt%; Table 2) that, with the exception of the high H_2O-content experiments described below, quenched to a homogeneous glass. Large (150 to 700μm) pools of quench-growth-free glass are present at the top of the capsule in most experiments. Crystalline phases are subhedral to euhedral and equant or tabular. Pyroxenes are generally 20 to 40 μm across,

while Oliv grains are typically 50 to 100 μm across and contain pyroxene inclusions. Orthopyroxene grains are commonly overgrown by a rim of quench amphibole. Garnets are large (200 to 400 μm), and poikilitically enclose pyroxene grains. Spinels typically occur as small (5-10 μm), equant grains near the bottom of the charge. Mineral compositions are similar to those found in mantle peridotite. The forsterite (Fo) contents of Oliv range from 86.7 to 90.7, while the Mg# of the Opx are 86.7 to 91.7. The Cpx have Mg# of 87.9 to 91.7, and are characterized by relatively high CaO contents (17.3 to 21.2 wt%). The silicate melt could not be quenched to a glass in the experiments designed to produce melts with high (~12 wt%) dissolved H_2O contents. The silicate melt in these experiments underwent extensive quench modification, and was typically gouged out of the charge during polishing. Glass was present among the crystals, but the presence of quench rims on the pyroxenes made glass compositions unreliable. The compositions of the crystalline phases are reported for 2 of these experiments (B310 and B326) in Table 3. The silicate melts in the remaining experiments contain 4.8 to 7.5 wt% H_2O, and have Mg# of 70.0 to 75.6.

Anhydrous Experiments

Anhydrous experiments on synthetic PUM peridotite or mixtures of 82-72f powder + synthetic PUM peridotite were performed to provide a baseline for interpreting the results of the hydrous experiments. Five anhydrous melting experiments produced silicate melt saturated with a mantle residual assemblage of Oliv + Opx + Cpx + Sp at pressures of 1.2 to 1.6 GPa and temperatures of 1315 to 1370°C. These experiments also produced large amounts of silicate melt (57.9 to 64.1 wt%; Table 2) that quenched to a homogeneous glass. A broad (100-200μm) layer of glass was present at the top of the charges. Morphology of the crystalline phases range from anhedral (Cpx) to euhedral, and equant to tabular. Silicate minerals are generally 50-80 μm across. Orthopyroxene grains are commonly rimmed by quench Cpx. Spinel grains are typically much larger (20 to 50

μm) than in the hydrous melting experiments. The Fo content of the Oliv ranges from 88.1 to 89.4, while the Mg# of the Opx are 88.9 to 89.6. The Cpx have Mg# of 88.0 to 88.9, and are characterized by systematically lower CaO contents (12.8 to 15.0 wt%) than in the hydrous melting experiments. The silicate melts have Mg# of 70.6 to 72.9

Two experiments performed on the PUM composition at sub-solidus conditions produced mantle assemblages of Oliv + Opx + Cpx + Sp. These experiments were used to determine the composition of mantle minerals at anhydrous pressure-temperature conditions corresponding to those of the hydrous melting experiments, and to constrain the location of the spinel to garnet transition in pressure-temperature space under anhydrous conditions. The silicate minerals in these experiments are anhedral to subhedral, with grain sizes of 10 to 20 μm. Spinel forms 5 to 10 μm subhedral grains.

DISCUSSION

The Compositions of Hydrous Mantle Melts

The nature of H_2O-bearing mantle melts has been the subject of debate for nearly 30 years. The pioneering work of Kushiro in basalt analog systems demonstrated that H_2O produces an expansion of the olivine primary phase volume, resulting in mantle melts with higher normative SiO_2 (Kushiro et al., 1968a; Kushiro, 1969; Kushiro, 1972). This observation supported the hypothesis that subduction-related andesites are primary partial melts of mantle peridotite produced at H_2O-saturated conditions (Poldervaart, 1955; O'Hara, 1965), and subsequent experimental studies of the effects of H_2O on mantle melting focused on the origin of andesite (Nichols and Ringwood, 1972, 1973; Nichols 1974; Green, 1973, 1976; Mysen and Boettcher, 1975a,b). The H_2O-saturated conditions at which these studies were conducted made quenching the silicate melt to a homogeneous glass extremely difficult, and hindered the accurate determination of the compositions of hydrous mantle melts. Although it is now widely accepted that subduction-related andesites are derived from basaltic parent magmas through shallow-

level processes such as crystallization differentiation and assimilation of felsic crust (e.g., Gill, 1981; Grove and Baker, 1984; Grove and Kinzler, 1986), recent studies have demonstrated that the pre-eruptive H_2O contents of arc basalts range from negligible to as high as 6 wt% (Sisson and Grove, 1993a,b; Danyushevsky et al., 1993; Gaetani et al., 1993; Sisson and Layne, 1993). These findings emphasize the need for a quantitative understanding of the process of mantle melting under hydrous conditions.

The loci of liquids saturated with a mantle residual assemblage define a complex multi-dimensional surface in pressure-temperature-composition (P-T-X) space. Visualization of the P-T-X relationships that define this surface is facilitated through the use of pseudo-ternary liquidus diagrams. Kinzler and Grove (1992a,b) used a parameterization of the pseudo-quaternary system Oliv-Cpx-plagioclase (Plag)-quartz (Qtz) to isolate the effects of individual P-T-X variables on the mantle melting process under anhydrous conditions, and to formulate a predictive model. At low pressures, dissolved H_2O produces large shifts in the positions of multiply-saturated silicate melts in pseudo-ternary liquidus diagrams due to the destabilization of Plag and Opx (Yoder, 1965; Sisson and Grove, 1993a; Gaetani et al., 1993). At higher pressures, where Sp replaces Plag as the aluminous phase in mantle peridotite, shifts in the compositions of hydrous multiply-saturated liquids are much less pronounced. The magnitude of the compositional shift attributable to 7.5 wt% H_2O dissolved in the melt is shown in Fig 1, a pseudo-ternary projection from Plag onto the Oliv-Cpx-SiO_2 plane. The filled circles in Fig. 1 represent the compositions of silicate melts saturated with a spinel lherzolite assemblage determined from 2 experiments performed at 1.2 GPa that have similar melt fractions (58.6 wt% and 59.0 wt%). They differ in the amounts of H_2O dissolved in the silicate melt (anhydrous and 7.5 wt% respectively), and their liquidus temperatures are 130°C apart. A comparison of these experimentally-produced melt compositions demonstrates that the effect of increasing dissolved H_2O is to offset the compositions of multiply saturated liquids along a vector toward Opx. A similar shift is evident in the 1.2 GPa hydrous

basalt-peridotite sandwich experiments of Kushiro (1990). The compositions of hydrous silicate melts saturated with a spinel lherzolite mineral assemblage determined from experiments performed at 1.2 and 1.6 GPa are also shown in Fig 1. These experiments contain similar melt fractions (71.2 and 73.0 wt% respectively) and have similar concentrations of H_2O dissolved in the melt (6.6-6.8 wt%). These melt compositions are also offset by a vector toward Opx, but in this case the change is due to pressure rather than dissolved H_2O. The compositional shifts shown in Fig. 1 demonstrate that, to a first approximation, the effects of increasing dissolved H_2O and of increasing pressure on the compositions of mantle melts are opposite. Increasing pressure tends to decrease the normative Opx component, while increasing dissolved H_2O increases it.

The compositional variations shown by multiply-saturated melts as a function of changing pressure and H_2O content are summarized in Table 6 and Figs. 2-4. Hydrous melt compositions are normalized to 100% on an anhydrous basis to facilitate comparisons with natural lavas, which experience extensive degassing prior to and during eruption (e.g., Dixon et al., 1995; Dixon and Stolper, 1995). As the H_2O content of the melt increases at constant pressure the FeO and MgO contents of multiply-saturated melts decrease, while SiO_2 and Al_2O_3 contents increase. At 1.2 GPa, the concentration of FeO in experimentally-produced multiply-saturated melt containing ~6 wt% H_2O is ~0.6 wt% lower at a given Mg# than in an anhydrous melt, and the concentration of MgO is lower by ~0.9 wt% (Fig. 2). The FeO and MgO contents of multiply-saturated melts increase and SiO_2 decreases with increasing P at both hydrous and anhydrous conditions (Table 6; Fig. 3). As predicted from the systematics observed in Fig. 1, the effects of increasing pressure and increasing H_2O content are essentially opposite. There are subtle differences in the compositional systematics discussed above if the comparisons are made on the basis of constant MgO content rather than constant melt fraction or constant Mg#. The apparent decrease in FeO content due to ~6 wt% H_2O dissolved in the melt is larger at a constant MgO than at a constant Mg# (Fig. 4). Oxides whose concentrations are not

influenced by changes in pressure or H_2O content when melt compositions are compared on a constant melt fraction basis, such as Na_2O and CaO, appear to either decrease or increase at a constant MgO content, depending on whether they behave compatibly or incompatibly during mantle melting (Table 6). This results from the sensitivity of MgO content to variations in pressure and H_2O content.

That pressure and dissolved H_2O should have opposite effects on the compositions of mantle melts can be understood by considering their effects on the melting point of mantle peridotite. Increasing pressure favors phases with smaller molar volumes (solids) leading to an increase in the temperature of the peridotite solidus. Increasing P_{H_2O} stabilizes the melt relative to the solid, lowering the melting point of mantle peridotite. As the solubility of H_2O in silicate melts increases with increasing pressure, the peridotite solidus temperature decreases dramatically (Kushiro et al., 1968b). Equilibria that are strongly temperature dependent, such as the partitioning of MgO and FeO between olivine and silicate melt (Roeder and Emslie, 1970), will be strongly affected by these variations in the mantle solidus. Plots of the logarithm of the molar olivine/melt partition coefficients for Fe and Mg versus reciprocal temperature demonstrate that hydrous and anhydrous experiments follow a single linear trend (Fig. 5). This observation is consistent with temperature representing the primary control on the FeO and MgO contents of multiply-saturated melts. Melt structural changes attributable to dissolved H_2O do not appear to directly affect these equilibria. The hydrous melts have lower FeO and MgO than the anhydrous melts because they coexist with mantle minerals at a lower temperature, and the partition coefficients for Mg and Fe are higher at these conditions.

There is abundant spectroscopic evidence that H_2O dissolves in silicate melts as both molecular H_2O and OH^- (Stolper, 1982a,b; Newman et al., 1986; Silver et al., 1990; Shen and Keppler, 1995). Hydroxyl is formed through a dissociation reaction involving molecular H_2O and O that is bonded to 2 tetrahedrally-coordinated cations (typically Si^{4+} or Al^{3+}) in the aluminosilicate network (bridging O) (Burnham, 1975; Stolper, 1982a).

This dissociation reaction results in a less polymerized melt, and has the potential to significantly affect the activity coefficient for SiO_2. The lack of a significant H_2O dependence for olivine/melt partitioning of MgO suggests that the activity of MgO (and of FeO) in basaltic melts is not strongly affected by the depolymerization of the aluminosilicate network that accompanies the formation of hydroxyl ions.

Peridotite Melting Reactions Under Hydrous Conditions

A quantitative understanding of the stoichiometry that governs mantle melting reactions places important constraints on the compositions of both partial melts and their mantle residues (Kinzler and Grove, 1992a), the behavior of trace elements during partial melting (Walter et al., 1995), and the modal mineralogy of the residues from partial melting events (Kinzler et al., 1993). Several experimental studies have determined the stoichiometry of mantle melting reactions at upper mantle pressures under anhydrous conditions (Kinzler and Grove, 1992a; Walter and Presnall, 1994; Baker and Stolper 1994; Walter et al., 1995; Kinzler, 1996). Our experiments allow a determination of the nature of mantle melting reactions under hydrous conditions at pressures of 1.2 to 2.0 GPa.

Melting of spinel lherzolite at moderate pressures (~1.0 to 1.7 GPa) under anhydrous conditions occurs through a peritectic reaction in which Cpx, Opx, and Sp are consumed to produce liquid + Oliv (e.g., Kinzler and Grove, 1992a; Baker and Stolper 1994). As pressure increases, changes in the compositions of coexisting Cpx and melt lead to progressive changes in the stoichiometry of this reaction (Stolper, 1980). First, at pressures of ~1.7 to 2.0 GPa, Opx switches from being consumed during lherzolite melting to being produced along with Oliv. At still higher pressures Oliv, Cpx, and Sp are consumed during anhydrous mantle melting, producing liquid + Opx (Kinzler, 1996).

The stoichiometric coefficients for spinel lherzolite melting reactions determined experimentally under hydrous and anhydrous conditions are compared in Table 7. At 1.0

and 1.2 GPa, anhydrous, Cpx dominates the mass of material entering the melt. The spinel lherzolite melting reactions determined at 1.0 to 1.2 GPa from our experiments and those of Hirose and Kawamoto (1995) demonstrate that under hydrous conditions the proportion of Opx entering the melt increases relative to Cpx when compared with the anhydrous melting reactions. This is shown graphically in Figs. 6a and 6b, which are pseudo-ternary projections from Sp onto the Oliv-Cpx + Jadeite (Jd)-SiO_2 plane. The relative positions of mantle minerals and melts in this type of projection can be used to infer the nature of melting reactions (Grove et al., 1983; Baker and Stolper, 1994; Kinzler, 1996). The 1.2 GPa spinel lherzolite melting reaction is represented by a tie-line connecting the compositions of Oliv and silicate melt that pierces a compositional plane defined by Cpx, Opx, and Sp (Fig. 6a,b). The location of the piercing point in this plane relative to the apices defined by the three phases that are being consumed (Cpx, Opx, and Sp) gives their relative proportions in the melting reaction. The compositional differences between the Cpx that coexists with multiply-saturated melts under hydrous and anhydrous conditions results in a shift of the Oliv-melt tie line piercing point away from the Cpx apex, decreasing the proportion of Cpx entering the melt relative to Opx. The stoichiometric coefficients for Cpx and Opx in the spinel lherzolite melting reactions under hydrous conditions are sub-equal (Table 7).

A comparison of the systematic variations in spinel lherzolite melting reaction stoichiometry with increasing pressure, under anhydrous conditions, and with increasing H_2O dissolved in the melt, at constant pressure, demonstrates that they are opposite. As the pressure at which melting occurs increases under anhydrous conditions, the Cpx coefficient increases until Opx shifts to the product side of the melting reaction (Kinzler, 1996). As the concentration of H_2O dissolved in the melt increases at constant pressure, the Cpx coefficient decreases and the proportion of Opx entering the melt progressively increases. The changes in pyroxene compositions that produce these variations in melting reaction coefficients are related to the temperature at which melting occurs. As in the case

of the FeO and MgO contents of hydrous mantle melts, temperature plays an important role in determining in the stoichiometry of mantle melting reactions under hydrous conditions.

The stoichiometric coefficients for the 1.2 GPa peridotite melting reaction should vary considerably over the first few percent partial melting for a mantle containing a moderate amount of H_2O vapor. The first melt will form several hundred degrees below the anhydrous mantle solidus at the H_2O-saturated solidus (Kushiro et al., 1968b). As melting proceeds, and the vapor phase is exhausted, the concentration of H_2O dissolved in the melt will be continuously diluted, requiring a sharp temperature increase for melting to continue. The effect of temperature on the compositions of coexisting low- and high-Ca pyroxenes is illustrated in Fig 6c, in which pyroxene compositions from an anhydrous experiment performed at 1.2 GPa, 1315°C, are compared with those from experiments performed at 1.2 GPa in which the melt contained ~6 wt% H_2O at 1200°C, and ~12 wt% H_2O at 1115°C. Clinopyroxene has a higher CaO content at lower temperatures, while the Opx is less calcic. The sharp temperature increase that accompanies melting at H_2O-undersaturated conditions will produce a strong variation in pyroxene composition. This, in turn, increases the melting reaction coefficient for Cpx, while decreasing the Opx coefficient. In systems containing progressively more vapor, an increasing proportion of the melting will occur at H_2O-saturated conditions, and the melting reaction will be less variable.

A comparison of the phase compositions from anhydrous and hydrous melting experiments saturated with a spinel lherzolite assemblage at 1.6 GPa indicates that Opx is unlikely to be produced during melting within the spinel stability field under hydrous conditions (Fig. 7). At 1.6 GPa, anhydrous, the compositions of coexisting Cpx and melt are such that Opx is beginning to appear on the product side of the melting reaction (Table 7). Under hydrous conditions, the Cpx still has a significant wollastonite ($CaSiO_3$) component and, therefore, the nature of the melting reaction is the same as that

determined at 1.2 GPa, although the Cpx coefficient will be larger. At 2.0 GPa, the hydrous melting experiments produced melts saturated with a Gt lherzolite assemblage. The inferred melting reaction at this pressure has Cpx + Opx + Gt producing Oliv + melt.

Two of the hydrous melting experiments performed at 1.6 GPa produced melts in equilibrium with a mantle residual assemblage in which Sp and Gt coexist. These experiments allow the nature of peridotite melting reactions at pressures corresponding with the spinel to garnet transition to be inferred. A lherzolite melting reaction involving both Sp and Gt is shown schematically in Fig. 8. The phases entering the melt are represented by filled circles, while the open circles are those phases being produced. The coexistence of Sp and Gt produces a compositional tetrahedron with the Cpx-Opx-Sp plane at its base and Gt at its apex. There are 2 faces of this tetrahedron that are pierced by the Oliv-melt tie line. The first is the compositional plane defined by Cpx, Opx, and Sp, while the second is defined by Cpx, Opx, and Gt. The overall melting reaction is a combination of the two reactions defined by the Oliv-melt tie line piercing points. At P-T conditions within the Gt stability field, the point at which the Oliv-melt tie line pierces the Cpx-Opx-Gt compositional plane governs the peridotite melting reaction, as in our 2.0 GPa experiments. At P-T conditions within the spinel stability field the compositional tetrahedron shown in Fig. 8 collapses due to the absence of Gt in the solid assemblage, and mantle peridotite melts by spinel lherzolite reactions similar to those determined from our 1.2 GPa experiments.

Maximum Extents of Melting Under Hydrous Conditions

The maximum extent to which the mantle melts is thought to be limited by the disappearance of one of the phases involved in the peridotite melting reaction. High-Ca clinopyroxene is the least abundant silicate mineral in mantle peridotite, and it is also the phase with the largest stoichiometric coefficient in melting reactions. Therefore, the disappearance of Cpx should define the end of melting. Our experimental results

demonstrate that under hydrous conditions the proportion of Cpx entering the melt decreases, and that of Opx increases, allowing mantle melting to proceed to higher extents before the disappearance of Cpx. To estimate the magnitude of this effect, the extent of partial melting at which one of the mineral phases is exhausted was calculated on the basis of the hydrous and anhydrous 1.2 GPa melting reactions given in Table 7. The mode of the depleted MORB mantle was taken from Kinzler (1996). The calculations indicate that the maximum extent of melting under hydrous conditions increases by 21% relative to anhydrous conditions, from 20.7% to 25% melting, and is marked by the disappearance of Sp rather than Cpx (Table 8). Clinopyroxene is exhausted after 27% partial melting. It is probable that the coefficients for the peridotite melting reaction will actually vary significantly with extent of melting as the concentration of H_2O dissolved in the melt decreases, as discussed in the previous section. The good agreement between the reactions calculated from our experiments and those of Hirose and Kawamoto (1995) indicates that the coefficients in Table 7 and the extents of melting in Table 8 provide a good first approximation for melting reactions and extents of melting under hydrous conditions. Generally higher extents of melting under hydrous conditions are consistent with the observation that peridotites from subduction zones are considerably more refractory than those from tectonic environments where H_2O does not play an important role in melt generation (Bonatti and Michael, 1989). It also explains the common occurrence of highly magnesian Oliv and Cpx phenocrysts in primitive arc basalts (e.g, Anderson, 1974; Barsdell, 1988; Barsdell and Berry, 1990; Eggins, 1993; Foden, 1983; Graham and Hackett, 1987; Nye and Reid, 1986).

The Spinel to Garnet Transition

A comparison of the mineral assemblages in our hydrous and anhydrous experiments shows that for a constant bulk composition (on an anhydrous basis), Gt joins the mantle residual assemblage at a lower pressure under hydrous conditions (1.6 GPa)

than under anhydrous conditions (Gt is present in a 2.0 GPa anhydrous experiment that is not reported due to severe quench growth in the melt). This may reflect either the lower temperature at which the hydrous melting experiments were performed, or changes in the structure of the silicate melt due to dissolved H_2O. The relative stabilities of Sp and Gt in simple system peridotite analogs are known to be sensitive to such variables as the Cr content of the Sp and the Fe content of the silicate minerals (O'Neill, 1981). The Mg#s of the silicate phases and the Cr content of the Sp in the Gt-bearing experiments are the same as, or higher than, those in anhydrous 1.6 GPa experiments that did not crystallize Gt. Two experiments were performed on the PUM synthetic peridotite composition at P-T conditions similar (1260°C, 1.6 and 1.8 GPa) to those under which Gt and Sp coexist in our hydrous melting experiments to constrain the stable aluminous phase for a peridotite bulk composition. Garnet was not present in either experiment. Although this may indicate that Sp is the stable aluminous phase at these conditions, it is also possible that Gt simply failed to nucleate. O'Neill (1981) was unable to bracket the Sp to Gt transition to any better than 0.55 GPa at 1000°C due to nucleation difficulties. It is, therefore, not possible to state conclusively whether the presence of Gt at 1.6 GPa in our hydrous melting experiments is simply related to temperature, as are the variations in melt FeO and MgO content and melting reaction stoichiometry, or whether melt structural changes also play an important role in stabilizing Gt.

Placing Quantitative Constraints on Hydrous Mantle Melting

Forward models for the compositions of anhydrous partial melts produced during adiabatic decompression of mantle peridotite have been used to place constraints on the conditions under which melt is generated beneath mid-ocean ridges (e.g., Klein and Langmuir, 1987; Kinzler and Grove, 1992a,b; Langmuir et al., 1992). The thermal structure of subduction zones is dominated by the presence of the subducted slab, which cools the surrounding mantle. Various subduction zone thermal models have been

proposed, but the predicted temperatures are strongly dependent on assumed heat sources and sinks (McKenzie, 1969; Oxburgh and Turcotte, 1970; Toksöz et al., 1971; Anderson et al., 1976; Davies and Stevenson, 1992). Independent estimates of P-T conditions in the mantle wedge from experimental determinations of the liquidus temperatures of primitive arc basalts are much higher than those predicted by thermal models, even if the effects of H_2O are taken into account (e.g., Tatsumi et al., 1983; Baker et al., 1994). A quantitative understanding of the melt generation process has the potential to place new constraints on the thermal structure and dynamics of subduction zones. Developing methods to predict the compositions and liquidus temperatures of hydrous mantle melts is an important prerequisite for quantifying this process.

The preferred method for modeling hydrous mantle melting would be to predict liquidus temperature and the concentrations of all of the major elements as a function of pressure and mantle residue composition (e.g., Kinzler and Grove, 1992a,b). Due to the limited amount of experimental data that currently exists for hydrous multiply-saturated melts, especially at low extents of melting, we have taken an alternative approach. The compositions of anhydrous mantle melts were calculated using the methods of Kinzler and Grove (1992a,b), then the liquidus temperatures and FeO and MgO contents of equivalent extent melts from mantles containing varying amounts of H_2O vapor were calculated using the constraints provided by olivine/melt equilibria (e.g., Roeder and Emslie, 1970; Hanson and Langmuir, 1978). This approach allowed us to use a database of experimentally-produced olivine-saturated melt compositions from the literature consisting of 69 hydrous and 65 anhydrous basaltic melts coexisting with olivine at temperatures of 940°C to 1511°C, and pressures of 0.1 MPa to 2.3 GPa (Kinzler and Grove, 1992a; Sisson and Grove, 1993a,b; Gaetani et al., 1994; Hirose and Kawamoto, 1995; Wagner et al., 1995; Kinzler, 1996; Grove et al., 1996). The range of K_2O (0.04 to 2.04 wt%) and Na_2O (0.78 to 4.7 wt%) concentrations in the hydrous melts are broad enough to allow meaningful predictions to be made regarding low extent partial melts.

Expressions were developed to describe the molar olivine/melt distribution coefficients for MgO and FeO as functions of pressure, temperature, and melt composition. The melt compositions used in the calibration were recalculated into the components of Bottinga and Weill (1972) including the mole fraction of H_2O. Each expression was formulated by performing multiple linear regressions of the natural logarithm of the olivine/melt distribution coefficient against various P-T-X parameters to determine which were significant. Outlier rejection techniques were then used to limit the uncertainty in the final calibration. Temperature accounts for most of the variability in the olivine/melt distribution coefficients, consistent with the results from experimental studies of anhydrous systems (e.g., Roeder and Emslie, 1970; Longhi et al., 1978). For example, a linear expression describing the distribution of MgO between olivine and basaltic melt as a function of inverse temperature has a correlation coefficient (r^2) of 0.93 and recovers the data with a mean uncertainty of ±7.2% relative (1σ). The addition of compositional terms to account for the alkalis ($NaAlO_2$, $KAlO_2$) improve the model, in agreement other studies (Kinzler and Grove, 1992a,b; Langmuir et al., 1992), but terms accounting explicitly for pressure and H_2O content are not significant. The final calibration contains 120 experiments, and gives the relationship:

$$\mathrm{Ln}\frac{X_{MgO}^{Oliv}}{X_{MgO}^{Liq}} = 6.0 + \frac{5519}{T(K)} - 1.6(1 - X_{NaAlO_2}^{Melt})^2 - 6.9(1 - X_{KAlO_2}^{Melt})^2$$

where X_i^j is the mole fraction of component *i* in phase *j*. The r^2 value is 0.99. This expression was used to calculate the effect of H_2O on the liquidus temperatures of mantle melts, following the olivine/liquid thermometer for hydrous melts developed by Sisson and Grove (1993b). It recovers temperatures for the calibration dataset with a mean uncertainty of ±20°C (1σ) (Fig. 9), and predicts the liquidus temperatures for the experimentally-produced spinel lherzolite partial melts of Baker and Stolper (1994) with a mean uncertainty of ±10°C (1σ).

The expression describing the distribution of FeO between olivine and melt is similar to that for MgO, but requires an explicit pressure term. This is consistent with the pressure dependence for the olivine/melt exchange $K_D^{Fe/Mg}$ (Takahashi and Kushiro, 1983). The final calibration consists of 117 experiments which give the expression:

$$\text{Ln}\,\frac{X_{FeO}^{Oliv}}{X_{FeO}^{Liq}} = 9.4 + \frac{5588}{T(K)} + 0.019\frac{(P-1)}{T(K)} - 0.65(1-X_{NaAlO_2}^{Melt})^2 - 12.5(1-X_{KAlO_2}^{Melt})^2$$

where P is expressed in bars. The r^2 value is 0.98, and the expression recovers FeO with a mean uncertainty of ±4.8% relative (1σ) (Fig. 10). The FeO contents predicted for the experimentally-produced melts of Baker and Stolper (1994) are systematically high by ~0.65 wt%. This is attributable to uncertainty in the calibration related to the presence of Fe_2O_3.

Although anhydrous mantle melting is thought to be polybaric and near fractional, a quantitative understanding of isobaric batch melting provides valuable insights into the processes by which the mantle melts. This is a process in which peridotite melts at a constant pressure in response to an increase in temperature, and the melt remains in equilibrium with the solid throughout the melting process. Near-fractional melting under hydrous conditions can only proceed as long as a vapor phase exists. At vapor-undersaturated conditions all of the H_2O is dissolved in the melt, and will be transported out of the system during a near-fractional process. A significant change in P-T conditions will then be required in order for melting to continue. Therefore, some form of batch melting process may control melt generation in subduction zones.

Anhydrous batch melts representing from 1 to 15% partial melting of a depleted mid-ocean ridge basalt source were calculated at 1.5 GPa using the methods of Kinzler and Grove (1992a,b). The expression for the olivine/melt MgO distribution coefficient was then used to calculate the liquidus temperatures for partial melts from mantles containing 0.15, 0.50, and 1.0 wt% H_2O. These temperatures were then used to calculate

the FeO content of the melts. For the purpose of these calculations H_2O was assumed to behave as a perfectly incompatible element. The solubility of H_2O in basaltic melt at 1.5 GPa was assumed to be 15 wt%, by analogy with solubility limits determined in the system diopside-H_2O (Perchuk et al., 1988). This assumption is important only while melting occurs under H_2O-saturated conditions The calculations also assume that amphibole is not a stable phase by the time 1% partial melting has taken place.

The results from the liquidus temperature calculations are shown in Fig. 11, a plot of temperature versus melt fraction. The calculated FeO and MgO contents of the partial melts are plotted versus melt fraction in Fig. 12. The liquidus temperatures of the anhydrous melts increase systematically from 1315°C at 1% melting to 1365°C at 15% melting. Their FeO (6.09 to 7.78 wt%) and MgO (8.91 to 12.77 wt%) contents also increase monotonically with increasing melt fraction.

The 1% melt from each of the hydrous mantles is vapor saturated and, therefore, has the same liquidus temperature (1043°C), FeO content (4.61 wt%), and MgO (7.47 wt%) content. The temperature of the mantle containing 0.15 wt% H_2O must be raised by 237°C to increase the melt fraction from 1% to 5%, as compared with a temperature increase of only 27°C during anhydrous melting. The concentrations of FeO and MgO also increase significantly between 1% and 5% partial melting. These rapid changes in liquidus temperature and melt composition are due to a sharp decrease in the concentration of H_2O dissolved in the melt, from 15 wt% in the 1% melt to 3 wt% in the 5% melt. Melting from 5% to 15% increases the liquidus temperature by 66°C as the concentration of H_2O decreases from 3 wt% to 1 wt%. The increases in FeO and MgO contents are also less extreme over this melting interval. The temperature increase required to increase the melt fraction from 5% to 15% under anhydrous conditions is 23°C.

The mantles containing 0.50 and 1.0 wt% H_2O remain vapor saturated until 3.3% and 6.7% partial melting respectively. The liquidus temperatures and compositions for

partial melts from both of these mantles are the same as long as there is vapor in the system. Once all of the H_2O enters the melt, their melting paths diverge with the drier mantle producing hotter melts that are richer in normative olivine at a given extent of melting. These calculations demonstrate that the amount of H_2O in the system has a significant influence on the melting process. Although melting begins at the H_2O-saturated solidus for all three of the hydrous mantles, the subsequent melting paths are quite different. With increasing H_2O in the system, a higher percentage of the overall melting process occurs at low temperatures.

Quantifying the effect of H_2O on the melt production rates is an important step in understanding hydrous mantle melting. The melt production rate for an isobaric batch melting process is the change in melt fraction for a given temperature increase (dF/dT), and can be determined from temperature-melt fraction curves such as those shown in Fig. 11. For the anhydrous melts calculated using the methods of Kinzler and Grove (1992a,b) the melt production rate is relatively constant at 0.27%/°C, although in detail it increases slightly with increasing extent of melting. The melt production rate for the mantle containing 0.15 wt% H_2O varies considerably between 1% and 15% partial melting, and is especially low between 1% and 3.3 % melting (0.079%/°C). This low melting production rate is due to a rapid dilution of the H_2O dissolved in the melt, from 15 wt% to 4.5 wt%. The temperature-melt fraction curves for the mantles containing 0.50 and 1.0 wt% H_2O demonstrate that isobaric batch melt production rates remain relatively high as long as the system is vapor saturated. Low melt production rates are characteristic of melting under vapor-absent conditions, where the dissolved H_2O is being diluted during the melting process.

Melt production rates determined for isobaric batch melting can be used to draw inferences about melt production rates during adiabatic decompression melting (dF/dP). For a given bulk composition, isobaric batch melting rates describe the spacing of melt fraction contours above the solidus in P-T space. The spacing of these contours will

influence polybaric melt production rates for a batch melting process (e.g., Cawthorn, 1975; Langmuir et al., 1992). Closely spaced contours favor high melt production rates, while widely spaced contours favor lower rates. If the isobaric batch melting rate is constant, the contours are evenly spaced, while a strongly non-linear temperature-melt fraction curve will result in variable spacing. The melt fraction contours for a hydrous mantle will be closely spaced near the H_2O-saturated solidus, where melting takes place in the presence of a vapor phase. The large temperature increase required to produce a given amount of melt at H_2O-undersaturated conditions results in widely spaced melt fraction contours as soon as the vapor is exhausted. The melt fraction contours will become more closely spaced again at higher temperatures, where the temperature-melt fraction curves gradually approach the slope of the anhydrous curve.

A distinction should be made between the compositions of partial melts, which contain H_2O, and lavas, which are likely to be nearly anhydrous. The strong pressure dependence of H_2O solubility in basaltic melts leads to significant degassing during ascent, so that most lavas are vapor saturated at eruption (e.g., Stolper and Newman, 1994). Comparisons of experimentally-produced melts on an anhydrous basis is therefore relevant to the interpretation of the major element compositions of lavas. This is most important when considering the concentration of SiO_2. As discussed earlier, when hydrous and anhydrous melt compositions are compared on a volatile-free basis the hydrous melts are enriched in SiO_2. If their compositions are compared directly, however, the opposite is true. For example, on a volatile-free basis the hydrous silicate melt from Experiment B329 has higher SiO_2 (48.4 wt%) than the anhydrous melt from Experiment B287 (46.9 wt%). If, however, the composition of the melt in B329 is considered with H_2O included in the composition, it has the lower SiO_2 content (44.8 wt%). The former comparison is relevant for interpreting lava compositions, while the latter is important for understanding the phase equilibria of mantle melting.

The calculated FeO and MgO contents can be combined with the compositional systematics listed in Table 6 to qualitatively assess the compositional differences that would be observed in lavas generated by isobaric batch melting of source regions with varying H_2O contents. The calculated FeO and MgO contents from the anhydrous and hydrous partial melts are compared on an anhydrous basis in Fig. 13. The melting paths for the 4 mantles are subparallel. The overall variations in FeO and MgO contents are less extreme than those in Fig. 12 because the low extent melts contained more H_2O. The opposite is likely to be true for SiO_2. The decrease in SiO_2 that occurs over the first few percent partial melting under anhydrous conditions will be accentuated under hydrous conditions by the loss of volatiles.

CONCLUSIONS

The presence of H_2O produces fundamental changes in the mantle melting process. These changes affect melt compositions, melting reactions, and maximum extents of melting. The compositional variations associated with increasing the concentration of H_2O dissolved in a mantle melt are opposite to those attributable to increasing the pressure at which melting occurs. When considering the influence of H_2O on mantle melting, it is equally important to consider the influence of temperature. The most direct effect that H_2O has on mantle melting is to lower the temperature of the peridotite solidus by several hundred degrees. Many of the effects observed in this study are directly attributable to the decreased mantle solidus under hydrous conditions. Melting paths under hydrous conditions are strongly dependent on the amount of H_2O in the system. At H_2O-undersaturated conditions the compositions and liquidus temperatures of partial melts generated by isobaric batch melting change rapidly as melting proceeds. This is due to the dilution of the concentration of H_2O dissolved in the melt with increasing degree of melting.

REFERENCES

Akella J. and Kennedy G.C. (1971) Melting of gold, silver, and copper – Proposal for a new high-pressure calibration scale. *J. Geophys. Res.*, **76**, 4969-4977.

Anderson A.T. (1974) Evidence for picritic, volatile-rich magma beneath Mount Shasta, California. *J. Petrol.*, **15**, 243-267.

Anderson R.N., Uyeda S., and Miyashiro A. (1976) Geophysical and geochemical constraints at converging plate boundaries - I: Dehydration in the downgoing slab. *Geophys. J. R. Astr. Soc.*, **44**, 333-357.

Baker M.B., Grove T.L., and Price R. (1994) Primitive basalts and andesites from the Mt. Shasta region, N. California: Products of varying melt fraction and H_2O content. *Contrib. Mineral. Petrol.*, **118**, 111-129.

Baker M.B. and Stolper E.M. (1994) Determining the composition of high-pressure mantle melts using diamond aggregates. *Geochim. Cosmochim. Acta*, **58**, 2811-2827.

Barsdell M. (1988) Petrology and petrogenesis of clinopyroxene-rich tholeiitic lavas, Merelava Volcano, Vanuatu. *J. Petrol.*, **29**, 927-964.

Barsdell M. and Berry R.F. (1990) Origin and evolution of primitive island arc ankaramites from western Epi, Vanuatu. *J. Petrol.*, **31**, 747-777.

Bonatti E. and Michael P.J. (1989) Mantle peridotites from continental rifts to ocean basins to subduction zones. *Earth Planet. Sci. Lett.*, **91**, 297-311.

Bottinga Y. and Weill D.F. (1972) The viscosity of magmatic silicate liquids: A model for calculation. *Am J. Sci.*, **272**, 438-475.

Boyd F.R. and England J.L. (1960) Apparatus for phase equilibrium studies at pressures up to 50 kbars and temperatures up to 1750° C. *J. Geophys. Res.*, **65**, 741-748.

Bryan W.B., Finger L.W., and Chayes F. (1969) Estimating proportions in petrographic mixing equations by least squares approximation. *Science*, **163**, 926-927.

Burnham C.W. (1975) Water and magmas; a mixing model. *Geochim. Cosmochim. Acta.*, **39**, 1077-1084.

Cawthorn R.G. (1975) Degree of melting in mantle diapirs and the origin of ultrabasic liquids. *Earth Planet. Sci. Lett.*, **27**, 113-120.

Chou I.-M. (1985) Permeability of precious metals to hydrogen at 2 kb and the quantification of the oxygen buffer technique (abst.) *EOS, Trans. Am. Geophys. Un.*, **66**, 407.

Danyushevsky L.V., Falloon T.J., Sobolev A.V., Crawford A.J., Carroll M., and Price R.C. (1993) The H_2O content of basalt glasses from South West Pacific back-arc basins. *Earth Planet. Sci. Lett.*, **117**, 347-362.

Davies J.H. and Stevenson D.J. (1992) Physical model of source region of subduction zone volcanics. *J. Geophys. Res.*, **97**, 2037-2070.

Dixon J.E. and Stolper E.M. (1995) An experimental study of water and carbon dioxide solubilities in mid-ocean ridge basaltic liquids. Part II: Applications to degassing. *J. Petrol.*, **36**, 1633-1646.

Dixon J.E., Stolper E.M., and Holloway J.R. (1995) An experimental study of water and carbon dioxide solubilities in mid-ocean ridge basaltic liquids. Part I: Calibration and solubility models. *J. Petrol.*, **36**, 1607-1631

Eggins S.M. (1993) Origin and differentiation of picritic arc magmas, Ambae (Aoba), Vanuatu. *Contrib. Mineral. Petrol.*, **114**, 79-100.

Foden J.D. (1983) The petrology of the calcalkaline lavas of Rindjani Volcano, East Sunda Arc: A model for island arc petrogenesis. *J. Petrol.*, **24**, 98-130.

Fram M.S. and Longhi J. (1992) Phase equilibria of dikes associated with Proterozoic anorthosite complexes. *Am. Mineral.*, **77**, 605-616.

Gaetani G.A., Grove T.L., and Bryan W.B. (1993) The influence of water on the petrogenesis of subduction-related igneous rocks. *Nature*, **365**, 332-334.

Gaetani G.A., Grove T.L., and Bryan W.B. (1994) Experimental phase relations of basaltic andesite from Hole 839b under hydrous and anhydrous conditions. In, Hawkins, J., Parsons, L., Allan, J., et al., *Proc. O.D.P. Sci. Results*, 135: College Station, TX (Ocean Drilling Program), 557-564.

Gill, J.B. (1981) *Orogenic Andesites and Plate Tectonics*. Springer-Verlag.

Graham I.J. and Hackett W.R. (1987) Petrology of calc-alkaline lavas from Ruapehu Volcano and related vents, Taupo Volcanic Zone, New Zealand. *J. Petrol.*, **28**, 531-567.

Green D.H. (1973) Experimental melting studies on a model upper mantle composition at high pressure under water-saturated and water-undersaturated conditions. *Earth Planet. Sci. Lett.*, **19**, 37-53.

Green D.H. (1976) Experimental testing of "equilibrium" partial melting of peridotite under water-saturated, high-pressure conditions. *Can. Min.*, **14**, 255-268.

Grove T.L. and Baker M.B. (1984) Phase equilibrium controls on the tholeiitic versus calc-alkaline differentiation trends. *J. Geophys. Res.*, **89**, 3253-3274.

Grove T.L., Donnelly-Nolan J.M., and Housh T. (1996) Experimental and geochemical investigations of magmatic processes at Glass Mountain, Medicine Lake Highland, N. California. *Contrib. Mineral. Petrol.*, Submitted.

Grove T.L., Gerlach D.C., Sando T.W., and Baker M.B. (1983) Origin of calc-alkaline series lavas at Medicine Lake volcano by fractionation, assimilation, and mixing: Corrections and clarifications. *Contrib. Mineral. Petrol.*, **82**, 407-408.

Grove T.L. and Kinzler R.J. (1986) Petrogenesis of andesites. *Ann. Rev. Earth Planet. Sci.*, **14**, 417-454.

Hanson G.N. and Langmuir C.H. (1978) Modelling of major elements in mantle-melt systems using trace element approaches. *Geochim. Cosmochim. Acta.*, **42**, 725-741.

Hanson M. (1958) *Constitution of Binary Alloys.* McGraw-Hill.

Hart S.R. and Zindler A. (1986) In search of a bulk Earth composition. *Chem. Geol.*, **57**, 247-267.

Hays J.F. (1966) Lime-alumina-silica. *Carnegie Inst. Washington Yearbook*, **65**, 234-239.

Hirose K. and Kawamoto T. (1995) Hydrous partial melting of lherzolite at 1 GPa: The effect of H_2O on the genesis of basaltic magmas. *Earth Planet. Sci. Lett.*, **133**, 463-473.

Johannes W., Bell P.M., Mao H.K., Boettcher A.L., Chipman D.W., Hays J.F., Newton R.S., and Seifert F. (1971) An inter-laboratory comparison of piston-cylinder pressure calibration using the albite breakdown reaction. *Contrib. Mineral. Petrol.*, **32**, 24-38.

Johnson M.C. and Walker D. (1993) Brucite [$Mg(OH)_2$] dehydration and the molar volume of H_2O to 15 GPa. *Am. Min.*, **78**, 271-284

Kawamoto T. and Hirose K. (1994) Au-Pd sample containers for melting experiments on iron and water bearing systems. *Eur. J. Mineral.*, **6**, 381-385.

Kinzler R.J. (1996) Melting of mantle peridotite at pressures approaching the spinel to garnet transition: Applications to the generation of mid-ocean ridge basalts. *J. Geophys. Res.*, in press.

Kinzler R.J. and Grove T.L. (1992a) Primary magmas of mid-ocean ridge basalts 1. Experiments and methods. *J. Geophys. Res.*, **97**, 6885-6906.

Kinzler R.J. and Grove T.L. (1992b) Primary magmas of mid-ocean ridge basalts 2. Applications. *J. Geophys. Res.*, **97**, 6907-6926.

Kinzler R.J., Niu Y.-L., and Langmuir C.H. (1993) Modal mineralogy and composition of abyssal peridotites: Problems and solutions (abst.). *EOS, Trans. Am. Geophys. Un.*, **74**, 623.

Klein E.M. and Langmuir C.H. (1987) Global correlations of oceanic ridge basalt chemistry with axial depth and crustal thickness. *J. Geophys. Res.*, **92**, 8089-8115.

Kushiro I. (1969) The system forsterite-diopside-silica with and without water at high pressures. *Am. J. Sci.*, **267A**, 269-294.

Kushiro I. (1972) Effect of water on the composition of magmas formed at high pressures. *J. Petrol.*, **13**, 311-334.

Kushiro I. (1990) Partial melting of mantle wedge and evolution of island arc crust. *J Geophys. Res.*, **95**, 15929-15939.

Kushiro I., Yoder H.S. Jr., and Nishikawa M. (1968a) Effect of water on the melting of enstatite. *Geol. Soc. Am. Bull.*, **79**, 1685-1692.

Kushiro I., Syono Y., Akimoto S.-I. (1968b) Melting of a peridotite nodule at high pressures and high water pressures. *J. Geophys. Res.*, **73**, 6023-6029.

Langmuir C.H., Klein E.M., and Plank T. (1992) Petrological systematics of mid-ocean ridge basalts: Constraints on melt generation beneath ocean ridges. In *Mantle Flow and Melt Generation at Mid-Ocean Ridges, Geophys. Monogr. Ser.*, vol. 71, (ed. J. Phipps Morgan, D.K. Blackman, and J.M. Sinton), 183-280, AGU, Washington, D.C.

Lindsley D.H., Kesson S.E., Hartzman M.J., and Cushman M.K. (1974) The stability of armalcolite: Experimental studies in the system Mg-Fe-Ti-O. *Proc. Lunar Planet Sci Conf.*, **5**, 521-534.

Longhi J., Walker D., and Hays J.F. (1978) The distribution of Fe and Mg between olivine and lunar basaltic liquids. *Geochim. Cosmochim. Acta*, **42**, 1545-1558.

Maury R.C., Defant M.J., and Joron J.-L. (1992) Metasomatism of the sub-arc mantle inferred from trace elements in Philippine xenoliths. *Nature*, **360**, 661-663.

McKenzie D.P. (1969) Speculations on the consequences and causes of plate motions. *Geophys. J. Royal Astron. Soc.*, **18**, 1-32.

McKenzie D. and Bickle M.J. (1988) The volume and composition of melt generated by extension of the lithosphere. *J. Petrol.*, **29**, 625-679.

Mysen B.O. and Boettcher A.L. (1975a) Melting of a hydrous upper mantle: Phase equilibria of a natural peridotite at high pressures and high temperatures as a function of controlled activities of water, hydrogen, and carbon dioxide. *J. Petrol.*, **16**, 520-548.

Mysen B.O. and Boettcher A.L. (1975b) Melting of a hydrous upper mantle: II. Geochemistry of crystals and liquid formed by anatexis of mantle peridotite at high pressures and high temperatures as a function of controlled activities of water, hydrogen, and carbon dioxide. *J. Petrol.*, **16**, 549-593.

Newman S., Stolper E.M., and Epstein S. (1986) Measurement of water in rhyolitic glasses: Calibration of an infrared spectroscopic technique. *Am Min.*, **71**, 1527-1541.

Nichols I.A. (1974) Liquids in equilibrium with peridotite mineral assemblages at high water pressures. *Contrib. Mineral. Petrol.*, **45**, 289-316.

Nichols I.A. and Ringwood A.E. (1972) Production of silica-saturated tholeiitic magmas in island arcs. *Earth Planet. Sci. Lett.*, **17**, 243-246.

Nichols I.A. and Ringwood A.E. (1973) Effect of water on olivine stability in tholeiites and the production of silica-saturated magmas in the island-arc environment. *J. Geol.*, **81**, 285-300.

Nye C.J. and Reid M.R. (1986) Geochemistry of primary and least fractionated lavas from Okmok Volcano, Central Aleutians: Implications for arc magmagenesis. *J. Geophys. Res.*, **91**, 10271-10287.

O'Hara M.J. (1965) Primary magmas and the origin of basalt. *Scottish J. Geol.*, **1**, 19-40

O'Neill H. St. C. (1981) The transition between spinel lherzolite and garnet lherzolite, and its use as a geobarometer. *Contrib. Mineral. Petrol.*, **77**, 185-194.

Oxburgh E.R. and Turcotte D.L. (1970) Thermal structure of island arcs. *Geol. Soc. Am. Bull.*, **81**, 1665-1688.

Perchuk L.L., Kushiro I., and Kosyakov A.V. (1988) Experimental determination of the liquidus surface in the system diopside-water. *Geokhimia*, **7**, 942-955.

Poldervaart A. (1955) Chemistry of the Earth's crust. In, *Crust of the Earth* (ed. A. Poldervaart). Geol. Soc. Am. Special Paper, **2**, 119-144.

Roeder P.L. and Emslie R.F. (1970) Olivine-liquid equilibrium. *Contrib. Mineral. Petrol.*, **29**, 275-289.

Schiano P., Clocchiatti R., Shimizu N., Maury R.C., Jochum K.P., and Hoffman A.W. (1995) Hydrous, silica-rich melts in the sub-arc mantle and their relationship with erupted arc lavas. *Nature*, **377**, 595-600.

Shcheka S.A. and Shcheka Zh.A. (1973) New find of chrome amphibole. *Dokl. Akad. Nauk SSSR, Earth Sci. Sect.*, **211**, 134-138.

Shen A. and Keppler H. (1995) Infrared spectroscopy of hydrous silicate melts to 1000°C and 10 kbar: Direct observation of H_2O speciation in a diamond-anvil cell. *Am. Min.*, **80**, 1335-1338.

Silver L.A., Ihinger P.D., and Stolper E.M. (1990) The influence of bulk composition on the speciation of water in silicate glasses. *Contrib. Mineral. Petrol.*, **104**, 142-162.

Sisson T.W. and Grove T.L. (1993a) Experimental investigations of the role of H_2O in calc-alkaline differentiation and subduction zone magmatism. *Contrib. Mineral. Petrol.*, **113**, 143-166.

Sisson T.W. and Grove T.L. (1993b) Temperatures and H_2O contents of low-MgO high-alumina basalts. *Contrib. Mineral. Petrol.*, **113**, 167-184.

Sisson T.W. and Layne G.D. (1993) H_2O in basaltic andesite glass inclusions from four subduction-related volcanoes. *Earth Planet. Sci. Lett.*, **117**, 619-635.

Stolper E.M. (1980) A phase diagram for mid-ocean ridge basalts: Preliminary results and implications for petrogenesis. *Contrib. Mineral. Petrol.*, **74**, 13-27.

Stolper E.M. (1982a) The speciation of water in silicate melts. *Geochim. Cosmochim. Acta.*, **46**, 2609-2620.

Stolper E.M. (1982b) Water in silicate glasses: An infrared spectroscopic study. *Contrib. Mineral. Petrol.*, **81**, 1-17.

Stolper E.M. and Newman S. (1994) The role of water in the petrogenesis of Mariana trough magmas. *Earth Planet. Sci. Lett.*, **121**, 293-325.

Takahashi E. and Kushiro I. (1983) Melting of dry peridotite at high pressures and basalt magma genesis. *Am. Min.*, **68**, 859-879.

Tanaka T. and Aoki K.-I. (1979) Petrogenetic implications of REE and Ba data on mafic and ultramafic inclusions from Itinome-gata, Japan. *J. Geol.*, **89**, 369-390.

Tatsumi Y., Sakuyama M., Fukuyama H., and Kushiro I. (1983) Generation of arc basalt magmas and thermal structure of the mantle wedge in subduction zones. *J. Geophys. Res.*, **88**, 5815-5825.

Toksöz M.N., Minear J.W., and Julian B.R. (1971) Temperature field and geophysical effects of a downgoing slab. *J Geophys. Res.* **76**, 1113-1138.

Vidal Ph., Dupuy C., Maury R., and Richard M. (1989) Mantle metasomatism above subduction zones: trace-element and radiogenic isotope characteristics of peridotite xenoliths from Batan Island (Philipines). *Geology*, **17**, 1115-1118.

Wagner T.P., Donnelly-Nolan J.M., and Grove T.L. (1995) Evidence of hydrous differentiation and crystal accumulation in the low-MgO, high-Al_2O_3 Lake Basalt from Medicine Lake volcano, California. *Contrib. Mineral. Petrol.*, **121**, 201-216.

Walter M.J. and Presnall D.C. (1994) Melting behavior of simplified lherzolite in the system CaO-MgO-Al_2O_3-SiO_2-Na_2O from 7 to 35 kbar. *J. Petrol.*, **35**, 329-359.

Walter M.J., Sisson T.W., and Presnall D.C. (1995) A mass proportion method for calculating melting reactions and applications to melting of model upper mantle lherzolite. *Earth Planet Sci. Lett.*, **135**, 77-90.

Yoder H.S. Jr. (1965) Diopside-anorthite-water at five and ten kilobars and its bearing on explosive volcanism. *Yearb. Carnegie Inst. Wash.*, **64**, 82-89.

Table 1. Compositions of starting materials.

						Kilbourne Hole Xenolith Minerals			
	82-72f	85-44	93-26	PUM	FP1	Cpx	Opx	Oliv	Sp
n	25	25	25	–	–	27	25	21	25
SiO_2	47.7(2)	51.6(2)	50.9(2)	45.97	44.68	51.8(4)	54.8(4)	40.3(1)	0.06(2)
TiO_2	0.62(3)	0.59(3)	1.28(4)	0.18	0.18	0.58(2)	0.12(2)	0.06(1)	0.11(3)
Al_2O_3	19.05(9)	15.95(9)	17.7(2)	4.06	4.25	7.1(1)	4.7(2)	0.02(1)	57.3(4)
Cr_2O_3	0.12(4)	0.16(4)	0.06(2)	0.47	0.58	0.72(2)	0.37(3)	0.08(2)	9.9(2)
FeO*	7.8(1)	8.1(1)	8.1(1)	7.54	7.53	2.70(6)	6.39(7)	9.8(1)	10.3(2)
MnO	0.15(5)	0.11(4)	0.15(3)	0.13	0.11	0.08(3)	0.10(3)	0.12(2)	0.10(3)
MgO	10.49(8)	11.30(9)	8.6(1)	37.79	37.86	15.5(2)	32.8(2)	49.8(2)	22.4(2)
CaO	11.75(9)	9.4(1)	8.89(6)	3.21	4.26	20.41(9)	0.71(2)	0.06(2)	0.02(1)
Na_2O	2.4(1)	2.6(1)	3.4(1)	0.33	0.38	1.76(5)	0.10(2)	–	–
K_2O	0.08(1)	0.31(2)	0.74(2)	0.03	–	–	–	–	–
P_2O_5	0.08(2)	0.15(3)	0.31(3)	0.00	–	–	–	–	–
NiO	–	–	–	0.28	0.18	–	–	0.32(2)	0.40(2)
Total	100.24	100.27	100.13	99.99	100.01	100.65	100.09	100.56	100.59
Mg#	70.6	71.3	65.4	89.9	90.0	91.1	90.1	90.1	79.5

Notes: Units in parentheses represent 1 standard deviation of least units cited on the basis of replicate analyses; thus, 47.7(2) should be read as 47.7±0.2. n = number of electron microprobe analyses.

Table 2. Experimental conditions and phase assemblages

Expt.	Pressure (GPa)	Temperature (°C)	Duration (hr)	H_2O (wt%)	Basalt:Peridotite Ratio	Run Products	Phase Proportions wt%	K_D Cpx	Opx	Oliv	Sp	Gt	Fe Exchange[a] (wt% relative)	ΣR^2
82-72f Experiments														
B333	1.2	1245	25	4.8	60 : 40	Gl, Cpx, Opx, Oliv, Sp	68.7 : 1.5 : 9.4 : 20.2 : 0.2	0.35	0.34	0.34	0.75		−0.88	0.02
B305	1.2	1230	24	6.4	64 : 36	Gl, Opx, Oliv, Sp	74.7 : 6.5 : 18.5 : 0.4		0.33	0.34	0.88		+2.5	0.06
B304	1.2	1215	24	6.5	69 : 31	Gl, Cpx, Opx, Oliv, Sp	68.6 : 3.9 : 10.8 : 16.5 : 0.2	0.35	0.34	0.35	0.66		−0.39	0.02
B330	1.2	1200	29	6.6	70 : 30	Gl, Cpx, Opx, Oliv, Sp	71.2 : 6.8 : 4.4 : 16.9 : 0.7	0.32	0.33	0.35	0.76		+1.2	0.02
B329	1.2	1185	26	7.5	70 : 30	Gl, Cpx, Opx, Oliv, Sp	59.0 : 14.4 : 10.6 : 13.8 : 2.2	0.29	0.32	0.34	0.58		+1.1	0.05
B326	1.2	1115	28	~12	70 : 30	Qch, Cpx, Opx, Oliv, Sp								
B310	1.2	1100	24	~12	70 : 30	Qch, Cpx, Opx, Oliv, Sp								
B303	1.2	1345	24	—	65 : 35	Gl, Cpx, Opx, Oliv, Sp	61.0 : 12.4 : 12.2 : 12.7 : 1.7	0.34	0.31	0.32	0.49		+1.2	0.07
B292	1.2	1330	24	—	70 : 30	Gl, Cpx, Opx, Oliv, Sp	59.5 : 18.9 : 8.3 : 11.2 : 2.1	0.32	0.30	0.32	0.47		+0.65	0.02
B287	1.2	1315	24	—	70 : 30	Gl, Cpx, Opx, Oliv, Sp	58.6 : 16.9 : 14.4 : 7.7 : 2.4	0.33	0.30	0.32	0.49		+0.90	0.03
B359	1.6	1260	20	5.9	70 : 30	Gl, Cpx, Opx, Oliv, Sp, Gt	67.1 : 4.7 : 8.7 : 10.4 : tr : 9.1	0.35	0.33	0.34	0.56	0.59	−0.52	0.03
B277[b]	1.6	1255	10	6.6	69 : 31	Gl, Cpx, Opx, Oliv, Sp, Gt	66.6 : 8.2 : 11.4 : 12.7 : 1 1 : tr	0.35	0.34	0.35	0.64	0.59	+0.39	0.008
B348	1.6	1245	20	6.8	70 : 30	Gl, Cpx, Opx, Oliv, Sp	73.0 : 3.9 : 14.1 : 9.0 : tr	0.34	0.33	0.34	0.59		−0.61	0.01
B366	1.6	1230	22	6.4	70 : 30	Gl, Cpx, Opx, Oliv, Gt	56.5 : 12.0 : 11.1 : 8.3 : 12.1	0.33	0.34	0.36		0.66	+2.0	0.08
B394	1.6	1370	24	—	70 : 30	Gl, Cpx, Opx, Oliv, Sp	64.1 : 14.1 : 15.2 : 4.8 : 1.8	0.34	0.31	0.32	0.48		+0.89	0.05
B302	1.6	1355	24	—	70 : 30	Gl, Cpx, Opx, Oliv, Sp	57.9 : 20.2 : 15.1 : 4.2 : 2.6	0.34	0.30	0.32	0.46		+1.2	0.08
B365	2.0	1290	15	5.6	70 : 30	Gl, Cpx, Opx, Oliv, Gt	60.6 : 9.0 : 13.0 : 3.3 : 14.1	0.34	0.35	0.36		0.63	+2.1	0.11
B399	2.0	1275	15	7.5	70 : 30	Gl, Cpx, Opx, Oliv, Gt	63.6 : 7.9 : 8.5 : 6.1 : 13.9	0.31	0.32	0.34		0.59	0.0	0.01
85-44 Experiments														
B384	1.2	1200	30	7.2	70 : 30	Gl, Opx, Oliv	67.7 : 23.0 : 9.3		0.31	0.33			+2.3	0.13
B388	1.2	1200	28	8.0	60 : 40	Gl, Opx, Oliv	61.6 : 21.1 : 17.3		0.34	0.36			−0.85	0.12
B392	1.2	1170	30	7.6	60 : 40	Gl, Cpx, Opx, Oliv	46.0 : 11.5 : 24.5 : 18.0	0.33	0.33	0.36			−1.1	0.02
93-26 Experiments														
B408	1.2	1200	24	6.0	70 : 30	Gl, Opx, Oliv	75.2 : 14.0 : 10 8		0.31	0.33			−1.8	0.06
PUM Experiments														
B414	1.6	1260	72	—	—	Cpx, Opx, Oliv, Sp	14.9 : 32.2 : 50.9 : 2.0						+3.2	0.12
B412	1.8	1260	70	—	—	Cpx, Opx, Oliv, Sp	15.7 : 33.8 : 48.8 : 1.7						+2.3	0.08

[a]Fe Exchange is the difference between the FeO content of the bulk composition used in the experiment and the FeO for the bulk composition as predicted by the mass balance calculation in relative weight percent. Positive values indicate apparent Fe gain, while negative values indicate apparent Fe loss.

[b]Experiment was performed using FP1 peridotite composition.

Table 3. Electron microprobe analyses of run products from H_2O-undersaturated melting experiments.

Expt	Phase	Analyses	SiO_2	TiO_2	Al_2O_3	Cr_2O_3	FeO*	MnO	MgO	CaO	Na_2O	K_2O	P_2O_5	Total
B333	Gl	10	48.1(3)	0.64(2)	17.9(1)	0.09(3)	7.2(1)	0.14(2)	12.02(7)	11.5(1)	2.1(1)	0.14(1)	0.09(4)	95.18
	Cpx	9	52.4(6)	0.14(5)	6.0(11)	0.9(2)	4.1(2)	0.08(5)	19.4(8)	17.6(5)	0.49(5)	—	—	101.11
	Opx	10	55.0(6)	0.09(3)	6.0(9)	0.8(1)	6.4(1)	0.13(4)	31.2(4)	1.7(1)	0.05(3)	—	—	101.37
	Oliv	7	40.4(2)	0.01(1)	0.07(1)	0.04(2)	10.03(8)	0.13(1)	49.9(2)	0.18(2)	—	—	—	100.76
	Sp	2	0.17(2)	0.15(2)	49.4(17)	18.6(23)	10.0(2)	0.12(5)	22.20(8)	0.05(5)	—	—	—	100.69
B305	Gl	10	48.1(1)	0.58(3)	16.87(9)	0.18(3)	7.6(1)	0.12(4)	13.18(9)	11.0(1)	2.1(1)	0.06(2)	0.18(3)	93.57
	Opx	10	53.6(8)	0.08(4)	5.2(10)	1.0(2)	6.0(1)	0.09(4)	31.4(3)	1.6(1)	0.08(2)	—	—	99.05
	Oliv	7	40.3(3)	0.10(2)	0.05(3)	0.08(3)	9.6(1)	0.14(3)	48.7(4)	0.17(3)	—	—	—	99.14
	Sp	2	0.31(1)	0.10(1)	41.1(17)	27.3(21)	10.6(4)	0.12(3)	21.0(2)	0.03(2)	—	—	—	100.56
B304	Gl	10	47.7(1)	0.63(4)	18.65(8)	0.06(5)	7.3(1)	0.08(6)	11.46(9)	11.5(1)	2.4(1)	0.09(3)	0.18(2)	93.54
	Cpx	15	51.3(5)	0.19(5)	7.2(7)	0.50(6)	3.9(1)	0.09(3)	17.6(3)	19.1(3)	0.50(3)	—	—	100.38
	Opx	10	52.9(4)	0.09(6)	6.9(4)	0.50(6)	6.72(6)	0.12(6)	30.6(3)	1.63(9)	0.07(2)	—	—	99.53
	Oliv	7	40.2(4)	0.05(3)	0.07(2)	0.12(3)	10.7(2)	0.17(5)	48.0(2)	0.21(2)	—	—	—	99.52
	Sp	5	0.15(1)	0.11(3)	58.9(16)	7.9(15)	9.6(2)	0.09(2)	23.0(4)	0.08(8)	—	—	—	99.83
B330	Gl	10	48.3(2)	0.64(2)	18.89(8)	0.12(2)	7.4(1)	0.13(2)	10.99(9)	10.95(9)	2.3(1)	0.11(1)	0.11(3)	93.37
	Cpx	15	52.0(3)	0.18(2)	6.2(5)	0.8(1)	3.9(1)	0.09(4)	18.0(3)	18.9(3)	0.43(2)	—	—	100.50
	Opx	10	55.0(4)	0.09(2)	5.4(5)	0.71(9)	7.0(1)	0.11(3)	31.1(2)	1.50(9)	0.04(2)	—	—	100.95
	Oliv	7	40.5(2)	0.02(1)	0.06(1)	0.12(2)	11.3(2)	0.13(3)	48.3(3)	0.17(1)	—	—	—	100.60
	Sp	5	0.3(2)	0.16(1)	54.0(8)	14.0(9)	10.9(1)	0.09(3)	21.3(4)	0.15(8)	—	—	—	100.90
B329	Gl	10	48.4(1)	0.69(2)	19.4(1)	0.09(3)	7.8(1)	0.15(2)	10.2(1)	10.59(8)	2.5(1)	0.13(1)	0.08(2)	92.51
	Cpx	15	51.4(3)	0.22(3)	7.1(5)	0.31(6)	3.9(2)	0.09(4)	17.5(4)	19.3(4)	0.51(3)	—	—	100.33
	Opx	10	54.1(7)	0.10(2)	6.5(7)	0.42(4)	7.41(7)	0.18(2)	30.5(3)	1.35(6)	0.06(1)	—	—	100.62
	Oliv	7	40.3(1)	0.00(1)	0.06(2)	0.12(2)	12.2(1)	0.15(3)	47.3(2)	0.17(2)	—	—	—	100.30
	Sp	5	0.3(3)	0.12(2)	63.0(5)	4.2(8)	10.0(2)	0.09(1)	22.5(2)	0.3(2)	—	—	—	100.51
B326	Cpx	15	52.3(5)	0.18(4)	4.6(6)	0.9(1)	2.8(2)	0.05(4)	17.5(4)	21.2(4)	0.37(4)	—	—	99.90
	Opx	4	55.0(5)	0.07(1)	4.6(16)	0.8(2)	5.37(8)	0.09(4)	33.1(4)	1.2(1)	0.1(1)	—	—	100.33
	Oliv	7	40.9(4)	0.05(3)	0.03(2)	0.06(4)	9.0(2)	0.12(4)	49.5(4)	0.13(2)	—	—	—	99.79
B310	Cpx	15	51.9(6)	0.32(3)	7.1(7)	0.4(1)	3.6(2)	0.09(4)	16.6(3)	20.6(4)	0.42(5)	—	—	101.03
	Opx	10	54.0(4)	0.13(3)	7.3(4)	0.33(5)	7.2(1)	0.12(4)	31.0(3)	1.2(1)	0.02(2)	—	—	101.30
	Oliv	7	40.6(3)	0.02(2)	0.11(4)	0.08(2)	11.3(2)	0.13(2)	48.5(5)	0.18(2)	—	—	—	100.92
	Sp	1	0.21	0.11	60.6	7.5	10.6	0.07	21.6	0.18	—	—	—	100.87
B359	Gl	10	46.7(2)	0.70(3)	18.3(1)	0.08(4)	7.8(1)	0.08(5)	12.53(8)	11.05(8)	2.5(1)	0.12(1)	0.16(4)	94.11
	Cpx	15	51.0(5)	0.17(3)	8.0(5)	0.37(8)	3.9(2)	0.10(5)	17.8(4)	18.1(6)	0.66(6)	—	—	100.10
	Opx	10	53.6(5)	0.10(4)	7.1(6)	0.33(5)	6.39(6)	0.12(3)	31.0(3)	1.55(7)	0.08(3)	—	—	100.27
	Oliv	7	40.0(2)	0.02(2)	0.07(2)	0.04(5)	10.4(2)	0.10(4)	49.1(4)	0.18(2)	—	—	—	99.91
	Sp	5	0.24(6)	0.05(6)	63.1(9)	4.2(8)	8.5(2)	0.07(4)	24.4(2)	0.11(3)	—	—	—	100.67
	Gt	7	42.3(5)	0.18(6)	23.6(6)	0.66(7)	7.24(8)	0.27(4)	19.6(5)	6.5(4)	0.01(2)	—	—	100.36
B277	Gl	10	46.8(3)	0.63(3)	18.0(2)	0.09(2)	7.9(1)	0.18(2)	12.75(8)	11.21(8)	2.3(1)	0.09(1)	0.08(2)	93.44
	Cpx	15	51.7(3)	0.19(7)	7.4(5)	0.6(1)	3.8(2)	0.08(4)	17.7(5)	18.8(4)	0.6(1)	—	—	100.87
	Opx	10	54.3(5)	0.08(2)	6.5(6)	0.50(7)	6.6(1)	0.10(4)	30.9(4)	1.5(2)	0.06(2)	—	—	100.54
	Oliv	7	40.7(2)	0.02(2)	0.06(1)	0.04(3)	10.7(2)	0.09(3)	48.8(3)	0.17(1)	—	—	—	100.58
	Sp	5	0.16(3)	0.06(4)	60.1(13)	7.4(11)	9.2(2)	0.05(4)	23.3(4)	0.11(4)	—	—	—	100.38
	Gt	7	42.8(2)	0.17(2)	24.0(3)	0.82(8)	7.1(1)	0.26(2)	19.4(4)	6.5(5)	0.02(2)	—	—	101.07
B348	Gl	10	46.7(2)	0.68(4)	18.07(9)	0.10(3)	7.83(7)	0.16(4)	12.64(8)	11.3(1)	2.43(9)	0.05(3)	0.07(4)	93.19
	Cpx	15	51.5(3)	0.15(4)	7.7(4)	0.48(9)	3.8(1)	0.07(5)	18.1(3)	18.3(5)	0.60(3)	—	—	100.70
	Opx	10	53.7(5)	0.03(3)	7.3(5)	0.38(5)	6.46(6)	0.09(4)	31.3(2)	1.55(8)	0.08(2)	—	—	100.89
	Oliv	7	40.4(2)	0.03(2)	0.02(2)	0.11(5)	10.4(2)	0.12(4)	49.2(5)	0.13(4)	—	—	—	100.41
	Sp	2	0.20(3)	0.08(3)	63.0(3)	4.9(4)	8.65(1)	0.10(0)	23.76(9)	0.11(3)	—	—	—	100.80

Table 3. Continued.

Expt	Phase	Analyses	SiO_2	TiO_2	Al_2O_3	Cr_2O_3	FeO*	MnO	MgO	CaO	Na_2O	K_2O	P_2O_5	Total
B366	Gl	10	47.2(3)	0.71(3)	17.97(9)	0.12(2)	8.30(8)	0.14(3)	12.2(1)	10.5(1)	2.6(1)	0.11(2)	0.17(2)	91.64
	Cpx	15	51.6(5)	0.19(6)	7.1(10)	0.32(7)	4.1(1)	0.06(5)	18.2(4)	18.4(4)	0.45(3)	—	—	100.42
	Opx	10	54.5(8)	0.03(6)	6.1(7)	0.3(1)	7.0(3)	0.10(5)	30.7(10)	1.8(10)	0.07(3)	—	—	100.60
	Oliv	7	40.3(2)	0.06(4)	0.04(3)	0.04(2)	11.7(2)	0.13(2)	48.3(2)	0.17(4)	—	—	—	100.74
	Gt	9	41.8(2)	0.18(5)	23.3(2)	0.7(1)	8.3(1)	0.32(4)	18.6(2)	6.8(2)	0.02(2)	—	—	100.02
B365	Gl	10	46.5(1)	0.67(2)	16.33(5)	0.16(3)	8.7(1)	0.13(5)	14.2(1)	10.9(1)	2.3(2)	0.11(2)	0.10(2)	94.40
	Cpx	15	52.7(4)	0.12(4)	6.2(2)	0.26(6)	4.1(1)	0.09(4)	19.4(2)	17.3(3)	0.48(2)	—	—	100.65
	Opx	10	55.2(4)	0.11(3)	5.6(4)	0.29(5)	6.7(1)	0.10(4)	31.3(2)	1.71(7)	0.06(3)	—	—	101.07
	Oliv	7	40.5(3)	0.01(2)	0.05(2)	0.13(4)	10.75(6)	0.09(4)	48.6(3)	0.20(2)	—	—	—	100.33
	Gt	10	42.1(4)	0.11(4)	23.7(3)	0.6(1)	7.54(9)	0.27(2)	19.5(2)	5.9(3)	0.00(1)	—	—	99.72
B399	Gl	10	47.2(2)	0.70(2)	16.26(9)	0.08(3)	8.4(1)	0.12(5)	13.73(6)	10.6(1)	2.6(1)	0.13(2)	0.23(2)	92.49
	Cpx	15	53.1(4)	0.17(2)	6.0(4)	0.18(5)	3.6(1)	0.10(3)	19.0(3)	18.0(4)	0.76(4)	—	—	100.91
	Opx	10	55.9(4)	0.09(2)	4.7(7)	0.21(5)	6.24(9)	0.07(3)	32.2(2)	1.65(7)	0.09(2)	—	—	101.15
	Oliv	6	40.5(3)	0.11(2)	0.10(3)	0.02(2)	10.2(1)	0.16(2)	49.6(2)	0.27(3)	—	—	—	100.96
	Gt	10	42.2(2)	0.14(3)	23.9(2)	0.5(1)	7.1(2)	0.25(2)	19.9(2)	6.1(1)	0.01(1)	—	—	100.10
B384	Gl	10	49.4(1)	0.61(3)	17.0(1)	0.13(3)	8.0(1)	0.12(3)	11.04(9)	10.2(3)	2.9(1)	0.38(2)	0.23(3)	92.83
	Opx	10	55.4(3)	0.10(4)	4.1(2)	0.66(9)	7.2(1)	0.13(5)	32.0(2)	1.43(7)	0.06(2)	—	—	101.08
	Oliv	7	40.4(2)	0.02(1)	0.08(4)	0.15(2)	11.6(1)	0.15(4)	48.6(2)	0.15(1)	—	—	—	101.15
B388	Gl	10	49.8(2)	0.62(3)	17.0(2)	0.16(3)	7.2(1)	0.10(2)	11.31(6)	10.37(7)	2.89(9)	0.38(2)	0.16(2)	92.02
	Opx	10	55.7(2)	0.10(3)	4.2(2)	0.71(7)	7.0(1)	0.16(2)	32.0(2)	1.31(7)	0.04(2)	—	—	101.22
	Oliv	7	41.1(2)	0.01(1)	0.08(2)	0.03(1)	11.1(1)	0.10(3)	48.7(2)	0.13(1)	—	—	—	101.25
B392	Gl	10	50.0(3)	0.74(3)	19.5(3)	0.07(3)	6.9(2)	0.08(3)	9.17(9)	9.54(4)	3.3(2)	0.48(2)	0.24(3)	92.38
	Cpx	15	51.9(4)	0.28(3)	6.7(7)	0.65(9)	4.2(1)	0.12(2)	17.2(3)	19.2(4)	0.62(6)	—	—	100.87
	Opx	10	54.6(3)	0.10(2)	6.3(3)	0.59(9)	7.7(1)	0.14(3)	30.6(2)	1.37(7)	0.07(1)	—	—	101.47
	Oliv	7	40.7(2)	0.11(2)	0.09(2)	0.07(2)	12.7(2)	0.17(2)	47.3(2)	0.18(2)	—	—	—	101.32
B408	Gl	10	49.7(2)	1.27(3)	17.21(6)	0.13(3)	7.4(1)	0.11(4)	10.35(7)	9.46(9)	3.3(1)	0.75(3)	0.34(3)	94.05
	Opx	10	55.3(2)	0.19(2)	4.4(2)	0.75(4)	7.04(7)	0.13(3)	31.8(2)	1.53(4)	0.07(2)	—	—	101.21
	Oliv	7	40.3(1)	0.05(2)	0.05(3)	0.10(3)	11.5(1)	0.13(3)	48.9(1)	0.17(1)	—	—	—	101.20

Notes: Units in parentheses as in Table 1. Glass analyses normalized to total 100% on an anhydrous basis, with all Fe as FeO.

Table 4. Electron microprobe analyses of run products from anhydrous melting experiments

Expt	Phase	Analyses	SiO_2	TiO_2	Al_2O_3	Cr_2O_3	FeO*	MnO	MgO	CaO	Na_2O	K_2O	P_2O_5	Total
B303	Gl	10	47.5(3)	0.66(3)	17.8(1)	0.17(4)	8.1(2)	0.10(5)	11.8(1)	10.98(7)	2.2(1)	0.08(2)	0.12(3)	99.51
	Cpx	15	51.5(8)	0.18(4)	8.0(11)	0.49(8)	4.9(2)	0.10(4)	20.9(11)	13.8(10)	0.49(3)	—	—	100.36
	Opx	10	53.6(7)	0.12(2)	6.6(11)	0.35(7)	6.4(2)	0.10(3)	30.3(5)	2.3(2)	0.12(2)	—	—	99.89
	Oliv	7	40.0(3)	0.05(3)	0.12(1)	0.06(4)	10.7(1)	0.10(3)	48.3(4)	0.31(2)	—	—	—	99.64
	Sp	5	0.5(1)	0.07(7)	62.1(7)	4.5(3)	8.1(1)	0.11(2)	24.0(3)	0.03(3)	—	—	—	99.41
B292	Gl	10	48.0(1)	0.68(2)	18.3(2)	0.13(3)	8.3(2)	0.16(3)	11.16(7)	10.57(7)	2.5(2)	0.12(1)	0.11(3)	100.03
	Cpx	15	51.7(7)	0.26(5)	8.9(9)	0.35(7)	4.8(3)	0.10(3)	20.1(9)	14.3(10)	0.52(4)	—	—	101.03
	Opx	10	53.2(6)	0.11(3)	7.8(8)	0.28(3)	6.6(1)	0.15(3)	29.7(4)	2.1(1)	0.11(2)	—	—	100.05
	Oliv	7	40.2(3)	0.05(2)	0.12(1)	0.14(3)	11.42(8)	0.10(2)	47.6(2)	0.27(1)	—	—	—	99.90
	Sp	5	0.42(7)	0.14(1)	63.6(3)	3.2(3)	8.3(2)	0.08(2)	23.9(3)	0.07(2)	—	—	—	99.71
B287	Gl	10	46.9(2)	0.66(3)	17.9(1)	0.07(2)	8.4(1)	0.12(4)	11.4(1)	10.71(6)	2.5(1)	0.12(1)	0.13(2)	98.91
	Cpx	15	51.7(6)	0.25(5)	8.4(9)	0.44(5)	4.8(2)	0.14(2)	19.9(8)	15.0(7)	0.56(3)	—	—	101.19
	Opx	10	53.8(7)	0.12(3)	7.3(12)	0.35(6)	6.75(7)	0.13(2)	30.4(4)	2.08(7)	0.10(2)	—	—	101.03
	Oliv	7	40.3(3)	0.02(2)	0.13(4)	0.09(3)	11.3(1)	0.12(2)	48.3(3)	0.27(2)	—	—	—	100.53
	Sp	3	0.58(2)	0.08(3)	62.7(2)	4.64(9)	8.6(2)	0.09(0)	23.97(5)	0.08(2)	—	—	—	100.74
B394	Gl	10	46.3(2)	0.60(3)	17.1(1)	0.18(3)	8.62(8)	0.16(4)	13.0(1)	10.66(8)	2.22(5)	0.12(1)	0.14(2)	99.10
	Cpx	15	51.5(5)	0.20(4)	8.7(6)	0.31(3)	4.6(2)	0.11(3)	20.6(4)	13.9(4)	0.63(3)	—	—	100.55
	Opx	10	54.1(4)	0.12(3)	7.4(6)	0.35(2)	6.30(8)	0.11(3)	30.6(4)	2.13(3)	0.12(1)	—	—	101.23
	Oliv	6	40.2(3)	0.11(1)	0.03(8)	0.14(2)	10.41(7)	0.10(3)	49.5(2)	0.29(2)	—	—	—	100.78
	Sp	2	0.38(3)	0.14(1)	64.2(5)	2.9(1)	7.9(1)	0.10(3)	25.0(2)	0.07(0)	—	—	—	100.69
B302	Gl	10	46.4(3)	0.68(4)	17.2(2)	0.13(3)	8.9(2)	0.11(4)	12.5(2)	10.8(1)	2.3(1)	0.07(2)	0.15(5)	99.24
	Cpx	15	51.9(7)	0.20(7)	8.8(8)	0.29(4)	5.1(3)	0.11(4)	20.9(12)	12.8(12)	0.62(6)	—	—	100.72
	Opx	10	53.0(5)	0.10(3)	7.3(9)	0.25(3)	6.50(5)	0.10(3)	30.1(3)	2.2(1)	0.13(3)	—	—	99.68
	Oliv	7	40.2(4)	0.08(3)	0.12(1)	0.10(3)	10.9(2)	0.07(5)	48.2(4)	0.31(2)	—	—	—	99.98
	Sp	4	0.7(2)	0.13(5)	64.4(4)	3.0(1)	8.0(1)	0.10(3)	24.33(3)	0.13(1)	—	—	—	100.79
B414	Cpx	15	52.3(6)	0.48(7)	6.7(8)	0.7(2)	4.0(2)	0.06(5)	18.8(7)	17.4(9)	0.88(8)	—	—	101.32
	Opx	10	54.7(4)	0.20(3)	5.8(6)	0.55(7)	6.39(9)	0.10(5)	31.3(4)	1.66(8)	0.16(4)	—	—	100.86
	Oliv	7	40.7(3)	0.09(2)	0.3(2)	0.14(5)	9.9(1)	0.10(3)	49.0(5)	0.3(2)	—	—	—	100.53
	Sp	2	0.9(2)	0.34(1)	52.5(13)	14.5(12)	9.7(4)	0.09(6)	22.5(2)	0.22(2)	—	—	—	100.75
B412	Cpx	15	52.1(6)	0.44(4)	6.8(4)	0.68(8)	4.0(2)	0.05(6)	18.8(7)	16.8(8)	0.87(5)	—	—	100.54
	Opx	10	54.4(4)	0.20(4)	6.1(5)	0.57(5)	6.28(6)	0.08(5)	32.0(2)	1.52(4)	0.16(5)	—	—	101.31
	Oliv	7	40.7(3)	0.02(2)	0.2(2)	0.17(2)	10.0(1)	0.12(6)	49.1(2)	0.16(1)	—	—	—	100.47
	Sp	2	0.6(3)	0.33(1)	53.7(3)	14.0(4)	10.0(1)	0.10(1)	22.7(1)	0.09(1)	—	—	—	101.52

Notes: Units in parentheses as in Table 1.

Table 5. Comparison of replicate analyses of glasses used aselectron microprobe secondary standards

Expt	Analyses	SiO_2	TiO_2	Al_2O_3	Cr_2O_3	FeO*	MnO	MgO	CaO	Na_2O	K_2O	P_2O_5	Total
839b-23[1]	370	52.7(3)	0.65(3)	15.2(1)	0.12(5)	8.8(2)	0.15(5)	9.2(1)	11.4(1)	1.46(9)	0.26(2)	0.12(8)	100.06
839b-23[2]	10	53.3(2)	0.60(3)	15.16(8)	0.05(3)	8.85(8)	0.22(2)	9.36(5)	11.3(1)	1.48(5)	0.30(2)	0.11(3)	100.73
70-002[1]	30	49.6(3)	1.28(3)	16.3(2)	0.10(5)	8.9(2)	0.16(4)	8.60(8)	11.9(1)	2.6(1)	0.09(2)	0.22(3)	99.75
70-002[3]	368	49.6(1)	1.20(2)	15.8(2)	–	8.98(7)	0.17(3)	8.66(6)	11.9(1)	2.67(6)	0.10(1)	0.12(4)	99.20

[1]This study.
[2]Analysis from Gaetani et al. (1994).
[3]Analysis from Kinzler and Grove (1992a).

Table 6. Comparison of multiply-saturated melt compositions.

Oxide	Constant F	Constant MgO
Increasing H_2O at Constant P		
SiO_2	I	I
Al_2O_3	I	I
FeO	D	D
MgO	D	–
CaO	C	I
Na_2O	C	D
Increasing P at Constant H_2O		
SiO_2	D	D
Al_2O_3	C	I
FeO	I	I
MgO	I	–
CaO	C	D
Na_2O	C	I
Increasing P Anhydrous		
SiO_2	D	D
Al_2O_3	D	C
FeO	I	I
MgO	I	–
CaO	C	D
Na_2O	C	I

Notes: I = increases; D = decreases; C = constant.
[1]Determined on the basis of comparison of batch melt compositions calculated using the methods of Kinzler (1996).

Table 7. Comparison of experimentally-determined stoichiometric coefficients for mantle melting reactions under hydrous and anhydrous conditions.

Expts	P (Gpa)	ΔT (°C)	X_{Cpx}	X_{Opx}	X_{Oliv}	X_{Sp}
Anhydrous						
20-24[1,2]	1.0	1270-1330	0.71	0.38	–0.22	0.13
B287-B303[3,4]	1.2	1315-1345	0.82	0.42	–0.34	0.10
B52-B30[4,5]	1.2	1300-1315	1.08	0.17	–0.36	0.07
B302-B394[2,3]	1.6	1355-1370	0.99	–0.02	–0.10	0.13
H200-H179[4,5]	1.6	1320-1340	1.34	–0.15	–0.25	0.07
Hydrous						
38-41[2,6]	1.0	1200-1300	0.64	0.50	–0.16	0.02
B329-B330[2,3]	1.2	1185-1200	0.62	0.51	–0.25	0.12

[1]Baker and Stolper (1994)
[2]Coefficients determined using change in phase proportions.
[3]This Study.
[4]Coefficients determined using 2 lquid method.
[5]Kinzler and Grove (1992a).
[6]Hirose and Kawamoto (1995).

Table 8. Comparison of extent of melting at which one phase will be exhausted and residue modes calculated on the basis of stoichiometric coefficients for mantle melting reactions at 1.2 GPa under hydrous and anhydrous conditions.

F	Cpx	Opx	Oliv	Sp
Initial Mantle Mode[1]				
	17.0	27.0	53.0	3.0
Residue from Anhydrous Partial Melting				
20.7	–	23.1	75.7	1.2
Residue from Hydrous Partial Melting				
25.0	2.0	19.0	79.0	–

[1]Depleted MORB mantle mode of Kinzler (1996)

FIGURE CAPTIONS

Figure 1. Pseudoternary projection from Plag onto the Oliv-Cpx-SiO_2 plane illustrating effect of increasing H_2O content at constant pressure (filled circles) and of increasing pressure at constant H_2O content (open circles) on the compositions of melt saturated with a spinel lherzolite mineral assemblage.

Figure 2. Plots of molar Mg/(Mg + Fe) versus the concentrations of FeO (a) and MgO (b) in silicate melts saturated with a spinel lherzolite assemblage illustrating the lower FeO and MgO contents of hydrous multiply saturated melts relative to anhydrous ones. All hydrous melt compositions have been normalized to 100% on a volatile-free basis.

Figure 3. Plots of molar Mg/(Mg + Fe) versus the concentrations of FeO (a) and MgO (b) in silicate melts saturated with a mantle residual assemblage illustrating the increase in FeO and MgO contents of hydrous multiply saturated melts with increasing pressure of melting. All hydrous melt compositions have been normalized to 100% on a volatile-free basis.

Figure 4. Plot of MgO versus FeO in silicate melts saturated with a mantle residual assemblage illustrating similarity between the concentration of FeO at a given MgO content in hydrous melts produced at 1.6 GPa and anhydrous melts produced at 1.2 GPa. All hydrous melt compositions have been normalized to 100% on a volatile-free basis.

Figure 5. Plots of molar $\log D_{Fe}^{Olivine/Silicate\ Melt}$ and $\log D_{Mg}^{Olivine/Silicate\ Melt}$ versus inverse temperature illustrating that hydrous and anhydrous melts follow the same linear trend.

This indicates the lower FeO and MgO contents of hydrous mantle melts are related to their lower liquidus temperatures.

Figure 6. Pseudoternary projections from Sp onto the Oliv-Cpx-SiO_2 plane illustrating the stoichiometry of spinel lherzolite melting reactions at 1.2 GPa under (a) hydrous and (b) anhydrous conditions, and (c) the systematic change in the compositions of experimentally produced pyroxenes with increasing H_2O dissolved in the silicate melt. The experiment at 1315°C is anhydrous, while the experiment at 1200°C has 6.6 wt% H_2O in the melt, and the experiment at 1100°C has ~12 wt% H_2O in the melt.

Figure 7. Pseudoternary projections from Sp onto the Oliv-Cpx-SiO_2 plane illustrating the stoichiometry of spinel lherzolite melting reactions at 1.6 GPa under (a) hydrous and (b) anhydrous conditions.

Figure 8. Schematic illustration of melting reaction for peridotite containing coexisting Sp and Gt at 1.6 GPa under hydrous conditions.

Figure 9. Plot of observed versus predicted temperature for thermometer based on the distribution of MgO between olivine and basaltic melt. Open symbols are anhydrous experiments, and filled symbols contain various amounts of H_2O dissolved in the silicate melt.

Figure 10. Plot of observed FeO versus FeO predicted using expression for partitioning of FeO between Oliv and silicate melt. Open symbols are anhydrous experiments, and filled symbols contain various amounts of H_2O dissolved in the silicate melt.

Figure 11. Plot of melt fraction versus temperature comparing the liquidus temperatures of anhydrous batch melts at 1.5 GPa predicted using the methods of Kinzler and Grove (1992a,b) with the liquidus temperatures of hydrous batch melts from mantles with 3 different bulk H_2O contents, predicted using the partitioning of MgO between olivine and basaltic melt.

Figure 12. Plot of melt fraction versus (a) FeO and (b) MgO comparing anhydrous batch melts at 1.5 GPa predicted using the methods of Kinzler and Grove (1992a,b) with the hydrous batch melts from mantles with 3 different bulk H_2O contents, predicted using the partitioning of FeO and MgO between olivine and basaltic melt.

Figure 13. Plot of MgO versus FeO comparing 1.5 GPa anhydrous batch melts predicted using the methods of Kinzler and Grove (1992a,b) with hydrous batch melts predicted using the partitioning of FeO and MgO between olivine and basaltic melt. All hydrous melt compositions have been normalized to 100% on a volatile-free basis.

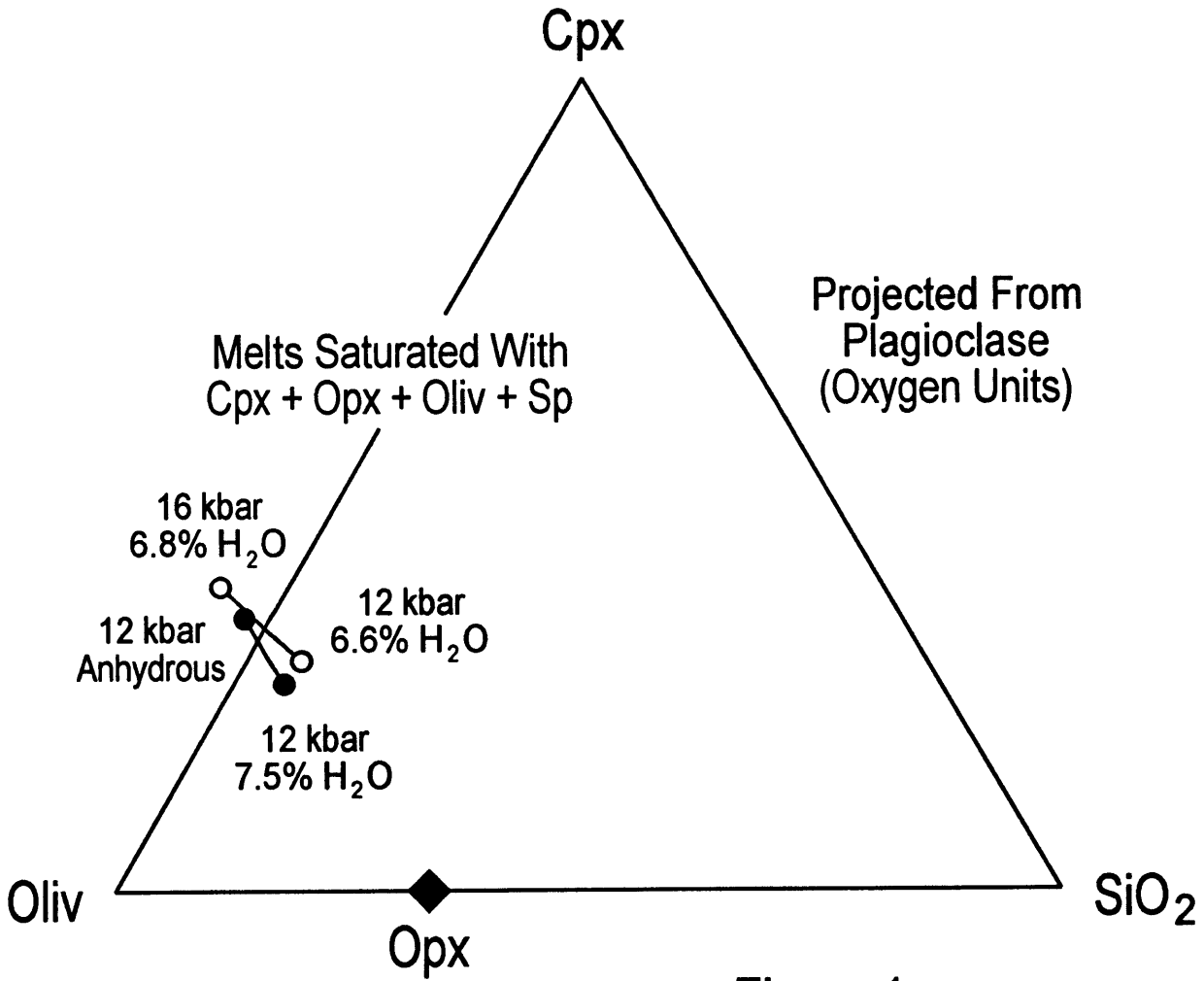
Cpx
Projected From
Plagioclase
(Oxygen Units)
Melts Saturated With
Cpx + Opx + Oliv + Sp
16 kbar
6.8% H2O
12 kbar
6.6% H2O
12 kbar
Anhydrous
12 kbar
7.5% H2O
Oliv
Opx
SiO2

Figure 1

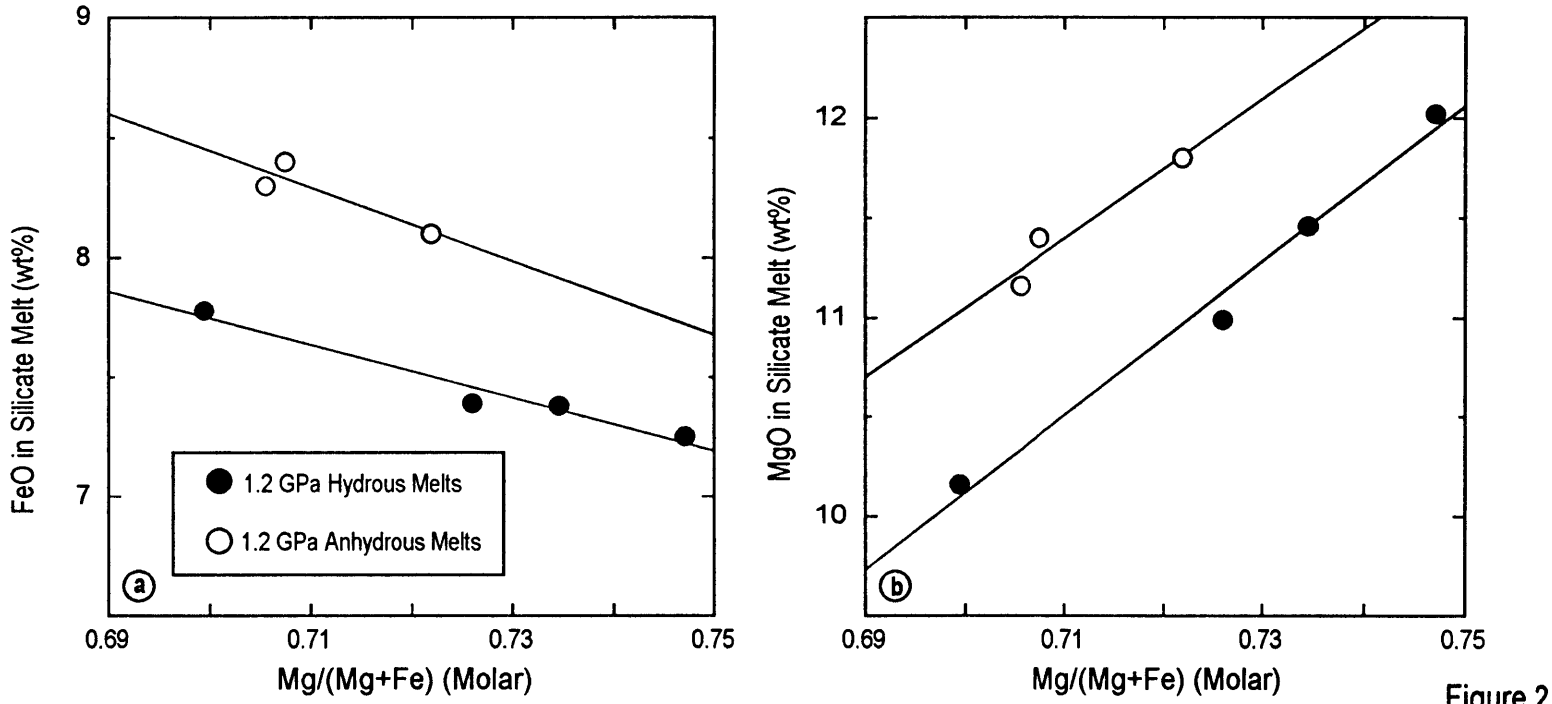
9
8
7
FeO in Silicate Melt (wt%)
1.2 GPa Hydrous Melts
1.2 GPa Anhydrous Melts
a
0.69
0.71
0.73
0.75
Mg/(Mg+Fe) (Molar)
12
11
10
MgO in Silicate Melt (wt%)
b
0.69
0.71
0.73
0.75
Mg/(Mg+Fe) (Molar)

Figure 2

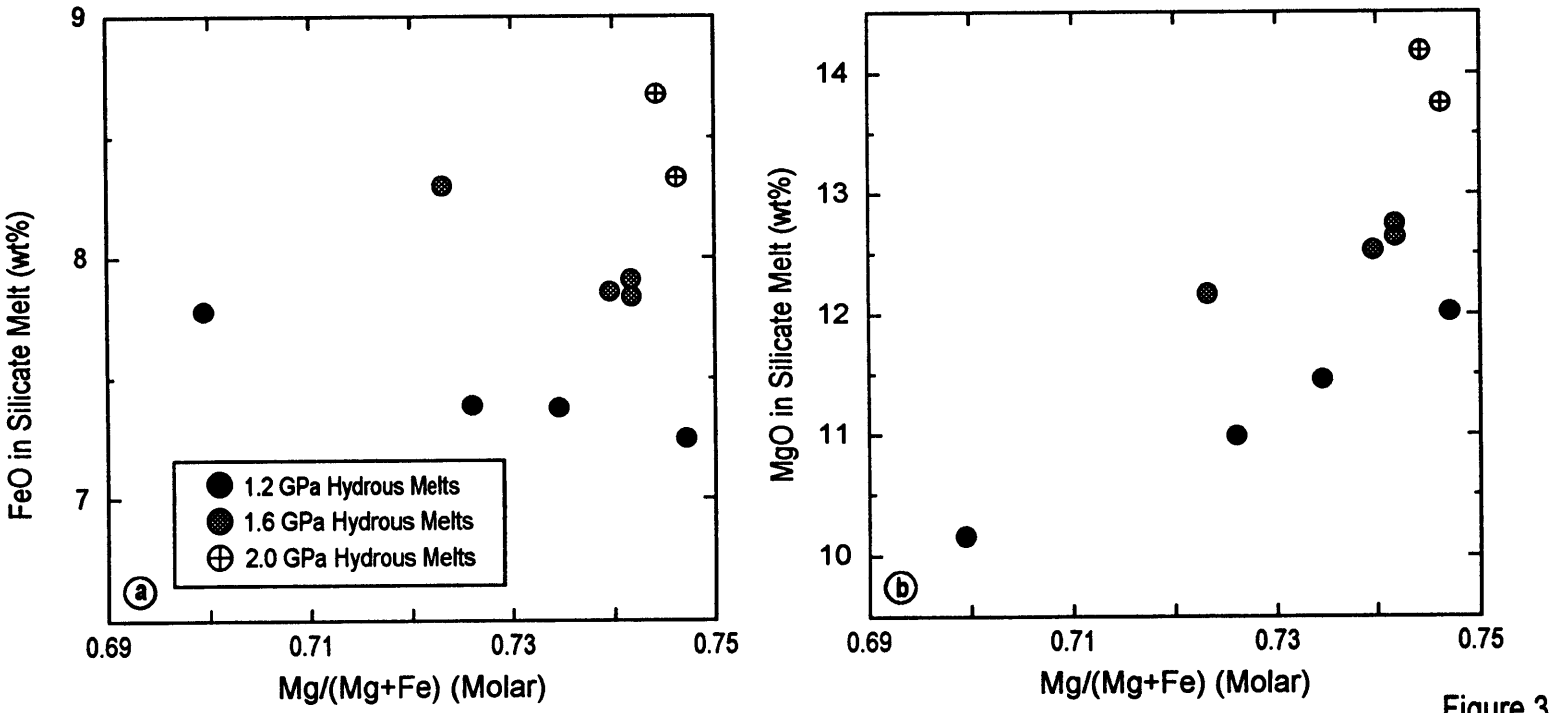
9
8
7
FeO in Silicate Melt (wt%)
1.2 GPa Hydrous Melts
1.6 GPa Hydrous Melts
2.0 GPa Hydrous Melts
a
0.69
0.71
0.73
0.75
Mg/(Mg+Fe) (Molar)
14
13
12
11
10
MgO in Silicate Melt (wt%)
b
0.69
0.71
0.73
0.75
Mg/(Mg+Fe) (Molar)

Figure 3

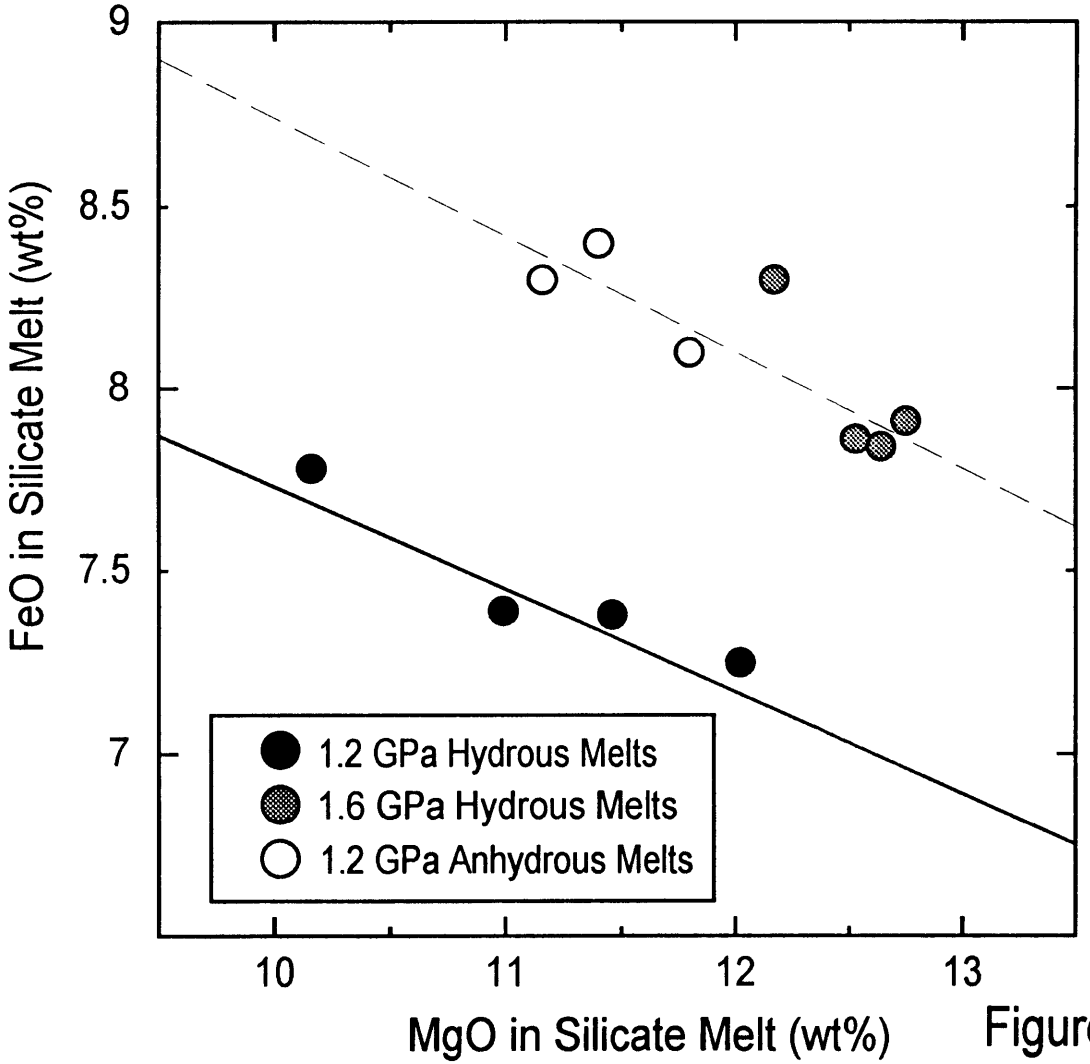
9
8.5
8
7.5
7
FeO in Silicate Melt (wt%)
10
11
12
13
MgO in Silicate Melt (wt%)
1.2 GPa Hydrous Melts
1.6 GPa Hydrous Melts
1.2 GPa Anhydrous Melts

Figure 4

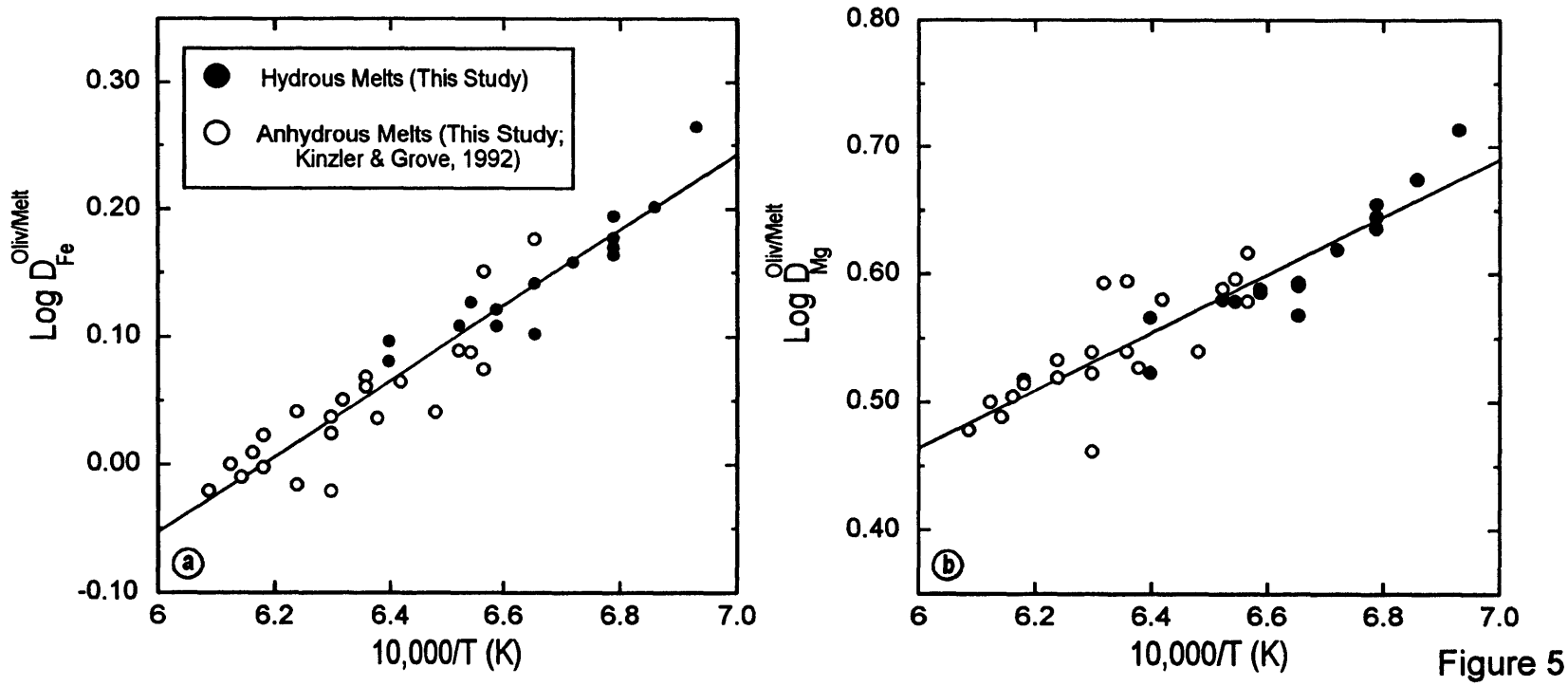
Hydrous Melts (This Study)
Anhydrous Melts (This Study; Kinzler & Grove, 1992)
Log $D_{Fe}^{Oliv/Melt}$
0.30
0.20
0.10
0.00
-0.10
6
6.2
6.4
6.6
6.8
7.0
10,000/T (K)
a
Log $D_{Mg}^{Oliv/Melt}$
0.80
0.70
0.60
0.50
0.40
10,000/T (K)
b

Figure 5

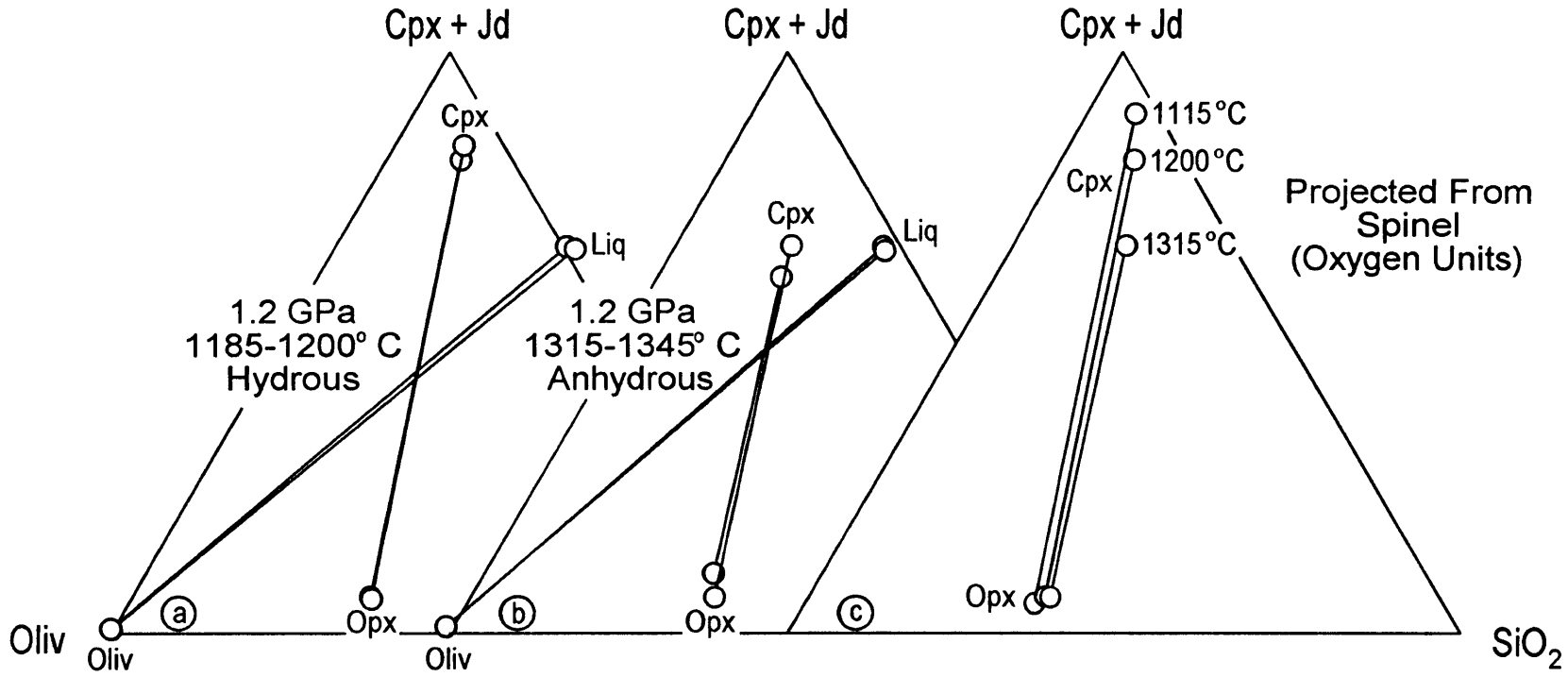
Cpx + Jd
Cpx + Jd
Cpx + Jd
Cpx
Liq
1.2 GPa
1185-1200° C
Hydrous
Cpx
Liq
1.2 GPa
1315-1345° C
Anhydrous
1115°C
1200°C
Cpx
1315°C
Projected From
Spinel
(Oxygen Units)
Oliv
a
Opx
Oliv
b
Opx
c
Opx
SiO2

Figure 6

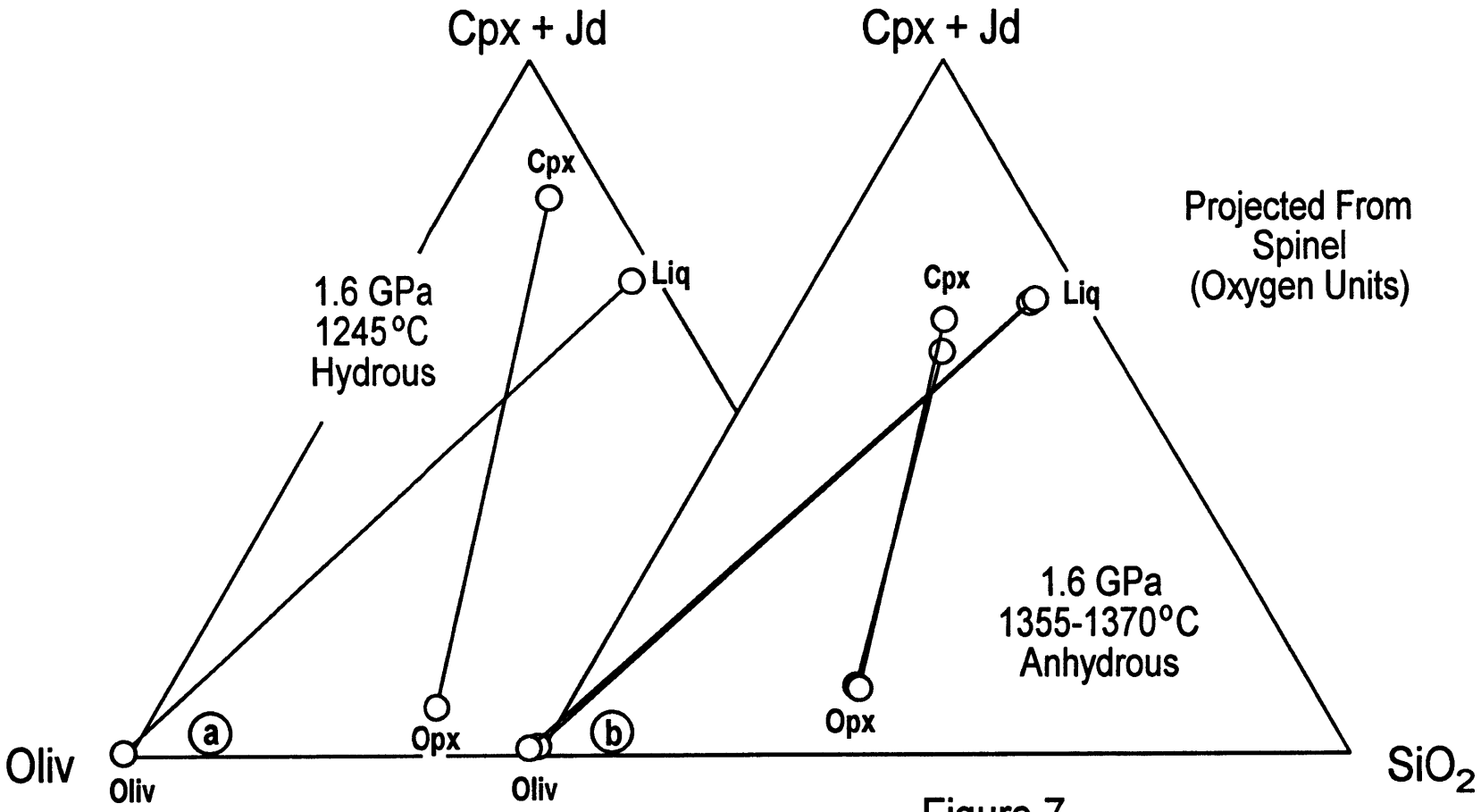
Cpx + Jd
Cpx + Jd
Cpx
Liq
1.6 GPa
1245°C
Hydrous
Projected From
Spinel
(Oxygen Units)
Cpx
Liq
1.6 GPa
1355-1370°C
Anhydrous
a
b
Opx
Opx
Oliv
Oliv
Oliv
SiO2

Figure 7

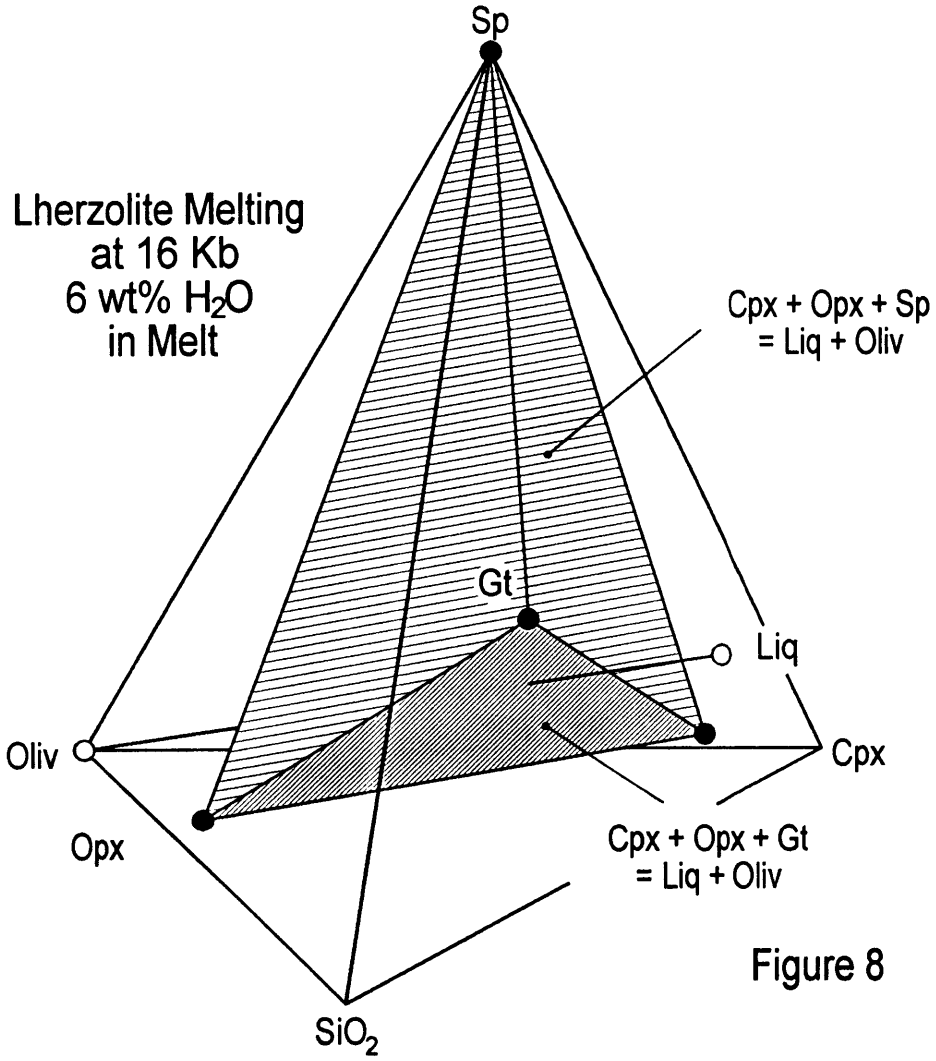
Lherzolite Melting
at 16 Kb
6 wt% H_2O
in Melt
Sp
Cpx + Opx + Sp
= Liq + Oliv
Gt
Liq
Oliv
Cpx
Opx
Cpx + Opx + Gt
= Liq + Oliv
SiO_2

Figure 8

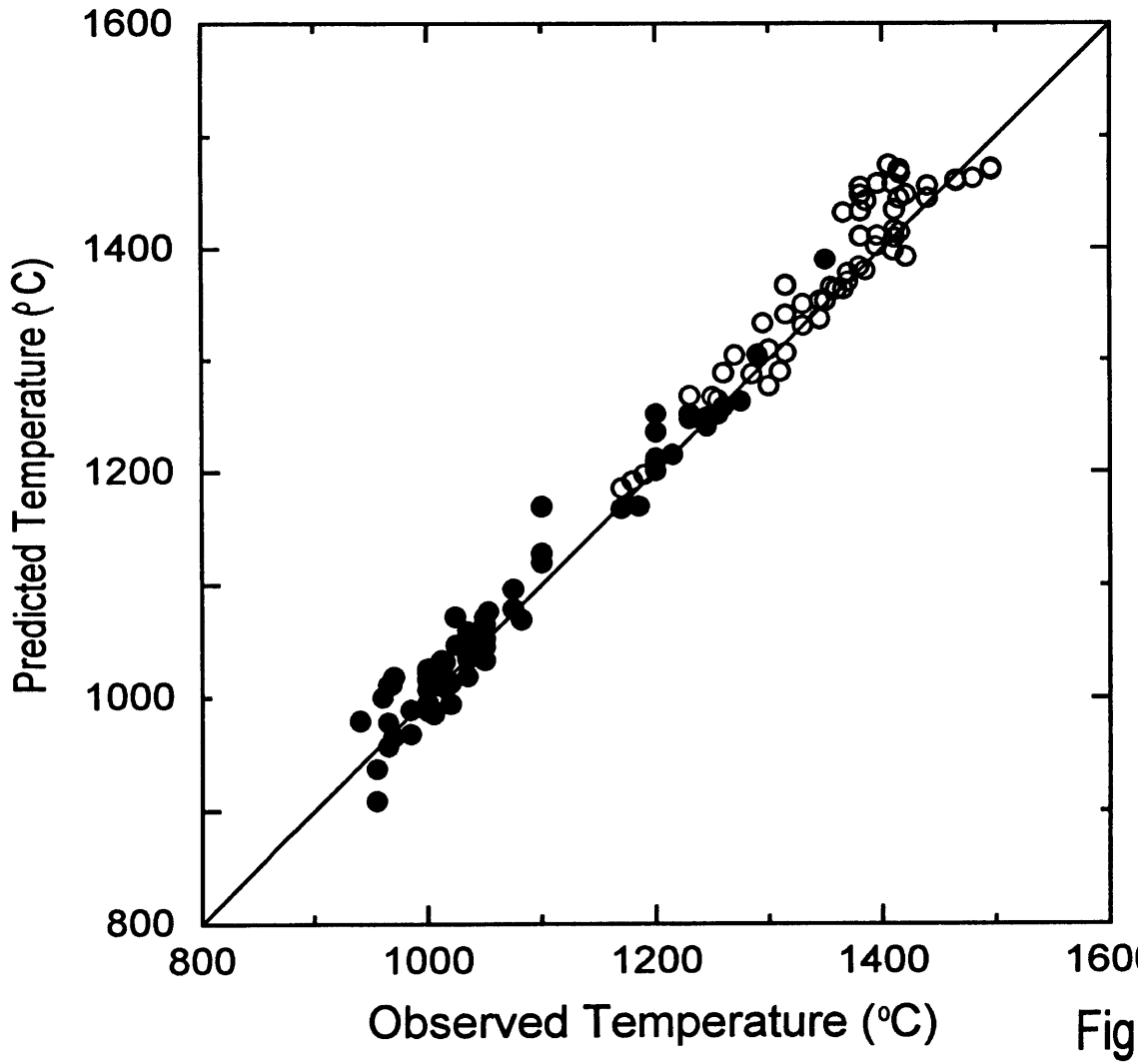
1600
1400
1200
1000
800
Predicted Temperature (°C)
800
1000
1200
1400
1600
Observed Temperature (°C)

Figure 9

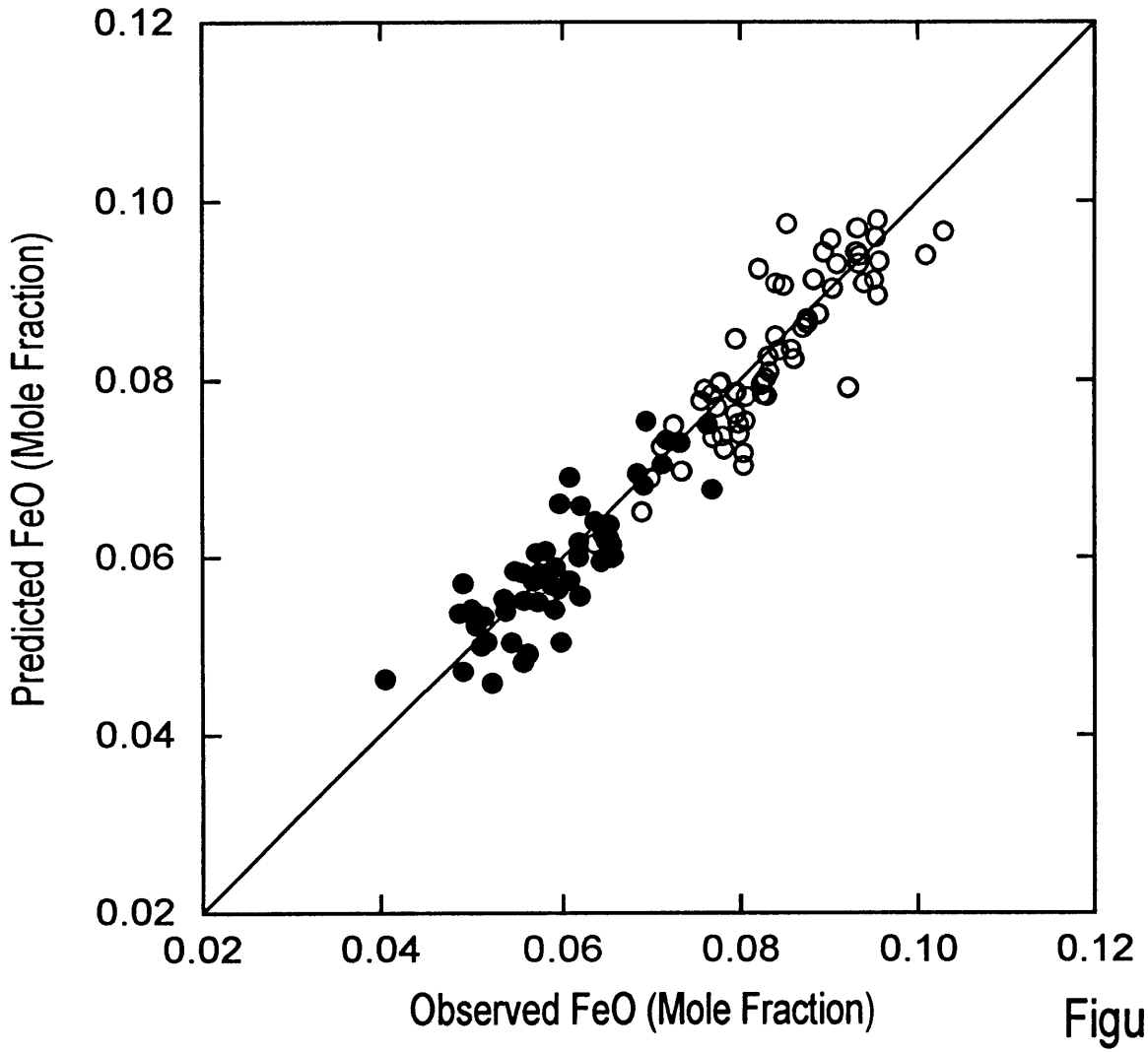
0.12
0.10
0.08
0.06
0.04
0.02
Predicted FeO (Mole Fraction)
0.02
0.04
0.06
0.08
0.10
0.12
Observed FeO (Mole Fraction)

Figure 10

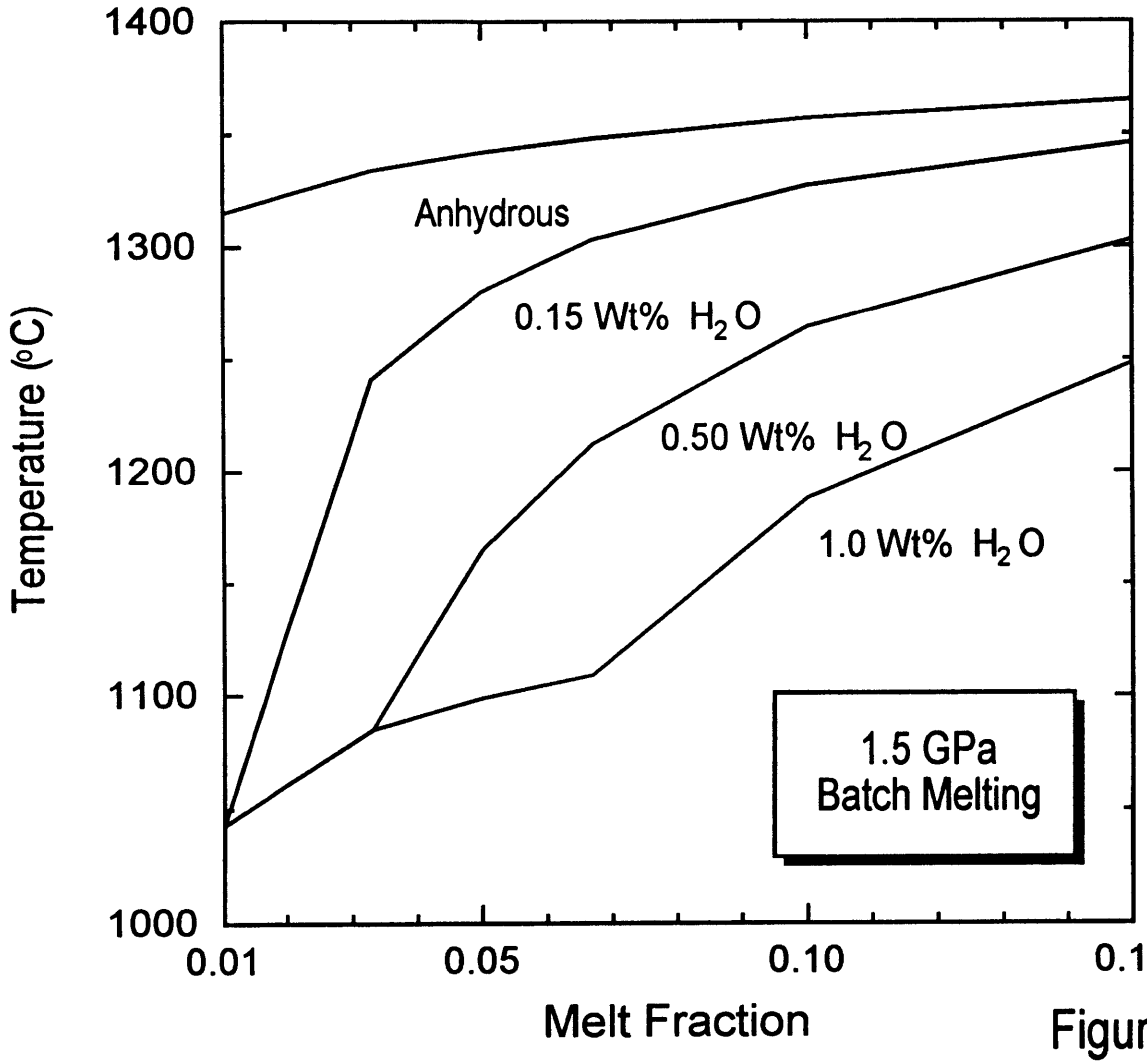
1400
1300
1200
1100
1000
Temperature (°C)
Anhydrous
0.15 Wt% H_2O
0.50 Wt% H_2O
1.0 Wt% H_2O
1.5 GPa
Batch Melting
0.01
0.05
0.10
0.15
Melt Fraction

Figure 11

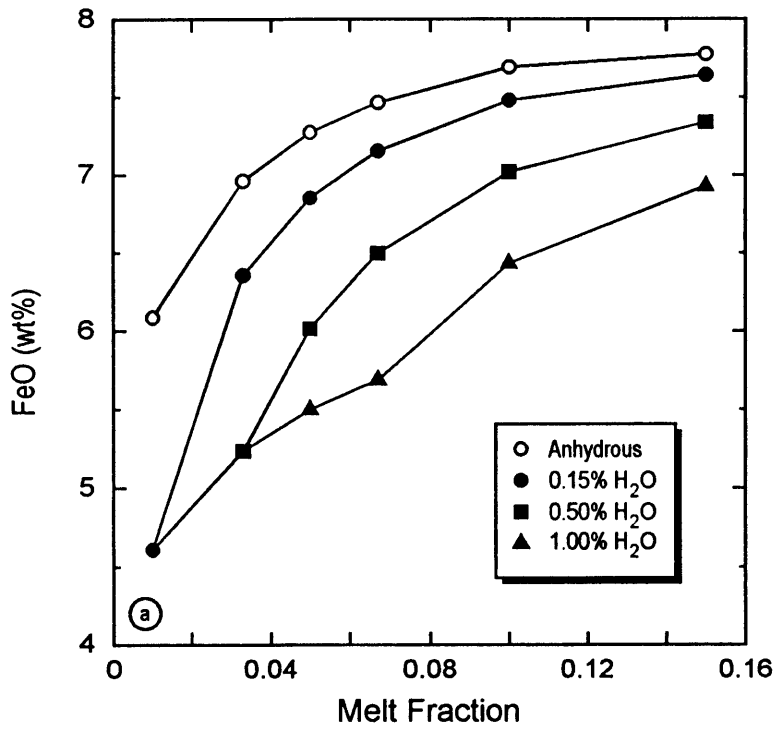
FeO (wt%)
Melt Fraction
Anhydrous
0.15% H_2O
0.50% H_2O
1.00% H_2O
a

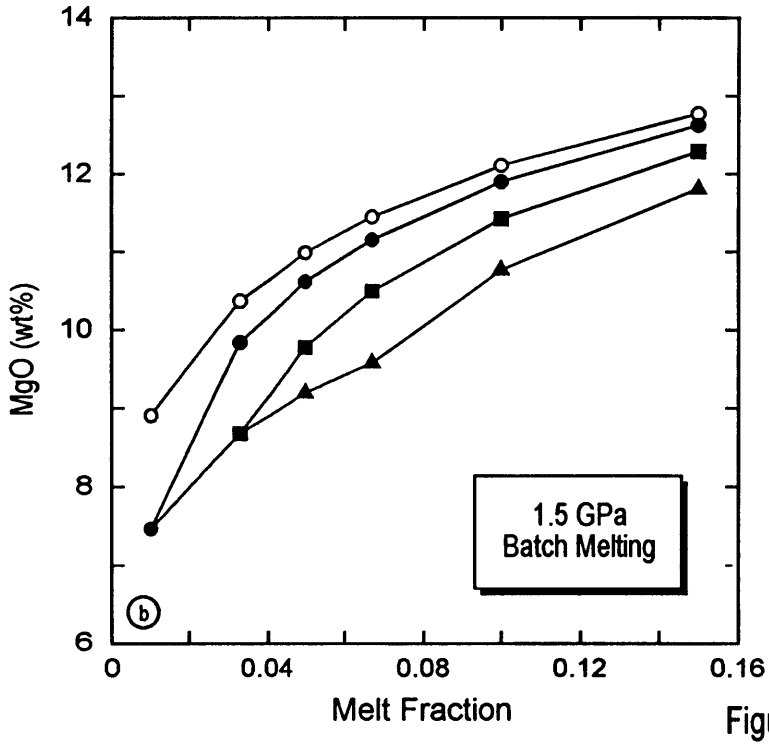
MgO (wt%)
Melt Fraction
1.5 GPa
Batch Melting
b

Figure 12

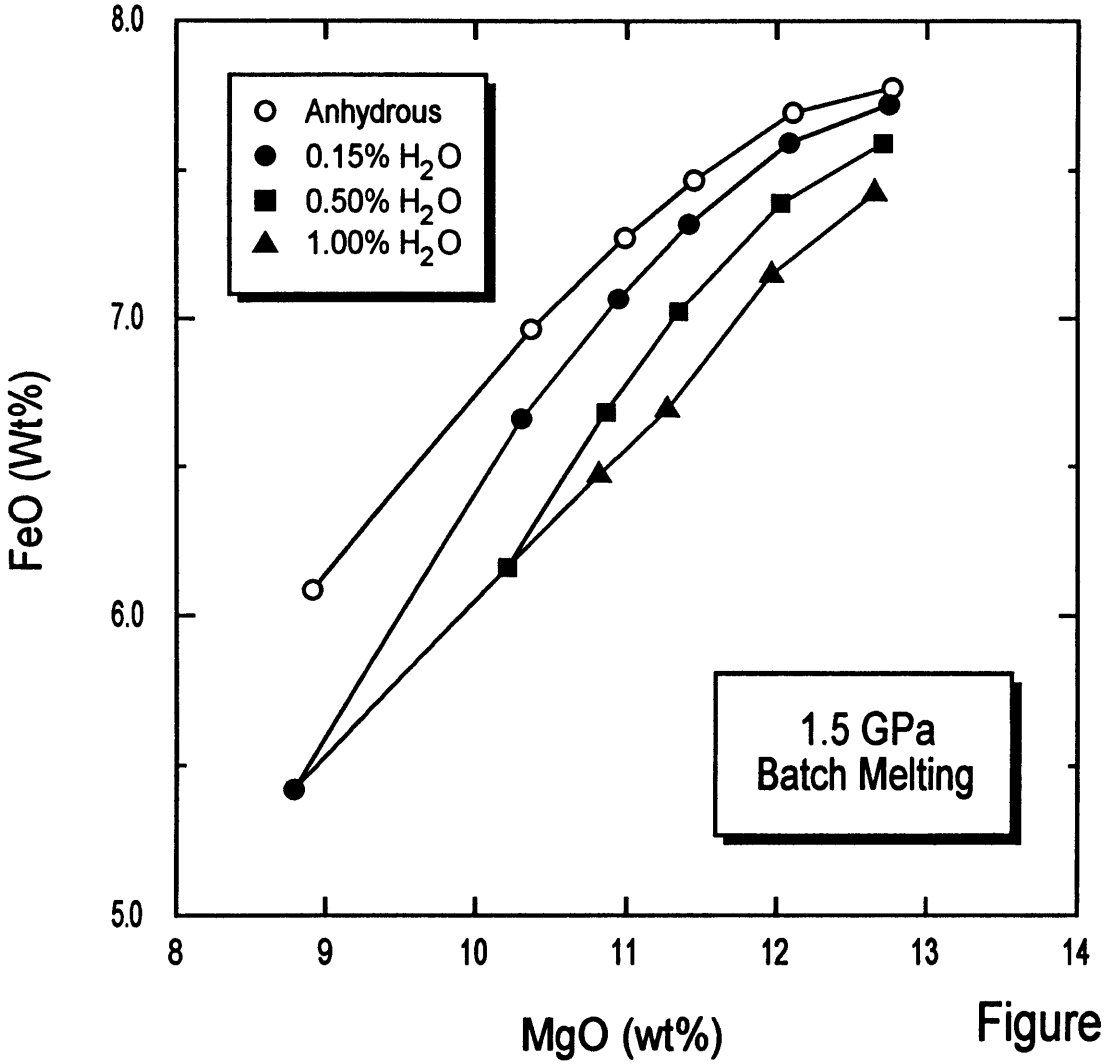
8.0
7.0
6.0
5.0
8
9
10
11
12
13
14
FeO (Wt%)
MgO (wt%)
Anhydrous
0.15% H_2O
0.50% H_2O
1.00% H_2O
1.5 GPa
Batch Melting

Figure 13

CHAPTER 2.

WETTING OF MANTLE OLIVINE BY CORE-FORMING MELTS: THE INFLUENCE OF VARIABLE f_{O_2}/f_{S_2} CONDITIONS.

ABSTRACT

The distribution and connectivity of small amounts of melt in polycrystalline materials depends on the excess free energies at solid/melt and solid/solid interfaces. The ratio of these interfacial energies produces a characteristic angle (dihedral angle) where two contacting crystals bound a pocket of melt. Dihedral angles determine the amount of melt necessary to achieve interconnectivity. Experiments performed on aggregates of mantle olivine and iron sulfide melt over a range of oxygen and sulfur fugacity conditions demonstrate that the amount of oxygen dissolved in the melt has a strong influence on olivine/sulfide melt dihedral angles. At f_{O_2}/f_{S_2} conditions reducing enough to stabilize metal, an iron sulfide melt will contain dissolved oxygen at parts-per-million concentration levels. These melts form dihedral angles close to 90° in polycrystalline olivine aggregates, trapping a significant amount of melt in isolated pockets at four-grain junctions. At present-day upper mantle f_{O_2}/f_{S_2} conditions, iron sulfide melts contain several weight percent dissolved oxygen and form dihedral angles of 60° or less in olivine-rich rocks. These melts form an interconnected network in mantle peridotite even at very low melt fractions. Thus, percolation of oxygen-rich iron sulfide melts downward through the mantle may have been an important mechanism for segregating material into the Earth's core.

INTRODUCTION

The Earth's outer core is composed of a metallic liquid with a density that is ~10% lower than that of FeNi metal at comparable conditions (Birch, 1964), while the inner core is solid (Julian et al., 1972). The presence of light alloying elements, such as S and O, could explain both the outer core's low melting point and its low density (Mason, 1966; Murthy and Hall, 1970; Ringwood, 1977). Most core formation models involve accretion of the Earth as an initially homogeneous mass of silicates and metal, with the segregation of core-forming material occurring either in a catastrophic event following accretion (Elsasser, 1963) or gradually as material was added to the Earth (Stevenson, 1981). The addition of a veneer of chondritic material to the Earth following formation of the core has been postulated to explain the apparent over-abundance of siderophile elements in the upper mantle (Morgan et al., 1980; Wänke, 1981).

Constraining the core formation process is of fundamental importance for understanding the early thermal history of the Earth. Catastrophic core formation would have released enough gravitational energy to raise the temperature of the Earth by 2000°C, resulting in a global magma ocean (Birch, 1965; Flaser and Birch, 1973). Segregation of core-forming material continuously during accretion would have released gravitational energy more gradually, lessening the thermal effects. In order for continuous core formation to proceed by porous flow, Fe-Ni-S-O melts must form an interconnected network in mantle peridotite.

One way to gain a clearer understanding of the core formation process is to explore the chemical factors that control the physics of Fe-Ni-S-O melt distribution in mantle peridotite. Recent experimental studies have indicated that increasing the total anion (S ± O) content of a metallic liquid may reduce the olivine/melt interfacial energy, promoting connectivity (Ip and Toguri, 1993; Minarik et al., 1996). Here we report experimental results demonstrating that the amount of O dissolved in an Fe-Ni-S-O melt represents an important control on olivine/melt interfacial energy. As the O content of the

melt increases the ratio of solid/liquid interfacial energy to solid/solid interfacial energy decreases, producing lower dihedral angles and allowing interconnectivity to occur at small melt fractions.

EXPERIMENTAL AND ANALYTICAL METHODS

Experiments were performed in a vertical gas mixing furnace at 1350°C, 1 atm pressure, with f_{O_2} and f_{S_2} controlled by mixing CO_2, CO, and SO_2 gases. The gas mixture required for each set of f_{O_2}/f_{S_2} conditions was calculated using thermochemical data from the JANAF tables (Chase et al., 1985). Crucibles were fabricated from single crystals of San Carlos olivine (Fo_{89-91}) following the methods described by Ehlers et al. (1992). Olivine crucibles are ideal containers for these experiments because they are inert with respect to both the experimental charge and the S-rich furnace gases. Experimental conditions and durations are listed in Table 1. The starting composition consisted of a 30:70 mixture, by weight, of synthetic FeS and powdered San Carlos olivine. Olivine/Fe-Ni-S-O melt dihedral angles were determined for each experiment by matching a theoretical distribution to the distribution of 200 measured angles (Harker and Parker, 1945) (Fig 1.). Angle measurements were made using reverse-polarity SEM images at a magnification of 3600x. The compositions of experimental products were determined using the JEOL 733 electron microprobe at MIT. The dihedral angles determined from short (24 hr) and long (216 hr) duration experiments do not differ significantly, indicating that textural equilibrium is approached in a relatively short time (Table 1).

EXPERIMENTAL RESULTS

The melts produced in our experiments consist dominantly of Fe, S, and O, with minor amounts of Ni, Mn, and Cr derived from the olivine starting material. The concentration of O dissolved in the Fe-Ni-S-O melt increases systematically as the f_{O_2}/f_{S_2} ratio of the experiment increases (Table 1) governed by the equilibria:

$$FeS^{\text{Sulfide Melt}} + \frac{1}{2}O_2^{\text{Gas}} = FeO^{\text{Sulfide Melt}} + \frac{1}{2}S_2^{\text{Gas}}.$$

As f_{O_2} increases relative to f_{S_2} this reaction is driven to the right, resulting in a larger FeO component in the Fe-Ni-S-O melt.

The relationships among olivine/Fe-Ni-S-O melt dihedral angle, f_{O_2}/f_{S_2} ratio, and the logarithm of the mole fraction of O dissolved in the Fe-Ni-S-O melt determined from our experiments are shown in Figure 2. In the experiments conducted at the lowest f_{O_2}/f_{S_2} ratio conditions the melt is composed dominantly of FeS with a small NiS component. The large interfacial energy between olivine and melt of this composition is demonstrated by a mean dihedral angle for 5 experiments of 87° (Table 1). At these conditions Fe-Ni-S-O melt forms convex-faced tetrahedra at 4 grain junctions in olivine-rich rocks (Smith, 1964; von Bargen and Waff, 1986). An example of the textures in an experiment that produced a dihedral angle of 86° is shown in Fig. 3a. With increasing f_{O_2}/f_{S_2} ratio, the dihedral angle and the curvature on the faces of the tetrahedra decrease until, at an angle of 70.5°, the faces are planar. With a continued increase of the f_{O_2}/f_{S_2} ratio, the decreasing dihedral angle results in concave faces as the surface area wetted by the melt increases. When the dihedral angle reaches 60° the apices of the tetrahedra have extended far enough along the three-grain junctions that an interconnected network of melt is formed. Our experimental results demonstrate that this situation occurs at f_{O_2}/f_{S_2} conditions where the Fe-Ni-S-O contains 2.7±0.9 wt% O. An olivine/Fe-Ni-S-O melt dihedral angle of 60° was reported by Minarik et al. (1996) for a melt containing 2.9±0.3 wt% O at 3.9 GPa, 1500°C. In our highest f_{O_2}/f_{S_2} ratio experiment the Fe-Ni-S-O melt contains 8.6±0.6 wt% O and the dihedral angle is only 53° (Fig. 3b).

DISCUSSION

Compositional Controls on Olivine/Sulfide Melt Dihedral Angles

The influence of O on olivine/Fe-Ni-S-O liquid dihedral angles can be understood by considering the nature of the interface between the two phases. The excess free energy associated with a crystal surface results from the presence of atoms on that surface

that are not surrounded by the same periodic arrangement of atoms that characterizes the internal structure of the crystal, resulting in unsatisfied bonds (Porter and Easterling, 1981). The excess free energy that characterizes a crystal/liquid interface is a reflection of the suitability of the liquid's constituent components for satisfying the bonds on the surface of the crystal. The minerals that make up the Earth's mantle are composed of a matrix of oxygen anions bonded to interstitial cations. The interfacial energy between these O-rich minerals and melts composed of FeS ± Fe° is large because the melt components do not readily satisfy cation-oxygen bonds and, therefore, wetting of the solid grains is not energetically favorable. As the O content of the melt increases, however, the bonds at the surfaces of these crystals are more easily satisfied by the increased FeO component, leading to a reduction of the excess free energy associated with the crystal/liquid interface.

The dependence of solid/melt interfacial energy on composition is a reflection of the thermodynamic relationship between interfacial energy and the chemical potential of the components in the system, and is given by the Gibbs adsorption isotherm:

$$\partial\gamma = -RT\Gamma_i \partial \mathrm{Log} X_i$$

where γ is the interfacial energy, Γ_i is the excess concentration of the surface-active component at the interface, and X_i is the mole fraction of the surface-active component in one of the phases (e.g., Castellan, 1983). If the interfacial energy decreases with an increase in one of the components at constant pressure and temperature, there should be a linear relationship between the interfacial energy and the logarithm of the mole fraction of that component. The slope of the line will be proportional to the excess concentration of the component at the interface and, therefore, will be negative for components that lead to a decrease in the interfacial energy. The ratio of the solid/liquid to solid/solid interfacial energies in our experiments decreases linearly with an increase in the logarithm of the

mole fraction of O dissolved in the melt (Fig. 4). This trend indicates that O (or FeO) is the surface active component leading to a reduction in the interfacial energy.

Implications for Core Formation

Models calling for accretion of the Earth as a relatively cool, homogeneous mixture of silicates and metal require a mechanism to transport metallic phases downward, through solid silicate, to form the core. Some portion of the material segregating into the core would have been molten, even if the Earth were relatively cold, due to the melting-point lowering effect of light alloying elements on metallic Fe. Estimates for the amount of S (~11 wt%) or O (~9 wt%) required to explain the density of the outer core indicate that 30-40 % of the core, by weight, may be composed of an FeS or FeO component, and that 60-70 % consists of metallic FeNi (Poirier, 1994). The experimental results presented here provide important constraints on the f_{O_2}/f_{S_2} conditions under which a light component could have segregated into the core via porous flow in response to buoyancy forces.

Under the f_{O_2}/f_{S_2} conditions at which FeNi metal would have been stable in the early Earth, Fe-Ni-S-O liquids would not have been interconnected at low melt fractions. If percolation did occur at these conditions connectivity would have been transient, and at least 6 vol% melt would have been trapped in isolated pockets in the mantle (von Bargen and Waff, 1986). This value is more than twice the amount allowed by the inefficient core formation model of Jones and Drake (1986) (~3 vol%), and would result in an upper mantle with siderophile element and S abundances in excess of the observed values. Therefore, a mechanism other than porous flow is required to segregate Fe-Ni-S-O melts (and metal) during the early stages of core formation. Mixtures of FeNi metal and Fe-Ni-S-O melt may have migrated through the mantle as negatively-buoyant diapirs, but this is unlikely to have been an efficient transport mechanism (Stevenson, 1990).

Conversely, our experimental results indicate that at f_{O_2}/f_{S_2} conditions comparable to those of the present day upper mantle (Christie et al., 1986; Peach et al., 1994), Fe-Ni-

S-O liquids could form an interconnected network in peridotite at low melt fractions. Some bulk Earth models call for accretion of both a reduced component (80-85%) and an oxidized component (15-20%) (Ringwood, 1979; Wänke, 1981). If the oxidized component was dominant during the later stages of accretion, as suggested by Wänke (1981), then the f_{O_2}/f_{S_2} conditions may have been similar to present-day values. This scenario would have allowed efficient percolation of Fe-Ni-S-O liquids from the final 15-20% of the material added to the Earth. Although determinations of dihedral angles between oxygen-rich Fe-Ni-S-O liquids and the phases that make up the transition zone and lower mantle do not yet exist, the effect of increasing O in interfacial energies may be similar to that found for olivine. In this case, Fe-Ni-S-O melts could percolate efficiently into the core. Models that invoke the addition of a chondritic veneer to the Earth following segregation of the core need to be reexamined in light of the Fe-Ni-S-O melt connectivity that would be expected at upper mantle f_{O_2}/f_{S_2} conditions. The experimental results presented here indicate that as this oxidized, late stage material was mixed into the mantle, Fe-Ni-S-O melts could have segregated from it by a porous flow.

Connectivity of Fe-Ni-S-O melts at upper mantle f_{O_2}/f_{S_2} conditions also provides a mechanism for extraction of core-forming material from the mantle continuously over geologic time. If segregation of Fe-Ni-S-O melts from the mantle fractionates Re from Os, as is currently thought, then the mobility of these melts could result in local variations in the Re/Os ratio of the mantle. Over time, this could produce the heterogeneities in the isotopic composition of Os that are observed in mantle-derived rocks (Hattori and Hart, 1991; Martin, 1991).

REFERENCES

Birch F. (1964) Density and composition of mantle and core. *J. Geophys. Res.* **69**, 4377-4388.

Birch F. (1965) Energetics of core formation. *J. Geophys. Res.*, **70**, 6217-6221.

Castellan G.W. (1983) *Physical Chemistry*. 3rd ed. Benjamin/Cummings.

Chase M.W. Jr, Davies C.A., Downey J.R. Jr., Frurip D.J., McDonald R.A., and Syverud A.N. (1985) JANAF Thermochemical Tables, 3rd ed.. *J. Phys. Chem. Ref. Data.*, 14, Suppl. 1, Part I, Al-Co, Part II, Cr-Zr.

Christie D.M., Carmichael. I.S.E., and Langmuir C.H. (1986) Oxidation state of mid-ocean ridge basalt glasses. *Earth Planet. Sci. Lett.* **79**, 397-411.

Ehlers K., Grove T.L., Sisson T.W., Recca S.I., and Zervas D.A. (1992) The effect of oxygen fugacity on the partitioning of nickel and cobalt between olivine, silicate melt, and metal. *Geochim. Cosmochim. Acta*, **56**, 3733-3743.

Elsasser W.M. (1963) Early history of the Earth. In *Earth Science and Meteoritics* (ed. J. Geiss and E. Goldberg), pp. 1-31, North-Holland, Amsterdam.

Flaser F.M. and Birch F. (1973) Energetics of core formation: A correction. *J Geophys. Res.*, **78**, 6101-6103.

Harker D. and Parker E.R. (1945) Grain shape and grain growth. *Trans. Am. Soc. Met.* **34**, 156-201.

Hattori K. and Hart S.R. (1991) Osmium-isotope ratios of platinum group mineral associated with ultramafic intrusions: Os-isotopic evolution of the mantle. *Earth Planet. Sci. Lett.* **107**, 499-514.

Ip S.W. and Toguri J.M. (1993) Surface and interfacial tension of the Ni-Fe-S, Ni-Cu-S, and fayalite slag systems. *Metall. Trans. B.*, **24B**, 657-668.

Jones J.H. and Drake M.J. (1986) Geochemical constraints on core formation in the Earth. *Nature* **322**, 221-228.

Julian B.R., Davies D., and Sheppard R.M. (1972) PKJKP. *Nature* **235**, 317-318.

Martin C.E. (1991) Osmium isotopic characteristics of mantle-derived rocks. *Geochim. Cosmochim. Acta* **55**, 1421-1434.

Mason B. (1966) Composition of the Earth. *Nature* **211**, 616-618.

Minarik W.G., Ryerson F.J., and Watson E.B. (1996) Textural entrapment of core-forming melts. *Science*, **272**, 530-533.

Morgan J.W., Wandless G.A., Petrie R.K., and Irving A.J. (1980) Composition of the Earth's upper mantle - II: Volatile trace elements in ultramafic xenoliths. *Proc. Lunar Planet. Sci. Conf.* **11**, 213-233

Murthy V.R. and. Hall H.T. (1970) The chemical composition of the Earth's core: Possibility of sulfur in the core. *Phys. Earth Planet. Int.* **2**, 276-282.

Peach C.L., Mathez E.A., Keays R.R., and Reeves S.J. (1994) Experimentally determined sulfide melt-silicate melt partition coefficients for iridium and palladium. *Chem. Geol.* **117**, 361-377.

Poirier J.-P. (1994) Light elements in the Earth's outer core: A critical review. *Phys. Earth Planet. Int.* **85**, 319-337.

Porter D.A. and Easterling K.E. (1981) *Phase Transformations in Metals and Alloys.* Chapman and Hall.

Ringwood A.E. (1977) Composition of the core and implications for origin of the Earth. *Geochem. J.*, **11**, 111-135.

Ringwood A.E. (1981) *Origin of the Earth and Moon.* Springer-Verlag.

Smith C.S. (1964) Some elementary principles of polycrystalline microstructure. *Metall. Rev.* **9**, 1-48.

Stevenson D.J. (1981) Model's of the Earth's core. *Science*, **214**, 611-619.

Stevenson D.J. (1990) Fluid dynamics of core formation. In *Origin of the Earth* (ed. H.E. Newsom and J.H. Jones), pp. 231-249, Oxford University Press.

von Bargen N. and Waff H.S. (1986) Permeabilities, interfacial areas and curvatures of partially molten systems: Results of numerical computations of equilibrium microstructures. *J. Geophys. Res.* **91**, 9261-9276

Wänke H. (1981) Constitution of the terrestrial planets. *Phil. Trans. R. Soc. Lond.* A **303**, 287-302.

Table 1. Experimental conditions and results.

					Olivine	Sulfide Melt				
Expt.	Duration	log f_{O_2}	log f_{S_2}	θ	Fo	Fe	Ni	S	O	Total
FeS-4	24 hr	−10.3	−1.5	89°	94.6	61.9(5)	0.43(2)	36.7(5)	n.d.	99.03
FeS-7	72 hr	−10.3	−1.5	89°	94.7	60.5(10)	0.61(9)	38.2(7)	n.d	99.31
FeS-1	120 hr	−10.3	−1.5	86°	94.7	60.7(9)	0.72(8)	38.3(7)	n.d	99.72
FeS-3	216 hr	−10.3	−1.5	85°	94.8	62.6(4)	0.64(7)	36.7(2)	n.d	99.84
FeS-14	72 hr	−9.5	−1.5	80°	90.7	62.6(6)	0.76(7)	37.5(7)	0.09(3)	100.95
FeS-9	72 hr	−8.6	−1.5	72°	89.4	61.0(6)	0.77(6)	37.6(3)	0.34(15)	99.71
FeS-13	72 hr	−7.9	−1.6	60°	89.0	58.4(6)	1.3(3)	37.4(12)	2.7(9)	99.80
FeS-6	72 hr	−7.9	−2.5	53°	89.8	65.6(6)	0.8(1)	25.8(12)	8.6(6)	100.80

Notes: θ = dihedral angle measured in degrees. Units in parentheses represent one standard deviation of least unit cited, on the basis of replicate analyses. Therefore, 61.9(5) should be read as 61.9 ± 0.5.

FIGURE CAPTIONS

Figure 1. Comparison of theoretical (open circles) and observed (filled circles) frequency distribution of 200 apparent angles measured in Experiments FeS-3.

Figure 2. Experimentally-determined relationships among dihedral angle, $\log f_{S_2}^{1/2} - \log f_{O_2}^{1/2}$, and logarithm of the mole fraction of O dissolved in the sulfide melt.

Figure 3. (a) Back-scattered electron image showing textures in Experiment FeS-1. (b) Back-scattered electron image showing textures in Experiments FeS-6.

Figure 4. Experimentally-determined relationships among the ratio of solid/liquid to solid/solid interfacial energy, $\log f_{S_2}^{1/2} - \log f_{O_2}^{1/2}$, and logarithm of the mole fraction of O dissolved in the sulfide melt.

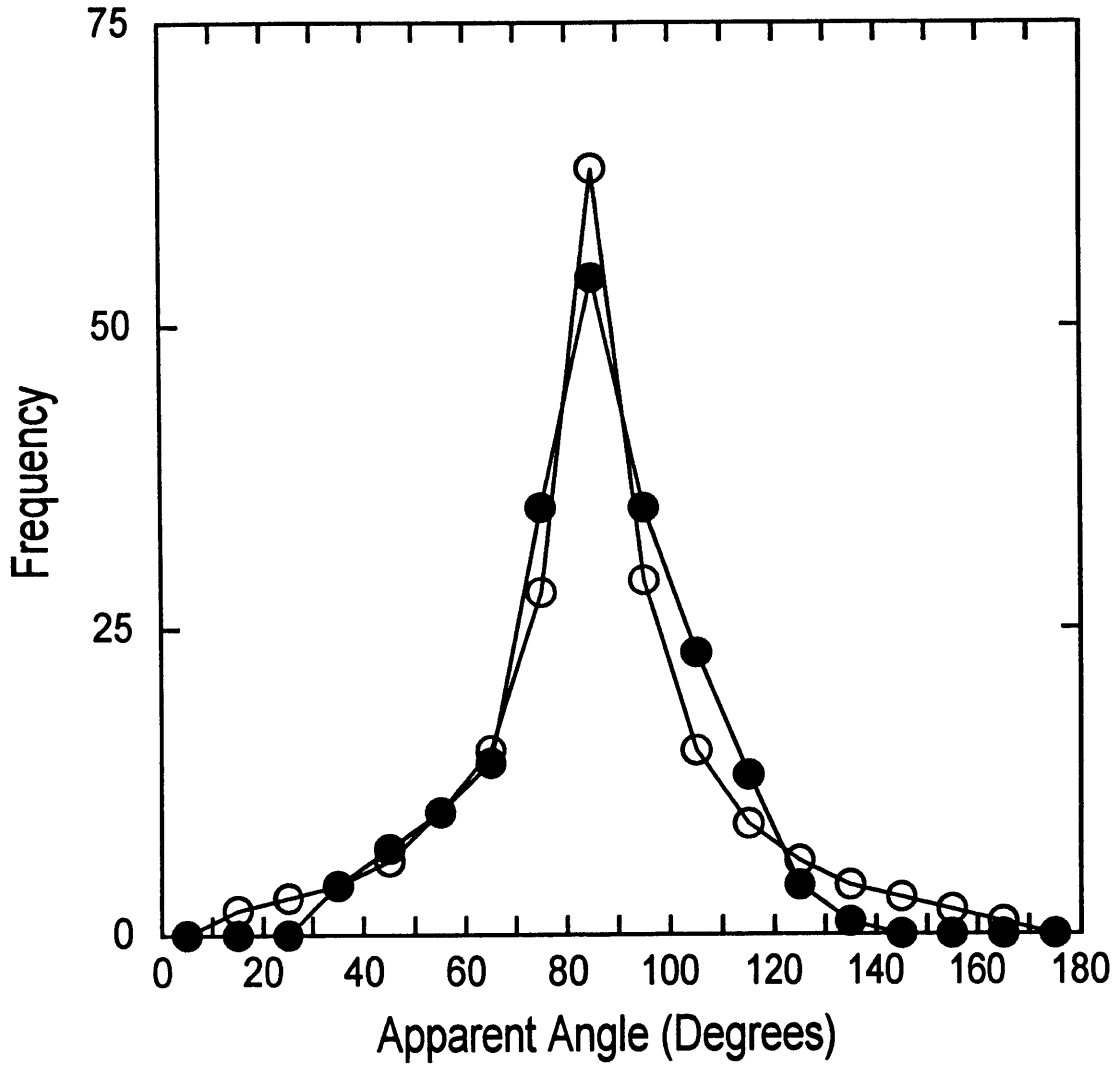
75
50
25
0
Frequency
0
20
40
60
80
100
120
140
160
180
Apparent Angle (Degrees)

Figure 1

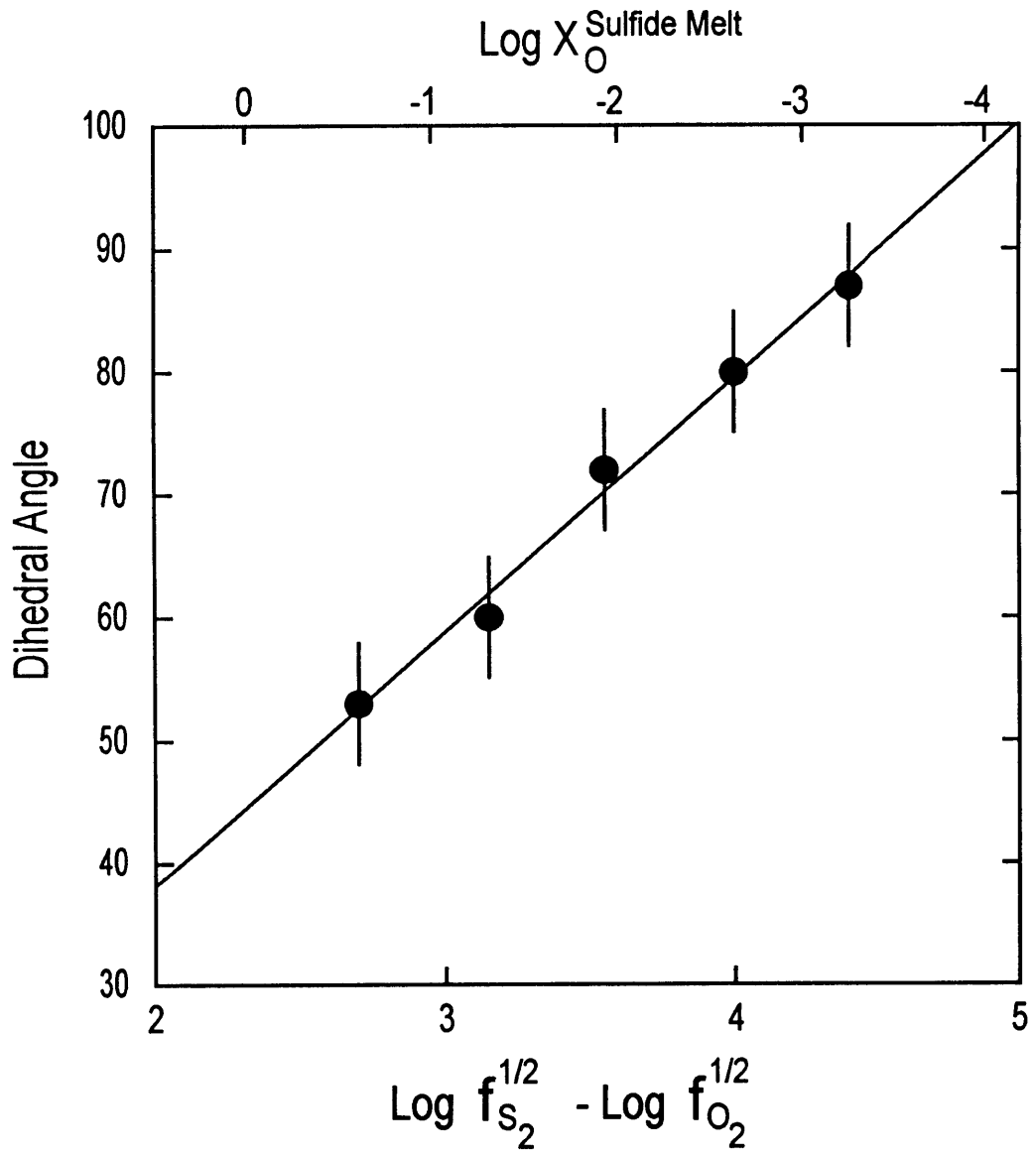
Log $X_O^{Sulfide\ Melt}$
0
-1
-2
-3
-4
100
90
80
70
60
50
40
30
Dihedral Angle
2
3
4
5
Log $f_{S_2}^{1/2}$ - Log $f_{O_2}^{1/2}$

Figure 2

100

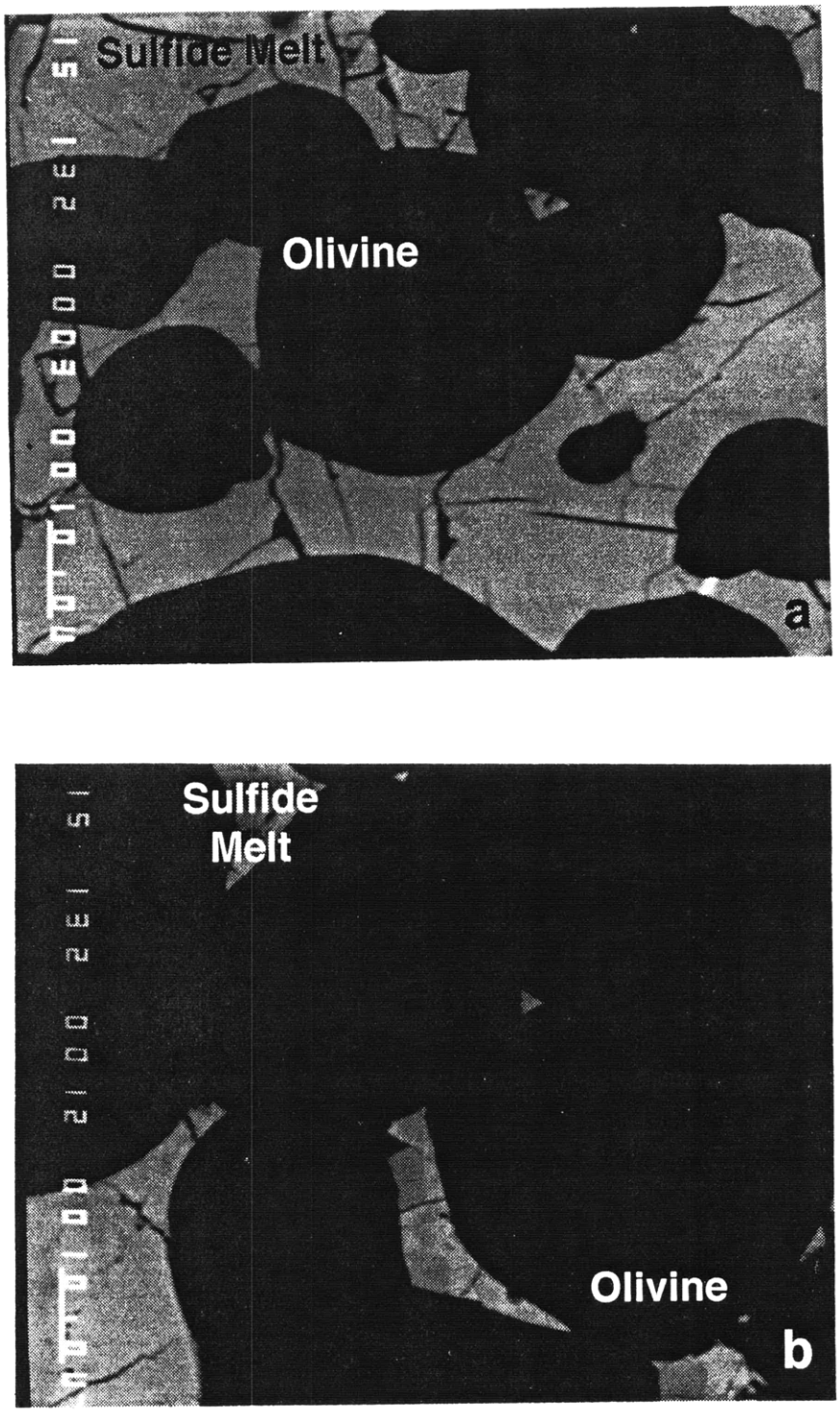

Figure 3

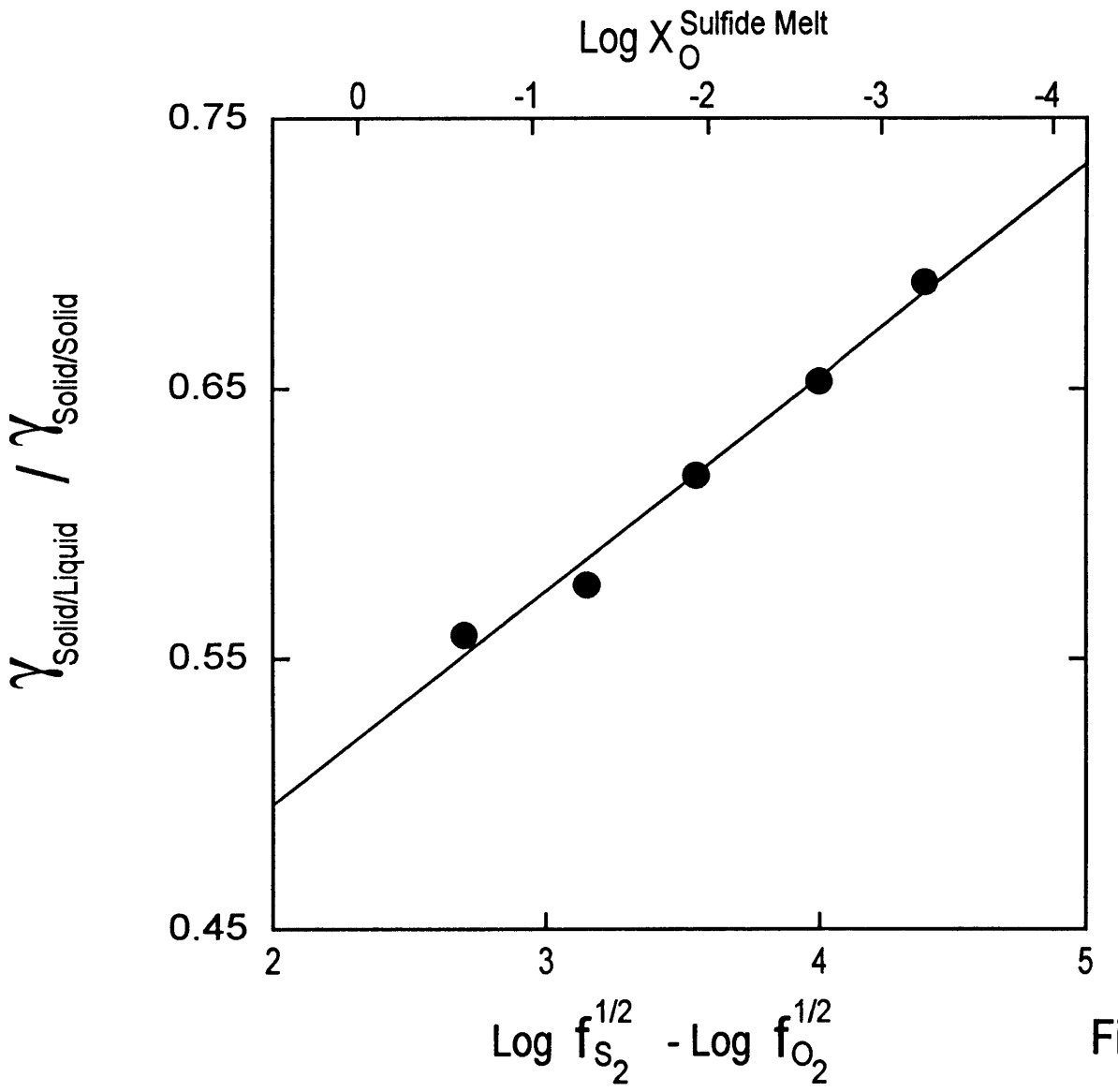
Log $X_O^{Sulfide\ Melt}$
0
-1
-2
-3
-4
0.75
0.65
0.55
0.45
$\gamma_{Solid/Liquid}$ / $\gamma_{Solid/Solid}$
2
3
4
5
Log $f_{S_2}^{1/2}$ - Log $f_{O_2}^{1/2}$

Figure 4

CHAPTER 3.

PARTITIONING OF MODERATELY SIDEROPHILE ELEMENTS AMONG OLIVINE, SILICATE MELT, AND SULFIDE MELT: CONSTRAINTS ON CORE FORMATION IN THE EARTH AND MARS

ABSTRACT

This study investigates the effects of variations in the fugacities of oxygen and sulfur on the partitioning of first series transition metals (V, Cr, Mn, Co, Ni, and Cu) and W among coexisting sulfide melt, silicate melt, and olivine. Experiments were performed at 1 atm. pressure, 1350°C, with the fugacities of oxygen and sulfur controlled by mixing CO_2, CO, and SO_2 gases. Starting compositions consisted of a CaO-MgO-Al_2O_3-SiO_2-FeO-Na_2O analog for a chondrule from an ordinary chondrite and a synthetic komatiite. The f_{O_2}/f_{S_2} conditions ranged from log f_{O_2} = −7.9 to −10.6, with log f_{S_2} values ranging from −2.5 to −1.0. Our experimental results demonstrate that the f_{O_2}/f_{S_2} dependencies of sulfide melt/silicate melt partition coefficients for the first series transition metals are proportional to their valence state. Variations in f_{O_2}/f_{S_2} conditions have no significant effect on olivine/melt partitioning other than those resulting from f_{O_2}-related changes in valence state. Application of our experimentally-determined partition coefficients to modeling segregation of sulfide and metal from the silicate portion of the early Earth to form the core demonstrates that the influence of S does not account for the anomalous abundances of siderophile elements in the upper mantle. Modeling core formation in the Shergottite parent body (Mars) using f_{O_2}/f_{S_2}-dependent partition coefficients gives estimates for the size of the Martian core (~20 to 25 wt% of the planet), and its S content (~0.35 wt%). In a Mars-sized body such a core would be solid.

INTRODUCTION

The segregation of metallic cores from silicate mantles is the most significant differentiation event in the evolution of terrestrial planets. In the Earth, for example, the inner and outer cores combined comprise ~33% of the planet's mass. In contrast, the extraction of basalt from the upper mantle at mid-ocean ridges produces an oceanic crust comprising only ~0.08 % of the mass of the Earth. The absolute and relative abundances of siderophile elements (elements that partition strongly into metallic phases) in a planet's silicate mantle provide the only direct geochemical evidence relating to the core formation process. The conditions under which core formation took place may have significantly influenced the mantle's siderophile element abundance pattern through variations in silicate/metal partitioning. The effects of variables such as temperature (Murthy, 1991; Walker et al., 1993), and pressure (Jones and Walker, 1991; Keppler and Rubie, 1993) on siderophile element partitioning are beginning to be understood and quantified. In this study, we present experiments that investigate the effect of variations in the fugacities of oxygen (f_{O_2}) and sulfur (f_{S_2}) on the partitioning of moderately siderophile elements (V, Cr, Mn, Co, Ni, Cu, and W) among coexisting olivine, silicate melt, and sulfide melt. The experimental results are used to constrain the role of sulfide in producing the siderophile element abundance pattern in the Earth's upper mantle, and the conditions under which core formation took place in the parent body of Shergottite meteorites (Mars).

EXPERIMENTAL AND ANALYTICAL METHODS

Experiments were performed at 1 atm. pressure in either a Pt-wound or Deltech vertical quenching furnace fitted with a 19 mm outer diameter fused-silica muffle tube. End pieces were fabricated from fired pyrophyllite and attached to the muffle tube using General Electric Red RTV 106 high temperature silicone rubber adhesive sealant. The values of f_{O_2} and f_{S_2} were controlled by mixing CO_2, CO, and SO_2 gases, which were fed into the furnace through a tube in the upper pyrophyllite plug (Fig 1). The gases exited

through a tube in the lower plug, and were fed into a pyrex flask through a silica-glass tube wrapped with heating tape, and then vented into a fume hood. Temperature in the furnace hot spot was continuously monitored using a $Pt\text{-}Pt_{90}Rh_{10}$ thermocouple calibrated against the melting points of NaCl, Au, and Pd on the 1968 International Practical Temperature Scale (Biggar, 1972). The thermocouple was positioned on the outside of the muffle tube to avoid contamination by S-rich gases, and the temperature difference between the position of the thermocouple and the position of the sample was calibrated.

The mixtures of CO_2, CO, and SO_2 gases required for the experiments were calculated by assuming that the gas behaves as an ideal solution at high temperature and low pressure and are given in Table 1. Expressions relating Gibbs free energy change to equilibrium constants for independent reactions involving nine gas species were written using thermochemical data from the JANAF tables (Chase et al., 1985). Mass balance equations relating each element (C, O, and S) to the stable gas species were then used to determine the gas mixture necessary to achieve the desired combination of f_{O2} and f_{S2}. This calculation procedure gives results that are in agreement with those determined using the method of steepest descent (White et al., 1958; Haughton et al., 1974).

Starting materials consisted of either a $CaO\text{-}MgO\text{-}Al_2O_3\text{-}SiO_2\text{-}FeO\text{-}Na_2O$ analog for a chondrule from an ordinary chondrite (Fo86 of Ehlers et al., 1992) or a synthetic Munro Township komatiite (KOM; Composition B of Kinzler and Grove, 1985) to which synthetic FeS and various combinations of Johnson-Matthey high-purity NiO, CuO, Cr_2O_3, CoO, V_2O_5, or WO_3 were added. FeS was synthesized by melting a 2 gram stoichiometric mixture of Fe metal sponge and S chips in an evacuated silica-glass tube. The tube containing the FeS mixture was placed in a Deltech vertical quenching furnace at 960° C, the temperature was raised to 1250° C over 2 h, then quickly to 1270° C and held there for 2 h before quenching the charge into water.

Experiments were performed by placing the sample in a crucible fabricated from a single crystal of gem quality San Carlos olivine ($Fo_{89\text{-}91}$) following the methods described

by Ehlers et al. (1992). Olivine crucibles are preferable to containers made from high-purity alumina because they prevent reaction between the crucible and charge. The crucible was fastened to the top of a silica-glass rod using 0.2 mm Pt wire, and placed into the furnace through the lower end of the muffle tube with the hot spot temperature set to 1078° C. The lower pyrophyllite plug was used to seal the furnace tube, and the gases were set to the desired flow rates. After the gases had been flowing for 30 min, the sample was raised into the hot spot. A second glass rod was placed between the benchtop and the rod holding the sample, and the hot spot temperature was raised to 1350° C over ~60 min. At the end of each experiment the lower glass rod was removed, and the upper rod slid down, quenching the experiment against the lower pyrophyllite plug. This method of quenching resulted in little or no quench growth in the silicate glass, but the sulfide melt generally consisted of a coarse intergrowth of quench phases, a common problem in experiments containing sulfide melts (e.g., Jones and Drake, 1983; Jones and Walker, 1991; Peach and Mathez, 1993). Evidence for the loss of Cu from the charges due to volatilization was found in experiments performed at relatively oxidizing conditions (log f_{O_2} = −7.9; log f_{S_2} = −2.0). This problem was minimized by keeping the gas flow rates low, and by using deep crucibles.

Experimental products were analyzed using either a 4- or 5-spectrometer JEOL 733 superprobe at the Massachusetts Institute of Technology. Analytical conditions for determination of the major elements in all phases were an accelerating voltage of 15 kV and a beam current of 10 nA with maximum counting times of 40 s. A ~3μm spot size was used for analyses of olivine and sulfide, while the beam was defocused to 10 μm to perform glass analyses. Each reported silicate analysis represents a mean of 10 spot analyses. On-line data reduction was accomplished using the phi-rho-z correction scheme. Trace elements in the silicate phases were analyzed separately from the major elements using a beam current of 200 nA and counting times ranging from 250-700 s depending on concentration. Elements present in the sulfide melt in trace amounts were analyzed using

beam currents of 50-200 nA and counting times of 250-500 s depending on concentration. The detection limits for trace elements were taken to be 3 standard deviations above background counts. Analyzing experiments containing V required corrections for peak overlap interferences from $Ti_{K\beta}$ on $V_{K\alpha}$ and from $V_{K\beta}$ on $Cr_{K\alpha}$. This was accomplished by determining the intensity of the interfering peak on the pure oxide of the interfering element (i.e., TiO_2 and V_2O_5), and then scaling the interference for a given analysis to the concentration of the interfering element and subtracting it from the measured intensity of the element of interest.

The olivine/silicate melt partition coefficients for Cu were determined by secondary ion mass spectrometry using the Cameca IMS 3f ion microprobe at Woods Hole Oceanographic Institution. Analyses were performed using a 2 nA beam of O^- ions focused to a spot size of 15 μm. Positive secondary ions were collected and counted by an electron multiplier. Molecular interferences were excluded by energy filtering using a ±10-V energy window and a −90V offset (Shimizu and Hart, 1982), and checked by determining the $^{63}Cu/^{65}Cu$ ratio for each spot. The relationships between intensity and concentration for olivine and glass were determined using experiment KOM-1s, in which the concentration of Cu in olivine is high enough to be determined by electron microprobe.

Accurate determinations of the compositions of experimentally-produced sulfide melts were complicated by the presence of coarse intergrowths of quench phases. This has been dealt with in other studies by performing multiple broad-beam analyses (Peach and Mathez, 1993), or by rastering the beam over large areas (Walker et al., 1993). Our approach to the problem was to analyze each quench phase separately, to use image analysis to determine their relative proportions, and then to calculate a weighted mean composition for the bulk sulfide melt. The uncertainty associated with the quench phase proportions was estimated by performing multiple determinations and calculating the standard deviation of the mean.

EXPERIMENTAL RESULTS

Synthesis Experiments

Experiments were performed on a synthetic Munro Township komatiite composition (KOM) to determine the partitioning behavior of V, Cr, Mn, Co, Ni, Cu, and W among coexisting olivine, sulfide melt, and ultramafic silicate melt. The partitioning behavior of Ni was also determined experimentally for the CaO-MgO-Al_2O_3-SiO_2-FeO-Na_2O chondrule analog composition (Fo86) studied by Ehlers et al. (1992). The komatiite serves as an analog for the type of high-degree partial melt that might be present if the silicate portion of a terrestrial planet were largely molten (e.g., Nisbet and Walker, 1982). The Fo86 experiments allow the partitioning behavior of Ni in a S-bearing system to be directly compared with the results of Ehlers et al. (1992), who performed experiments on Fo86 in a sulfur-free system. Experimental conditions were log f_{O_2} values ranging from −7.9 (1 log unit more reduced than the fayalite-magnetite-quartz (FMQ) oxygen buffer) to −10.6 (the iron-quartz-fayalite (IQF) oxygen buffer) and log f_{S_2} values from −2.5 to −1.0 (Table 1; Fig. 2). Both starting compositions produce silicate melts saturated with an immiscible sulfide melt and olivine similar in composition to San Carlos olivine at 1350°C. The KOM experiments crystallize chromite, while protoenstatite occurs in the FO86 experiments performed at the lowest f_{O_2}/f_{S_2} ratio conditions (Table 1). The KOM experiments containing W performed at reducing conditions contain a tungstate mineral.

Olivine grains in the KOM experiments are subhedral to euhedral in morphology, tend to be elongate, and are up to ~600 μm in their long dimension. Spinels occur as small (~5-20 μm), equant, euhedral grains. In the high f_{O_2}/f_{S_2} ratio experiments spinel is found in the silicate melt or included in olivine grains, while in the low f_{O_2}/f_{S_2} ratio experiments they occur exclusively within the sulfide melt (Table 1). The tungstate mineral occurs as small (~5 μm), spheroidal grains within the sulfide melt. The morphology of the sulfide melt changes dramatically depending on the f_{O_2}/f_{S_2} conditions of

the experiment. In the high f_{O_2}/f_{S_2} experiments, the sulfide melt is present as small (~10 μm) to moderate size (~250 μm) spheres throughout the upper portion of the charge. In the low f_{O_2}/f_{S_2} experiments the sulfide melt forms large (~1,500μm), lense-shaped bodies that segregate efficiently to the top of the silicate melt.

Olivine grains in the Fo86 experiments are subhedral to euhedral in morphology, and tend to be equant. The largest grains are typically 40-60 μm in diameter. Sulfide occurs as spherical to sub-spherical blebs, up to ~110 μm in diameter, distributed throughout the silicate melt. Pyroxene grains are subhedral to euhedral and tend to be elongate. The largest grains are up to ~700 μm in length. There is a distinct trend of increasing protoenstatite and decreasing olivine abundance with decreasing f_{O_2}/f_{S_2} ratio. There is also a decrease in the total number of crystals with decreasing f_{O_2}/f_{S_2} ratio.

The composition of the silicate melt varies systematically with changing f_{O_2}/f_{S_2} ratio for both starting compositions. The abundances of FeO, Ni, Cu, and Co all decrease with decreasing f_{O_2}/f_{S_2} ratio, while the abundance of dissolved S increases (Tables 3-5). The decrease in FeO causes a corresponding increase in the concentration of the other major elements, so that the composition of the silicate melt changes systematically as a function of the f_{O_2}/f_{S_2} ratio. This compositional variation leads to low-Ca pyroxene saturation in the Fo86 experiments performed at low f_{O_2}/f_{S_2} ratio conditions. The composition of the sulfide melt also varies as the f_{O_2}/f_{S_2} ratio decreases. The sulfide melt in the high f_{O_2}/f_{S_2} ratio experiments is Ni-rich, while in the low f_{O_2}/f_{S_2} experiments it is Fe-rich (Fig. 3). The concentrations of V, Cr, and Mn in the sulfide melt increase with decreasing f_{O_2}/f_{S_2} ratio. In contrast with the other first series transition metals, the abundances of Cu and Co do not vary in a systematic way. In the case of Cu, this may be related to the need to use higher doping levels to obtain accurate microprobe analyses of experiments performed at low f_{O_2}/f_{S_2} ratio conditions. The sulfur contents of the sulfide melts range from 28.8 to 38.3 wt%, and increase systematically with decreasing f_{O_2}/f_{S_2} ratio (Table 6).

The sulfide melt/silicate melt partition coefficients for all of the elements studied (with the possible exception of W) are strong functions of the f_{O_2}/f_{S_2} ratio (Table 7; Fig. 4). Olivine/silicate partition coefficients for Ni, Mn, Cr, and Cu do not show any systematic variation with changing f_{O_2}/f_{S_2} conditions, while those for V and W increase with decreasing f_{O_2}/f_{S_2} ratio (Table 8; Fig. 5). The Co partition coefficients are similar to those determined in a S-free systems by Ehlers et al. (1992) for the Fo86 composition.

Olivine/silicate melt partition coefficients for Ni are within 2 standard deviations of the values predicted by the model of Kinzler et al. (1990) in the experiments performed at conditions more oxidizing than the iron-wüstite solid oxygen buffer (IW), as is the case in the sulfur-free system (Ehlers et al., 1992). The olivine/silicate melt partition coefficient in the Fo86 experiment performed at conditions slightly more reducing than IW is 4.0±0.4, significantly lower than the value predicted on the basis of the composition of the coexisting olivine and melt (7.1 ± 0.9), but similar to the values reported by Ehlers et al. (1992) at comparable f_{O_2} conditions.

Approach to Equilibrium

The approach to equilibrium represented by our experiments was determined through (1) reproducibility of partition coefficients in different experiments performed at the same conditions, (2) comparison of the olivine/melt $K_D^{Fe/Mg}$ for olivine that crystallized directly from the melt with that for the olivine crucible adjacent to the melt, and (3) a reversal experiment.

Multiple experiments were carried out at log f_{O_2} = −7.9, log f_{S_2} = −1.8 (KOM-1s, -16s, -19s), at log f_{O_2} = −8.0, log f_{S_2} = −1.5 (KOM-6s, -20s, -23s), and at log f_{O_2} = −10.9, log f_{S_2} = −1.5 (KOM-3s, -10s, -11s, -18s) (Table 1). The sulfide melt/silicate melt partition coefficients for Ni measured in KOM-1s (540±10) and KOM-16s (510±10) overlap at the 2σ level, but that measured in KOM-19s (410±20) is low. The uncertainty resulting from the image analysis used to estimate the proportions of the quench phases is

difficult to quantify, and may explain this discrepancy. There is good agreement among the sulfide melt/silicate melt partition coefficients for Ni (550±10, 580±30, 550±20) and Mn (0.06±0.03, 0.07±1) measured at log f_{O_2} = –8.0, log f_{S_2} = –1.5. The same is true in the log f_{O_2} = –10.3, log f_{S_2} = –1.5 experiments for Ni (3600±200, 4400±400, 3800±400). The sulfide melt/silicate melt partition coefficients for Mn agree in KOM-10s (1.07±0.05), KOM-11s (1.09±0.03), and KOM-18s (1.07±0.04), but the Mn partition coefficient determined from KOM-3s is high (1.49±0.04). The sulfide melt/silicate melt partition coefficients for Cr agree in KOM-10s (4.8±0.2) and KOM-18s (4.9±0.2). There is also agreement between KOM-3s (7.2±0.3) and KOM-11s (6.3±0.5), but the partition coefficients from the two pairs of experiments do not overlap.

Equilibration of the crucible with the melt is an important perquisite for equilibration of the entire charge. Table 9 demonstrates that there is good agreement between the compositions of the olivine that crystallized from the komatiite melt and the olivine crucible within a few μm of the silicate melt. This indicates that although Fe/Mg exchange was necessary for the crucible to achieve equilibrium with the silicate melt at different f_{O_2}/f_{S_2}conditions, a close approach to equilibrium was achieved during each experiment.

A reversal of equilibrium was attempted by performing an experiment at log f_{O_2} = –7.9, log f_{S_2} = –1.5 for 72 hrs, then changing the gas flow rates to achieve log f_{O_2} = –10.3, log f_{S_2} = –1.5 and continuing the experiment for an additional 72 hrs. The run products from this experiment consist of glass, olivine, sulfide, and spinel. The abundance and morphology of the phases is identical to those found in synthesis experiments, with the sole exception of the presence of spinel inclusions in some of the olivine grains. The presence of these inclusions is an indication that their host olivine grew at the initial conditions of the experiment, during which spinel occurs either in the silicate melt or included in olivine grains. Analyses of the cores of these grains ($Fo_{96.4\pm0.2}$), which are 110 to 145 μm in diameter, are in good agreement with the composition of the rims and the

crucible adjacent to the glass (Table 9), indicating complete reequilibration. The sulfide melt/silicate melt partition coefficients for Cr (4.8±0.2, 4.9±0.2), Mn (1.07±0.05, 0.99±0.05), and Cu (900±100, 670±70) in KOM-10s and the reversal experiment overlap at the 2σ level. The partition coefficient for Ni in the reversal experiment is low (2400±300) relative to that in KOM-10s (3600±200), but they overlap at 2.4σ. This may again result from underestimating the uncertainty associated with the proportions of the quench phases.

DISCUSSION

Effect of Variable f_{O_2} and f_{S_2} on Siderophile Element Partitioning

Explicit dependence of sulfide melt/silicate melt partitioning on f_{O_2} and f_{S_2} is governed by an exchange reaction of the form:

$$M_X O_Y^{\text{Silicate Melt}} + \frac{Z}{2} S_2^{\text{Gas}} = M_X S_Z^{\text{Sulfide Melt}} + \frac{Y}{2} O_2^{\text{Gas}} \qquad (1)$$

where M is a metal cation and X, Y, and Z are stoichiometric coefficients. An increase in f_{S_2} at a constant f_{O_2} value will drive this reaction to the product side, increasing the sulfide melt/silicate melt partition coefficient, while an increase in f_{O_2} at a constant f_{S_2} will favor the reactants, leading to a decrease in the sulfide melt/silicate melt partition coefficient (e.g., Peach and Mathez, 1993). This relationship can be quantified by rewriting Equation 1 in terms of a single metal cation:

$$MO_{\frac{Y}{X}}^{\text{Silicate Melt}} + \frac{Z}{2X} S_2^{\text{Gas}} = MS_{\frac{Z}{X}}^{\text{Sulfide Melt}} + \frac{Y}{2X} O_2^{\text{Gas}} \qquad (2)$$

The equilibrium constant for this reaction is given by:

$$K_{eq} = \frac{a_{MS_{\frac{Z}{X}}}^{\text{Sulfide}} f_{O_2}^{\frac{Y}{2X}}}{a_{MO_{\frac{Y}{X}}}^{\text{Silicate}} f_{S_2}^{\frac{Z}{2X}}} \qquad (3)$$

Taking logarithms and rearranging gives:

$$\text{Log}\frac{a^{\text{Sulfide}}_{MS_{\frac{Z}{X}}}}{a^{\text{Silicate}}_{MO_{\frac{Y}{X}}}} = \text{Log}f_{S_2}^{\frac{Z}{2X}} - \text{Log}f_{O_2}^{\frac{Y}{2X}} + \text{Log Keq} \qquad (4)$$

If the ratio of the activity coefficients for the M species in the silicate and sulfide melts remains constant over the range of f_{O_2}/f_{S_2} conditions of interest, it can be combined into a single term with the equilibrium constant and a conversion factor allowing the ratio of the mole fractions to be replaced with the weight ratio partition coefficient. Then, if Y = Z, Equation 4 can be simplified to give the expression:

$$\text{Log } D_M^{\text{Sulfide Melt/Silicate Melt}} = \frac{Y}{X}\left[\text{Log}f_{S_2}^{\frac{1}{2}} - \text{Log}f_{O_2}^{\frac{1}{2}}\right] + C \qquad (5)$$

If the above-mentioned assumptions are met, there will be a linear relationship between $\text{logD}_M^{\text{Sulfide/Silicate}}$ and $\text{logf}_{S2}^{1/2} - \text{logf}_{O2}^{1/2}$ with a slope that is equal to the oxygen-, or sulfur-to-metal ratio for the oxide or sulfide species of interest. The strength of the f_{O_2}/f_{S_2} dependence for a given element should be proportional to its valence state.

Figure 4 is a plot of $\text{logD}_M^{\text{Sulfide/Silicate}}$ versus $\text{logf}_{S2}^{1/2} - \text{logf}_{O2}^{1/2}$ showing the partition coefficients determined from our experiments on the synthetic komatiite composition. The partition coefficient for W has been omitted because it could only be determined for a single experiment. The logarithms of the partition coefficients for all of the elements studied are strong linear functions of $\text{logf}_{S2}^{1/2} - \text{logf}_{O2}^{1/2}$, as expected. The slopes of the best-fit regression lines steepen from 0.38±0.06 for Cu to 1.4±0.2 for V (Table 7). The elements Co, Ni, and Cu are chalcophile at all f_{O_2}/f_{S_2} conditions investigated. The elements V, Cr, and Mn go from being incompatible in the sulfide melt at high f_{O_2}/f_{S_2} ratios, to being compatible at low f_{O_2}/f_{S_2} conditions. Due to the difference in their slopes, the partition coefficients for Mn and V reach a crossover point at $\text{logf}_{S2}^{1/2} - \text{logf}_{O2}^{1/2} = 4.35$, where V goes from being less compatible than Mn to being more compatible.

The relationship between the f_{O_2}/f_{S_2} dependence of sulfide melt/silicate melt partitioning and oxygen/sulfur-to-metal cation ratio means that any changes in valence

state will complicate the simple linear relationship given by Equation 5. The extent to which this occurs can be evaluated by considering olivine/silicate melt partitioning systematics. Exchange reactions such as that given by Equation 1 will not affect olivine/silicate melt partitioning. A significant and systematic change in olivine/silicate melt partitioning with varying f_{O_2}/f_{S_2} conditions is an indication of a change in valence state related to changing f_{O_2}. The olivine/silicate melt partition coefficients for Cr, Mn, Ni, Co, and Cu do not vary systematically with changing f_{O_2}/f_{S_2} conditions. The small amount of variability that does exist may be related to changes in the compositions of the coexisting olivine and silicate melt (e.g., Hart and Davis, 1978; Kinzler et al., 1990). Of these four elements, Cr (3+) and Mn (2+) have $\log D_M^{\text{Sulfide/Silicate}}$ versus $\log f_{S2}^{1/2} - \log f_{O2}^{1/2}$ slopes that are consistent with expected valence states (Table 7).

The Cr result is especially significant. The behavior of Cr in S-free systems has been investigated in a number of studies of both terrestrial and lunar basalt compositions (e.g., Schreiber and Haskin, 1976; Murck and Campbell, 1986; Barnes, 1986; Roeder and Reynolds, 1991). These studies demonstrated that the solubility of Cr in spinel-saturated silicate melts varies systematically with temperature, melt composition, and f_{O_2}. Although this effect has been attributed to variations in the Cr^{2+}/Cr^{3+} ratio of the silicate melt with changing conditions, the valence state of Cr as a function of f_{O_2} has only been directly measured in an Fe-free system (Schreiber and Haskin, 1976). Our experimental results are consistent with Cr^{3+} being the dominant species at 1350°C to conditions as reducing as the iron-quartz-fayalite oxygen buffer. A significant increase in the Cr^{2+}/Cr^{3+} ratio of the silicate melt with decreasing f_{O_2} would result in an increase in the olivine/silicate melt partition coefficient with decreasing f_{O_2} (Schreiber and Haskin, 1976). The presence of Fe^{3+} in the silicate melt may shift the transition from Cr^{3+} to Cr^{2+} to more reducing conditions than is the case for the Fe-free system, as suggested by Schreiber and Haskins (1976).

The slopes of the regression lines for Ni (0.65±0.04), Co (0.69±0.05), and Cu (0.38±0.03) indicate that the f_{O_2}/f_{S_2} dependencies of their sulfide melt/silicate melt partition coefficients are weaker than expected on the basis of their valence states. If these slopes resulted solely from the relationship given by Equation 5, it would imply that a significant proportion of each element is dissolved in the silicate melt as a neutral species even at f_{O_2} values 1 log unit below the FMQ buffer. This is improbable, especially given the constancy of their olivine/silicate melt partition coefficients over the range of conditions studied. The most obvious difference between these elements and Cr and Mn is that Co, Ni, and Cu are all strongly chalcophile. At conditions more reducing than FMQ, S dissolves in silicate melts as S^{2-} anions by displacing O^{2-} anions that are bonded with metal cations such as Fe^{2+} (Fincham and Richardson, 1954; Haughton et al., 1974). This solubility mechanism should lead to some percentage of the strongly chalcophile elements being bonded to S^{2-} rather than O^{2-} anions in the silicate melt, and could explain an f_{O_2}/f_{S_2} dependence that is weaker than expected. If the sulfide melt/silicate melt exchange reaction governing the distribution of Ni^{2+} is modified to take this possibility into account, as well as the observation that Ni is present in the sulfide melt as a heazlewoodite (Ni_3S_2) component, the governing reaction becomes:

$$Ni_XO_YS_{Z_1}^{\text{Silicate Melt}} + \frac{Z_2}{2}S_2^{\text{Gas}} = Ni_XS_{Z_2}^{\text{Sulfide Melt}} + \frac{Y}{2}O_2^{\text{Gas}} + \frac{Z_1}{2}S_2^{\text{Gas}} \qquad (6)$$

where $Y + Z_1 = X$, and $Z_2 = 2$. If Equation 6 is rewritten on the basis of a single Ni atom, and the S_2^{Gas} terms are collected on the left side of the equality, the reaction becomes:

$$NiO_{\frac{Y}{X}}S_{\frac{Z_1}{X}}^{\text{Silicate Melt}} + \frac{Z_2-Z_1}{2X}S_2^{\text{Gas}} = NiS_{\frac{Z_2}{X}}^{\text{Sulfide Melt}} + \frac{Y}{2X}O_2^{\text{Gas}} \qquad (7)$$

Following steps similar to Equations 3 and 4, the expression relating $D_{Ni}^{\text{Sulfide/Silicate}}$ to f_{O_2} and f_{S_2} becomes:

$$\text{Log } D_{Ni}^{\text{Sulfide Melt/Silicate Melt}} = \frac{1}{2X}\left[(Z_2 - Z_1)\text{Log}f_{S_2} - Y\text{Log}f_{O_2}\right] + C \qquad (8)$$

If some percentage of the Ni^{2+} dissolved in the silicate melt is present as NiS, and it is properly accounted for by substituting the correct value for Z_1, a regression of our experimental data should give a line with a slope of $\frac{1}{6}$. This relationship requires that ~31% of the Ni is present in the silicate melt as NiS. It is likely that the high f_{O_2}/f_{S_2} ratio experiments have less than 31%, and that the low f_{O_2}/f_{S_2} experiments contain more, as a homogeneous equilibrium of the form

$$NiO^{\text{Silicate Melt}} + \tfrac{1}{2}S_2^{\text{Gas}} = NiS^{\text{Silicate Melt}} + \tfrac{1}{2}O_2^{\text{Gas}} \qquad (9)$$

should control the NiS/NiO ratio of the silicate melt. A similar treatment of the experimental data of Peach and Mathez (1993) indicates that their silicate melts contain ~16% of the total Ni as NiS on average. Because the two sets of experiments were performed at different pressure-temperature conditions (1450° C, 8 kbars for Peach and Mathez (1993) as compared to 1350° C, 0.001 kbars for our experiments) it is not possible to determine directly whether this difference is an effect of pressure, temperature, or silicate melt composition. A similar analysis of the Cu and Co data, assuming that all Cu is monovalent and all Co is divalent in both phases, indicates that ~20% of the total Cu is present in the silicate melt as Cu_2S, and that ~31% of the Co is present as CoS.

A comparison of the f_{O_2}/f_{S_2} dependencies of the sulfide melt/silicate melt and the olivine/silicate melt partitioning of V demonstrates that its behavior is more complicated than the other elements studied. The strong, linear increase in $\log D_V^{\text{Oliv/Silicate Melt}}$ with decreasing f_{O_2}/f_{S_2} ratio indicates that it is undergoing a change in valence state related to changing f_{O_2}, most likely from 4^+ to 3^+. This should lead to curvature in the V partitioning data shown in Fig. 5, but none is apparent and the correlation coefficient is quite high (r^2 = 0.97). It is possible that additional experiments are needed to better constrain the curvature.

The systematics of sulfide melt/silicate melt partitioning for Ni determined in the experiments performed on the Fo86 composition differ from those found in the KOM

experiments. Figure 6 shows that whereas the Ni data from the komatiite experiments define a linear relationship between log $D^{Sulfide/Silicate}$ and $\log f_{S2}^{1/2} - \log f_{O2}^{1/2}$, there is significant curvature in the trend defined by the Fo86 experiments. The sulfide melt/silicate melt partition coefficients from the Fo86 experiments go from being larger than those from the KOM experiments at low $\log f_{S2}^{1/2} - \log f_{O2}^{1/2}$ values, to being smaller at high values. This curvature indicates that the ratio of the activity coefficients for Ni in sulfide and silicate melts is variable. Given that temperature and pressure are constant in these experiments, the variation in the activity-composition relationship must be attributable to compositional changes occurring in one of the phases. The wide range in Ni concentration in the sulfide melt (11.2 to 58.6 wt%) could lead to such deviations, but the V-doped komatiite experiments have a similar range in Ni and do not show any curvature. Therefore, it is probable that the curvature is due to changes in the composition of the silicate melt. That the low f_{O2}/f_{S2} ratio experiments are saturated with a low-Ca pyroxene indicates that as the FeO content of the melt decreases, the activity of SiO_2 must be increasing. Once pyroxene saturation is reached, the activity of SiO_2 is buffered, and there should be a linear relationship between log $D^{Sulfide/Silicate}$ and $\log f_{S2}^{1/2} - \log f_{O2}^{1/2}$. The filled symbols in Fig. 6 are those experiments that are saturated with pyroxene, and a linear relationship is apparent.

That the curvature in Fig. 6 is related to changing SiO_2 activity can be further tested by looking at how the sulfide capacity of the silicate melt (C_s = (wt% S dissolved in the silicate melt)×($f_{O2}^{1/2} / f_{O2}^{1/2}$)) varies in the Fo86 experiments. Sulfide capacity has been shown to be a strong function of the activity of the metal cations that bond with S^{2-} in the melt, especially Fe^{2+} (Fincham and Richardson, 1954; Haughton et al., 1974). It has also been demonstrated in simple binary systems that C_s will decrease with increasing SiO_2 activity as O^{2-} anions bonded solely to metal cations are replaced by O^{2-} anions in tetrahedral coordination with Si^{4+} (Fincham and Richardson, 1954; Abraham et al., 1960; Abraham and Richardson, 1960). Figure 7 is a plot of the sulfide capacity of the silicate

melts in all of our experiments versus the FeO content of the silicate melt. The curvature that is apparent in Fig. 7 is independent of any compositional changes occurring in the sulfide melt and is, therefore, related to the initial increase in SiO_2 activity. It is once again apparent that when low-Ca pyroxene saturation is reached and SiO_2 activity is buffered, the expected linear relationship, in this case between log C_s and FeO, is present. Note that the pyroxene-saturated experiments form linear trends that are sub-parallel to the KOM experiments, and are offset to lower values of both $D_{Ni}^{Sulfide/Silicate}$ and C_s. These results indicate that when sulfide melt coexists with relatively polymerized silicate melts, the sulfide melt/silicate melt partition coefficients for the siderophile elements are lower. This is the opposite of what would be predicted on the basis of experimental studies on the partitioning of Ni between olivine and silicate melt (e.g., Hart and Davis, 1978; Kinzler et al., 1990). These studies demonstrated the existence of a strong correlation between MgO content of the melt and D_{Ni}. Silicate melts with the same MgO content, but different SiO_2 do not show a significant variations in D_{Ni}. Our result may be related to a variation in the abundance of NiS dissolved in the silicate melt, rather than a change on polymerization affecting the activity of Ni^{2+} cations.

It is worth noting that an apparent lowering of the olivine/silicate melt partition coefficient, similar to that reported by Ehlers et al. (1992), is present in our experiment on the Fo86 composition performed at the most reducing conditions. This effect was initially attributed to S dissolved in the silicate melt bonding with Ni^{2+} and thereby changing its partitioning behavior (Gaetani et al., 1993; Gaetani and Grove, 1994). This effect is not found in the experiments performed on the synthetic komatiite composition, however, indicating that the lower olivine/silicate melt partition coefficient is unrelated to dissolved S. It is likely that our result is the valence state effect reported by Ehlers et al. (1992), and is related only to the variation in f_{O_2}. If it is the same effect observed by Ehlers et al. (1992), our results demonstrate that it occurs in experiments that are not metal saturated and so cannot be attributed to a colloidal suspension of sub-micron sized metal particles in

the silicate melt (e.g., Hirschmann and Ghiorso, 1994). That all of the experiments are sulfide saturated indicates that sub-micron sized sulfide particles are not responsible for the change in partitioning behavior.

The Role of Sulfide in Core Formation in the Earth

The origin of the siderophile element abundance pattern in the Earth's upper mantle is a long-standing problem in geochemistry. Ringwood (1966) first noted that the absolute and relative abundances of the siderophiles cannot be explained by the segregation of metal from silicate on the basis of known metal/silicate partition coefficients. Four models have subsequently been proposed to explain the pattern: (1) inefficient core formation, in which some percentage of metal remains in the mantle following segregation of the core, and is thereafter oxidized (Jones and Drake, 1986), (2) heterogeneous accretion, in which a veneer of chondritic material is accreted after segregation of the core (Morgan et al., 1980; Wänke, 1981), (3) equilibrium segregation of a sulfide melt from the upper mantle (Brett, 1984), and (4) segregation of the core from a superheated magma ocean (Murthy, 1991; Walker et al., 1993). The sulfide extraction model was conceived on the basis of the observations that the density of the outer core is 10% lower than that of iron at comparable conditions, requiring a light alloying element (Birch, 1961, 1964), and that sulfide melt/silicate melt partition coefficients for siderophile elements tend to be smaller than metal/silicate melt partition coefficients at comparable conditions (Brett, 1984). Our experimentally-determined partition coefficients allow a first order evaluation of the sulfide extraction model over a range of f_{O_2}/f_{S_2} conditions using an internally consistent data set.

Segregation of the core was modeled using the approach developed by Rammensee and Wänke (1977) and Newsom (1985). The bulk (metal+sulfide)/total-silicate partition coefficient ($D^{m/s}$) is given by:

$$D^{m/s} = \frac{D_i}{F_{liq} + (C^{sol} / C^{liq})(1 - F_{liq})}, \qquad (10)$$

where D_i is the (metal+sulfide)/silicate melt partition coefficient for a given siderophile element, F_{liq} is the fraction of silicate melt divided by the total fraction of silicates, and C^{sol}/C^{liq} is the solid-silicate/silicate melt partition coefficient for a given siderophile element. This expression is substituted into the equation:

$$X = \frac{a-1}{D^{m/s}+a-1}, \qquad (11)$$

where X is the weight fraction of metal + sulfide segregated into the core, and a is the depletion factor for a given element, to predict the size of the core that is required to produce a given depletion as a function of the extent of silicate partial melting that accompanied core formation. This is done for each element on the basis of a depletion factor and partition coefficients. If the abundances of the siderophile elements in the Earth's mantle can be explained by a single core formation event for which the given partition coefficients are appropriate, the curves predicted for all siderophile elements will intersect at a point that coincides with the size of the Earth's core.

The depletion factors used in our model were calculated on the basis of the primitive mantle abundances of Jagoutz et al. (1979) and are listed in Table 10. The sulfide melt/silicate melt partition coefficients appropriate for testing the sulfide equilibration model were calculated using the linear equations in Table 7. Because the f_{O_2}/f_{S_2} dependence of sulfide melt/silicate melt partitioning is proportional to the valence state of the element, the equations in Table 7 can be used to calculate partition coefficients at conditions different from those of our experiments as long as the valence states of the elements do not change. Brett (1984) proposed that upper mantle conditions during core formation were an f_{S_2}value equivalent to the FeFeS sulfur buffer (log f_{S_2} = –4.10 at 1350° C), and an f_{O_2} value equivalent to the IW buffer (log f_{O_2} = –10.20 at 1350° C). These conditions correspond to a $\log f_{S2}^{1/2} - \log f_{O2}^{1/2}$ value of 3.05. The metal/silicate melt partition coefficients at IW were determined from the experimental results of Schmidt et al. (1989) and of Drake et al. (1989). Extraction of 100% sulfide melt from the silicate

portion of the Earth would lead to a core with a S concentration far in excess of that allowed by seismic data, making a mixture of sulfide + metal a more reasonable choice. Extraction of a mixture consisting of 27 wt% sulfide melt (containing 35 wt% S) and 73 wt% metal will result in an outer core with a S content of 10 wt%, in agreement with current estimates (e.g., Poirier, 1994).

The results from our modeling are presented in Fig. 8. Because of the incompatible behavior of V, Cr, and Mn with respect to metal and sulfide melt at these conditions, their observed depletions in the upper mantle can only be explained by formation of an unreasonably large core (80 to 100% of the Earth by weight). It has been argued, however, that the depletion pattern for these elements is related to their relative volatilities (Drake et al., 1989), and therefore may have preceded core formation. The results for Co indicate a core that comprises ~22 wt% of the Earth, if the extent of partial melting accompanying segregation of the core was negligibly small. This is in reasonable agreement with the size of the Earth's core (~33 wt%), given the uncertainties inherent in this type of modeling. The cross-over point for Ni and Cu at these conditions, however, only allows for a core that is ~3.5 wt% of the mass of the Earth, with core formation accompanied by 36 wt% silicate partial melting. This core is too small by an order of magnitude. The lack of agreement among Ni, Co, and Cu precludes equilibrium segregation of a sulfide melt as the appropriate model to explain the Earth's siderophile element abundance pattern. Choosing f_{O_2}/f_{S_2} conditions other than those suggested by Brett (1984) does not improve the results. At more oxidizing conditions metal will not be stable, leading to a core that is 100% sulfide, and therefore too S rich. Reducing the f_{O_2}, or increasing the f_{S_2}, leads to larger sulfide melt/silicate melt partition coefficients, requiring an even smaller core. Our results do not eliminate the possibility that segregation of metal ± sulfide at extreme condition (i.e., extremely high temperatures) established the mantle's siderophile element abundance pattern.

Size and Sulfur Content of the Martian Core

The Shergottites-Nahklites-Chassigny (SNC) meteorites are a group of basaltic achondrites whose major and trace element compositions (e.g., Stolper and McSween, 1979; Stolper, 1979) and young crystallization ages (e.g., McSween et al., 1979; Walker et al., 1979) indicate that their parent body was one of the terrestrial planets rather than an asteroid. The composition of gases trapped in impact glasses provides the strongest evidence that they originated on Mars (e.g., Bogard and Johnson, 1983). The abundances of siderophile elements in these meteorites, therefore, provide clues to the processes involved in the formation of the Martian core. It has been proposed on the basis of cosmochemical models that the core of Mars is rich in S (e.g., Longhi et al. 1992). Because Mars is smaller than the Earth, only a S-rich core could have remained liquid to the present time. Therefore, constraining the S content of the Martian core has important implications for the internal structure of the planet.

Core formation in the Shergottite parent body (SPB) was modeled using the same methods as in the case of the Earth. The depletion factors were calculated using the SPB mantle abundances determined by Wänke and Dreibus (1988). In the case of the SPB, no assumptions were made regarding the metal-to-sulfide ratio of the core or the conditions under which core formation took place. Instead, the calculations were carried out with f_{O_2}/f_{S_2} conditions and sulfide content of the core as variables to determine if any combination gives a reasonable match to the depletions inferred on the basis of the siderophile element abundances of the Shergottite meteorites. The only constraint on f_{O_2}/f_{S_2} conditions was that if metal is required, the f_{O_2} must be at least as reducing as IW.

The results of our modeling are shown in Fig. 9. The best results for Ni, Co, and Cu were achieved at $\log f_{O_2} = -10.2$ (IW), and $\log f_{S_2} = -2.0$. The metal-to-sulfide ratio of the material that was segregated from the SPB mantle was 99:1, indicating that the Martian core contains only a small amount of S (0.35 wt% if the sulfide melt contained 35 wt% S). This implies that the Martial core is solid. The size of the core is between 20.2

and 25.9 wt% of the planet, slightly smaller than the Earth's core. This should be considered to be a maximum estimate, as core segregation at more reducing conditions would also produce a crossover for Co, Ni, and Cu, but because the metal/silicate melt and sulfide/silicate melt partition coefficients are larger, a smaller core is required to match the inferred depletions. Our results also indicate that the extent of silicate partial melting that accompanied formation of the Martian core was small (0.2 to 4.9 wt%). There is no estimate for the V depletion of the SPB mantle, and the depletion factors for Cr and Mn are both 1, so they could not be modeled in the same way as Ni, Co, and Cu. In order to use these elements to test our results, we rearranged Equation 1 of Newsom to solve for the depletion factor using the mean core size (23.05 wt%) and melt fraction (2.55 %) from our results with Ni, Co, and Cu. The calculated depletion factors for both Cr (1.07) and Mn (1.003) are close enough to 1 to justify our conclusions.

CONCLUSIONS

The partitioning of moderately siderophile elements between sulfide melts and silicate melts is governed by exchange equilibria. The f_{O_2}/f_{S_2} dependence of sulfide melt/silicate melt partitioning is proportional to the valence state of the element. The f_{O_2}/f_{S_2} dependence for partitioning of the chalcophile elements Co, Ni, and Cu is weaker than predicted on the basis of their valence states. This can be explained by bonding of some proportion of these elements to S^{2-}, rather than O^{2-}, in the silicate melt. Variations in f_{O_2}/f_{S_2} conditions do not directly effect the olivine/silicate melt partitioning of moderately siderophile elements. The strong f_{O_2}/f_{S_2} dependence for the olivine/silicate melt partitioning of V is attributable to a change on valence from 4+ to 3+ with decreasing f_{O_2}. Application of our experimentally-determined partition coefficients to modeling core formation in the Earth demonstrates that sulfide melt/silicate melt partition coefficients are too large to explain the overabundance of siderophile elements in the Earth's upper mantle. Modeling of core formation in the SPB demonstrates the core of Mars is likely to

represent 20 to 25% of the planet's mass, and contains only a small amount of S (~0.35 wt%). Therefore, the core of Mars is likely to be solid.

REFERENCES

Abraham K.P., Davies M.W., and Richardson F.D. (1960) Sulfide capacities of silicate melts. Part I. *J. Iron Steel Inst.*, **196**, 309-312.

Abraham K.P. and Richardson F.D. (1960) Sulfide capacities of silicate melts. Part II. *J. Iron Steel Inst.*, **196**, 313-317.

Barnes S.J. (1986) The distribution of chromium among orthopyroxene, spinel, and silicate liquid at atmospheric pressure. *Geochim. Cosmochim. Acta*, **50**, 1889-1909.

Biggar G.M. (1972) Diopside, lithium metasilicate and the 1968 temperature scale. *Mineral. Mag.*, **38**, 768-770.

Birch F. (1961) Composition of the Earth's mantle. *Geophys. J. R. Astron. Soc.*, **4**, 295-311.

Birch F. (1964) Density and composition of mantle and core. *J. Geophys. Res.*, **69**, 4377-4388.

Bogard D.D. and Johnson P. (1983) Martian gases in an Antarctic meteorite. *Science*, **221**, 651-654.

Brett R. (1984) Chemical equilibration of the Earth's core and upper mantle. *Geochim. Cosmochim. Acta*, **48**, 1183-1188.

Chase M.W. Jr, Davies C.A., Downey J.R. Jr., Frurip D.J., McDonald R.A., and Syverud A.N. (1985) JANAF Thermochemical Tables, 3rd ed.. *J. Phys. Chem. Ref. Data.*, 14, Suppl. 1, Part I, Al-Co, Part II, Cr-Zr.

Drake M.J., Newsom H.E., and Capobianco C.J. (1989) V, Cr, and Mn in the Earth, Moon, EPB, and SPB and the origin of the Moon: Experimental Studies. *Geochim. Cosmochim. Acta*, **53**, 2101-2111.

Ehlers K., Grove T.L., Sisson T.W., Recca S.I., and Zervas D.A. (1992) The effect of oxygen fugacity on the partitioning of nickel and cobalt between olivine, silicate melt, and metal. *Geochim. Cosmochim. Acta*, **56**, 3733-3743.

Fincham C.J.B. and Richardson F.D. (1954) The behavior of sulfur in silicate and aluminate melts. *Royal Soc. (London) Philos. Trans.*, **223**, 40-62.

Gaetani G.A., Grove T.L., and Jercinovic M.J. (1993) Partitioning of Ni among olivine, silicate melt and sulfide melt in sulfide-saturated magmas (abstract). *EOS, Transactions, American Geophysical Union*, **74**, 337.

Gaetani G.A. and Grove T.L. (1994) Influence of variable oxygen and sulfur fugacity on partitioning of Ni, Cu and Cr among olivine, silicate melt and sulfide melt (abstract). *Lunar and Planetary Science* **25**, 397-398.

Hart S.R. and Davis K. (1978) Nickel partitioning between olivine and silicate melt. *Earth Planet. Sci. Lett.*, **40**, 203-219.

Haughton D., Roeder P.L., and Skinner B.J. (1974) Solubility of sulfur in mafic magmas. *Econ. Geol.*, **69**, 451-467.

Hirschmann M.M. and Ghiorso M.S. (1994) Activities of nickel, cobalt, and manganese silicates in magmatic liquids and applications to olivine/liquid and to silicate/metal partitioning. *Geochim. Cosmochim. Acta*, **58**, 4109-4126.

Jagoutz E., Palme H., Baddenhausen H., Blum K., Cendales M., Dreibus G., Spettel B., Lorenz V., and Wänke H. (1979) The abundances of major, minor and trace elements

in the earth's mantle as derived from primitive ultramafic nodules. *Proc. Lunar Planet. Sci. Conf.*, **10**, 2031-2050.

Jones J.H. and Drake M.J. (1983) Experimental investigations of trace element fractionation in iron meteorites, II: The influence of sulfur. *Geochim. Cosmochim. Acta.*, **47**, 1199-1209.

Jones J.H. and Drake M.J. (1986) Geochemical constraints on core formation in the Earth. *Nature*, **322**, 221-228.

Jones J.H. and Walker D. (1991) Partitioning of siderophile elements in the Fe-Ni-S system: 1 bar to 80 kbar. *Earth Planet. Sci. Lett.*, **105**, 127-133.

Keppler H. and Rubie D. (1993) Pressure-induced coordination changes of transition-metal ions in silicate melts. *Nature*, **364**, 54-56.

Kinzler R.J. and Grove T.L. (1985) Crystallization and differentiation of Archean komatiite lavas from northeast Ontario: phase equilibrium and kinetic studies. *Amer. Mineral.*, **70**, 40-51.

Kinzler R.J., Grove T.L., and Recca S.I., (1990) An experimental study of the effect of temperature and melt composition on the partitioning of nickel between olivine and silicate melt. *Geochim. Cosmochim. Acta*, **54**, 1255-1265.

Longhi J., Knittle E., Holloway J.R., and Wänke H. (1992) The bulk composition, mineralogy and internal structure of Mars. In *Mars* (ed. H.H. Kieffer, B.M. Jakosky, C.W. Snyder, M.S. Matthews), pp. 184-212, Univ. Arizona Press.

McSween H.Y. Jr., Stolper E.M., Taylor. L.A., Muntean R.A., O'Kelley G.D., Eldridge J.S., Biswas S., Ngo H.T., and Lipschutz M.E. (1979) Petrogenetic relationship

between Allan Hills 77005 and other achondrites. *Earth Planet. Sci. Lett.*, **45**, 275-284.

Morgan J.W., Wandless G.A., Petrie R.K., and Irving A.J. (1980) Composition of the Earth's upper mantle – II: Volatile trace elements in ultramafic xenoliths. *Proc. Lunar Planet. Sci. Conf.*, **11**, 213-233.

Murck B.W., and Campbell I.H. (1986) The effects of temperature, oxygen fugacity, and melt composition on the behavior of chromium in basic and ultrabasic melts. *Geochim. Cosmochim. Acta*, **50**, 1871-1887.

Murthy V.R. (1991) Early differentiation of the Earth and the problem of mantle siderophile elements: a new approach. *Science*, **253**, 303-306.

Newsom H.E. (1985) Molybdenum in Eucrites: Evidence for a metal core in the Eucrite parent body. *Proc. Lunar Planet. Sci. Conf.*, **15**, C613-C617.

Nisbet E.G. and Walker D. (1982) Komatiites and the structure of the Archean mantle. *Earth Planet. Sci Lett.*, **60**, 105-113.

Peach C.L. and Mathez E.A. (1993) Sulfide melt-silicate melt distribution coefficients for nickel and iron and implications for the distribution of other chalcophile elements. *Geochim. Cosmochim. Acta.*, **57**, 3013-3021.

Poirier J.-P. (1994) Light elements in the Earth's outer core: A critical review. *Physics Earth Planet. Int.*, **85**, 319-337.

Rajamani V. and Naldrett A.J. (1978) Partitioning of Fe, Co, Ni, and Cu between sulfide liquid and basaltic melts and the composition of Ni-Cu sulfide deposits. *Econ. Geol.*, **73**, 82-93.

Rammensee W. and Wänke H. (1977) On the partition coefficient of tungsten between metal and silicate and its bearing on the origin of the moon. *Proc. Lunar Planet. Sci Conf.*, **8**, 399-409.

Ringwood A.E. (1966) Chemical evolution of the terrestrial planets. *Geochim. Cosmochim. Acta.*, **30**, 41-104.

Roeder P.L. and Reynolds I. (1991) Crystallization of chromite and chromium solubility in basaltic melts. *J. Petrol.*, **32**, 909-934.

Schmidt W., Palme H., and Wänke H. (1989) Experimental determination of metal/silicate partition coefficients for P, Co, Ni, Cu, Ga, Ge, Mo, and W and some implications for the early evolution of the Earth. *Geochim. Cosmochim. Acta.*, **53**, 173-185.

Schreiber H.D. and Haskin L.A. (1976) Chromium in basalts: Experimental determination of redox states and partitioning among synthetic silicate phases. *Proc. Lunar Sci. Conf.*, 7, 1221-1259.

Shimizu N. and Hart S.R. (1982) Applications of the ion microprobe to geochemistry and cosmochemistry. *Ann. Rev. Earth Planet. Sci.*, **10**, 483-526.

Stolper E.M. (1979) Trace elements in shergottite meteorites: Implications for the origin of planets. *Earth Planet Sci. Lett.*, **42**, 239-242.

Stolper E.M. and McSween H.Y. Jr. (1979) Petrology and origin of the shergottite meteorites. *Geochim. Cosmochim. Acta*, **43**, 1475-1498.

Walker D., Norby L., and Jones J.H. (1993) Superheating effects on metal-silicate partitioning of siderophile elements. *Science*, **262**, 1858-1861.

Walker D., Stolper E.M., and Hayes J.F. (1979) Basaltic volcanism: The importance of planet size. *Proc. Lunar Planet Sci. Conf.*, **10**, 1995-2015.

Wänke H. (1981) Constitution of the terrestrial planets. *Phil. Trans. R. Soc. London*, **A303**, 287-302.

Wänke H. and Dreibus G. (1988) Chemical composition and accretion history of terrestrial planets. *Phil. Trans. R. Soc. London*, **A235**, 545-557.

White W.B., Johnson S.M., and Dantzig G.B. (1958) Chemical equilibrium in complex mixtures. *J. Chem. Phys.*, **28**, 751-755.

Table 1. Experimental Conditions and Phase Assemblages for Partitioning Experiments.

Experiment	Duration (hr)	Log f_{O2}	Log f_{S2}	Gas Flow Rates (mL/s) CO_2 : CO : SO_2	Run Products
Ni-Doped Experiments					
Fo86-8s	48	−7.9	−2.5	1.53 : 0.41 : 0.11	Gl, Oliv, Slf
Fo86-5s	49	−7.9	−2.0	0.95 : 0.30 : 0.15	Gl, Oliv, Slf
Fo86-9s	48	−8.0	−1.5	0.51 : 0.30 : 0.18	Gl, Oliv, Slf, PrEn
Fo86-15s	49	−8.6	−1.5	0.39 : 0.39 : 0.08	Gl, Oliv, Slf, PrEn
Fo86-14s	48	−9.4	−1.5	0.27 : 0.71 : 0.08	Gl, Oliv, Slf, PrEn
Fo86-10s	48	−10.3	−1.5	0.08 : 1.44 : 0.12	Gl, Oliv, Slf, PrEn
Ni-Cr-Cu-Doped Experiments					
KOM-1s	48	−7.9	−1.8	0.46 : 0.17 : 0.10	Gl, Oliv, Sp, Slf
KOM-6s	48	−8.0	−1.5	0.51 : 0.30 : 0.18	Gl, Oliv, Sp, Slf
KOM-15s	72	−8.8	−1.5	0.50 : 0.61 : 0.10	Gl, Oliv, Sp, Slf
KOM-4s	48	−9.2	−1.0	0.00 : 0.77 : 0.20	Gl, Oliv, Sp[1], Slf
KOM-3s	48	−10.3	−1.5	0.08 : 1.44 : 0.12	Gl, Oliv, Sp[1], Slf
KOM-10s	72	−10.3	−1.5	0.10 : 1.66 : 0.13	Gl, Oliv, Sp[1], Slf
KOM-26s[2]	72	−7.9	−2.0	0.87 : 0.28 : 0.14	
	72	−10.3	−1.5	0.10 : 1.66 : 0.13	Gl, Oliv, Sp[1], Slf
KOM-9s	72	−10.6	−1.5	0.00 : 1.28 : 0.10	Gl, Oliv, Sp[1], Slf
Ni-Co-W-Doped Experiments					
KOM-16s	72	−7.9	−1.8	0.46 : 0.17 : 0.10	Gl, Oliv, Sp, Slf
KOM-20s	72	−8.0	−1.5	0.51 : 0.30 : 0.18	Gl, Oliv, Sp, Slf
KOM-13s	72	−9.4	−1.5	0.27 : 0.71 : 0.08	Gl, Oliv, Sp[1], Slf, (Tngst?)
KOM-11s	72	−10.3	−1.5	0.08 : 1.44 : 0.12	Gl, Oliv, Sp[1], Slf, Tngst
Ni-V-Doped Experiments					
KOM-19s	72	−7.9	−1.8	0.46 : 0.17 : 0.10	Gl, Oliv, Sp, Slf
KOM-23s	74	−8.0	−1.5	0.51 : 0.30 : 0.18	Gl, Oliv, Sp, Slf
KOM-22s	90	−9.1	−1.5	0.44 : 0.78 : 0.10	Gl, Oliv, Sp[1], Slf
KOM-18s	72	−10.3	−1.5	0.08 : 1.44 : 0.12	Gl, Oliv, Sp[1], Slf

Abbreviations: Gl = glass, Oliv = olivine; Slf = sulfide; PrEn = protoenstatite; Sp = spinel; Tngst = tungstate mineral.
[1]Spinel occurs within sulfide melt.
[2]Reversal experiment.

Table 2. Electron microprobe analyses of silicate run products from Ni-doped experiments on Fo86 starting composition.

Experiment	Phase	SiO_2	Al_2O_3	FeO*	MgO	CaO	Na_2O	NiO	S	Total
Fo86-8s	Gl	60.9(8)	11.3(2)	9.1(4)	13.5(7)	2.5(1)	2.4(2)	0.130(9)	0.031(3)	99.86
	Oliv	40.5(4)	0.05(2)	9.7(2)	49.2(5)	0.04(1)	—	0.97(4)	—	100.46
Fo86-5s	Gl	61.6(3)	11.7(1)	7.9(2)	13.2(2)	2.34(6)	3.2(3)	0.116(3)	0.028(1)	100.08
	Oliv	40.7(3)	0.08(2)	9.5(1)	49.5(3)	0.04(2)	—	0.84(2)	—	100.66
Fo86-9s	Gl	60.8(4)	11.5(1)	8.6(1)	14.6(1)	2.32(3)	2.5(1)	0.091(7)	0.041(4)	100.45
	Oliv	40.5(2)	0.1(2)	9.7(1)	49.8(5)	0.05(2)	—	0.59(2)	—	100.74
Fo86-15s	Gl	59.5(3)	13.2(2)	8.2(2)	14.4(1)	2.62(6)	2.76(6)	0.040(4)	0.047(5)	100.77
	Oliv	40.7(3)	0.03(1)	8.9(1)	50.6(5)	0.05(1)	—	0.28(2)	—	100.56
Fo86-14s	Gl	59.6(2)	14.9(1)	6.8(1)	13.6(1)	3.1(1)	2.61(7)	0.017(2)	0.060(1)	100.69
	Oliv	41.3(3)	0.04(2)	7.9(1)	51.1(4)	0.05(1)	—	0.120(5)	—	100.51
Fo86-10s	Gl	59.1(7)	16.5(2)	3.2(2)	16.0(4)	3.2(1)	2.3(1)	0.007(2)	0.080(2)	100.39
	Oliv	41.8(3)	0.07(1)	3.68(7)	54.9(4)	0.06(1)	—	0.028(3)	—	100.54

Notes: Units in parentheses represent 1 standard deviation of least units cited on the basis of replicate analyses; thus, 60.9(8) should be read as 60.9±0.8. Abbreviations as in Table 1.

Table 3. Electron Microprobe Analyses of Silicate Phases from Ni-Cr-Cu-Doped Experiments on KOM Starting Composition.

Experiment	Phase	SiO_2	TiO_2	Al_2O_3	Cr_2O_3	FeO	MnO	MgO	CaO	Na_2O	K_2O	NiO	CuO	S	Total
KOM-1s	Gl	51.4(3)	0.38(2)	10.9(1)	0.246(3)	11.2(2)	0.314(2)	15.2(1)	10.0(1)	0.23(4)	0.06(1)	0.086(2)	0.073(3)	0.065(2)	100.15
	Oliv	39.7(3)	—	0.07(1)	0.158(3)	10.89(9)	0.266(4)	47.8(3)	0.23(2)	—	—	0.58(1)	0.007(2)	—	99.69
KOM-6s	Gl	51.5(1)	0.35(2)	10.53(8)	0.371(3)	11.2(1)	0.296(2)	17.19(9)	9.33(9)	0.12(2)	0.02(1)	0.096(2)	0.026(2)	0.081(2)	101.11
	Oliv	40.3(1)	—	0.07(3)	0.22(1)	9.7(1)	0.225(2)	49.2(2)	0.23(1)	—	—	0.551(3)	—	—	100.50
KOM-15s	Gl	51.5(2)	0.34(2)	10.47(5)	0.530(3)	9.4(1)	0.300(4)	17.65(6)	9.32(6)	0.08(1)	0.01(0)	0.024(2)	0.011(2)	0.131(1)	99.77
	Oliv	40.4(2)	—	0.12(2)	0.324(5)	8.44(7)	0.214(3)	49.8(3)	0.21(1)	—	—	0.134(5)	—	—	99.64
KOM-4s	Gl	53.6(1)	0.35(2)	11.0(1)	0.271(1)	6.8(2)	0.322(4)	18.4(1)	9.84(5)	0.11(2)	0.01(1)	0.010(1)	0.011(2)	0.140(2)	100.86
	Oliv	41.3(2)	—	0.04(2)	0.178(5)	6.1(3)	0.230(2)	52.5(4)	0.21(1)	—	—	0.062(4)	—	—	100.62
KOM-3s	Gl	55.5(2)	0.36(2)	11.4(1)	0.222(1)	3.72(6)	0.311(3)	18.38(6)	10.3(1)	0.17(2)	0.03(1)	—	0.0086(5)[1]	0.154(3)	100.56
	Oliv	41.9(4)	—	0.03(1)	0.140(1)	3.55(6)	0.220(2)	54.6(7)	0.22(1)	—	—	0.017(1)	—	—	100.68
KOM-10s	Gl	55.5(2)	0.33(1)	11.22(6)	0.672(3)	4.2(1)	0.289(2)	18.3(1)	9.77(8)	0.05(1)	0.00	0.0043(8)	0.010(2)	0.140(3)	100.49
	Oliv	41.6(2)	—	0.08(2)	0.429(4)	3.81(7)	0.200(2)	54.4(2)	0.19(1)	—	—	0.030(6)	—	—	100.74
KOM-26s	Gl	55.0(1)	0.34(2)	11.54(8)	0.716(2)	4.09(8)	0.301(2)	18.41(9)	9.9(1)	0.07(2)	0.01(0)	0.007(2)	0.012(2)	0.133(5)	100.53
	Oliv	41.7(3)	—	0.07(2)	0.458(5)	3.70(9)	0.205(2)	54.4(3)	0.22(2)	—	—	0.045(7)	—	—	100.80
KOM-9s	Gl	56.1(2)	0.34(2)	11.23(4)	0.561(3)	2.94(5)	0.263(2)	19.3(1)	9.92(4)	0.08(2)	0.01(0)	—	0.012(2)	0.151(2)	100.91
	Oliv	42.1(2)	—	0.07(2)	0.354(3)	2.54(5)	0.179(2)	55.7(2)	0.21(1)	—	—	0.017(2)	—	—	101.17

Notes: Units in parentheses as in Table 2. Abbreviations as in Table 1.
[1]Determined by ion microprobe.

Table 4. Electron microprobe analyses of silicate phases from Ni-Co-W-doped experiments on KOM starting composition.

Experiment	Phase	SiO_2	TiO_2	Al_2O_3	Cr_2O_3	FeO	MnO	MgO	CaO	Na_2O	K_2O	NiO	CoO	WO_3	S	Total
KOM-16s	Gl	49.1(2)	0.35(2)	10.59(7)	0.226(5)	11.7(2)	0.279(5)	16.0(1)	9.03(4)	0.13(2)	0.02(1)	0.121(3)	0.48(2)	1.03(2)	0.064(2)	99.12
	Oliv	39.8(2)	—	0.07(0)	0.13(1)	11.2(2)	0.191(9)	46.2(2)	0.22(2)	—	—	0.67(9)	0.87(8)	0.016(3)	—	99.37
KOM-20s	Gl	50.4(1)	0.35(2)	10.67(8)	0.254(2)	11.1(1)	0.297(3)	16.9(1)	9.23(9)	0.05(2)	0.00(1)	0.079(2)	0.435(2)	0.973(8)	0.08(1)	100.82
	Oliv	40.5(2)	—	0.09(1)	0.151(2)	9.68(9)	0.217(4)	49.0(2)	0.22(1)	—	—	0.45(1)	0.85(1)	0.052(5)	—	101.21
KOM-13s	Gl	51.9(3)	0.34(2)	10.6(1)	0.213(3)	8.2(2)	0.286(2)	17.71(8)	9.35(6)	0.05(1)	0.01(1)	0.018(2)	0.136(3)	0.71(2)	0.136(9)	99.66
	Oliv	41.0(2)	—	0.04(2)	0.134(3)	7.6(1)	0.205(4)	50.9(2)	0.20(1)	—	—	0.097(2)	0.263(5)	0.028(5)	—	100.47
KOM-11s	Gl	55.0(1)	0.37(2)	11.1(3)	0.163(1)	3.7(1)	0.285(2)	18.7(1)	9.8(1)	0.04(2)	0.01(1)	0.0034(9)	0.0357(6)	0.669(7)	0.141(2)	100.02
	Oliv	41.9(2)	—	0.03(2)	0.107(2)	3.39(6)	0.200(2)	54.5(2)	0.19(2)	—	—	0.024(3)	0.070(2)	0.036(6)	—	100.45

Notes: Units in parentheses as in Table 2. Abbreviations as in Table 1.

Table 5. Electron Microprobe Analyses of Silicate Phases from Ni-V-Doped Experiments on KOM Starting Composition.

Experiment	Phase	SiO_2	TiO_2	Al_2O_3	Cr_2O_3	FeO	MnO	MgO	CaO	Na_2O	K_2O	NiO	V_2O_5	S	Total
KOM-19s	Gl	50.0(2)	0.346(3)	10.6(1)	0.240(2)	11.4(2)	0.288(3)	16.6(1)	9.37(7)	0.14(3)	0.03(1)	0.176(3)	1.00(1)	0.062(3)	100.25
	Oliv	40.1(3)	0.005(1)	0.07(0)	0.148(3)	10.0(2)	0.212(2)	47.9(3)	0.24(2)	—	—	1.05(2)	0.096(3)	—	99.82
KOM-23s	Gl	49.6(2)	0.347(3)	10.64(9)	0.250(2)	11.9(2)	0.293(3)	17.2(1)	8.81(7)	0.15(2)	0.02(1)	0.095(3)	1.048(5)	0.101(6)	100.45
	Oliv	40.4(2)	0.004(1)	0.06(2)	0.145(2)	10.2(1)	0.217(2)	48.7(2)	0.22(2)	—	—	0.52(2)	0.104(2)	—	100.57
KOM-22s	Gl	51.3(2)	0.356(4)	10.7(1)	0.247(6)	9.9(2)	0.303(5)	17.9(1)	9.17(6)	0.06(1)	0.01(1)	0.027(5)	0.99(1)	0.145(3)	101.11
	Oliv	40.8(2)	0.0047(7)	0.07(2)	0.147(1)	8.9(1)	0.216(3)	50.4(2)	0.21(1)	—	—	0.152(4)	0.157(2)	—	101.06
KOM-18s	Gl	55.0(2)	0.367(2)	11.15(8)	0.162(2)	3.87(7)	0.290(2)	18.64(8)	9.9(1)	0.09(2)	0.02(1)	0.006(1)	0.811(5)	0.153(1)	100.45
	Oliv	41.6(3)	0.0062(8)	0.06(2)	0.105(2)	3.4(1)	0.205(2)	54.3(2)	0.19(2)	—	—	0.027(2)	0.276(1)	—	100.17

Notes: Units in parentheses as in Table 2. Abbreviations as in Table 1.

Table 6. Electron microprobe analyses of experimentally-produced sulfide melts.

Experiment	Fe	Ni	Cu	Cr	Mn	Co	W	V	S	Total
Fo86-8s†	13.3(3)	58.6(3)	—	—	—	—	—	—	28.8(2)	100.7
Fo86-5s	14.9(3)	56.3(8)	—	—	—	—	—	—	29.6(2)	100.8
Fo86-9s	21.9(6)	46.5(6)	—	—	—	—	—	—	31.3(1)	99.7
Fo86-15s	42.2(12)	24.0(9)	—	—	—	—	—	—	34.7(3)	100.9
Fo86-14s	43.9(5)	21.8(4)	—	—	—	—	—	—	33.9(3)	99.6
Fo86-10s†	50.7(8)	11.2(6)	—	—	—	—	—	—	38.3(5)	100.2
KOM-1s	19.9(2)	36.4(2)	14.8(2)	—[1]	—[1]	—	—	—	30.0(1)	101.10
KOM-6s	20.9(5)	41.6(7)	6.5(1)	0.034(8)	0.013(8)	—	—	—	31.7(3)	100.75
KOM-15s	36.7(7)	21.2(6)	4.8(2)	0.14(5)	0.060(6)	—	—	—	36.6(1)	99.50
KOM-4s	44.6(6)	11.2(5)	6.1(3)	0.4(1)	0.17(1)	—	—	—	36.8(2)	99.27
KOM-3s	51.0(3)	7.9(2)	6.5(3)	1.1(1)	0.36(1)	—	—	—	34.3(2)	101.16
KOM-10s	43.3(5)	12.1(3)	6.8(3)	2.2(2)	0.24(1)	—	—	—	34.9(2)	99.54
KOM-26s	42.5(7)	13.2(4)	6.6(4)	2.4(3)	0.23(1)	—	—	—	34.9(2)	99.83
KOM-9s	43.1(6)	10.0(2)	9.3(3)	2.6(2)	0.37(3)	—	—	—	34.1(4)	99.47
KOM-16s	13.9(4)	48.5(4)	—	—[2]	—[2]	6.7(1)	—[1]	—	30.1(2)	99.20
KOM-20s	23.5(3)	36.0(5)	—	—[1]	—[1]	8.3(2)	—[1]	—	33.0(3)	100.80
KOM-13	36.6(4)	22.1(4)	—	0.26(3)	0.067(9)	6.6(1)	—[1]	—	34.7(2)	100.33
KOM-11s	48.6(6)	11.7(3)	—	0.7(2)	0.24(1)	4.6(1)	0.06(1)	—	34.7(2)	100.60
KOM-19s	14.0(3)	56.4(3)	—	—[2]	—[2]	—	—	0.014(1)	30.4(3)	100.81
KOM-23s	25.9(8)	41.1(9)	—	—[1]	0.015(6)	—	—	0.013(1)	33.3(4)	100.33
KOM-22s	39.9(7)	24.8(6)	—	0.18(4)	0.060(4)	—	—	0.10(2)	35.9(2)	100.94
KOM-18s	47.5(3)	17.7(3)	—	0.54(6)	0.21(1)	—	—	0.6(2)	34.4(2)	100.95

Notes: Units in parentheses as in Table 2. Abbreviations as in Table 1.
[1]Concentration is at or below detection limit.
[2]Not determined.

Table 7. Regression parameters for logarithm of sulfide melt/silicate melt partition coefficient versus one-half the logarithm of the sulfur fugacity/oxygen fugacity ratio.

$$\mathrm{LogD_i^{Sulfide/Silicate}} = m\tfrac{1}{2}\mathrm{Log}\frac{f_{S2}}{f_{O2}} + b$$

Element	Number of Expts.	m	b	r^2	Calculated Valence	Possible Valence
Weight Ratio Partition Coefficients						
Ni	13	0.65(4)	0.64(15)	0.9570	1.30^+	2^+
Cu	7	0.38(3)	1.3(1)	0.9768	0.76^+	1^+-2^+
Mn	11	1.12(7)	-4.9(3)	0.9675	2.24^+	2^+
Cr	10	1.37(8)	-5.3(3)	0.9733	2.74^+	2^+-3^+
Co	4	0.69(5)	-0.88(20)	0.9878	1.38^+	2^+
V	4	1.36(17)	-5.9(6)	0.9742	2.80^+	3^+-4^+
Molar Ratio Partition Coefficients						
Ni	13	0.65(4)	0.97(16)	0.9547	1.30^+	2^+
Cu	7	0.38(2)	1.59(8)	0.9846	0.76^+	1^+-2^+
Mn	11	1.09(6)	-4.4(2)	0.9744	2.18^+	2^+
Cr	10	1.38(8)	-5.0(3)	0.9753	2.76^+	2^+-3^+
Co	4	0.69(6)	-0.55(22)	0.9859	1.38^+	2^+
V	4	1.36(16)	-5.6(6)	0.9728	2.80^+	3^+-4^+

Notes: Units in parentheses are 1σ uncertainties in regression parameters.

Table 8. Experimentally-determined partition coefficients

Experiment	Δf^1	D_{Ni}	D_{Cr}	D_{Mn}	D_{Cu}	D_{Co}	D_W	D_V
Sulfide Melt/Silicate Melt Partition Coefficients								
KOM-1s	3.05	540(10)	—	—	250(20)	—	—	—
KOM-6s	3.25	550(10)	0.13(3)	0.06(3)	313(9)	—	—	—
KOM-15s	3.65	1100(100)	0.39(5)	0.26(4)	500(100)	—	—	—
KOM-4s	4.10	1430(50)	2.2(2)	0.68(2)	690(50)	—	—	—
KOM-3s	4.40	—	7.2(3)	1.49(4)	960(50)	—	—	—
KOM-10s	4.40	3600(200)	4.8(2)	1.07(5)	900(100)	—	—	—
KOM-26s[2]	4.40	2400(300)	4.9(2)	0.99(5)	690(70)	—	—	—
KOM-9s	4.55	—	6.8(3)	1.8(1)	970(50)	—	—	—
KOM-16s	3.05	510(10)	—	—	—	17.7(5)	—	—
KOM-20s	3.25	580(30)	—	—	—	24.3(9)	—	—
KOM-13s	3.95	1600(100)	1.8(1)	0.30(2)	—	62(4)	—	—
KOM-11s	4.40	4400(400)	6.3(5)	1.09(3)	—	164(7)		—
KOM-19s	3.05	410(20)	—	—	—	—	—	0.025(1)
KOM-23s	3.25	550(20)	—	0.07(1)	—	—	—	0.022(1)
KOM-22s	3.80	1170(80)	1.1(1)	0.26(1)	—	—	—	0.18(1)
KOM-18s	4.40	3800(400)	4.9(2)	1.07(4)	—	—	—	1.3(1)
Olivine/Silicate Melt Partition Coefficients								
KOM-1s	3.05	6.74(6)	0.642(4)	0.847(4)	0.096(9)	—	—	—
KOM-6s	3.25	5.74(4)	0.593(8)	0.760(3)	0.075(8)	—	—	—
KOM-15s	3.65	5.6(1)	0.611(3)	0.713(4)	0.133(7)	—	—	—
KOM-4s	4.10	6.2(2)	0.657(6)	0.714(4)	0.11(2)	—	—	—
KOM-3s	4.40	—	0.631(2)	0.707(3)	0.19(3)	—	—	—
KOM-10s	4.40	7.0(7)	0.64(1)	0.692(3)	0.09(1)	—	—	—
KOM-26s[2]	4.40	6.4(6)	0.640(2)	0 681(2)	—	—	—	—
KOM-9s	4.55	—	0.631(2)	0.681(3)	0.08(1)	—	—	—
KOM-16s	3.05	5.5(2)	0.58(1)	0.69(1)	—	1.81(6)	0.016(1)	—
KOM-20s	3.25	5.7(1)	0.594(3)	0.731(5)	—	1.954(4)	0.053(2)	—
KOM-13s	3.95	5.4(2)	0.629(6)	0.717(5)	—	1.93(2)	0.039(2)	—
KOM-11s	4.40	7.1(6)	0.656(4)	0.702(3)	—	1.96(2)	0.054(3)	—
KOM-19s	3.05	5.97(6)	0.617(4)	0.736(3)	—	—	—	0.096(1)
KOM-23s	3.25	5.47(8)	0.580(3)	0.741(3)	—	—	—	0.099(1)
KOM-22s	3.80	5.6(3)	0.595(5)	0.713(5)	—	—	—	0.159(1)
KOM-18s	4.40	4.5(3)	0.648(4)	0.707(2)	—	—	—	0.340(1)

Notes: Units in parentheses represent 1σ uncertainties calculated by propagating the standard deviation of the mean.

[1] $\Delta f = \log f_{S2}^{1/2} - \log f_{O2}^{1/2}$

[2] Reversal experiment.

Table 9. Forsterite contents and Fe/Mg exchange K_D values for San Carlos olivine crucibles and experimentally-produced olivines.

Experiment	Crucibles Fo	K_d	Olivines Fo	K_d
KOM-1s	88.7	0.31	88.7	0.31
KOM-6s	89.9	0.31	90.0	0.31
KOM-15s	91.2	0.32	91.3	0.32
KOM-4s	93.9	0.31	93.9	0.31
KOM-3s	96.2	0.35	96.5	0.32
KOM-10s	96.0	0.33	96.2	0.31
KOM-26s	96.2	0.31	96.3	0.31
KOM-9s	97.4	0.31	97.5	0.30
KOM-16s	88.2	0.33	88.0	0.33
KOM-20s	89.9	0.30	90.0	0.30
KOM-13s	92.3	0.32	92.3	0.32
KOM-11s	96.5	0.33	96.6	0.32
KOM-19s	89.2	0.31	89.5	0.31
KOM-23s	89.6	0.30	89.5	0.30
KOM-22s	91.1	0.31	91.0	0.32
KOM-18s	96.5	0.31	96.6	0.30

Table 10. Parameters used in core segregation modeling.

Depletion Factors						Partition Coefficients					
V	Cr	Mn	Co	Ni	Cu	V	Cr	Mn	Co	Ni	Cu
Earth						*Metal/Silicate Melt*					
1.5	1.7	3.9	9.5	10.3	8.9	0.007	0.12	0.004	71	1211	13
						Sulfide Melt/Silicate Melt					
						0.02	0.08	0.03	17	437	272
						Olivine/Silicate Melt					
						0.34	0.61	0.71	1.9	5.9	0.11
Shergittite Parent Body						*Metal/Silicate Melt*					
–	1.0	1.0	14.4	53.6	44.7	–	0.12	0.004	71	1211	13
						Sulfide Melt/Silicate Melt					
						–	2.2	0.55	92	2127	685
						Olivine/Silicate Melt					
						–	0.61	0.71	1.9	5.9	0.11

FIGURE CAPTIONS

Figure 1. Schematic of the furnace assembly used to perform siderophile element partitioning experiments.

Figure 2. Plot of log f_{O_2} versus log f_{S_2} showing experimental conditions (filled circles). Diagonal lines represent constant $\log f_{S2}^{1/2} - \log f_{O2}^{1/2}$ values. Vertical lines represent iron-quartz-fayalite (IQF), iron-wüstite (IW), and fayalite-magnetite-quartz (FMQ) oxygen buffers. Horizontal line represents iron-iron sulfide (FeFeS) sulfur buffer.

Figure 3. Plot of the ternary system Fe-Ni-S comparing the compositions of sulfide melts from partitioning experiments performed on the Fo86 starting composition (filled circles) with those from experiments performed by Rajamani and Naldrett (1978) and Peach and Mathez (1993).

Figure 4. Plot of $\log D_M^{\text{Sulfide Melt/Silicate Melt}}$ versus $\log f_{S_2}^{1/2} - \log f_{O_2}^{1/2}$ illustrating the linear dependence of sulfide melt/silicate melt partitioning on f_{O_2}/f_{S_2} conditions.

Figure 5. Plot of $\log D_M^{\text{Olivine/Silicate Melt}}$ versus $\log f_{S_2}^{1/2} - \log f_{O_2}^{1/2}$ illustrating the constancy of olivine/silicate melt partition coefficients for Cr, Mn, Co, Ni, and Cu. The sharp increases in the partition coefficients for V and W are attributable changing valence states with decreasing f_{O_2}.

Figure 6. Plot of $\log D_{Ni}^{\text{Sulfide Melt/Silicate Melt}}$ versus $\log f_{S_2}^{1/2} - \log f_{O_2}^{1/2}$ comparing the linear dependence of sulfide melt/silicate melt partitioning on f_{O_2}/f_{S_2} conditions found in the

KOM experiments (open circles) with the curvature that is apparent in the experiments performed on the Fo86 starting composition (squares). The experiments represented by the open squares are olivine saturated, while those represented by the filled squares are saturated with an olivine + low-Ca pyroxene assemblage.

Figure 7. Plot of logarithm of silicate melt sulfide capacity (log C_S) versus FeO content comparing the linear dependence of log C_S on FeO found in the KOM experiments (open circles) with the curvature found in the experiments performed on the Fo86 starting composition (squares). The experiments represented by the open squares are olivine saturated, while those represented by the filled squares are saturated with an olivine + low-Ca pyroxene assemblage.

Figure 8. Plot of core size versus extent of silicate partial melting that accompanied core formation showing results of modeling V, Cr, Mn, Co, Ni, and Cu depletions in the Earth's upper mantle. Conditions for core formation tested in this model are log f_{O_2} = –10.2, and log f_{S_2} = –4.1 at 1350°C.

Figure 9. Plot of core size versus extent of silicate partial melting that accompanied core formation showing best results for modeling Co, Ni, and Cu depletions in the SPB mantle (Mars). Conditions for core formation tested in this model are log f_{O_2} = –10.2, and log f_{S_2} = –2.0 at 1350°C.

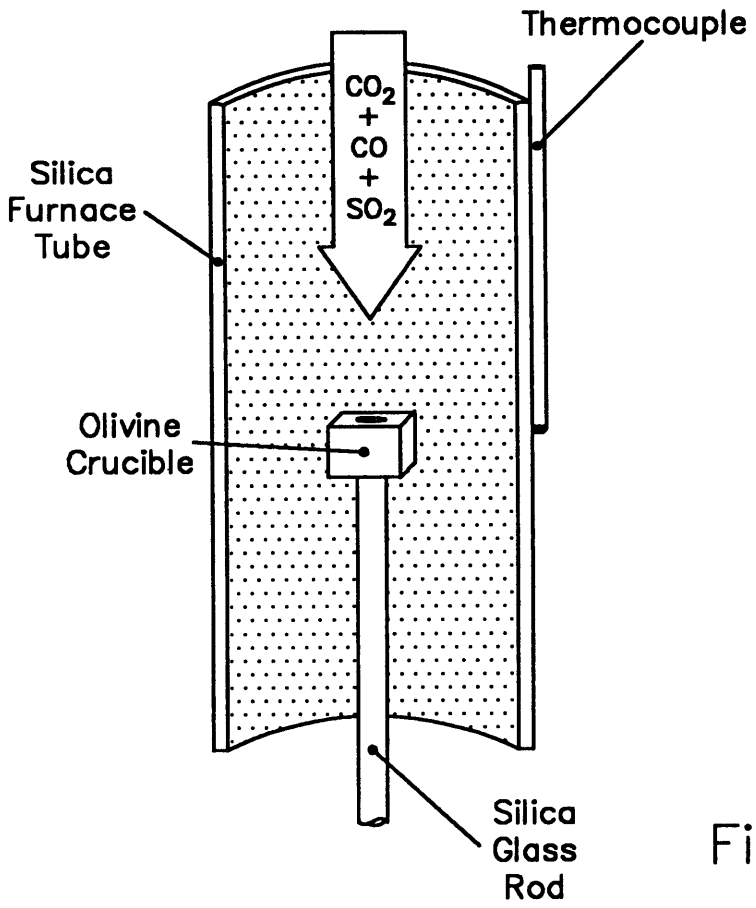
Thermocouple
CO_2 + CO + SO_2
Silica Furnace Tube
Olivine Crucible
Silica Glass Rod

Figure 1

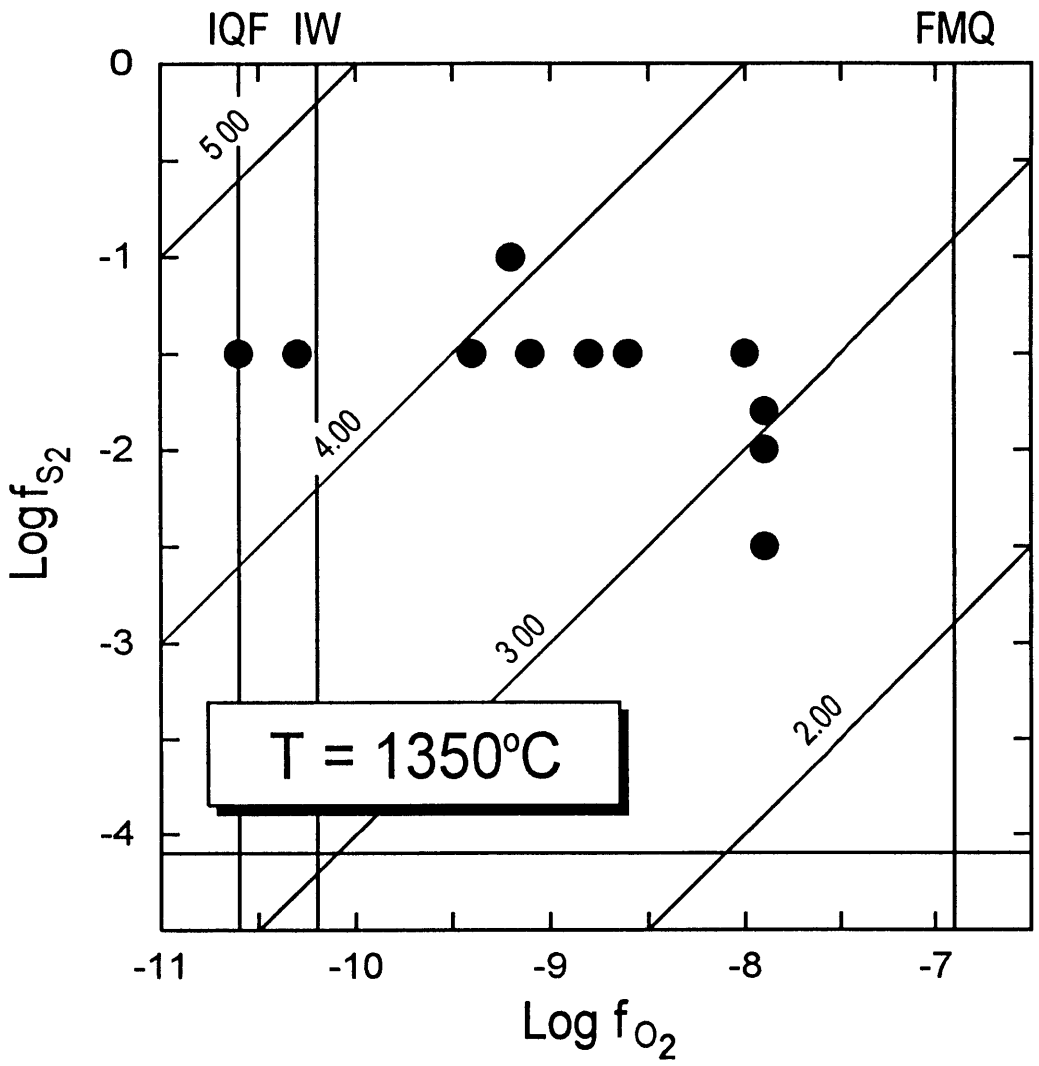
IQF
IW
FMQ
0
-1
-2
-3
-4
5.00
4.00
3.00
2.00
T = 1350°C
FeFeS
-11
-10
-9
-8
-7
Log f_{S_2}
Log f_{O_2}

Figure 2

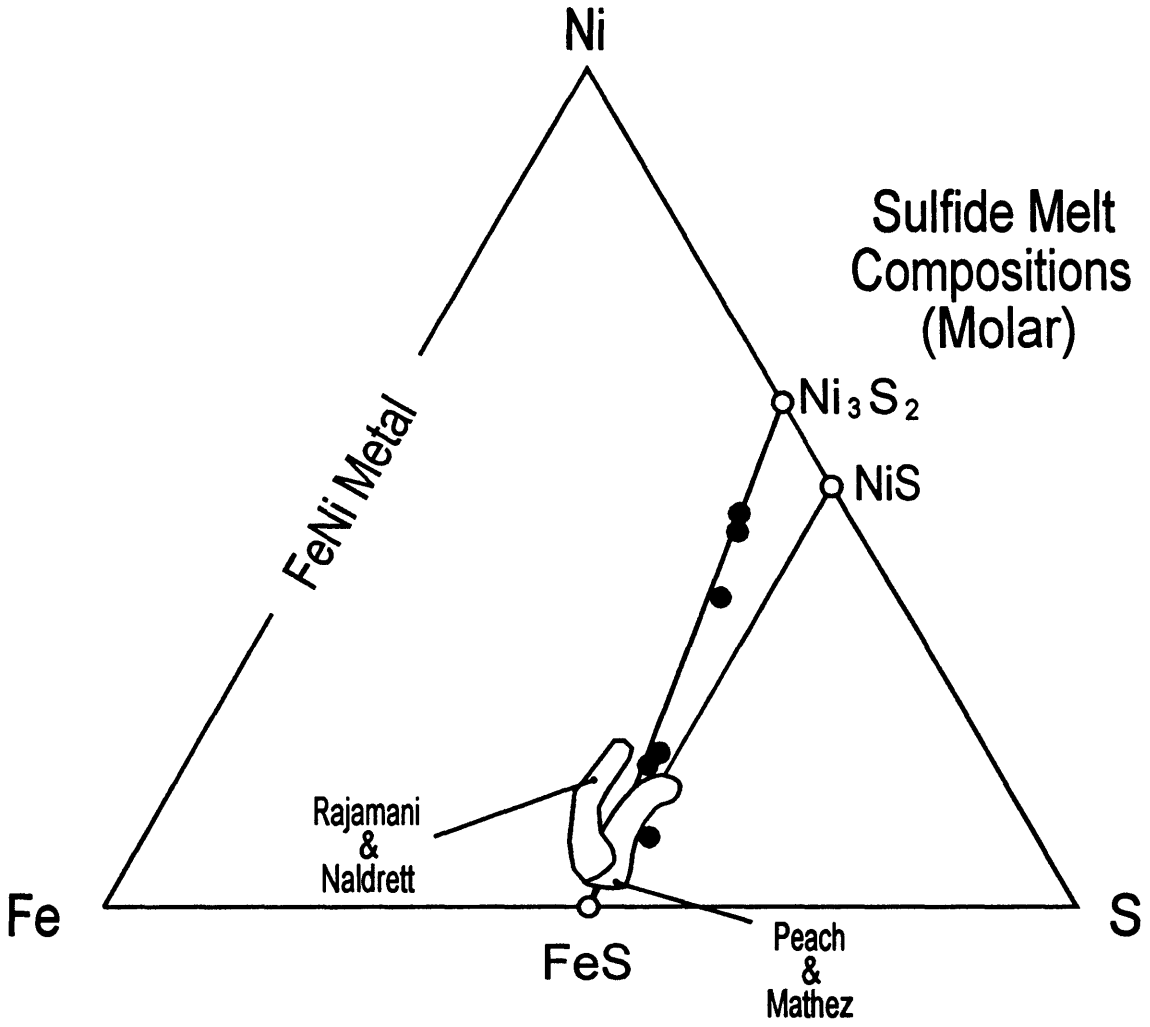
Ni
Sulfide Melt
Compositions
(Molar)
Ni3S2
NiS
FeNi Metal
Rajamani
&
Naldrett
Fe
FeS
S
Peach
&
Mathez

Figure 3

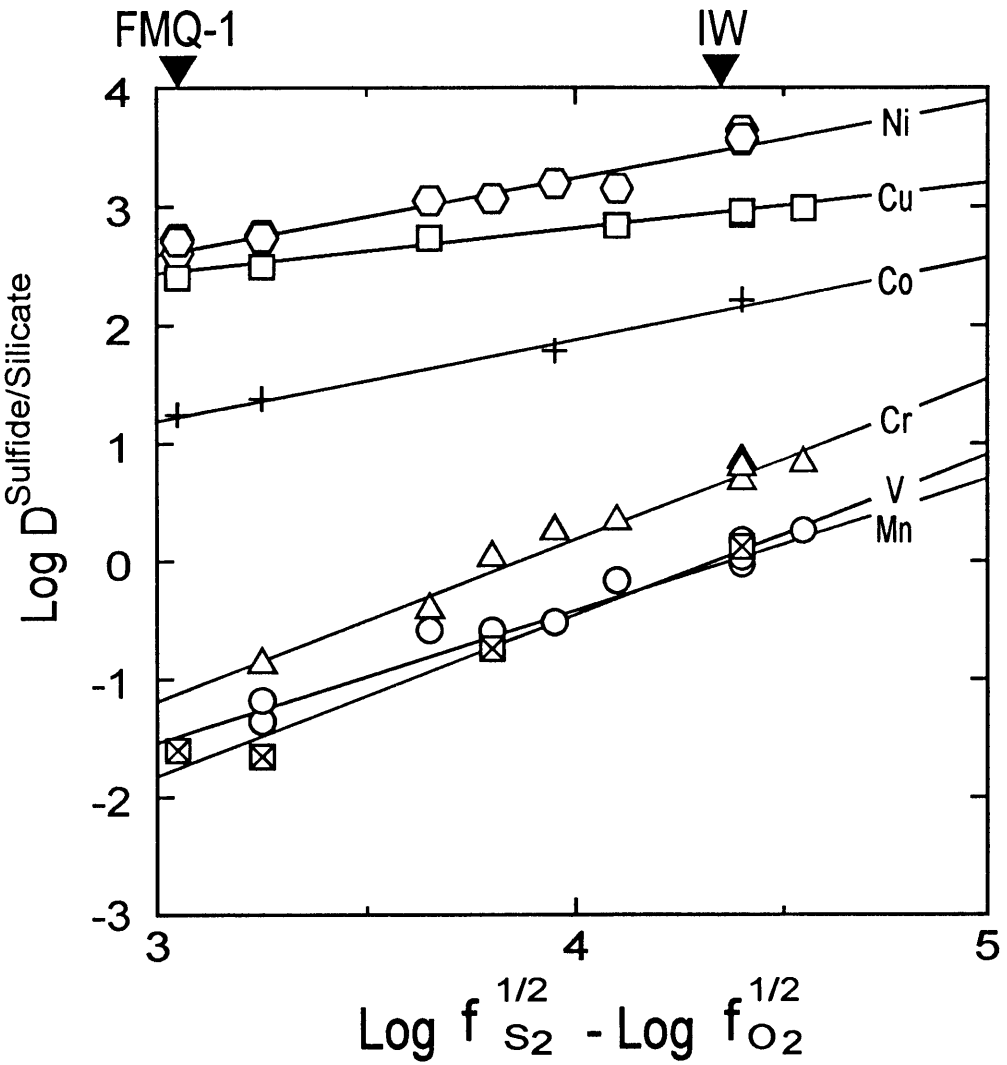
FMQ-1
IW
Ni
Cu
Co
Cr
V
Mn
Log D Sulfide/Silicate
Log f S2 1/2 - Log f O2 1/2
4
3
2
1
0
-1
-2
-3
3
4
5

Figure 4

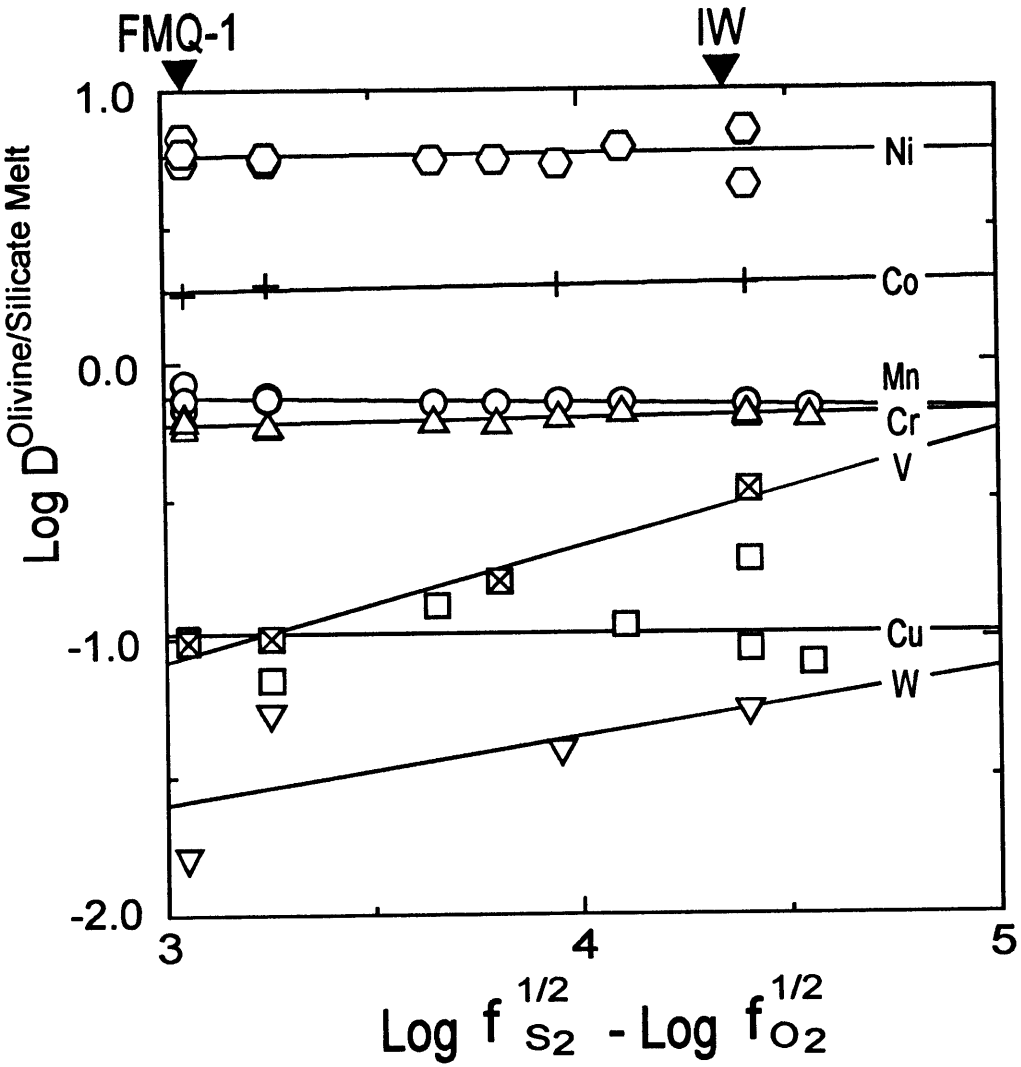
FMQ-1
IW
1.0
0.0
-1.0
-2.0
3
4
5
Log D Olivine/Silicate Melt
Log f S2 1/2 - Log f O2 1/2
Ni
Co
Mn
Cr
V
Cu
W

Figure 5

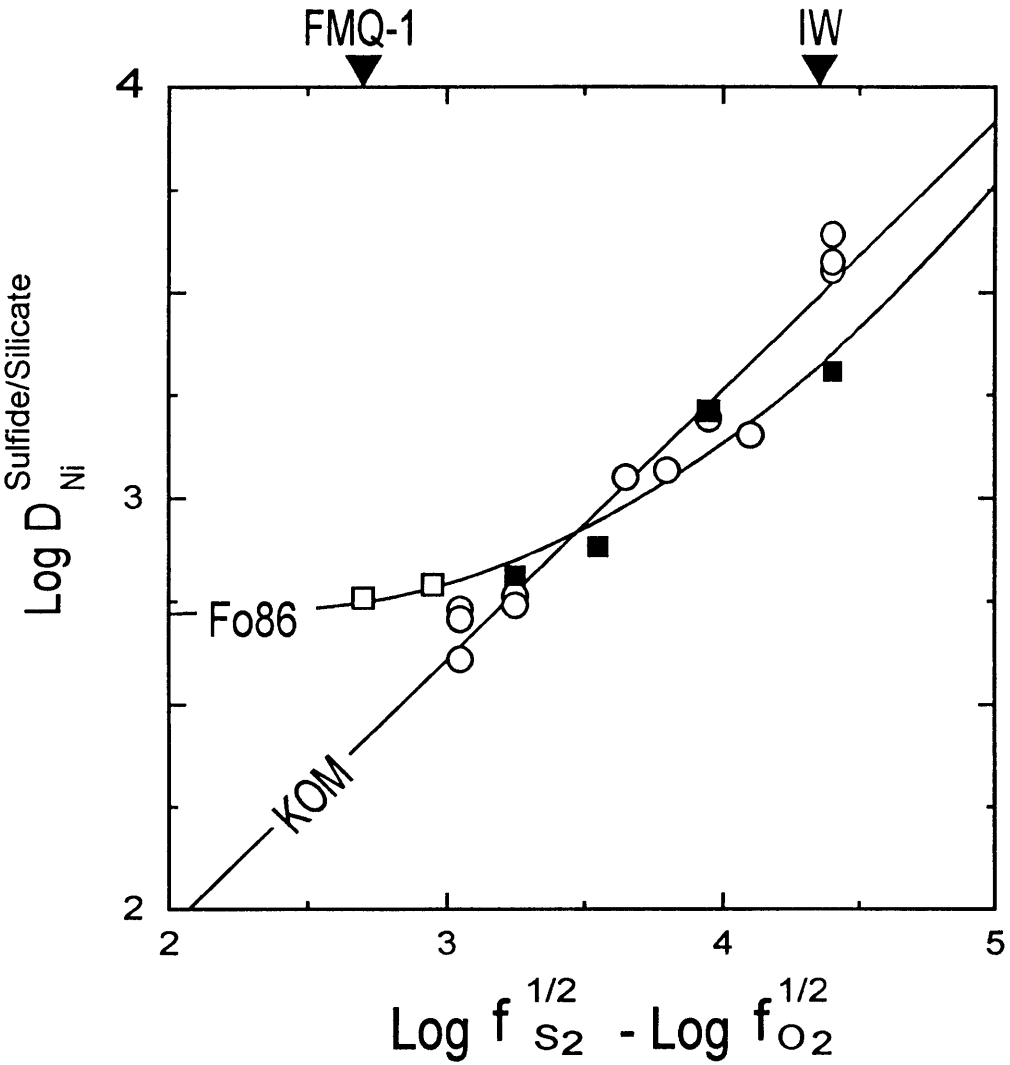
FMQ-1
IW
4
3
2
Log D Ni Sulfide/Silicate
Fo86
KOM
2
3
4
5
Log f S2 1/2 - Log f O2 1/2

Figure 6

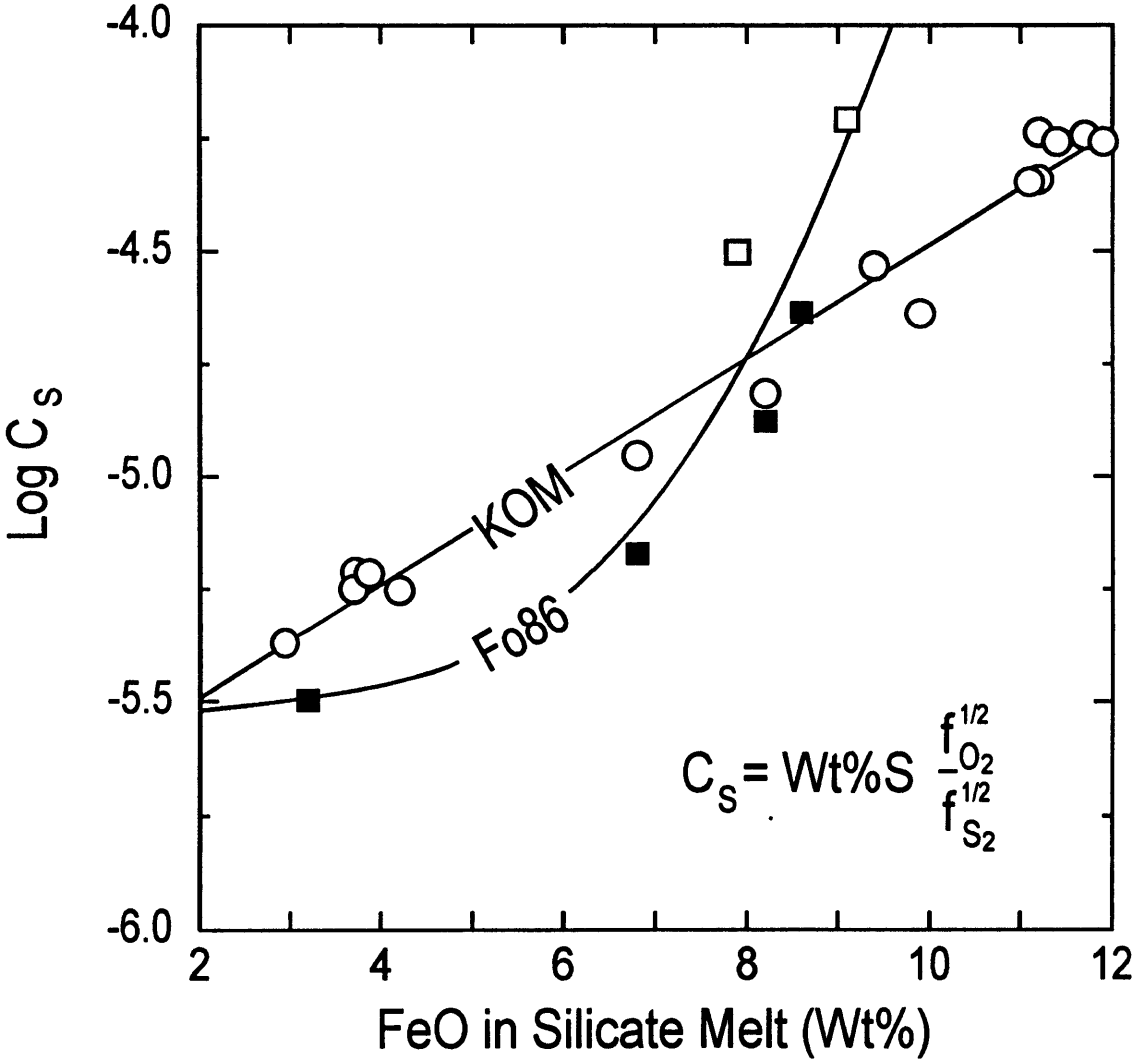
-4.0
-4.5
-5.0
-5.5
-6.0
Log C_S
2
4
6
8
10
12
FeO in Silicate Melt (Wt%)
KOM
Fo86
C_S = Wt%S $\frac{f_{O_2}^{1/2}}{f_{S_2}^{1/2}}$

Figure 7

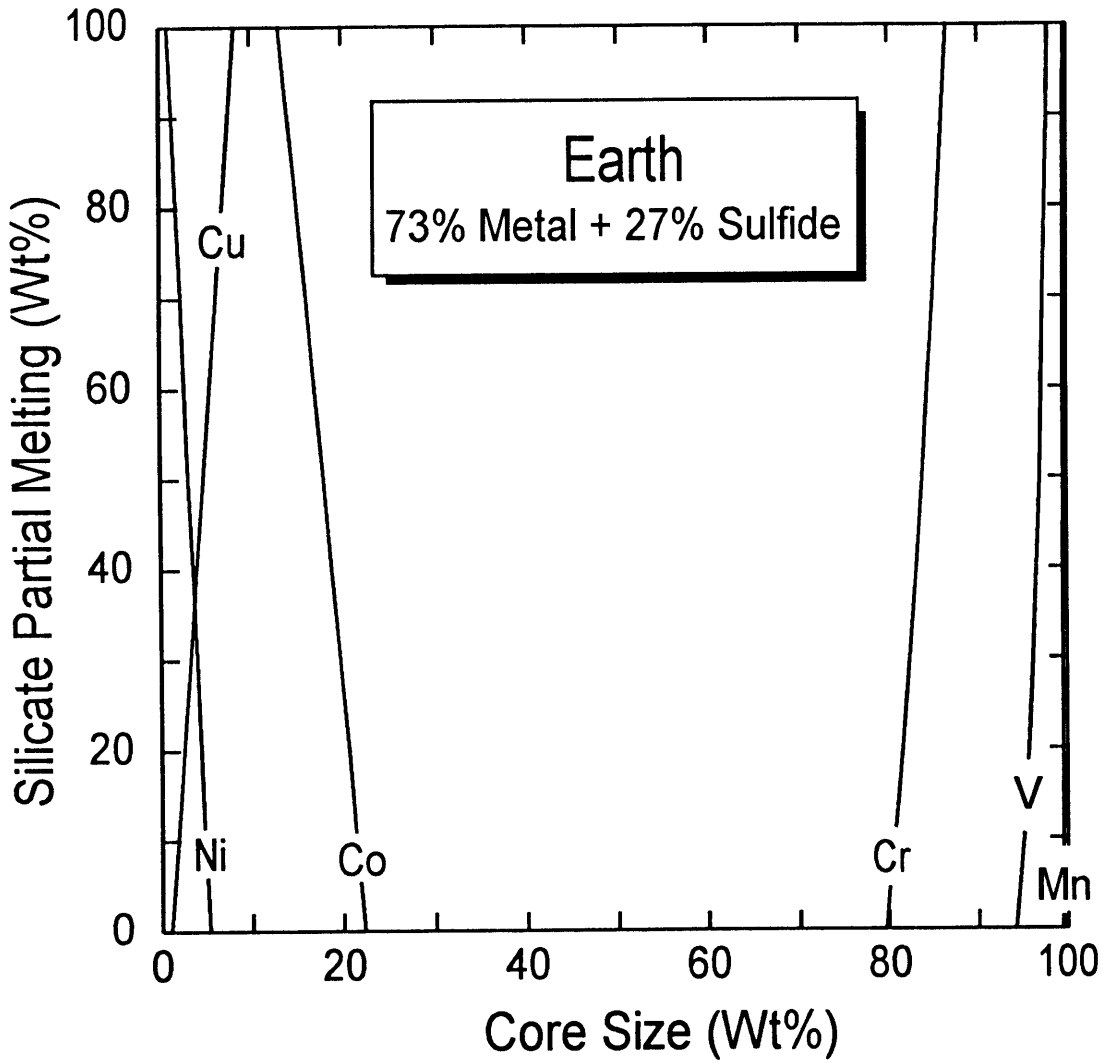
Earth
73% Metal + 27% Sulfide
Cu
Ni
Co
Cr
V
Mn
Silicate Partial Melting (Wt%)
Core Size (Wt%)
0
20
40
60
80
100

Figure 8

150

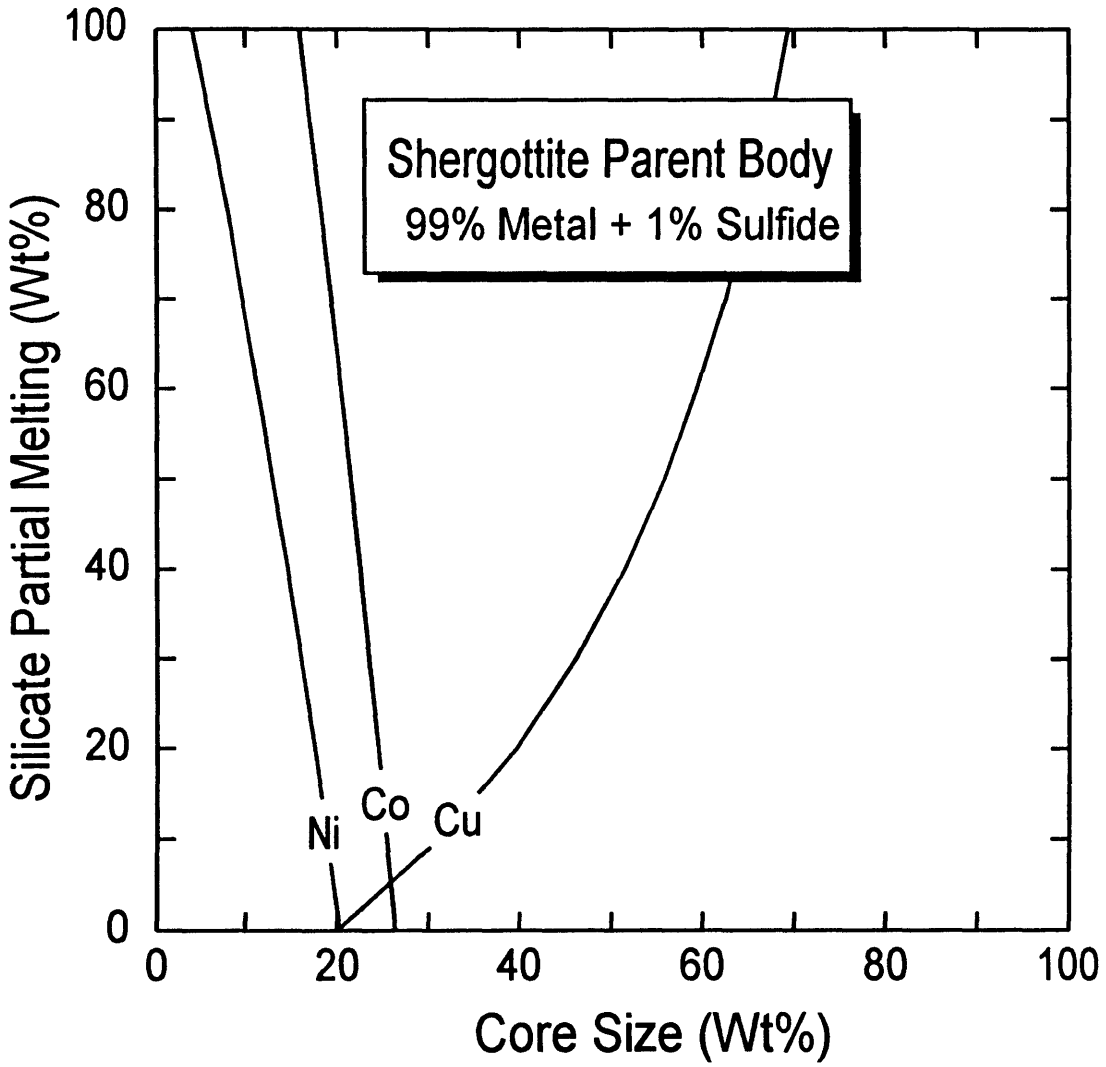
Shergottite Parent Body
99% Metal + 1% Sulfide
Ni
Co
Cu
Silicate Partial Melting (Wt%)
Core Size (Wt%)
0
20
40
60
80
100

Figure 9

CHAPTER 4.

PARTITIONING OF RARE EARTH ELEMENTS BETWEEN CLINOPYROXENE AND SILICATE MELT: CRYSTAL-CHEMICAL CONTROLS

ABSTRACT

This study explores some of the effects of major element compositional variations on the partitioning of trivalent rare earth elements between high-Ca clinopyroxene and silicate melt. Experiments performed in the system CaO-MgO-Al_2O_3-SiO_2 at 1 atm pressure, over a small temperature range, differentiate crystal-chemical controls on mineral/melt partitioning from the effects of pressure and temperature. The experimental results demonstrate that the Ca-Tschermakite content of high-Ca clinopyroxene exercises an important control on rare earth element partitioning for pyroxene co-existing with basaltic melt. A comparison of our experimental results with those from two-liquid partitioning and thermal diffusion studies demonstrates that melt structure has only a minor influence on clinopyroxene/melt partitioning for basaltic compositions, but becomes progressively more important as polymerization of the melt increases. Melt structure exercises the dominant control on partitioning for highly polymerized melts such as high-silica rhyolites. Semi-empirical expressions developed using equilibrium constants for pyroxene/melt exchange reactions successfully predict the partitioning of Ce^{3+} and Yb^{3+} for a broad range of synthetic and natural co-existing melt and clinopyroxene compositions. The ability of our model to predict the partitioning behavior of trivalent rare earth elements over a wide range of experimental conditions (0.0001 to 3.0 GPa; 1234 to 1430°C) indicates that consideration of the compositions of coexisting clinopyroxene and melt is adequate to account for the effects of varying pressure and temperature.

INTRODUCTION

High-Ca clinopyroxene (Cpx) is a major repository for trivalent rare earth elements (REE^{3+}) during mantle melting and low-pressure crystallization. Variations in pyroxene composition affect the incorporation of REE^{3+} in two ways: (1) through variations in the size of the 6-8 coordinated M2 crystallographic site related to Ca^{2+} content (McKay et al., 1986; Gallahan and Nielsen, 1992), and (2) through the ability of the pyroxene to charge balance trivalent trace elements (Colson et al., 1989; Gaetani and Grove, 1991; Gallahan and Nielsen, 1992; Hauri et al., 1994). There is also evidence that increasing the degree of polymerization of the co-existing silicate melt decreases the number of sites suitable for REE^{3+}, leading to higher Cpx/melt partition coefficients (Watson, 1976; Ryerson and Hess, 1978; Green and Pearson, 1985; Lesher, 1986; Ellison and Hess, 1989). This paper presents the results of experiments that investigate the relative importance of the various crystal-chemical controls on partitioning of trivalent rare earth elements (REE^{3+}) between high-Ca clinopyroxene and silicate melt. The experimental results are combined with data from the literature to develop semi-empirical expressions that predict the Cpx/silicate melt partitioning behavior of Ce^{3+} and Yb^{3+} as a function of the composition of co-existing pyroxene and melt.

EXPERIMENTAL AND ANALYTICAL METHODS

Starting materials were prepared as 5 g batches from Johnson-Matthey high purity SiO_2, Al_2O_3, MgO, and $CaCO_3$ or a prepared mix of $CaSiO_3$. They were ground under ethanol for 6 hours in an agate mortar, fused at 1300°C for 2 hours in a Pt crucible, and re-ground for 6 hours. Each mix was then doped with ~0.30 wt% each of Johnson-Matthey high purity CeO_2 and Yb_2O_3, and re-ground for 6 hours.

Each starting composition was conditioned by fusing at 1300°C for 2 hours in the hot spot of a Deltech DT31VT vertical quenching furnace, with the fugacity of oxygen controlled near the fayalite-magnetite-quartz (FMQ) buffer by mixing CO_2 and H_2 gases.

The resulting glasses were powdered and used as starting material. The fusion step ensured that all Ce was trivalent at the start of each experiment.

Experiments were performed isothermally by placing ~10 mg of starting material in a Pt crucible and suspending it in the furnace hot spot. Temperature was continuously monitored using Pt-$Pt_{90}Rh_{10}$ thermocouples calibrated against the melting point of NaCl, Au, and Pd on the IPTS 1968 temperature scale (Biggar, 1972). Oxygen fugacity was controlled near the FMQ buffer and continuously monitored using a solid ZrO_2-CaO electrolyte oxygen sensor calibrated against the Fe-FeO, Ni-NiO, and Cu-Cu_2O buffers. Charges were quenched by dropping into water at the end of each experiment. Experiments were typically run for 215 to 264 hours, although experiments run for 24 hours produced comparable partition coefficients.

All analyses were performed on the five-spectrometer JEOL 733 electron microprobe at the Massachusetts Institute of Technology. Accelerating potential was 15 kV and sample current was 50 nA for all analyses. Spot size was ~3 μm for analyses of crystalline phases and 10 μm for glasses. Analyses of Cpx grains were performed as close to the rim as possible. Mineral standards were enstatite for SiO_2 and MgO, anorthite for Al_2O_3 and CaO, and the glass standards of Drake and Weill (1972) for Ce_2O_3 and Yb_2O_3. Maximum counting times were 40 s for SiO_2, Al_2O_3, MgO and CaO, and 200 s for Ce_2O_3 and Yb_2O_3. On-line data reduction was performed using ZAF correction procedures. Replicate analyses of a synthetic glass working standard (SB from Table 1) were performed to ensure the consistency of analyses over the course of the study. The standard deviation of the means (1σ) are 0.1% relative for SiO_2 and MgO, 0.07% relative for Al_2O_3, 0.2% for CaO, 0.7% relative for Ce_2O_3 and 0.8% relative for Yb_2O_3. Relative uncertainties estimated for the same synthetic glass on the basis of counting statistics are 0.19% for SiO_2 and CaO, 0.29% for Al_2O_3 and MgO, 2.1% for Ce_2O_3 and 4.7% for Yb_2O_3 (1σ).

EXPERIMENTAL RESULTS

Synthesis Experiments

In order to determine the influence of variations in the compositions of co-existing Cpx and silicate melt on REE^{3+} partitioning, experiments were performed on 5 different starting compositions (Table 1) that lie on or near the *liquid = forsterite + anorthite + diopside* boundary in the CaO-MgO-Al_2O_3-SiO_2 (CMAS) system (Libourel et al., 1989). Experimental products consist of Cpx, plagioclase (Plag), olivine (Oliv), with the exception of experiments performed on the SB starting composition, and abundant glass (Table 2). Clinopyroxene grains are subhedral-to-euhedral in shape and generally 10-30 μm in size, with the exception of experiment MS5 in which they are substantially larger (70-100 μm). Experiments at the high-, and low-SiO_2 ends of the boundary are saturated with Oliv + Plag + Cpx at 1241°C and 1234°C respectively (Table 2). The total temperature variation necessary to investigate melt compositions from near melilite saturation (43.4 wt% SiO_2) to near low-Ca pyroxene saturation (54.5 wt% SiO_2) is only ~30°C due to the existence of a thermal maximum where the saturation boundary crosses the Oliv-Plag-Cpx compositional plane. Melt compositions that lie along this boundary and are saturated with the assemblage Oliv + Plag + Cpx represent the best analogs in the CMAS system for the range of compositional and structural variation found in naturally-occurring basalts.

The silicate melts produced in our experiments show significant variations in SiO_2 (43.4-54.5 wt%) and CaO (27.0-16.1 wt%), while variations in Al_2O_3 (17.4-16.3 wt%) and MgO (11.4-12.8 wt%) are limited (Fig. 1; Table 3). Pyroxene compositions are characterized by increasing Al_2O_3 (1.5-10.9 wt%) and CaO (20.6-25.1 wt%), and decreasing MgO (22.9-14.8 wt%) with increasing SiO_2-undersaturation of the silicate melt. The Cpx compositions from our experiments are recalculated into enstatite ($Mg_2Si_2O_6$; En), wollastonite ($Ca_2Si_2O_6$; Wo) and Ca-Tschermakite ($CaAlSiAlO_6$; CaTs) components and plotted in a ternary diagram in Figure 2. The pyroxenes that crystallize from the quartz-normative melts are characterized by higher En (~60 mol%), lower Wo (~

37 mol%) and lower CaTs (~3 mol%). As the SiO_2-saturation of the melt decreases, there is a corresponding increase in both Wo and CaTs components, coupled with a decrease in En. The Wo content of the pyroxene passes through a maximum of ~44 mol% in melts with intermediate SiO_2 contents (~48 wt %), and then decreases to ~37 mol% in the highly SiO_2-undersaturated melt compositions; CaTs increases monotonically from 3 to 23 mol% with increasing SiO_2-undersaturation (Table 4).

Clinopyroxene/melt partition coefficients determined from our experiments are reported in Table 4, along with the temperature at which each experiment was performed, the mole fractions of CaTs (X_{CaTs}) and Wo (X_{Wo}) in the Cpx, the cation fraction of the M2 site occupied by Ca^{2+} ($X_{Ca(M2)}$) and of the tetrahedral site occupied by Al^{3+} ($X_{Al(T)}$). There are monotonic increases in the partition coefficients for both Ce^{3+} (D_{Ce}) and Yb^{3+} (D_{Yb}) between pyroxene and melt with increasing X_{CaTs}. This is shown graphically in Fig. 3a, a plot of X_{CaTs} versus both D_{Ce} and D_{Yb}. Figure 3b is a plot of Wo content of the pyroxene versus the partition coefficients for Ce^{3+} and Yb^{3+}. In contrast with the strong positive correlations among X_{CaTs} and D_{REE3+}values, our data show no correlations with X_{Wo}.

Approach to Equilibrium

An approach to equilibrium was demonstrated by first performing a 214 hours synthesis experiment on the BGL starting composition at 1235°C. The products from this experiment consisted of glass, Cpx, Oliv and Plag of the same composition as those in experiment BGL7 (Table 3) which contains Cpx with high REE^{3+} concentrations (~0.11 wt% Ce_2O_3; ~0.26 wt% Yb_2O_3) and large Cpx/melt partition coefficients (D_{Ce} = 0.27±0.01; D_{Yb} = 0.65±0.03). The products were crushed and then ground, under ethanol, in 1:1 proportions with a high-SiO_2 synthetic glass powder, to produce a bulk composition the same as the EC starting material (Table 1). This mixture was held at 1236°C for 216 hours. The reversal experiment contains Cpx grains that are generally unzoned but includes a few with high-Al_2O_3 cores, relict from the starting material, surrounded by low-Al_2O_3 rims (Fig. 4). The REE^{3+} Cpx/melt partition coefficients

calculated for the rims (D_{Ce} = 0.16±0.02; D_{Yb} = 0.27±0.04) are within analytical uncertainty of those measured in the EC15 synthesis experiment (D_{Ce} = 0.14±0.01; D_{Yb} = 0.24±0.03). The dotted lines in Figure 3a connect the pyroxene composition at the start (circle) and end (square) of the reversal experiment.

Henry's Law Behavior

In order to analyze our experimental products by electron microprobe, it was necessary to dope the starting compositions at levels (~3000 ppm) significantly higher than those found in naturally-occurring basalts (10's of ppm). Previous REE^{3+} partitioning studies have demonstrated adherence to Henry's Law behavior at concentration levels ranging from 100 ppm to as high as 2 wt% (Grutzeck et al., 1974; Nicholls and Harris, 1980; Ray et al. 1983; Gallahan and Nielsen, 1992). The existence of a lower limit on Henrian behavior due to the influence of defects in the structure of the crystalline phase has also been proposed (e.g., Mysen, 1978, 1979; Harrison and Wood, 1980). Although defects may play a role in partitioning at low total REE^{3+} concentration levels, they are likely to be saturated in natural systems (Watson, 1985). Further, a re-examination of the experimental evidence for a lower limit on Henrian behavior suggests that it is an artifact of the optical autoradiography technique used to analyze the experimental products (Beattie, 1993). The Ce_2O_3 and Yb_2O_3 contents of our silicate melts (0.34 to 0.80 wt%) fall well below the upper limit for Henry's law, so that no deviation from Henrian behavior is to be expected.

DISCUSSION

Crystal Chemical Controls on Trivalent REE Partitioning

The ability of a crystalline or melt phase to incorporate a given trace element into its structure is controlled by the size of the available crystallographic sites and the ability of the phase to charge balance the incorporated cation. These controls are well illustrated by peaks corresponding with specific crystallographic sites found on plots of Ln D versus ionic radius (Onuma diagrams) for cations of a given valence state in a given mineral

(Onuma et al., 1968). The nature of the compositional variations shown by the pyroxenes in our experiments allows an examination of some of the crystal-chemical controls on the incorporation of REE^{3+}. The Cpx that crystallizes from the SiO_2-rich melts is characterized by relatively low Wo and CaTs, and both components increase with decreasing SiO_2 in the melt. In strongly SiO_2-undersaturated melts, however, the variations in Wo and CaTs are decoupled, with CaTs increasing and Wo decreasing with decreasing SiO_2 in the melt (Table 4; Fig 2). Therefore, an evaluation of the relative importance of the structural changes associated with these two components for REE^{3+} partitioning can be made.

In the Cpx structure, increasing Wo content correlates with an increase in the mean M-O distance for the M2 crystallographic site (Cameron and Papike, 1981), making incorporation of large trace elements possible. A correlation between Wo content and REE^{3+} partition coefficients was first recognized by McKay et al. (1986), on the basis of partitioning experiments involving Cpx ranging from pigeonite to augite. The CaTs component involves substitution of Al^{3+} for Mg^{2+} in the M1 site, charge balanced by substituting Al^{3+} for Si^{4+} in the tetrahedral (or T) site. The latter substitution can also be used to charge balance tri-, or quadra-valent trace elements in the M1 or M2 crystallographic site as demonstrated for low-Ca pyroxene by Colson et al. (1989). Figure 3a shows the strong correlations among the mole fraction of the CaTs component in Cpx and D_{REE3+} values in our experiments. Figure 3b demonstrates that a unique partition coefficient cannot be determined on the basis of Wo content for any of our experiments. If the correlations among Wo content and D_{REE3+} values noted by McKay et al. (1986) represented the dominant control on the incorporation REE^{3+} into the clinopyroxenes in our experiments there should be only a single value of D_{Ce} or D_{Yb} for a given Wo content. That there is not demonstrates that for these pyroxenes the structural changes associated with increasing Wo are not as important for incorporating REE^{3+} as those related to increasing the CaTs component.

There are important compositional differences between the high-Ca clinopyroxenes in our experiments and those studied by McKay et al. (1986). Our experiments contain Cpx covering a broad range of CaTs contents but a limited range of relatively high Wo values (X_{CaTs} = 0.030–0.23; X_{Wo} = 0.37–0.44), while the synthetic Shergotty melts of McKay et al. (1986) crystallized Cpx with significant Wo variations but uniformly low CaTs contents (X_{CaTs} = 0.0004–0.044; X_{Wo} = 0.091–0.35) (Fig. 5). Figures 6a and 6b compare the X_{CaTs} and X_{Wo} values for the Cpx from both studies with the Cpx/melt partition coefficients for Ce^{3+} and Yb^{3+}. The data of McKay et al. (1986) show strong correlations among D_{Ce}, D_{Yb}, and X_{CaTs} as well as X_{Wo}, although the correlations involving X_{CaTs} are steeper than those defined by our experiments. The covariation of CaTs and Wo in the experiments of McKay et al. (1986) means that the relative importance of structural changes associated with these two components for incorporation of REE^{3+} into clinopyroxenes with low Ca-contents cannot be resolved.

To gain a clearer understanding of the structural changes that result from the compositional variations observed in our experimentally-produced pyroxenes, site occupancies must be considered. Both Wo and CaTs contain Ca^{2+} in the M2 site, so that the cation fraction of the M2 site occupied by Ca^{2+} provides a better estimate of how that site is changing than simply considering Wo content. Structural changes related specifically to the CaTs component result from the substitution of Al^{3+} for Mg^{2+} in the M1 site, and for Si^{4+} in the T site. We have chosen to use the cation fraction of the T site occupied by Al^{3+} as a measure of these changes.

Figure 7a is a plot of $X_{Al(T)}$ versus REE^{3+} partition coefficients. The strong positive correlations among D_{REE3+} values and $X_{Al(T)}$ are essentially the same as those seen for CaTs (Fig. 3a; Table 4). Figure 7b is a plot of D_{Ce} and D_{Yb} versus $X_{Ca(M2)}$. The experiments in which both Wo and CaTs increase with decreasing SiO_2-saturation of the coexisting melt show an increase in $X_{Ca(M2)}$ from 0.77 to 0.97 (Table 4), and define positive correlations among $X_{Ca(M2)}$ and both D_{Ce} and D_{Yb}. The experiments in which

CaTs increases and Wo decreases all have $X_{Ca(M2)}$ of 0.97. Despite the constant value of $X_{Ca(M2)}$ the values of both D_{Ce} and D_{Yb} continue to increase in these experiments, indicating that structural changes associated with the CaTs component affect REE^{3+} partitioning.

Substitution of Al^{3+} for Mg^{2+} in the M1 site will not promote incorporation of REE^{3+} on the basis of charge balance. The small ionic radius of Al^{3+} relative to Mg^{2+} also leads to smaller M1-O and M2-O bond lengths in CaTs than in diopside (Cameron and Papike, 1981). This could cause an increased preference for the heavy REE relative to the lights, but not to the observed increase in the partition coefficients for both Ce^{3+} and Yb^{3+} with increasing CaTs. This leaves the possibility that the variations in REE^{3+} partitioning are related to structural changes occurring in the T site. Increasing the CaTs component in Cpx with high Ca contents correlates with an increase in the mean T-O distance for T site (Cameron and Papike, 1981). Trivalent REE cannot be incorporated into the pyroxene structure without a charge balance mechanism. The increased T-O distance may facilitate additional substitution of Al^{3+} for Si^{4+}, and thereby promote increased solubility of trace components charge balanced by a Tschermakite-style substitution. The overall effect is to change the activity coefficient associated with a REE-Tschermakite component in Cpx in such a way that as the CaTs content of the pyroxene increases the values of D_{REE3+} also increase.

When determining crystal chemical controls on trace element partitioning it is also important to account for changes in melt structure. In addition to the correlations among CaTs content of the Cpx and D_{REE3+} values already discussed, our data show strong correlations among REE^{3+} partition coefficients and Al_2O_3 in the melt, identical to those observed by Gallahan and Nielsen (1992). It is not immediately clear whether these correlations are related to a reduction in the number of sites suitable for REE^{3+} in the melt or to an increase of $X_{Al(T)}$ in the Cpx with increasing Al_2O_3 in the melt. The results of experimental studies examining REE^{3+} partitioning between immiscible silicate liquids

(Watson, 1976; Ryerson and Hess, 1978; Ellison and Hess, 1989) and of Soret diffusion studies (Lesher, 1986) indicate that decreasing the degree of polymerization of the silicate melt will favor retention of REE^{3+}. Therefore, increasing SiO_2-saturation should lead to an increase in D_{REE3+} values if concomitant changes in the pyroxene structure do not significantly affect partitioning.

The ratio of network formers ($SiO_2 + Al_2O_3$) to network modifiers ($MgO + CaO - 0.5Al_2O_3$) in our experimentally-produced melts increases from 2.02 in BGL5 to 3.48 in EC15. This indicates that the degree of polymerization of the melt is increasing with increasing SiO_2 despite a corresponding decrease in Al_2O_3. Figure 8 compares the variation in the Cpx/melt partition coefficient for Ce^{3+} observed in our experiments (open circles) with those expected solely from variations in melt structure (solid curve) on the basis of the Soret diffusion experiments of Lesher (1986). The affinity of Ce^{3+} for relatively depolymerized melts found in Lesher's experiments indicates that if melt structure alone were controlling the partitioning of REE^{3+}, D_{Ce} should increase by 64% between experiments BGL5 and EC15 (from 0.27 to 0.44). That our experimentally-determined Cpx/melt partition coefficient for Ce^{3+} decreases by 48% (from 0.27 to 0.14) indicates that the effect of changing melt structure on the partitioning of REE^{3+} is overwhelmed by the influence of the concurrent changes in the pyroxene structure. The increase in the abundance of tetrahedrally-coordinated Al^{3+} in the pyroxene represents the dominant crystal-chemical control.

It is possible that changes in melt structure attributable to the addition of FeO and/or alkalis could affect the systematics observed in our experiments. Alkali and alkaline earth cations act to charge balance network-forming AlO_4^{5-} anions in silicate melts (Bottinga and Weill, 1972; Hess, 1980). Although our experimentally-produced melts contain Ca^{2+} in excess of that necessary to charge balance all of the AlO_4^{5-} anions, Hess and Wood (1982) demonstrated that alkaline aluminate species (e.g., $KAlO_2$, $NaAlO_2$) behave differently than AlO_4^{5-} coordinated with alkaline earth cations (e.g., $CaAl_2O_4$,

$MgAl_2O_4$). As alkalis are added to the melt, Al^{3+} is preferentially stabilized as $KAlO_2$ and $NaAlO_2$ relative to $CaAl_2O_4$ species. Alkaline aluminate species form more polymerized melt structures (networks) than $MgAl_2O_4$ or $CaAl_2O_4$ species (sheets and/or chains). Therefore, melts similar in composition to ours that contain several weight percent Na_2O and K_2O (i.e., alkali basalts) might contain fewer sites appropriate for REE^{3+}. This would result in D_{REE3+} values slightly larger than ours for a given Cpx composition. FeO behaves as a network modifier, in the same way as REE^{3+}, and will influence partitioning behavior if it competes successfully for the same sites in the melt. Ellison and Hess (1989) noted that, in general, cations with the same valence state mix nearly ideally in silicate melts. Given this observation it seems likely that REE^{3+} and Fe^{2+} occupy different sites in silicate melts, just as they do in ferromagnesian minerals. Therefore, although the addition of alkalis or FeO to the silicate melt could affect mineral/melt partitioning of REE^{3+}, the structure of the aluminosilicate network, determined by the amount of SiO_2 + Al_2O_3 present, is likely to exert the dominant control on the number of sites suitable for REE^{3+} in the melt.

Changes in melt structure appear to play a subordinate role in controlling REE^{3+} partitioning in basaltic melts. In contrast, the silicate melt model of Toop and Samis (1962) and the Soret diffusion study of Lesher (1986) predict that there should be a dramatic increase in its importance for highly polymerized melts, such as high-silica rhyolites. Further, the partitioning experiments of Green and Pearson (1985) show a steady increase in D_{REE3+} as SiO_2 in the melt increases from ~50 wt% (basalt) to ~69 wt% (rhyodacite) at a constant temperature and pressure. Ryerson and Hess (1978) determined Yb^{3+} partition coefficients for a single Cpx co-existing with immiscible high (74.3 wt%) and low (38.4 wt%) silica melts. The partition coefficient for the highly polymerized melt is larger by nearly a factor of 17. Taken together, these studies suggest an increasing role for melt structure in controlling trace element partitioning with increasing polymerization.

A first order estimate of the relative importance of pyroxene structure versus melt structure on REE partitioning for highly polymerized melts can be obtained by comparing the $X_{Ca(M2)}$ and $X_{Al(T)}$ values for the pyroxenes from our experiments with those for Cpx from the natural high-silica rhyolite samples studied by Sisson (1991). Assuming that the effects of temperature and dissolved volatiles on REE^{3+} partitioning are minor, relatively small D_{REE3+} values (D_{Ce} ~ 0.14–0.17; D_{Yb} ~ 0.24–0.29) would be predicted on the basis of Sisson's Cpx compositions ($X_{Ca(M2)}$ = 0.75-0.85; $X_{Al(T)}$ = 0.007-0.016). The measured partition coefficients are, in fact, larger than these values by approximately a factor of 10 (D_{Ce} = 1.1 – 2.5; D_{Yb} = 1.5 – 2.1). Michael (1988) reported similar Cpx/high-silica rhyolite Ce^{3+} partition coefficients. Given that the increase in D_{REE3+} noted by Green and Pearson (1985) occurs in melts more polymerized than basalts, and that all of our experiments were performed on basalt analogs, it appears that melt structure becomes increasingly important in andesites, dacites and rhyolites. This leads to a gradual reversal of the relative influence of melt structure and pyroxene structure on the partitioning of REE^{3+}, with melt structure exerting the dominant control for extremely polymerized melts.

Predictive Model

In developing a model to predict Cpx/melt partitioning of Ce^{3+} and Yb^{3+} we have chosen to follow the tradition of formulating thermodynamic expressions on the basis of formation and exchange reactions (e.g., Ray et al., 1983; Kinzler et al., 1990; Beckett et al., 1990). This requires solution models for both solid and melt. The effect of temperature on the equilibrium constants (K_{eq}) calculated from our experimental data is negligible. The experiments performed on compositions at the high (EC15) and low (BGL7) SiO_2 ends of the Oliv + Plag + Cpx saturation boundary were at temperatures only 7°C apart (Table 2). Therefore, our data provide a test of the adequacy of various ideal solution models for describing the activity-composition relations for silicate melt and

pyroxene over a broad compositional range. Figure 9 shows the results of K_{eq} calculations for the exchange reaction:

$$(CaMgSi_2O_6)^{Cpx} + (CeO_{1.5})^{L} + (AlO_{1.5})^{L} =$$
$$(CeMgSiAlO_6)^{Cpx} + (CaO)^{L} + (SiO_2)^{L} \qquad (1)$$

using various ideal solution models for pyroxene and silicate melt in a plot of SiO_2 in the silicate melt versus Ln K_{eq}. The equilibrium constants in Fig. 9a were calculated using a molecular mixing model for Cpx, in which the activity of each component is equal to its mole fraction. The activity of components in the silicate melt were calculated using four different ideal solution models: (1) an oxide model, in which the activity of each oxide is equal to its mole fraction (circles), (2) a similar model using the components proposed by Bottinga and Weill (1972) (squares), (3) the two-lattice model used by Ray et. al. (1983), which employs Bottinga-Weill components (octagons), and (4) the two-lattice model of Nielsen (1985) (triangles). Because temperature variation is negligible, there should be little or no variation in Ln K_{eq} if the pyroxene and melt behave as ideal solutions. The calculations show large variations in Ln K_{eq} for each ideal solution model. Fig. 9b is a second plot of SiO_2 in the silicate melt versus Ln K_{eq}. In this case, an ionic solution model was employed for the Cpx in which the activity-composition relations for each component are derived using the expression for the ideal entropy of mixing (Temkin, 1945). Use of this solution model for Cpx results in Ln K_{eq} values that are systematically lower than those obtained using the molecular mixing model, but significant variations in Ln K_{eq} still exist.

The failure of the ideal solution models necessitates formulation of a non-ideal model for the melt and/or pyroxene. We have chosen to model non-ideality using semi-empirical terms that resemble binary symmetric Margules parameters (e.g., Thompson, 1967). This simplified approach minimizes the number of binary interaction parameters and assumes that higher order interaction terms are negligible. Stepwise multiple linear

regressions involving the pseudo-binary interaction terms for each component were used to determine the parameters that best model the non-ideality in melt and pyroxene solutions. The silicate melt components of Bottinga and Weill (1972) were found to provide a better model of melt activity than oxide components. A molecular mixing model using end-member pyroxene components provides an adequate model for the pyroxene. Use of an ionic solution model for the pyroxene did not significantly improve our modeling results, and made recovery of molar partition coefficients more difficult. The inclusion of a temperature term in our expressions did not improve the results.

The results of our modeling of exchange reactions similar to Eqn. 1 are given in Table 5. In addition to our experimental data, we have incorporated the experiments of Hart and Dunn (1993), Hauri et al. (1994), and Johnson (1994 and unpublished data) into the calibration of the model. These experiments contain both Ce^{3+} and Yb^{3+} at natural (i.e., undoped) concentration levels, and provide complete major element analyses of both glass and clinopyroxene. They were conducted using natural basalt starting materials at conditions relevant to the upper mantle (0.8–3.0 GPa; 1245–1430°C), extending the calibration of our model. Expressions involving excess free energy terms for $CaAl_2O_4$, CaO and MgO in the silicate melt and CaTs in the pyroxene (Table 5) were found to recover the data with mean uncertainties (1σ) of 11% relative for Ce^{3+} and 12% relative for Yb^{3+} (Fig. 10).

To test the predictive capability of the model, we calculated Ce^{3+} and Yb^{3+} partition coefficients for 5 of Johnson's experiments using a calibration of the model from which they were excluded. Johnson's data set was designed to explore partitioning over a range of upper mantle conditions (0.8 to 2.5 GPa; 1245 to 1390°C). The model predicted the partitioning of Ce^{3+} with a mean uncertainty of 16%, and of Yb^{3+} with a mean uncertainty of 21% (1σ). Uncertainty in ion probe analyses of REE at natural concentration levels are typically ±10–15% relative for light REE and ±10–20% relative for heavy REE (Johnson et al., 1990), leading to 1σ uncertainties in calculated partition

coefficients of ±14-28% relative, similar to the uncertainties in our model predictions. The inclusion of all of Johnson's data in the calibration of the model presented in Table 5 doubles the number of natural-system experiments in our database, and should provide even better predictive capability. We recommend that application of the expressions be limited to basaltic melt compositions and high-Ca clinopyroxenes (i.e., excluding pigeonite).

By performing experiments in the CMAS system we were able to explore a wide range of melt compositions over a small temperature range, but the influence on REE^{3+} partitioning of some of the components present in natural basalts could not be determined. The incorporation of Fe^{3+} into the T site may provide an additional mechanism for charge balancing trivalent cations incorporated into the M2 site, leading to REE^{3+} partition coefficients for Cpx containing Fe that are slightly larger than those determined in the CMAS system. Similarly, the incorporation of Na^{1+} cations into the pyroxene structure allows the coupled substitution:

$$(Na^{1+})^{M2} + (REE^{3+})^{M2} = 2\,(Ca^{2+})^{M2} \qquad (2)$$

that could provide the necessary charge balance without replacing Si^{4+} in the T site with Al^{3+} or Fe^{3+}. This could also lead to larger D_{REE3+} values in natural systems than those determined in CMAS. The presence of H_2O could affect REE partitioning through substitutions similar to Equation 2 involving H^+ cations, as well as through its dramatic depolymerizing effect on silicate melt structure (e.g., Stolper, 1982), although the magnitude of these effects is largely unknown. Our model successfully predicts partitioning for anhydrous, natural systems in which charge balance involving Na^{1+} and Fe^{3+} is possible, indicating that a coupled substitution involving Al^{3+} in the T site is the most important mechanism by which REE^{3+} are incorporated into Cpx. Further, the ability of the model to predict partitioning over a wide range of conditions (0.0001 to 3.0 GPa; 1234 to 1430°C) without terms that take the effects of pressure and temperature into

account indicates that compositional dependencies successfully account for the effects of these other variables. Knowledge of the composition of the coexisting Cpx and melt is adequate to predict the partitioning behavior of REE^{3+}.

CONCLUSIONS

Experiments performed in the CMAS system demonstrate that changes in the compositions of co-existing Cpx and basaltic melt can cause REE^{3+} partition coefficients to vary by at least a factor of two to three. Strong positive correlations among the Ca-Tschermakite content of the clinopyroxene and Cpx/melt partition coefficients for the REE^{3+} reflect the importance of a Tschermakite-style coupled substitution for the incorporation of REE^{3+} into the pyroxene structure. Variations in the percentage of tetrahedrally-coordinated Al^{3+} can influence REE^{3+} partitioning without concurrent variations in the percentage of the M2 site occupied by Ca^{2+}. This may result from an expansion of the T site associated with increased CaTs component enhancing the solubility of trace elements charge balanced by a Tschermakite-style substitution. The effects of pyroxene structure on REE^{3+} partitioning dominate those attributable to melt structure for basaltic compositions. Knowledge of the compositional dependencies of REE^{3+} partitioning are adequate to account for the effects of variable pressure and temperature.

REFERENCES

Beattie P. (1993) On the occurrence of apparent non-Henry's Law behavior in experimental partitioning studies. *Geochim. Cosmochim. Acta* **57**, 47-55.

Beckett J.R., Spivack A.J., Hutcheon I.D., Wasserburg G.J., and Stolper E.M. (1990) Crystal chemical effects on the partitioning of trace elements between mineral and melt: An experimental study of melilite with applications to refractory inclusions from carbonaceous chondrites. *Geochim. Cosmochim. Acta* **54**, 1755-1774.

Biggar G.M. (1972) Diopside, lithium metasilicate and the 1968 temperature scale. *Mineral. Mag.* **38**, 768-770.

Bottinga Y. and Weill D.F. (1972) The viscosity of magmatic silicate liquids: A model for calculation. *Am. J. Sci.* **272**, 438-475.

Cameron M. and Papike J.J. (1981) Structural and chemical variations in pyroxenes. *Am. Mineral.* **66**, 1-50.

Colson R.O., McKay G.A., and Taylor L.A. (1989) Charge balancing of trivalent trace elements in olivine and low-Ca pyroxene: A test using experimental partitioning data. *Geochim. Cosmochim. Acta* **53**, 643-648.

Drake M.J. and Weill D.F. (1972) New rare earth element standards for electron microprobe analysis. *Chem. Geol.* **10**, 179-181.

Ellison A.J.G. and Hess P.C. (1989) Solution properties of rare earth elements: inferences from immiscible liquids. *Geochim. Cosmochim. Acta* **53**, 1965-1974.

Gaetani G.A. and Grove T.L. (1991) Partitioning of Ce and Yb between pyroxene and basaltic to andesitic melts: influence of mineral chemistry vs. melt structure. EOS **72**, 547-548 (abstr.).

Gallahan W.E. and Nielsen R.L. (1992) The partitioning of Sc, Y, and the rare earth elements between high-Ca clinopyroxene and natural mafic to intermediate lavas at 1 atmosphere. *Geochim. Cosmochim. Acta* **56**, 2387-2404.

Green T.H. and Pearson N.J. (1985) Rare earth element partitioning between clinopyroxene and silicate liquid at moderate to high pressure. *Contrib. Mineral. Petrol.* **91**, 24-36.

Grutzeck M., Kridelbaugh S., and Weill D. (1974) The distribution of Sr and REE between diopside and silicate liquid. *Geophys. Res. Lett.* **1**, 273-275.

Harrison W.J. and Wood B.J. (1980) An experimental investigation of the partitioning of REE between garnet and liquid with reference to the role of defect equilibria. *Contrib. Mineral. Petrol.* **72**, 145-155.

Hart S.R. and Dunn T. (1993) Experimental cpx/melt partitioning of 24 trace elements. *Contrib. Mineral. Petrol.* **113**, 1-8.

Hauri E.H., Wagner T.P., and Grove T.L. (1994) Experimental and natural partitioning of Th, U, Pb and other trace elements between garnet, clinopyroxene and basaltic melts. *Chem.Geol* **117**, 149-166.

Hess P.C. (1980) Polymerization model for silicate melts. In *Physics of Magmatic Processes* (ed. R.B. Hargraves), Chap. 1, pp. 3-48. Princeton University Press.

Hess P.C. and Wood M.I. (1982) Aluminum coordination in metaaluminous and peralkaline silicate melts. *Contrib. Mineral. Petrol.* **81**, 103-112.

Johnson K.T.M. (1994) Experimental cpx/ and garnet/melt partitioning of REE and other trace elements at high pressures: Petrogenetic implications. *Mineral. Mag.* 58A, 454-455 (extended abstr.).

Johnson K.T.M., Dick H.J.B., and Shimizu N. (1990) Melting in the oceanic upper mantle: an ion microprobe study of diopsides in abyssal peridotites. *J. Geophys. Res.* **95**, 2661-2678.

Kinzler R.J., Grove T.L., and Recca S.I. (1990) An experimental study on the effect of temperature and melt composition on the partitioning of nickel between olivine and silicate melt. *Geochim. Cosmochim. Acta* **54**, 1255-1265.

Lesher C.E. (1986) Effects of silicate liquid composition on mineral-liquid element partitioning from soret diffusion studies. *J. Geophys. Res.* **91**, 6123-6141.

Libourel G., Boivin P., and Biggar G.M. (1989) The univariant curve liquid = forsterite + anorthite + diopside in the system CMAS at 1 bar: solid solutions and melt structure. *Contrib. Mineral. Petrol.* **102**, 406-421.

McKay G., Wagstaff J., and Yang S.-R. (1986) Clinopyroxene REE distribution coefficients for Shergottites: the REE content of the Shergotty melt. *Geochim. Cosmochim. Acta* **50**, 927-937.

Michael P.J. (1988) Partition coefficients for rare earth elements in mafic minerals of high-SiO_2 rhyolites: the importance of accessory mineral inclusions. *Geochim. Cosmochim. Acta* **52**, 275-282.

Mysen B.O. (1978) Limits of solution of trace elements in minerals according to Henry's Law: review of experimental data. *Geochim. Cosmochim. Acta* **42**, 871-885.

Mysen B.O. (1979) Nickel partitioning between olivine and silicate melt: Henry's law revisited. *Amer. Mineral.* **64**, 1107-1114.

Nicholls I.A. and Harris K.L. (1980) Experimental rare earth element partition coefficients for garnet, clinopyroxene and amphibole coexisting with andesitic and basaltic liquids. *Geochim. Cosmochim. Acta* **44** 287-308.

Nielsen R.L. (1985) A method for the elimination of the compositional dependence of trace element distribution coefficients. *Geochim. Cosmochim. Acta* **49**, 1775-1779.

Onuma N., Higuchi H., Wakita H., and Nagasawa H. (1968) Trace element partition between two pyroxenes and the host lava. *Earth Planet. Sci. Lett.* **5**, 47-51.

Ray G.L., Shimizu N., and Hart S.R. (1983) An ion microprobe study of the partitioning of trace elements between clinopyroxene and liquid in the system diopside-albite-anorthite. *Geochim. Cosmochim. Acta* **47**, 2131-2140.

Ryerson F.J. and Hess P.C. (1978) Implications of liquid-liquid distribution coefficients to mineral-liquid partitioning. *Geochim. Cosmochim. Acta* **42**, 921-932.

Sisson T.W. (1991) Pyroxene-high silica rhyolite trace element partition coefficients measured by ion microprobe. *Geochim. Cosmochim. Acta* **55**, 1575-1585.

Stolper E.M. (1982) The speciation of water in silicate melts. *Geochim. Cosmochim. Acta* **46**, 2609-2620.

Temkin M. (1945) Mixtures of fused salts as ionic solutions. *Acta Physicochim. U.R.S.S.* **20**, 411-420.

Thompson J.B. Jr. (1967) Thermodynamic properties of simple solutions. In *Researches in Geochemistry,* (ed. P.H. Ableson), Vol. 2, pp. 340-361. Wiley and Sons.

Toop G.W. and Samis C.S. (1962) Activities of ions in silicate melts. *Trans. Metall. Soc. AIME* **224**, 878-887.

Watson E.B. (1976) Two-liquid partition coefficients: experimental data and geochemical implications. *Contrib. Mineral. Petrol.* **56**, 119-134.

Watson E.B. (1985) Henry's law behavior in simple systems and in magmas: Criteria for discerning concentration-dependent partition coefficients in nature. *Geochim. Cosmochim. Acta* **49**, 917-923.

Table 1. Electron microprobe analyses of starting materials.

	EC	MS	SB	SU	BGL
n	27	10	70	10	10
SiO_2	53.4(4)	51.5(4)	48.3(4)	45.9(3)	43.8(2)
Al_2O_3	16.3(1)	16.6(1)	16.3(1)	17.2(1)	17.5(1)
MgO	13.2(1)	13.6(1)	11.9(1)	12.6(0)	12.2(0)
CaO	16.8(1)	17.4(1)	23.0(3)	24.1(1)	26.4(1)
Ce_2O_3	0.32(1)	0.31(1)	0.33(2)	0.34(2)	0.36(1)
Yb_2O_3	0.29(1)	0.30(1)	0.29(2)	0.32(1)	0.33(1)
Total	100.31	99.71	100.12	100.46	100.59

Units on parentheses represent one standard deviation of least units cited, on the basis of replicate analyses. Therefore, 53.4(4) should be read as 53.4 ± 0.4. n = number of analyses.

Table 2. Experimental conditions and phase assemblages.

Experiment no.	T (°C)	log f_{O_2}	Duration (hr)	Run Products	Phase Proportions (wt %)
Synthesis Experiments					
EC15	1241	-8.23	240	Gl,Cpx,Plag,Oliv	75 : 12 : 11 : 2
MS5	1246	-8.32	215	Gl,Cpx,Plag,Oliv	78 : 7 : 11 : 4
SB28	1265	-8.13	264	Gl,Cpx,Plag	76 : 14 : 10
SB24	1264	-7.82	24	Gl,Cpx,Plag	63 : 22 : 15
SU4	1249	-8.19	24	Gl,Cpx,Plag,Oliv	87 : 4 : 7 : 2
SU5	1249	-8.11	216	Gl,Cpx,Plag,Oliv	70 : 14 : 13 : 3
SU7	1247	-8.40	240	Gl,Cpx,Plag,Oliv	80 : 8 : 9 : 3
BGL5	1240	-8.45	216	Gl,Cpx,Plag,Oliv	95 : 1 : 3 : 1
BGL7	1234	-8.28	241	Gl,Cpx,Plag,Oliv	93 : 2 : 3 : 2
Reversal Experiment					
REV9	1236	-8.26	216	Gl,Cpx,Plag,Oliv	

Letters in experiment no. represent starting compositions given in Table 1. Abbreviations are Gl = glass; Cpx = high-Ca clinopyroxene; Plag = plagioclase; Oliv = olivine.

Table 3. Electron microprobe analyses of experimental run products.

Experiment no.	T (°C)	Phase	SiO_2	Al_2O_3	MgO	CaO	Ce_2O_3	Yb_2O_3	Total
Synthesis Experiments									
EC15	1241	Gl	54.5(4)	16.3(3)	12.4(2)	16.1(2)	0.43(1)	0.37(1)	100.10
		Cpx	55.3(4)	1.5(3)	22.9(5)	20.6(7)	0.062(8)	0.09(2)	100.45
MS5	1246	Gl	53.1(4)	16.1(2)	12.8(1)	17.51(3)	0.405(9)	0.34(1)	100.26
		Cpx	54.8(6)	2.1(3)	20.9(4)	22.3(2)	0.07(1)	0.10(1)	100.27
SB28	1265	Gl	48.0(3)	16.15(8)	12.24(6)	22.85(5)	0.386(8)	0.34(1)	99.97
		Cpx	53.4(5)	3.4(4)	18.6(3)	24.9(1)	0.072(5)	0.095(9)	100.47
SB24	1264	Gl	48.0(2)	16.32(9)	12.37(5)	22.86(5)	0.497(5)	0.44(1)	100.49
		Cpx	52.9(3)	4.2(3)	18.3(2)	24.65(7)	0.09(1)	0.13(3)	100.27
SU4	1249	Gl	45.5(1)	16.62(3)	12.19(4)	24.64(6)	0.453(6)	0.36(1)	99.76
		Cpx	51.5(4)	6.1(6)	16.7(3)	25.2(1)	0.10(1)	0.13(1)	99.73
SU5	1249	Gl	45.2(3)	16.76(4)	12.14(3)	25.38(4)	0.472(7)	0.415(9)	100.37
		Cpx	51.7(4)	6.5(7)	16.7(2)	25.5(2)	0.09(2)	0.17(2)	100.66
SU7	1247	Gl	45.4(4)	16.7(1)	11.95(8)	25.13(9)	0.500(8)	0.44(2)	100.12
		Cpx	51.5(4)	6.9(6)	16.5(1)	24.9(2)	0.10(2)	0.18(4)	100.08
BGL5	1240	Gl	43.6(2)	17.18(5)	11.88(2)	26.87(6)	0.373(4)	0.377(8)	100.28
		Cpx	49.9(5)	9.4(8)	15.6(3)	25.4(1)	0.10(2)	0.18(2)	100.58
BGL7	1234	Gl	43.4(1)	17.40(7)	11.38(2)	26.99(9)	0.423(4)	0.40(1)	99.99
		Cpx	48.9(4)	10.9(4)	14.8(2)	25.1(2)	0.112(8)	0.26(2)	100.07
Reversal Experiment									
REV9	1236	Gl	54.5(3)	16.3(1)	12.49(8)	16.23(5)	0.365(5)	0.30(1)	100.19
		Cpx	55.6(4)	1.4(3)	22.8(5)	20.6(4)	0.06(1)	0.08(2)	100.54

Each reported analysis represents the mean of 10 spot analyses. Units in parentheses as in Table 1. Abbreviations as in Table 2.

Table 4. Experimentally-determined high-Ca clinopyroxene/melt partition coefficients for Ce and Yb.

Experiment	T (°C)	X_{CaTs}	X_{Wo}	$X_{Al(T)}$	$X_{Ca(M2)}$	$D_{Ce}^{Cpx/Gl}$	$D_{Yb}^{Cpx/Gl}$
Synthesis Experiments							
EC15	1241	0.030	0.37	0.016	0.77	0.14(1)	0.24(3)
MS5	1246	0.043	0.40	0.023	0.85	0.17(2)	0.29(2)
SB28	1265	0.070	0.44	0.037	0.94	0.187(8)	0.28(2)
SB24	1264	0.087	0.43	0.045	0.93	0.18(1)	0.30(4)
SU4	1249	0.13	0.42	0.066	0.97	0.22(1)	0.36(2)
SU5	1249	0.14	0.42	0.070	0.97	0.19(1)	0.41(3)
SU7	1247	0.15	0.41	0.074	0.97	0.20(2)	0.41(3)
BGL5	1240	0.20	0.39	0.10	0.97	0.27(4)	0.48(3)
BGL7	1234	0.23	0.37	0.12	0.97	0.27(1)	0.65(3)
Reversal Experiment							
REV9	1236	0.028	0.37	0.015	0.77	0.16(2)	0.27(4)

Units in parentheses represent 2σ uncertainties calculated by propogating the standard deviation of the mean. Therefore, 0.030(8) should be read as 0.030 ± 0.008. $X_{Al(T)} = Al^T/(Al^T + Si^T)$ in cations on a 6 oxygen basis; $X_{Ca(M2)} = Ca^{M2}/(Ca^{M2} + Mg^{M2})$ in cations on a 6 oxygen basis.

Table 5. Regression Results and Predictive Expressions for Cpx/melt partitioning of Ce^{3+} and Yb^{3+}.

Ce-Tschermakite Exchange Reaction:

$$(Ca(Mg,Fe)Si_2O_6)^{Cpx} + (CeO_{1.5})^{Liq} + 0.5(CaAl_2O_4)^{Liq} = (Ce(Mg,Fe)AlSiO_6)^{Cpx} + 1.5(CaO)^{Liq} + (SiO_2)^{Liq}$$

$$K_{eq} = \frac{X_{CeTs}^{Cpx} \bullet (X_{CaO}^{Liq})^{1.5} \bullet X_{SiO_2}^{Liq}}{X_{Di+Hed}^{Cpx} \bullet X_{CeO_{1.5}}^{Liq} \bullet \sqrt{X_{CaAl_2O_4}^{Liq}}}$$

$$LnK_{eq} = -1.39 + 15.88(1 - X_{CaAl_2O_4}^{Liq})^2 - 11.29(1 - X_{MgO}^{Liq})^2 - 6.47(1 - X_{CaO}^{Liq})^2 - 2.60(1 - X_{CaTs}^{Cpx})^2$$

$$r^2 = 0.9788$$

$$D_{Ce}^{Cpx/L} = \frac{X_{Di+Hed}^{Cpx} \bullet \sqrt{X_{CaAl_2O_4}^{Liq}}}{(X_{CaO}^{Liq})^{1.5} \bullet X_{SiO_2}^{Liq}} \bullet \exp[-1.39 + 15.88(1 - X_{CaAl_2O_4}^{Liq})^2 - 11.29(1 - X_{MgO}^{Liq})^2 - 6.47(1 - X_{CaO}^{Liq})^2 - 2.60(1 - X_{CaTs}^{Cpx})^2]$$

Yb-Tschermakite Exchange Reaction:

$$(Ca(Mg,Fe)Si_2O_6)^{Cpx} + (YbO_{1.5})^{Liq} + 0.5(CaAl_2O_4)^{Liq} = (Yb(Mg,Fe)AlSiO_6)^{Cpx} + 1.5(CaO)^{Liq} + (SiO_2)^{Liq}$$

$$K_{eq} = \frac{X_{YbTs}^{Cpx} \bullet (X_{CaO}^{Liq})^{1.5} \bullet X_{SiO_2}^{Liq}}{X_{Di+Hed}^{Cpx} \bullet X_{YbO_{1.5}}^{Liq} \bullet \sqrt{X_{CaAl_2O_4}^{Liq}}}$$

$$LnK_{eq} = -4.06 + 14.91(1 - X_{CaAl_2O_4}^{Liq})^2 - 5.95(1 - X_{MgO}^{Liq})^2 - 4.22(1 - X_{CaO}^{Liq})^2 - 3.77(1 - X_{CaTs}^{Cpx})^2$$

$$r^2 = 0.9183$$

$$D_{Yb}^{Cpx/L} = \frac{X_{Di+Hed}^{Cpx} \bullet \sqrt{X_{CaAl_2O_4}^{Liq}}}{(X_{CaO}^{Liq})^{1.5} \bullet X_{SiO_2}^{Liq}} \bullet \exp[-4.06 + 14.91(1 - X_{CaAl_2O_4}^{Liq})^2 - 5.95(1 - X_{MgO}^{Liq})^2 - 4.22(1 - X_{CaO}^{Liq})^2 - 3.77(1 - X_{CaTs}^{Cpx})^2]$$

X_i^j is mole fraction of component i in phase j.

FIGURE CAPTIONS

Figure 1. Plot of SiO_2 versus MgO (squares), Al_2O_3 (circle), and CaO (triangles) for experimentally-produced silicate melts on or near the Oliv + Plag + Cpx saturation boundary in the CMAS system.

Figure 2. Ternary diagram showing experimentally-produced high-Ca clinopyroxene compositions recalculated into En ($Mg_2Si_2O_6$), Wo ($Ca_2Si_2O_6$) and CaTs ($CaAlSiAlO_6$) components. Circles represent synthesis experiments; square represents reversal experiment. Arrow indicates direction corresponding to decreasing SiO_2 in the co-existing silicate melt.

Figure 3. (a) Plot of CaTs content of experimentally-produced clinopyroxene versus clinopyroxene/melt partition coefficients for Ce^{3+} (filled symbols) and Yb^{3+} (open symbols) demonstrating the strong positive correlations between CaTs and REE^{3+} partition coefficients. Circles represent synthesis experiments; squares represent reversal experiment. Dotted lines connect partition coefficients and CaTs contents at beginning and end of reversal experiment. (b) Plot of Wo content of experimentally-produced clinopyroxene versus clinopyroxene/melt partition coefficients for Ce^{3+} (filled circles) and Yb^{3+} (open circles) demonstrating the lack of a dependence of REE^{3+} partitioning on Wo content. Dashed arrow indicates increasing CaTs component in the clinopyroxene. Error bars are 2σ.

Figure 4. Back-scattered electron image of reversal experiment REV9 showing clinopyroxene grains with high-Al cores (light zones) and low-Al rims (darker zones) surrounded by glass, olivine (very dark grains), and plagioclase (grains slightly darker than the glass). Brightness is proportional to the mean atomic number of each phase. Scale bar is 10 μm

Figure 5. Comparison of the CaTs and Wo contents of experimentally-produced clinopyroxenes from this study (open squares) with those from McKay et al. (1986) (open circles).

Figure 6. Comparison of variations in cpx/melt partition coefficients for Ce^{3+} (filled symbols) and Yb^{3+} (open symbols) as a function of (a) CaTs and (b) Wo content for the clinopyroxenes from this study (squares) and those of McKay et al. (1986) (circles).

Figure 7. (a) Correlations among the cation fraction of Al^{3+} in the tetrahedral site of experimentally-produced clinopyroxene and clinopyroxene/melt partition coefficients for Ce^{3+} (filled circles) and Yb^{3+} (open circles). (b) The cation fraction of Ca^{2+} in the 6-8 coordinated M2 site in experimentally-produced clinopyroxene versus clinopyroxene/melt partition coefficients for Ce^{3+} (filled circles) and Yb^{3+} (open circles). Dashed arrow indicates increasing tetrahedrally-coordinated Al^{3+} in the clinopyroxene. Error bars are 2σ

.

Figure 8. Plot of M_f^{Ce} versus % network formers in the silicate melt comparing the predicted effect of variations in melt structure clinopyroxene/melt partitioning of Ce^{3+} (solid curve) (Lesher, 1986), with the variations observed in our experiments (open circles).

Figure 9. Plot of SiO_2 in silicate melt versus Ln K_{eq} for diopside/Ce-Tschermakite exchange reaction (Eqn. 1) using ideal solution models: (a) molecular mixing and (b) ionic solution models for Cpx. Ideal solution models for the silicate melt are oxide components (circles), the components of Bottinga and Weill (1972) (squares), the two-lattice model of Ray et al. (1983) (octagons), and the two-lattice model of Nielsen (1985) (triangles).

Figure 10. Plot of experimentally-determined partition coefficients for Ce^{3+} (filled symbols) and Yb^{3+} (open symbols) used in the calibration of our predictive model versus

values predicted using the expressions given in Table 5 and the conversion factor given by Eq 2. Circles are data from this study; squares are data from Hart and Dunn (1993), Hauri et al. (1994), and Johnson (1994 and unpublished data).

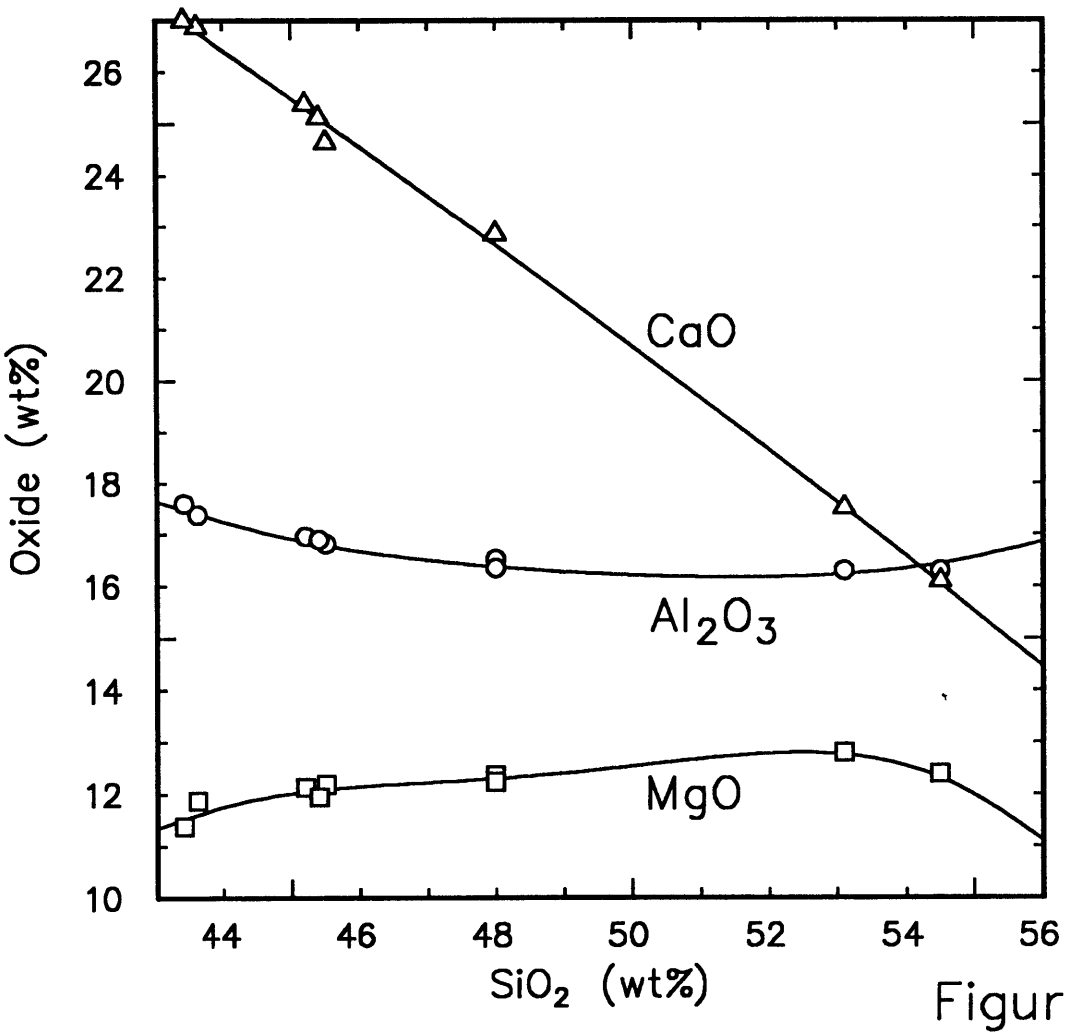
26
24
22
20
18
16
14
12
10
Oxide (wt%)
CaO
Al2O3
MgO
44
46
48
50
52
54
56
SiO2 (wt%)

Figure 1

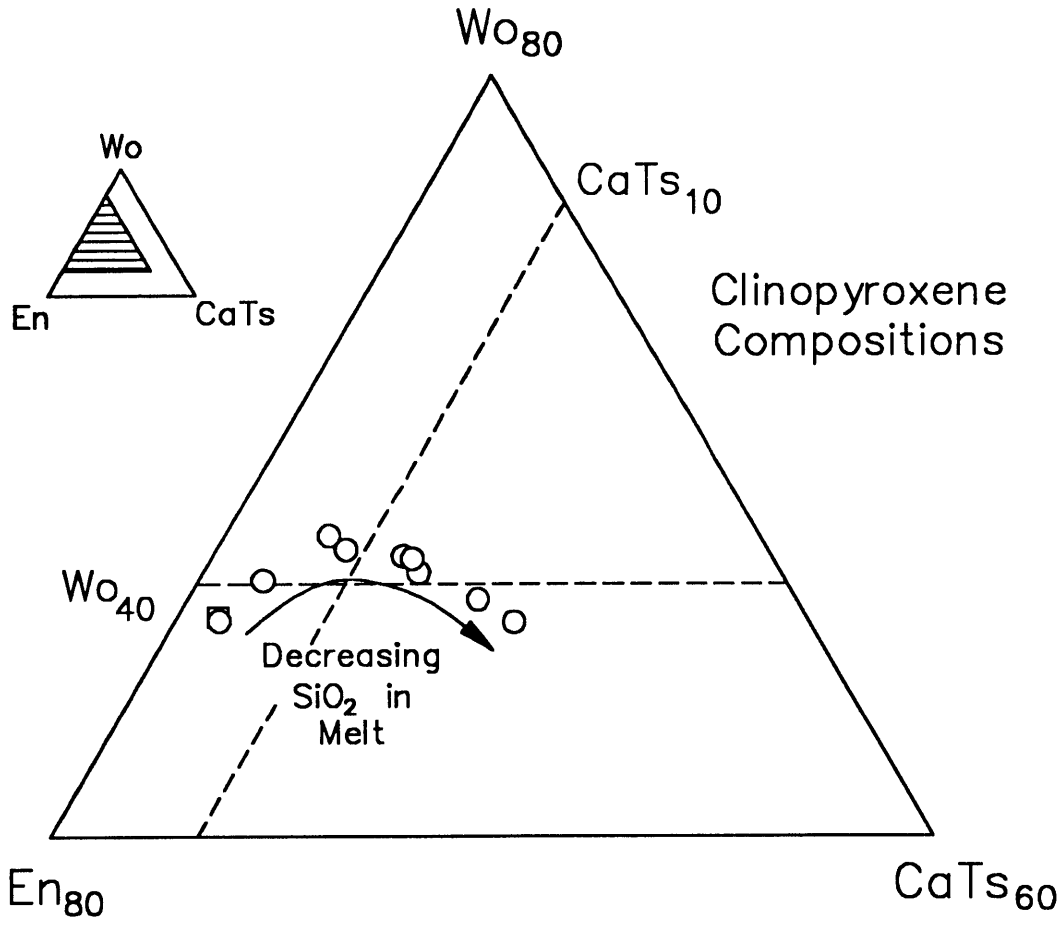
Wo
En
CaTs
Wo80
CaTs10
Clinopyroxene
Compositions
Wo40
Decreasing
SiO2 in
Melt
En80
CaTs60

Figure 2

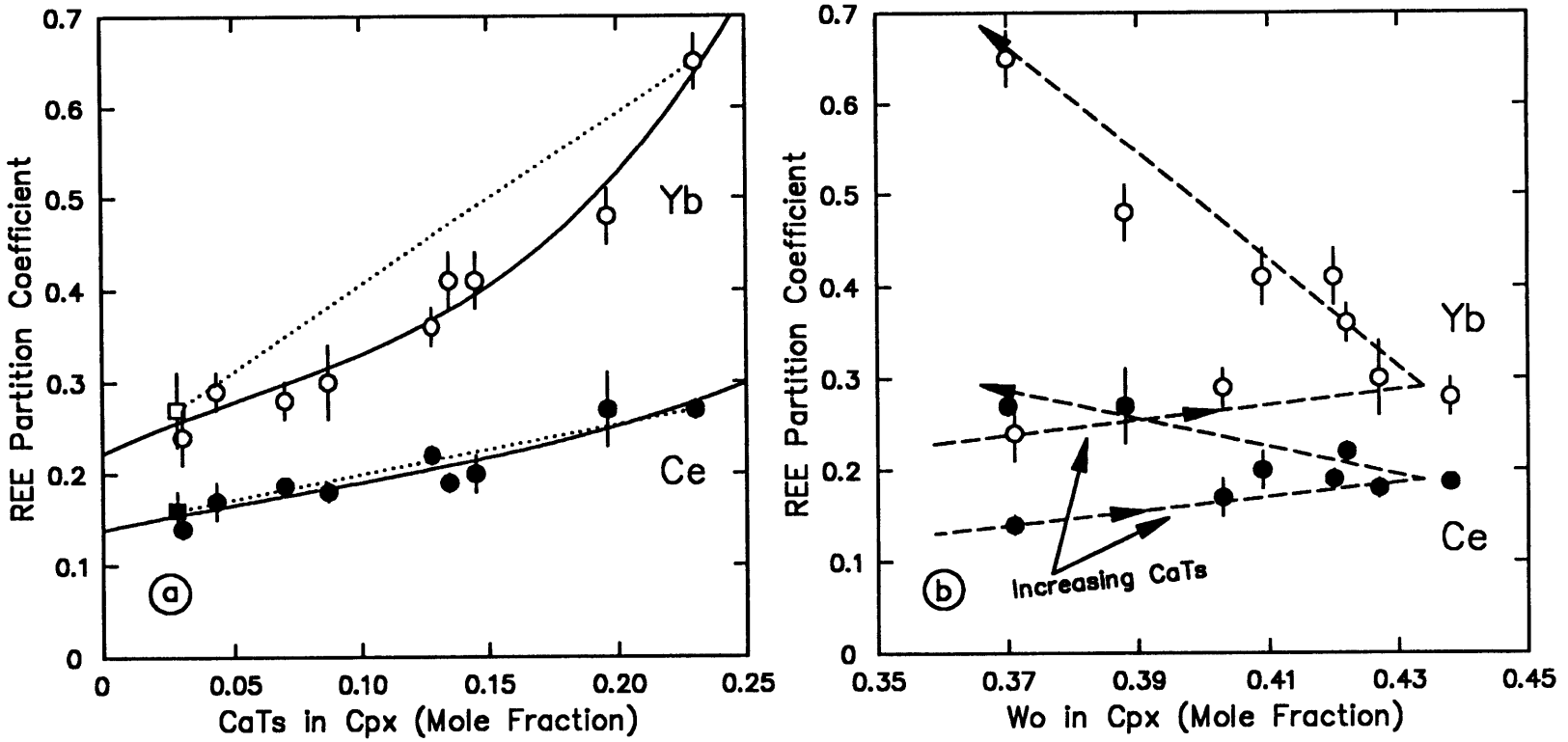
REE Partition Coefficient
0.7
0.6
0.5
0.4
0.3
0.2
0.1
0
Yb
Ce
a
0
0.05
0.10
0.15
0.20
0.25
CaTs in Cpx (Mole Fraction)
REE Partition Coefficient
Yb
Ce
b
Increasing CaTs
0.35
0.37
0.39
0.41
0.43
0.45
Wo in Cpx (Mole Fraction)

Figure 3

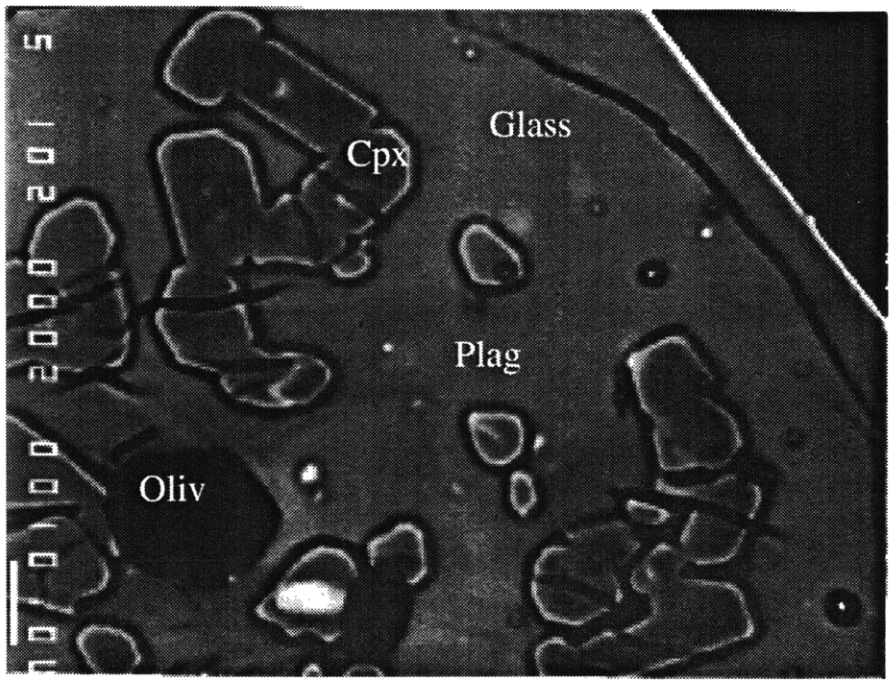

Figure 4

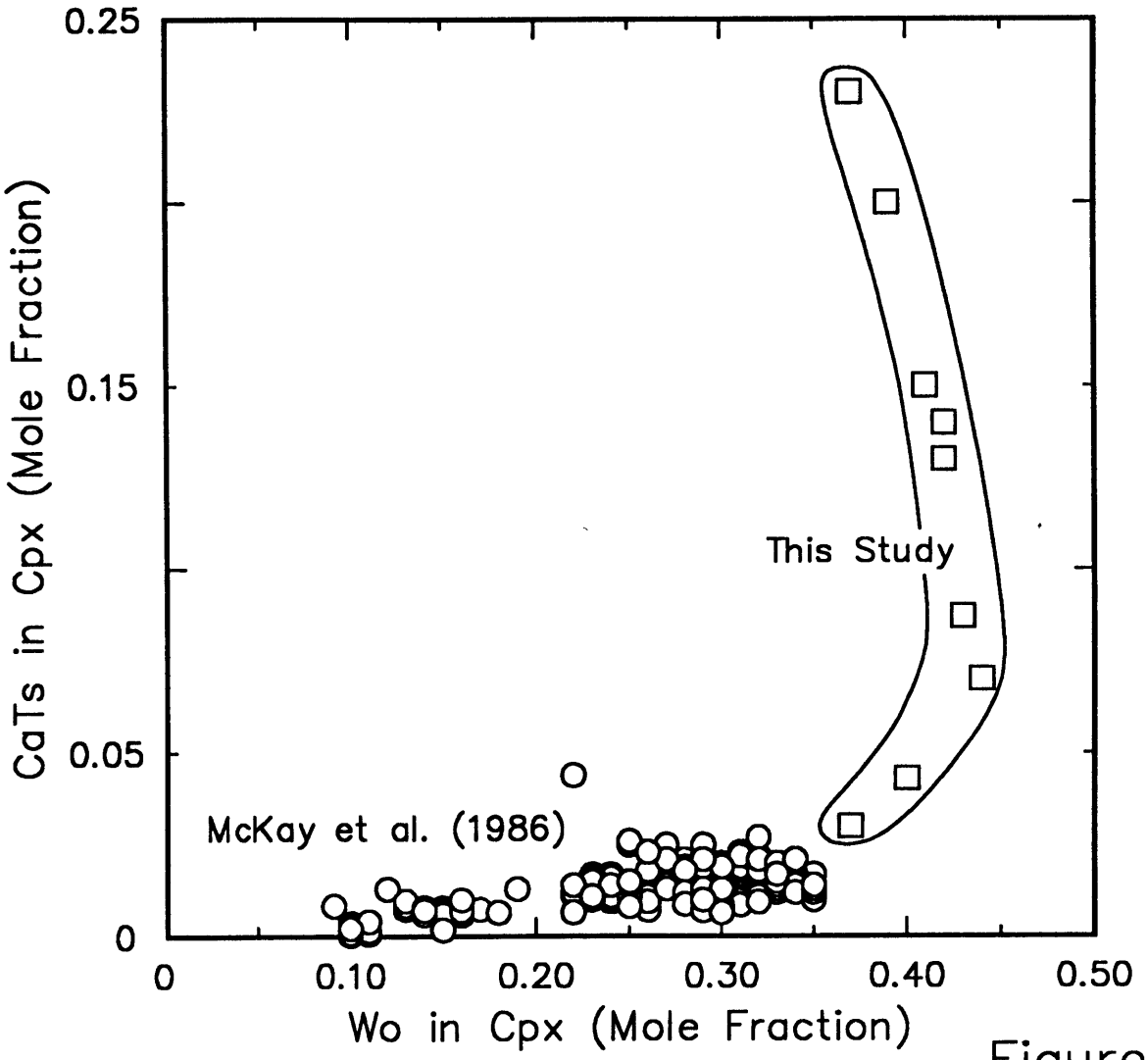
0.25
0.15
0.05
0
CaTs in Cpx (Mole Fraction)
This Study
McKay et al. (1986)
0
0.10
0.20
0.30
0.40
0.50
Wo in Cpx (Mole Fraction)

Figure 5

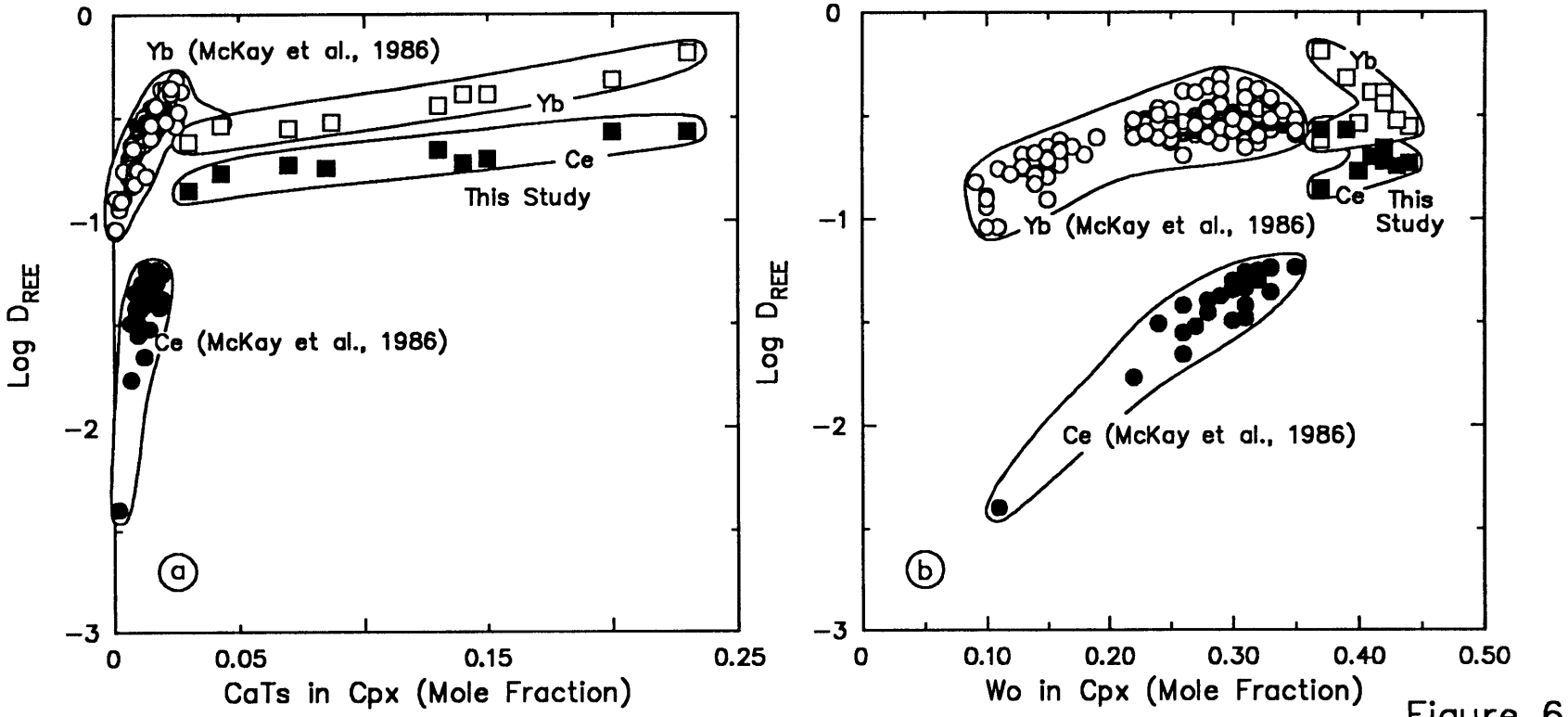
Yb (McKay et al., 1986)
Yb
Ce
This Study
Ce (McKay et al., 1986)
Log D_{REE}
CaTs in Cpx (Mole Fraction)
Yb
Ce
This Study
Yb (McKay et al., 1986)
Ce (McKay et al., 1986)
Wo in Cpx (Mole Fraction)

Figure 6

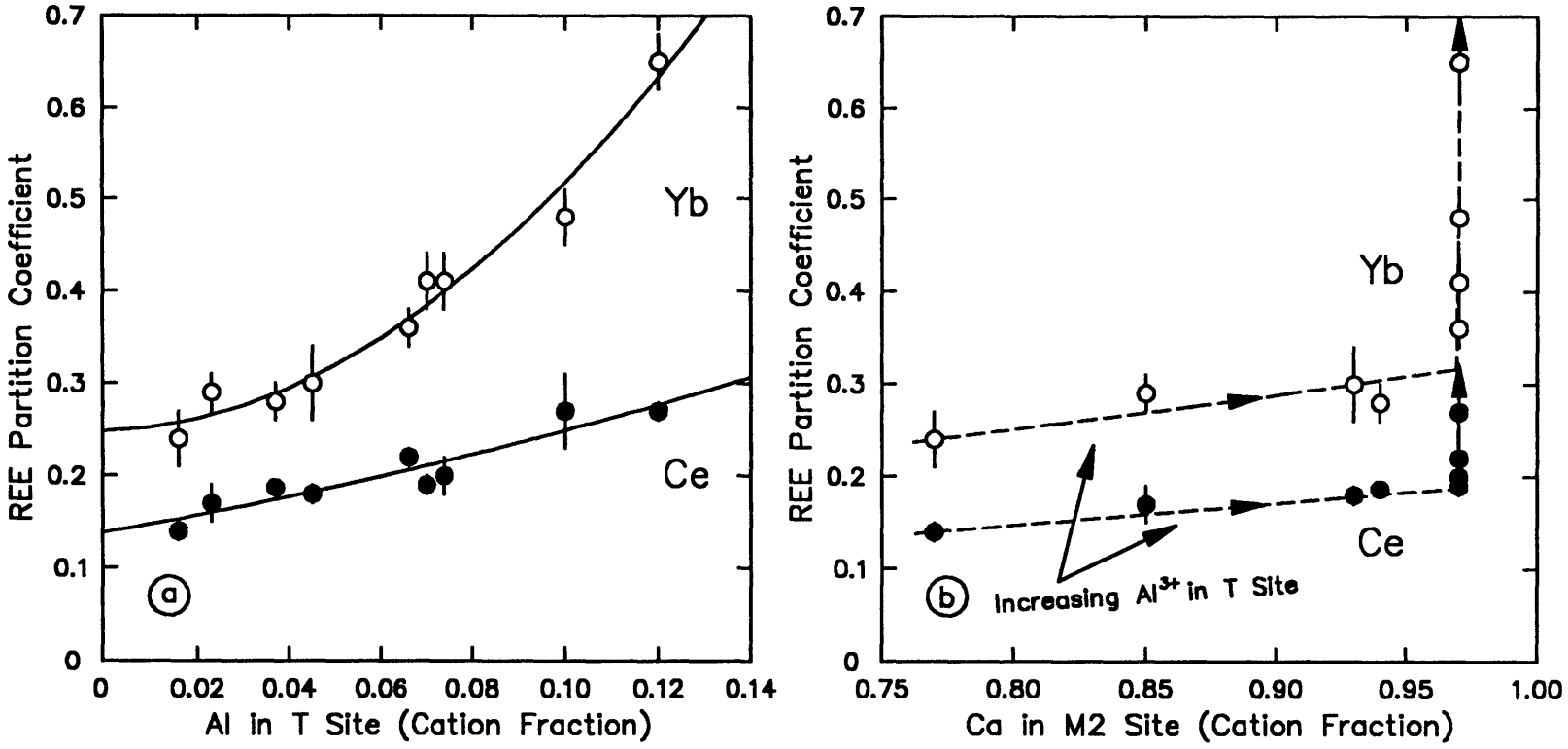
REE Partition Coefficient
0.7
0.6
0.5
0.4
0.3
0.2
0.1
0
Yb
Ce
(a)
0
0.02
0.04
0.06
0.08
0.10
0.12
0.14
Al in T Site (Cation Fraction)
REE Partition Coefficient
Yb
Ce
(b)
Increasing Al3+ in T Site
0.75
0.80
0.85
0.90
0.95
1.00
Ca in M2 Site (Cation Fraction)

Figure 7

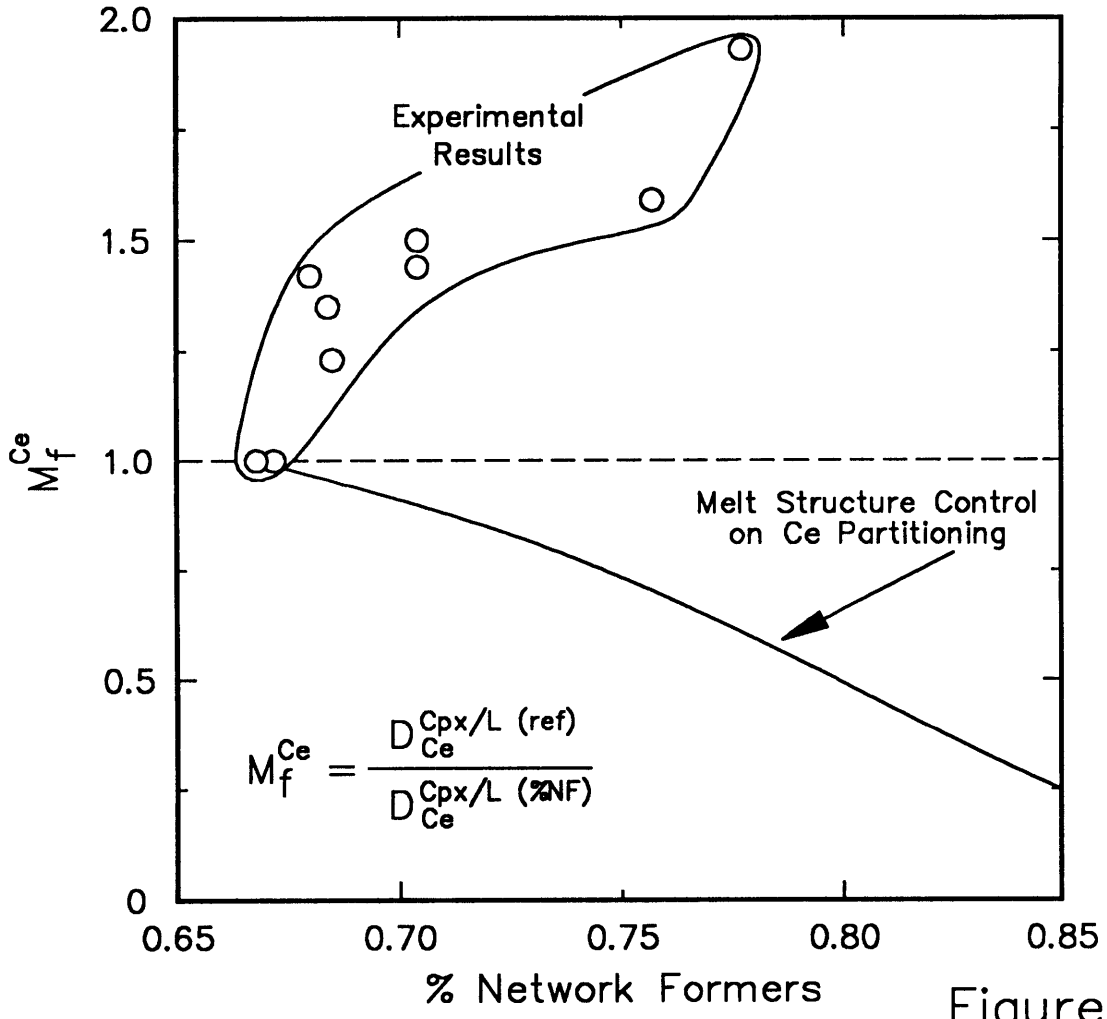
2.0
1.5
1.0
0.5
0
0.65
0.70
0.75
0.80
0.85
% Network Formers
M_f^{Ce}
Experimental Results
Melt Structure Control on Ce Partitioning
$M_f^{Ce} = \frac{D_{Ce}^{Cpx/L\ (ref)}}{D_{Ce}^{Cpx/L\ (\%NF)}}$

Figure 8

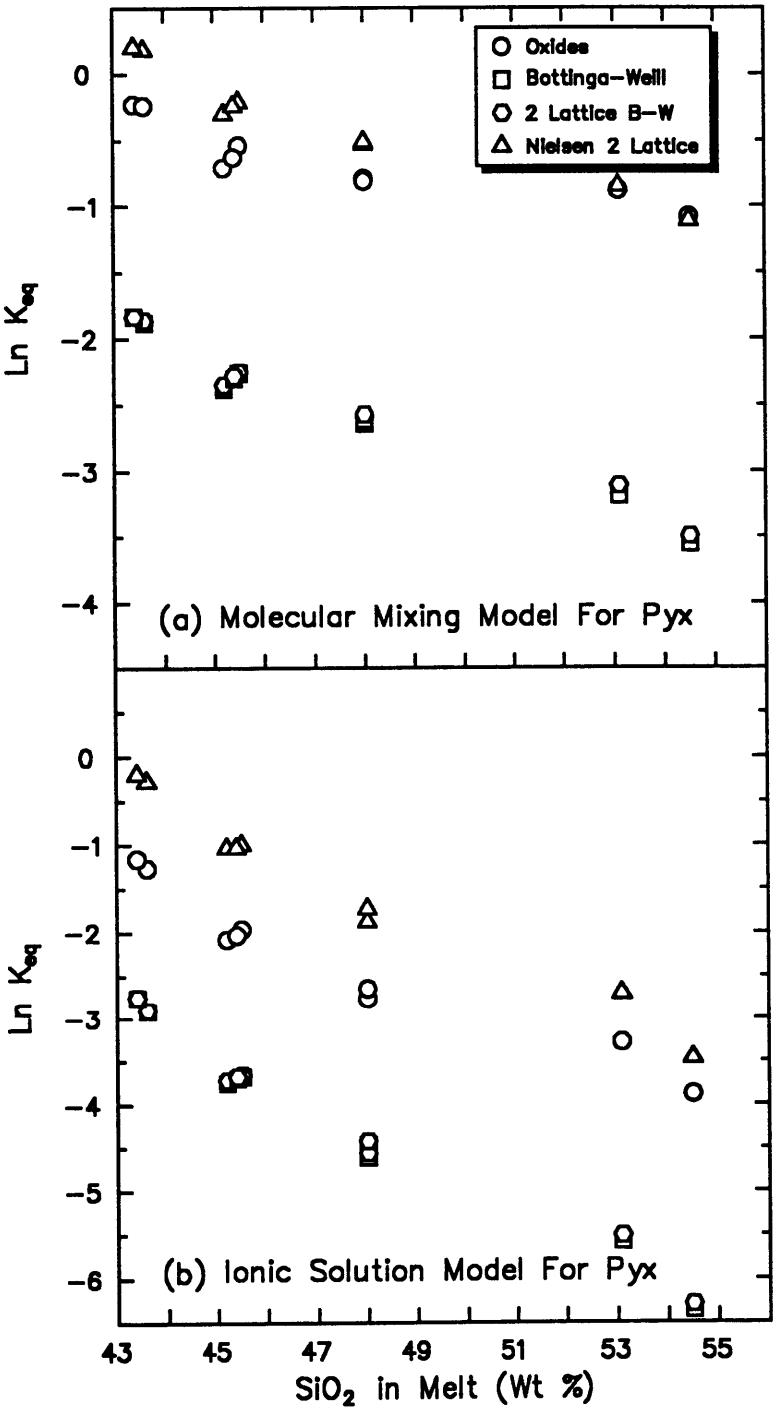
Oxides
Bottinga–Weill
2 Lattice B–W
Nielsen 2 Lattice
Ln K_{eq}
0
−1
−2
−3
−4
(a) Molecular Mixing Model For Pyx
Ln K_{eq}
0
−1
−2
−3
−4
−5
−6
(b) Ionic Solution Model For Pyx
43
45
47
49
51
53
55
SiO_2 in Melt (Wt %)

Figure 9

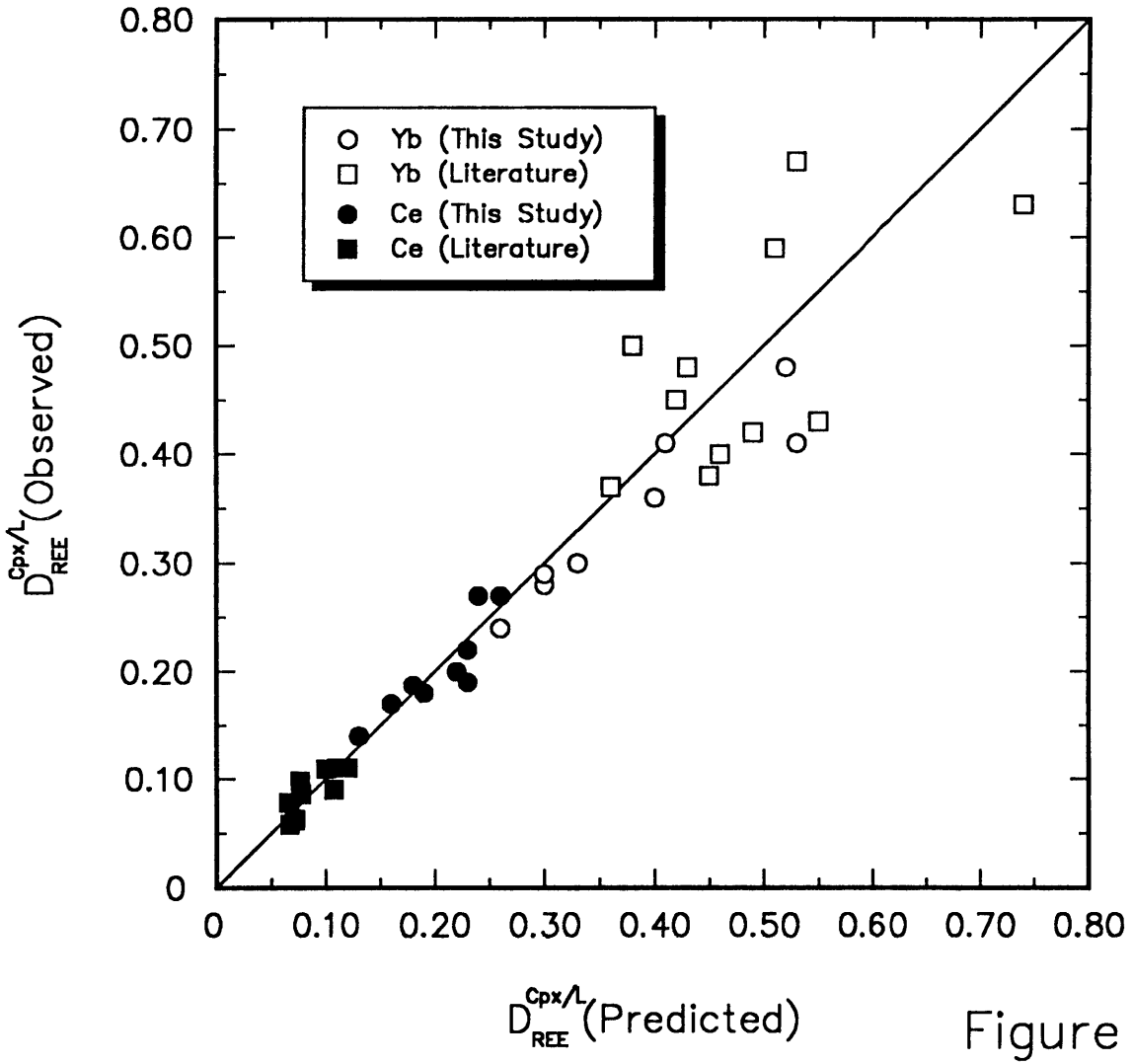
0.80
0.70
0.60
0.50
0.40
0.30
0.20
0.10
0
0
0.10
0.20
0.30
0.40
0.50
0.60
0.70
0.80
Yb (This Study)
Yb (Literature)
Ce (This Study)
Ce (Literature)
$D_{REE}^{Cpx/L}$(Observed)
$D_{REE}^{Cpx/L}$(Predicted)

Figure 10

APPENDIX A.

PROCEDURES FOR PERFORMING HYDROUS PISTON CYLINDER EXPERIMENTS IN AuPd CAPSULES

Inner capsules for hydrous piston-cylinder experiments are fabricated from a 0.25″ length of 0.100″ o.d. $Au_{80}Pd_{20}$ or $Au_{90}Pd_{10}$ tubing, with a wall thickness of 0.007″, that is triple-crimped at one end and welded shut. A drill blank is then inserted into the capsule, it is placed on a benchtop, and the drill blank is tapped with a hammer to flatten the bottom of the capsule. An outer capsule is fabricated in the same way from a 0.4″ length of 0.1875″ o.d. $Au_{80}Pt_{20}$ tubing with a wall thickness of 0.006″ wall thickness. The outer capsule can also be made from AuPd or Pt tubing.

A crucible to hold the inner capsule during conditioning is fabricated from a 0.5″ length of 0.25″ diameter MgO rod. A hole is drilled through the rod, approximately 0.05″-0.10″ from one end and perpendicular to it's long axis, using a #47 drill bit. A second hole is then drilled in the rod parallel to the long axis, 0.4″ deep, using 3 progressively larger drill bits (#47, #37, then #27). New drill bits are required after making 4-5 crucibles, as they tend to dull quickly.

Conditioning $Au_{80}Pd_{20}$ inner capsules for experiments is was done by packing the capsule with the rock powder to be used in the experiment, placing it into an open MgO crucible, and hanging it in the hotspot of a vertical gas mixing furnace using a loop of Pt wire that passes through the hole near the top of the crucible (Fig. 1). The capsule is held at 1250°C, with the f_{O_2} controlled at 1 log unit below the FMQ buffer, for 48 hrs. The silicate melt has a strong tendency to climb out of the metal capsules, so that they have to be removed from the furnace and repacked with rock powder every 2-3 hrs until the melt remains in place. When repacking a capsule that contains some silicate glass, it is important to carefully tap on the top of the glass using a drill blank, as it commonly forms a "skin" across the mouth of the capsule with no glass underneath. After completion of the conditioning run, the silicate glass is carefully chipped out of the capsule by breaking it

up with a drill blank and hammer, then cleaning out the capsule with a teasing needle. The metal tends to be brittle once it contains Fe, so chipping out the glass must be done very carefully or the capsule will rip.

Once most of the glass has been removed, the capsule is placed into an ultrasonic cleaner for 2-3 hrs in a warm bath of HF and dilute HNO_3 to dissolve any remaining silicate. Cleaning the capsule a second time is often required. The ternary alloy in the capsule from experiment B304, which experienced negligible Fe exchange with the silicate after 24 hrs at 1.2 GPa, 1215°C, consists of 78.2±0.6 wt% Au, 19.9±0.2 wt% Pd, and 1.35±0.05 wt% Fe.

The conditioning procedure is modified slightly for $Au_{90}Pd_{10}$ alloy due to its lower melting point (~1225°C versus ~1350°C for $Au_{80}Pd_{20}$ at 1 atm). Most high Mg# basalts are fairly crystalline at these lower temperatures, making conditioning inefficient. For these capsules, a silicate melt with similar FeO content (7.23 wt% versus 7.82 wt%) but significantly lower MgO (4.45 wt% versus 10.49 wt%) are recommended, in order to produce a large amount of melt at a lower temperature. It may be necessary to adjust the f_{O_2} to account for differences between the FeO content of the material used for conditioning and that present in experimental starting materials. The ternary alloy in the capsule from experiment B359, which experienced negligible Fe exchange with the silicate after 20 hrs at 1.6 GPa, 1260°C, consists of 88.5±0.6 wt% Au, 10.0±0.1 wt% Pd, and 0.68±0.01 wt% Fe.

After an inner capsule has been conditioned and cleaned out, ~15 mg of powdered starting material is packed into the capsule, it is closed using a single crimp across the top of the capsule, and it is welded shut. Welding AuPdFe alloys is especially easy. The sealed capsule is placed into a graphite sleeve, and then into an outer capsule made from either $Au_{80}Pt_{20}$ or Pt, depending on the temperature at which the experiment was to be performed (experiments performed at 2.0 GPa and temperatures of 1275°C or higher required Pt). Graphite powder is packed into the outer capsule, and it is welded shut and

placed into a high-density Al_2O_3 sleeve. This assembly is then centered in the hotspot of a graphite furnace using MgO spacers, and an MgO wafer is used to separate the thermocouple from the top of the capsule.

FIGURE CAPTIONS

Figure 1. Cut-away view of AuPd capsule inside of MgO crucible during conditioning run.

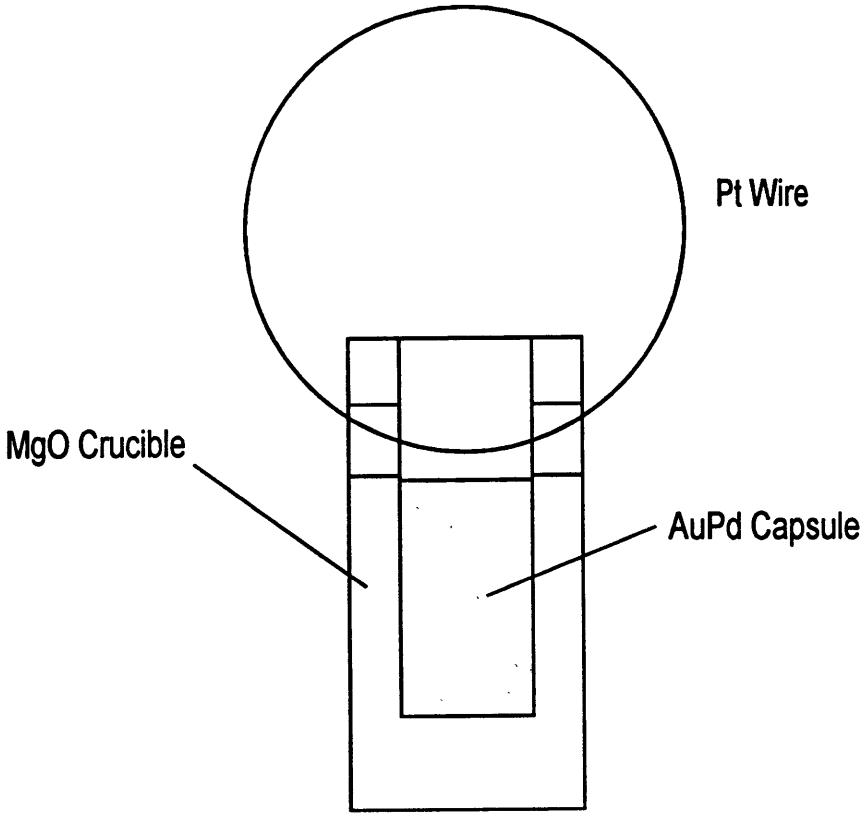

Figure 1

APPENDIX B.

CONSTRUCTION OF A SULFUR FURNACE AND PROCEDURES FOR PERFORMING GAS MIXING EXPERIMENTS

This appendix describes (1) the construction of a gas mixing furnace for performing experiments at controlled f_{O_2} and f_{S_2} conditions, (2) running phase equilibria experiments at controlled f_{O_2} and f_{S_2} conditions in San Carlos olivine crucibles, and (3) calculating the CO_2, CO, and SO_2 mixing proportions for a desired set of f_{O_2}/f_{S_2} conditions.

CONSTRUCTION OF A SULFUR FURNACE

The furnace used for performing gas mixing experiments at controlled f_{O_2} and f_{S_2} conditions is a Deltech DT31VT vertical quenching furnace fitted with a short (365 mm) alumina muffle tube. The short tube provides space between the benchtop and the bottom of the furnace for inserting the silica-glass tube that holds the experimental charge. The alumina tube is suspended so that the bottom hangs ~5 mm below the furnace box (Fig. 1). Donut-shaped pyrophyllite spacers are placed in the top and bottom of the alumina tube. These spacers are beveled on one side to fit snugly into the alumina tube, and there is a hole in the upper spacer for a thermocouple (Fig. 1). A 445 mm long silica-glass muffle tube (19 mm o.d.; 16 mm i.d.) is fitted through the holes in the center of the pyrophyllite spacers so that it is suspended in the center of the alumina tube. It is held in place using hose clamps on the top and bottom. Zirconia insulation is placed between the hose clamps and the silica-glass tube. This tube should be inserted with the furnace at room temperature, and then slowly heated to ~1000°C. Once at temperature, the silica-

glass tubes must be maintained at ~1000°C as they recrystallize at high temperature, and tend to crack if brought back down to room temperature. The top of the silica-glass tube is sealed using a pyrophyllite plug that is beveled on one side, and General Electric Red RTV 106 high temperature sealant.

A small silica-glass tube, which served as the gas inlet, is inserted into a hole in the center of the pyrophyllite plug prior to construction of the furnace, and sealed using RTV 106. Gases are fed into the furnace through a length of red rubber tubing that is fitted over this glass tube and sealed with RTV 106. The bottom of the silica-glass muffle tube is sealed using a pyrophyllite cup. This cup has a hole in the bottom for the silica-glass rod that holds the experiment, and a hole in the side for the gases to exit. The gas outlet consists of an "L" shaped silica-glass tube, wrapped with heating tape, that feeds the gas into a pyrex flask. The heating tape keeps sulfur from being deposited in the outlet tube. The gases exit the pyrex flask through a length of red rubber tubing, and are fed into the ventilation hood. Some of the furnace gas escapes through the space between the silica-glass rod holding the experiment and the pyropyllite cup.

A thermocouple is fitted through a hole in the upper pyrophyllite spacer so that it sits in the space between the alumina and silica-glass muffle tubes, with the bead at the same level as the experiment. It is held in place using an alligator clip. The temperature difference between the position of the thermocouple and the sample must be calibrated (it is 8°C for the MIT furnace). Best results are obtained by consistently placing the thermocouple bead against the silica-glass tube. The temperature readings will vary by 5-10°C if placement of the thermocouple is not consistent from experiment to experiment.

It is also important to frequently clean the copper leads that the thermocouple wires are attached to, as they tend to react with any sulfur that escapes from the bottom of the furnace.

PERFORMING CONTROLLED f_{O_2}/f_{S_2} GAS MIXING EXPERIMENTS

Crucibles fabricated from single crystals of San Carlos olivine provide capsules that do not react with sulfur-rich furnace gases, and are inert (although there may be some Fe/Mg exchange) with respect to olivine-saturated experiments (e.g., Ehlers et al., 1992). Crucibles are fabricated from 8-16 g tumbled crystals of San Carlos olivine cut, using a jeweler's saw, into blocks that are ~10-15 mm on a side (several blocks can be cut from a large crystal). A hole is cored into the center of the block that is 4 mm in diameter and ~5 mm deep. Notches are cut vertically into opposite sides of the crucible using the jewelers saw. A 235 mm length of solid silica-glass rod (?? mm in diameter) is cut, and horizontal notches are made a few millimeters from the top, on opposite sides of the rod. The crucible is packed with 40-70 mg of starting material, and fastened to the top of the glass rod using a length of 0.2 mm Pt wire that is fitted into the notches in the crucible and the rod.

Once the experimental charge has been assembled, the silica-glass rod is fitted through the hole in the bottom of the pyrophyllite cup that is used to seal the lower end of the glass furnace tube, so that the experiment sits in the bottom of the cup. The cup is then placed onto the bottom of the glass furnace tube, and held in place using a second glass rod inserted between the cup and the bench top. RTV 106 is then used to secure the cup. The RTV cures sufficiently after 30 minutes to support the weight of the cup, and

the glass rod holding it in place is removed. The gas outlet tube is placed into the hole in the side of the cup and the gases are turned on. The gases should be left flowing for 30 minutes to allow them to equilibrate in the furnace. The experiment is then pushed up into the furnace hot spot, a second glass rod is inserted between the one holding the experiment and the benchtop, and the 2 rods are fastened together using a piece of electrical tape. It is important that the second glass rod be cut to the proper length, so that the crucible sits in the furnace hot spot. The furnace is then brought to the run temperature over ~60 minutes. At the end of the experiment, the lower glass rod is removed and the upper rod slides down, quenching the experiment against the pyrophyllite cup.

CALCULATING GAS MIXING PROPORTIONS

Because there is no reliable method to directly measure the f_{O_2}/f_{S_2} conditions in a furnace such as the one described above, the mixing proportions of CO_2, CO, and SO_2 necessary to produce a desired set of conditions must be calculated. Source code for a PASCAL program to calculate these proportions is provided below. The calculation method is based on an assumption of ideal mixing of the gas components at high temperatures and low pressures. Expressions relating Gibbs free energy change to equilibrium constants for the following linearly independent reactions, involving 9 gas species, were written using thermochemical data from the JANAF tables (Chase et al., 1985):

$$CO + \frac{1}{2}S_2 = COS$$

$$CO_2 + S_2 = CS_2 + O_2$$

$$2SO_2 = S_2 + 2O_2$$

$$CO + SO_2 = SO + CO_2$$

$$CO_2 + SO_2 = SO_3 + CO$$

$$SO_2 + \frac{1}{2}O_2 = SO_3$$

Mass balance equations relating each element (C, O, and S) to the stable gas species are then used to determine the mixing proportions of CO_2, CO, and SO_2 required for a desired combination of f_{O2} and f_{S2}.

```
                    PROGRAM GasMix1350;
  (*Program to calculate mixing proportions of CO, CO2 and SO2 necessary for a desired
                  combination of oxygen and sulfur fugacities at 1350°C*)
USES
  Printer;

VAR
  PO2, PCO, PCO2, PCOS, PCS2, PS2, PSO, PSO2, PSO3, PTot,
  C1, C2, C3, C4, C, O, S, CO2, CO, SO2, GasTotal,
  GO2, GCO, GCO2, GCOS, GCS2, GS2, GSO, GSO2, GSO3,
  GFO2, GFCO, GFCO2, GFCOS, GFCS2, GFS2, GFSO,
  GFSO2, GFSO3, K1, K2, K3, K4, K5, K6, EXPT, PTotal,
  LgPO2, LgPS2, LgPSO, LgPSO2, LgPSO3, LgPCS2, LgPCOS,
  LgPCO, LgPCO2, Flow, SO2fl, COfl, CO2fl: REAL;

PROCEDURE DataTemp;
  (*Procedure calculates Gibb free energy function for desired temperature using JANAF
                      data for next highest and lowest temperatures*)
   BEGIN
    GFO2 := 232.768 + (234.462 - 232.768)*0.2315;
    GFCO := 224.216 + (225.839 - 224.216)*0.2315;
    GFCO2 := 253.753 + (256.343 - 253.753)*0.2315;
    GFCOS := 274.869 + (277.605 - 274.869)*0.2315;
    GFCS2 := 284.153 + (287.012 - 284.153)*0.2315;
    GFS2 := 258.748 + (260.582 - 258.748)*0.2315;
    GFSO := 250.791 + (252.547 - 250.791)*0.2315;
    GFSO2 := 289.533 + (292.144 - 289.533)*0.2315;
    GFSO3 := 312.793 + (316.398 - 312.793)*0.2315;
   END;

PROCEDURE Thermodata;
    (*Procedure calculates Gibbs free energies for the relevent gas species at 1350°C *)
  BEGIN
   EXPT := 1350 + 273.15;
   GO2 := (-(GFO2 * EXPT));
   GCO := (-110527 - (GFCO * EXPT));
   GCO2 := (-393522 - (GFCO2 * EXPT));
   GCOS := (-138407 - (GFCOS * EXPT));
   GCS2 := (116943 - (GFCS2 * EXPT));
   GS2 := (128600 - (GFS2 * EXPT));
   GSO := (5007 - (GFSO * EXPT));
   GSO2 := (-296842 - (GFSO2 * EXPT));
   GSO3 := (-395765 - (GFSO3 * EXPT));
  END;
```

```
PROCEDURE EquConst;
    (*Procedure calculates equilibrium constants for 6 linearly independent reactions at
          1350°C using the Gibbs free energies calculated in Thermodata *)
 BEGIN
  K1 := Exp(-((GCOS - ((0.5*GS2)+(GCO)))/(8.314*EXPT)));
  K2 := Exp(-(((GCS2 + GO2) - (GCO2 + GS2))/(8.314*EXPT)));
  K3 := Exp(-(((GS2 + (2*GO2)) - (2*GSO2))/(8.314*EXPT)));
  K4 := Exp(-(((GSO + GCO2) - (GCO + GSO2))/(8.314*EXPT)));
  K5 := Exp(-(((GSO3 + GCO) - (GCO2 + GSO2))/(8.314*EXPT)));
  K6 := Exp(-((GSO3) - (GSO2 + (0.5*GO2)))/(8.314*EXPT));
 END;

PROCEDURE CalcFugac;
     (*Procedure calculates fugacities of 6 gas species using the equilibrium constants
          calculated in EquConst, and 1 gas specie using the closure constraint*)
 BEGIN
  WRITELN;
  WRITE ('Enter desired -Log PO2: ');READLN (LgPO2);
  WRITE ('Enter desired -Log PS2: ');READLN (LgPS2);
  PO2 := Exp(2.303*(-LgPO2));PS2 := Exp(2.303*(-LgPS2));
  PTot := 1;K3 := Sqrt(K3);
  PSO2 := ((Sqrt(PS2))*(PO2))/(K3);
  PSO3 := (K6)*(PSO2)*(Sqrt(PO2));
  PSO := ((K4*K5)*(Sqr(PSO2)))/(PSO3);
  C1 := (K1*K5*PSO2*Sqrt(PS2))/(PSO3+(K5*PSO2)+(K1*K5*PSO2*Sqrt(PS2)));
  C2 := (K5*PSO2)/(PSO3 + (K5*PSO2));
  C3 := (K2*PS2)/(PO2 + (K2*PS2));
  C4 := ((C3*(1-C2)) + (C1*C3*(C2-1)))/(1 - (C3*C2) + (C1*C3*(C2-1)));
  PCS2 := C4*(PTot - PO2 - PS2 - PSO - PSO2 - PSO3);
  PCOS := C1*(PTot - PO2 - PS2 - PSO - PSO2 - PSO3 - PCS2);
  PCO := C2*(PTot - PO2 - PS2 - PSO - PSO2 - PSO3 - PCS2 - PCOS);
  PCO2 := (PTot - PO2 - PCO - PCOS - PCS2 - PS2 - PSO - PSO2 - PSO3);
  LgPSO := (Ln(PSO))/2.303;LgPSO2 := (Ln(PSO2))/2.303;
  LgPSO3 := (Ln(PSO3))/2.303;LgPCS2 := (Ln(PCS2))/2.303;
  LgPCOS := (Ln(PCOS))/2.303;LgPCO := (Ln(PCO))/2.303;
  LgPCO2 := (Ln(PCO2))/2.303;
 END;

PROCEDURE CalcGasMix;
  (*Procedure converts partial pressures calculated in CalcFugac into C, S, and O atoms,
                and then into CO2:CO:SO2 to be input into furnace*)
 BEGIN
  C := PCO + PCO2 + PCOS + PCS2;
  O := (2*PO2) + PCO + (2*PCO2) + PCOS + PSO + (2*PSO2) + (3*PSO3);
```

```
  S := PCOS + (2*PCS2) + (2*PS2) + PSO + PSO2 + PSO3;
  CO2 := O - (C + (2*S));
  CO := (2*(C + S)) - O;
  SO2 := S;
  GasTotal := CO2 + CO + SO2;
  CO2 := CO2/GasTotal; CO :=CO/GasTotal; SO2 := SO2/GasTotal;
 END;

PROCEDURE FlowRate;
                (*Procedures to calculate flow rates for individual gases*)
 BEGIN
  WRITELN;
  WRITE ('Enter desired total flow rate in mL/s: ');READLN (Flow);
  CO2fl := CO2*Flow; COfl := CO * Flow; SO2fl := SO2 * Flow;
END;

BEGIN
 DataTemp;
 ThermoData;
 EquConst;
 CalcFugac;
 CalcGasMix;
 FlowRate;
 WRITELN;
 WRITELN ('Partial pressures of gas species: ');
 WRITE ('Log PO2: ',-LgPO2:4:2); WRITE ('  Log PS2: ',-LgPS2:4:2);
 WRITELN ('  Log PSO2: ',LgPSO2:4:2);WRITE ('Log PSO3: ',LgPSO3:4:2);
 WRITE ('  Log PSO: ',LgPSO:4:2);WRITELN ('  Log PCS2: ',LgPCS2:4:2);
 WRITE ('Log PCOS: ',LgPCOS:4:2); WRITE ('  Log PCO: ',LgPCO:4:2);
 WRITELN ('  Log PCO2: ',LgPCO2:4:2);
 WRITELN;
 WRITELN ('Gas mixing ratios: ');
 WRITE ('CO2: ',CO2:4:2);WRITE ('  CO: ',CO:4:2);WRITELN ('  SO2: ',SO2:4:2);
 WRITELN;
 WRITELN ('Gas flow rates: ');
 WRITE ('CO2: ',CO2fl:4:2,' mL/s');
 WRITE ('  CO: ',COfl:4:2,' mL/s');
 WRITELN ('  SO2: ',SO2fl:4:2,' mL/s');
 WRITELN;
END.
```

REFERENCES

Chase M.W. Jr, Davies C.A., Downey J.R. Jr., Frurip D.J., McDonald R.A., and Syverud A.N. (1985) JANAF Thermochemical Tables, 3rd ed.. *J. Phys. Chem. Ref. Data.*, 14, Suppl. 1, Part I, Al-Co, Part II, Cr-Zr.

Ehlers K., Grove T.L., Sisson T.W., Recca S.I., and Zervas D.A. (1992) The effect of oxygen fugacity on the partitioning of nickel and cobalt between olivine, silicate melt, and metal. *Geochim. Cosmochim. Acta*, **56**, 3733-3743.

FIGURE CAPTIONS

Figure 1. Geometry of furnace for performing controlled f_{O_2}/f_{S_2} gas mixing experiments.

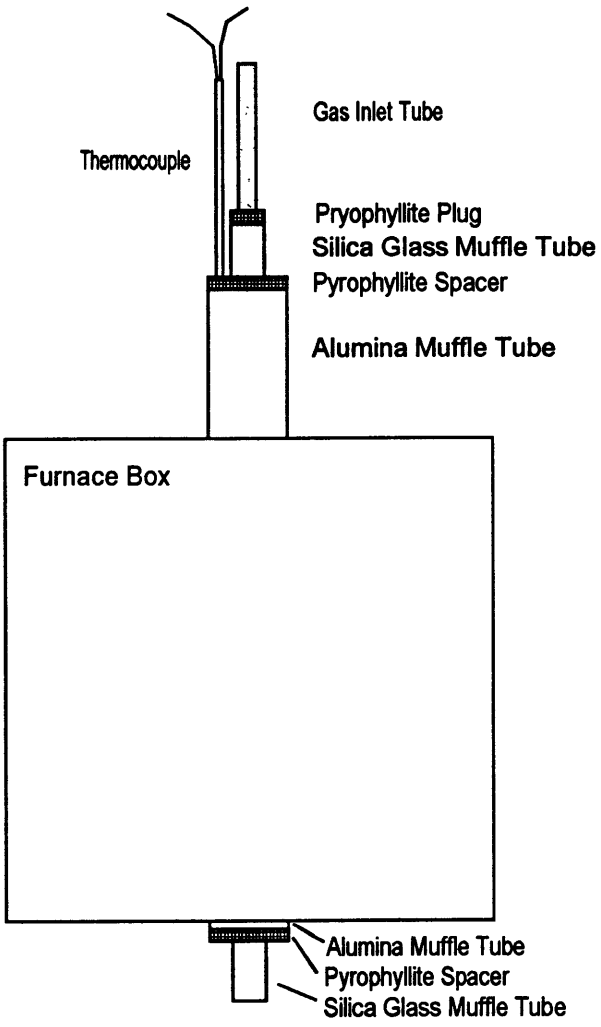
Gas Inlet Tube
Thermocouple
Pryophyllite Plug
Silica Glass Muffle Tube
Pyrophyllite Spacer
Alumina Muffle Tube
Furnace Box
Alumina Muffle Tube
Pyrophyllite Spacer
Silica Glass Muffle Tube

Figure 1

APPENDIX C.

APPARENT ANGLE MEASUREMENTS

This appendix contains the apparent angle measurements from the experimental study presented in Chapter 2. All measurements are in degrees. Angle measurements were made using a protractor and reverse-polarity SEM images at a magnification of 3600x.

Table 1. Apparent angle measurements for Experiment FeS-4.

90	70	90	68	46	64	82	81	102	60	90	96	106	72	51	104	72	41	96	125
90	59	59	102	63	70	103	90	90	112	100	81	90	77	130	90	98	121	75	108
96	122	116	149	126	113	90	107	76	90	90	98	69	78	94	99	75	66	90	78
84	90	90	67	90	65	121	110	90	46	100	105	115	114	74	79	95	106	90	95
108	75	75	44	119	104	47	69	98	77	51	90	51	97	136	119	105	77	98	130
59	72	68	143	98	135	58	102	90	115	123	122	63	98	66	58	90	90	115	65
90	107	90	125	107	65	81	61	77	74	66	94	93	124	90	81	105	52	68	76
44	65	100	80	90	73	99	80	106	67	46	90	117	101	98	90	50	104	99	90
119	107	90	90	109	64	69	95	82	54	105	113	118	100	98	104	48	68	81	45
77	86	101	107	115	113	127	56	90	90	115	76	90	101	58	102	90	82	55	77

Table 2. Apparent angle measurements for Experiment FeS-7.

96	110	43	71	57	75	122	90	103	100	90	73	113	90	90	95	44	75	45	90
90	60	98	98	100	118	120	79	125	90	78	73	90	76	70	103	90	80	86	90
69	55	110	115	77	65	82	110	98	112	90	86	97	70	134	59	90	140	85	99
67	45	90	118	102	75	77	78	93	78	60	90	90	62	100	65	70	97	68	111
106	86	110	87	94	81	90	96	110	90	97	106	114	90	80	105	61	78	38	43
46	80	90	105	115	60	68	84	84	90	102	76	97	106	82	95	80	125	118	61
32	66	90	119	108	118	90	74	90	64	68	75	76	109	84	83	87	104	75	74
100	105	101	97	102	33	90	117	54	105	75	87	105	85	65	102	108	114	104	37
53	55	74	59	105	130	80	82	101	99	115	117	96	66	100	121	96	96	97	84
72	99	136	120	61	110	130	97	98	118	111	127	72	86	89	83	120	90	90	110

Table 3. Apparent angle measurements for Experiment FeS-1.

91	90	76	52	113	80	90	64	73	90	62	76	52	87	65	82	97	90	56	84
80	95	94	88	84	84	102	114	95	90	116	75	66	90	92	54	96	55	98	83
99	75	59	62	72	78	85	108	96	120	77	94	84	100	51	84	90	81	84	81
96	72	114	73	118	85	68	75	115	59	70	116	90	85	74	67	90	104	62	78
60	85	106	100	43	90	53	53	103	84	57	101	101	101	99	87	80	98	98	65
81	86	72	63	87	65	102	82	90	98	100	95	80	84	65	85	82	89	93	97
82	71	30	85	80	99	63	97	93	70	113	96	102	104	90	101	76	84	59	75
90	101	96	100	99	78	61	50	84	80	73	73	50	99	94	65	67	76	81	70
100	92	39	85	78	93	75	95	90	72	109	102	83	80	99	114	100	85	67	81
96	66	99	93	71	117	102	100	60	85	98	63	60	79	100	84	109	84	81	80

Table 4. Apparent angle measurements for Experiment FeS-3.

81	60	82	79	91	99	64	78	117	85	71	115	77	98	82	62	90	96	97	102
78	66	40	62	82	90	82	79	74	78	79	79	98	129	90	94	136	101	94	98
90	58	100	114	85	90	106	80	53	98	80	96	80	86	102	77	85	97	90	58
126	101	53	59	62	90	75	81	74	74	74	107	102	82	100	102	90	90	99	90
99	130	81	64	112	115	78	83	49	93	102	76	52	90	52	84	44	71	101	90
61	79	102	111	108	106	100	97	80	64	96	41	32	75	66	90	108	103	87	85
96	101	104	86	108	85	80	81	93	95	112	80	94	44	102	86	98	130	83	74
95	83	76	90	116	109	73	117	73	61	90	84	85	48	81	78	43	94	80	90
100	90	45	68	99	90	105	52	35	90	97	90	40	67	85	90	90	77	100	99
95	114	112	95	106	60	114	71	65	84	101	80	116	100	90	76	68	90	81	90

Table 5. Apparent angle measurements for Experiment FeS-14.

90	92	75	63	62	93	105	67	68	116	97	72	90	74	53	85	90	86	69	59
84	76	113	64	90	107	98	70	50	85	40	75	80	95	74	78	60	81	52	85
65	105	101	70	115	69	78	82	54	96	77	103	94	97	75	95	96	85	79	99
80	50	134	86	73	121	60	72	82	80	65	111	115	63	76	65	106	99	80	88
81	90	104	90	82	49	15	49	84	57	74	82	66	47	81	69	78	42	70	96
88	81	94	95	103	69	78	58	66	84	106	90	83	90	75	104	64	84	90	94
84	85	72	81	60	77	79	90	67	77	96	105	49	85	64	92	96	100	113	84
111	96	102	70	82	85	82	101	50	75	90	82	52	90	59	95	50	76	90	87
68	68	84	78	86	36	55	82	107	103	90	78	87	38	78	68	109	94	91	81
60	70	106	100	80	76	75	40	83	42	56	81	76	71	61	57	73	67	90	98

Table 6. Apparent angle measurements for Experiment FeS-9.

40	64	73	82	80	82	90	98	100	104	62	75	46	75	68	69	75	74	40	63
75	65	67	53	73	99	65	96	80	72	90	69	71	50	74	85	79	75	104	105
76	90	65	98	57	76	70	66	104	67	76	45	75	41	62	86	77	85	79	48
30	52	80	73	82	62	70	54	90	90	60	43	57	66	102	51	78	70	72	82
75	73	59	55	22	90	114	82	78	68	104	96	70	101	53	65	61	110	90	82
76	68	90	69	75	34	70	67	67	115	18	118	70	80	67	66	84	60	81	103
52	63	72	40	43	61	76	65	100	90	77	46	30	90	97	70	60	75	70	50
62	98	90	33	64	75	60	76	82	110	61	65	77	55	23	80	50	60	70	30
47	74	80	45	65	62	74	56	68	68	52	90	90	80	90	65	65	55	85	90
90	85	60	68	62	63	73	80	76	72	76	83	34	45	90	103	90	67	80	64

Table 7. Apparent angle measurements for Experiment FeS-13.

57	51	69	55	39	30	60	61	71	75	87	75	42	17	58	84	80	73	90	72
104	68	52	57	32	25	55	42	64	40	33	48	69	68	102	64	64	79	86	84
90	60	61	54	98	66	46	50	59	84	77	130	57	42	51	61	96	48	40	54
62	58	80	64	65	73	58	75	90	79	50	54	66	67	62	63	83	69	81	24
28	42	46	73	53	39	66	58	66	35	50	33	25	53	103	70	76	56	58	48
59	81	70	67	43	59	47	51	61	36	79	77	34	58	56	42	59	51	62	30
78	65	56	29	29	56	27	43	49	59	61	73	54	67	55	63	35	54	65	56
71	65	84	56	59	72	58	72	39	90	57	37	76	52	31	77	53	82	31	44
36	72	67	46	43	61	45	90	52	63	61	50	77	55	72	51	54	63	67	78
55	40	55	60	61	75	53	84	50	39	40	47	61	132	58	63	63	48	52	84

Table 8. Apparent angle measurements for Experiment FeS-6.

39	80	36	82	60	69	58	55	35	50	57	53	52	15	90	38	38	90	64	35
90	66	56	53	65	51	45	51	78	38	33	44	81	61	44	50	57	43	30	50
68	45	40	38	48	48	45	26	49	45	41	52	42	60	52	48	32	29	61	69
52	48	65	45	25	53	74	45	77	50	27	33	50	30	90	24	29	69	66	75
78	49	52	40	42	23	52	30	60	40	71	35	48	40	40	75	48	63	45	56
63	55	57	75	71	49	50	62	58	83	61	29	55	48	32	56	73	65	52	53
79	60	48	29	34	42	42	49	43	60	57	62	89	48	73	62	65	55	40	53
38	43	40	59	80	66	60	57	78	56	51	25	65	67	57	60	69	50	48	58
48	54	60	54	40	69	41	31	68	58	54	44	52	54	41	90	90	90	40	38
46	56	58	30	48	61	42	40	54	51	48	63	35	45	54	33	16	26	49	72

APPENDIX D.

PROCEDURE FOR CALCULATING CPX/MELT PARTITION COEFFICIENTS

In order to calculate Cpx/melt partition coefficients using the predictive expressions given in Chapter 4, the melt composition must be recast according to the scheme of Bottinga and Weill (1972), and the pyroxene recalculated into endmember components on the basis of charge balance. As an example we have chosen the compositions of co-existing glass and clinopyroxene in lavas from the Galapagos spreading center (Perfit and Fornari, 1983) given in Table A1. The first step is to convert both basalt and pyroxene analyses from weight percent to mole fraction on a single cation basis. The melt is then recalculated according to the following steps:

(1) $SiO_2 = SiO_2 + PO_{2.5}$

(2) $TiO_2 = TiO_2$

(3) $FeO = FeO + FeO_{1.5}$

(4) $MnO = MnO$

(5) $KAlO_2 = KO_{0.5}$; $AlO_{1.5} = AlO_{1.5} - KO_{0.5}$

(6) $NaAlO_2 = NaO_{0.5}$; $AlO_{1.5} = AlO_{1.5} - NaAlO2$

(7a) If $CaO > \frac{1}{2} AlO_{1.5}$:

$CaAl_2O_4 = \frac{1}{2} AlO_{1.5}$, $CaO = CaO - \frac{1}{2} AlO_{1.5}$

$MgO = MgO$

(7b) If $CaO < \frac{1}{2} AlO_{1.5}$:

$CaAl_2O_4 = CaO$; $AlO_{1.5} = AlO_{1.5} - 2CaO$

$MgAl_2O_4 = \frac{1}{2} AlO_{1.5}$; $MgO = MgO - \frac{1}{2} AlO_{1.5}$

(8) $MeltSum = SiO_2 + TiO_2 + FeO + MnO + KAlO_2 + NaAlO_2 + CaAl_2O_4 + CaO + MgO + MgAl_2O_4$

The recalculated analysis is then normalized to 1.

The pyroxene recalculation involves determining the non-quadrilateral pyroxene components, followed by the quadrilateral components:

(1) Rhodonite = $\frac{1}{2}$ MnO

(2) Jadeite = $NaO_{0.5}$; $AlO_{1.5} = AlO_{1.5} - NaO_{0.5}$

(3) Ti-Tschermakite = TiO_2; $CaO = CaO - TiO_2$;

$AlO_{1.5} = AlO_{1.5} - 2TiO_2$

(4) Cr-CaTs = $CrO_{1.5}$; $CaO = CaO - CrO_{1.5}$;

$AlO_{1.5} = AlO_{1.5} - CrO_{1.5}$

(5) CaTs = $\frac{1}{2}AlO_{1.5}$; $CaO = CaO - \frac{1}{2}AlO_{1.5}$

(6) Diopside = CaO × Mg/(Mg+Fe); MgO = MgO – [CaO × Mg/(Mg+Fe)]

(7) Hedenbergite = CaO × Fe/(Mg+Fe); FeO = FeO – [CaO × Fe/(Mg+Fe)]

(8) Enstatite = $\frac{1}{2}$MgO; Ferrosilite = $\frac{1}{2}$FeO

(9) CpxSum = Rhod + Jad + Ti-Tsk + CrTs + CaTs + Di + Hed + En + Fs

The recalculated analysis is then normalized to 1, and the diopside and hedenbergite components are summed to form X_{Di+Hed}^{Cpx}

Once the basalt and pyroxene analyses have been recalculated, all of the relevant values are substituted into the predictive expressions for molar Ce and Yb partition coefficients given in Table 5. The molar partition coefficients predicted by the expressions are converted to weight ratio partition coefficients through multiplication by the conversion factor α:

$$\alpha = \left[\frac{\text{CpxSum}}{\text{MeltSum}}\right] \bullet \left[\frac{\sum_i \left(C_i^{Cpx} / mw_i\right)}{\sum_j \left(C_j^{Liq} / mw_j\right)}\right]$$

where C_i^{Cpx} is the weight percent of oxide *i* in the Cpx, mw_i is the molecular weight of oxide *i*, C_j^{Liq} is the weight percent of oxide *j* in the silicate melt, mw_j is the molecular weight of oxide *j*, and the summations are over all oxides in each phase.

REFERENCES

Bottinga Y. and Weill D.F. (1972) The viscosity of magmatic silicate liquids: A model for calculation. *Am. J. Sci.* **272**, 438-475.

Perfit M.R. and Fornari D.J. (1983) Geochemical studies of abyssal lavas recovered by DSRV *Alvin* from eastern Galapagos rift, Inca transform, and Ecuador rift 2. Phase chemistry and crystallization history. *J. Geophys. Res.* **88**, 10,530-10,550.

Table 1. Sample calculation of Cpx/melt partition coefficients for Ce and Yb.

Basaltic Glass and Clinopyroxene Compositions for Sample 1000-5B (Weight Percent)

Phase	SiO_2	TiO_2	Al_2O_3	Cr_2O_3	FeO*	MnO	MgO	CaO	Na_2O	P_2O_5	Total
Glass	51.40	1.33	14.17	—	11.43	0.19	7.37	11.39	2.42	0.14	99.84
Clinopyroxene	52.82	0.13	2.24	0.23	6.49	—	18.73	19.08	—	—	99.72

Bottinga-Weill Components (Mole Fraction)

SiO_2	TiO_2	FeO	MnO	$KAlO_2$	$NaAlO_2$	$CaAl_2O_4$	CaO	MgO	$MgAl_2O_4$	Total
0.5717	0.0111	0.1061	0.0018	0.0000	0.0521	0.0666	0.0688	0.1219	0.0000	1.0001

Clinopyroxene Components (Mole Fraction)

Rhod	Jad	Ti-Tsk	CrTs	CaTs	Di	Hed	En	Fs	Total
0.0000	0.0000	0.0035	0.0066	0.0410	0.5773	0.1122	0.2172	0.0422	1.0000

	Molar Partition Coefficients	α	Weight Partition Coefficients
Ce	0.2432	0.3062	0.0745
Yb	1.0654	0.3062	0.3262